UNIVERSITÉ LAVAL

Microstructural characterization and modeling of concrete damaged by Alkali-Silica Reaction (ASR)

Thèse

Chi Zhang

Doctorat en génie civil

Philosophiae doctor (Ph.D)

Québec, Canada

Microstructural characterization and modeling of concrete damaged by Alkali-Silica Reaction (ASR) expansion

Thèse de doctorat

Chi Zhang

Sous la direction de :

Luca Sorelli, directeur de recherche

Benoït Fournier, codirecteur de recherche

Josée Duchesne, codirecteur de recherche

Josée Bastien, codirecteur de recherche

Résumé

La réaction alcalis-silice (RAS) est un des principaux mécanismes nuisibles affectant la durabilité du béton. Le programme de recherche effectué dans le cadre de ce doctorat comprend deux parties (3 phases), soit la caractérisation microstructurale de produits de la RAS et la modélisation du mécanisme d'endommagement du béton par la RAS. Les résultats expérimentaux de cette recherche fourniront de nouvelles données sur les propriétés microstructurales de bétons affectés par la RAS.

Les travaux effectués lors de la première phase du programme expérimental avaient pour objectif de caractériser les propriétés micromécaniques des produits de la RAS à l'aide de nouvelles techniques de nano- et micro-indentation, avec emphase portée sur leur propriété en viscosité. Les échantillons de béton utilisés lors du programme d'essais ont été extraits d'un pavage en béton fortement affecté par la RAS et situé dans la région de Bécancour (Québec). Le béton est caractérisé par de nombreuses particules de granulats de calcaire à grains fins contenant des microfissures remplies de produits secondaires de RAS; les fissures s'étendent dans la pâte de ciment pour former un réseau se propageant de particule en particule. Après une préparation soigneuse de l'échantillon par polissage, la surface des particules de granulats et des veinules apparaissant dans ces particules (i.e. microfissures remplies de produits cristallins de réaction) ont été examinées par *Atomic Force Microscopy* (AFM) avant de procéder aux essais de nano-indentation. Des valeurs de module et de dureté ont été mesurées pour les produits de réaction par micro- et nano-indentation. Les résultats de ces essais indiquent que les produits cristallins de RAS offrent un comportement de relaxation important atteignant environ 40%. De plus, un modèle rhéologique simplifié est proposé permettant de reproduire les courbes de relaxation sous charge et les valeurs asymptotiques. Ces résultats suggèrent que la relaxation des produits de RAS est importante et principalement irréversible.

Les travaux de la deuxième phase du programme expérimental ont permis d'explorer l'utilisation d'une nouvelle technique de *microscratch* afin de caractériser l'énergie de fracturation (i.e. rigidité) des particules de granulats réactifs de type calcaire dans un béton fortement affecté par la RAS (viaduc routier de la région de Québec). Les particules de granulats montraient typiquement un zonage (zones gris-foncées et gris-pâles) entourant des veinules blanchâtres au sein des particules réactives. En tant que référence, un échantillon de calcaire vierge provenant d'une carrière de la région de Québec a été sélectionné et soumis aux mêmes procédures d'essais. En plus des propriétés élastiques, la rigidité des particules de granulats réactives ont été mesurées statistiquement et se situe autour de 1.5 $MPam^{1/2}$. La rigidité de fracturation des particules de granulats réactives a démontré n'être affecté ni par la direction d'essai par rapport au plan de litage, ni par la zonation qui a d'abord

été interprétée comme des portions montrant des signes de réaction. Ainsi, l'endommagement des particules de granulats semble se situer presqu'essentiellement au niveau des microfissures générées dans les particules réactives.

La dernière phase du programme expérimental s'est concentrée sur la caractérisation des propriétés en fluage et en relaxation des produits cristallins de RAS remplissant les microfissures des granulats calcaire réactifs (échantillons provenant du pavage fortement affecté par la RAS utilisés lors de la première phase du programme expérimental). Les essais de micro-indentation ont été réalisés sous deux conditions d'humidité relative. Il a été observé qu'une augmentation en humidité relative réduisait fortement la déformation de fluage irréversible des produits cristallins de RAS, qui montrent un temps caractéristique plus grand. Ainsi, la teneur en eau semble favoriser le mécanisme de glissement irréversible le long ou entre les plaquettes des produits cristallins (rosettes lamellaires) de RAS sous charge constante.

Finalement, les implications des résultats de ces travaux sont discutées en lien avec le processus de génération de pression à l'intérieur des particules de granulats réactives. Les propriétés rhéologiques des produits de RAS peuvent jouer un rôle critique lors du relâchement des contraintes internes induites par l'expansion de ces produits. Enfin, un modèle simplifié « 1D » est proposé comme nouvel outil de recherche, et ce afin de prendre en compte les principaux résultats de cette étude, i.e. les propriétés visco-élastiques des produits de RAS et les propriétés de rigidité des particules de granulats réactives.

Abstract

The Alkali-Silica Reaction (ASR) is one main detrimental factor to affect the durability of concrete. The research comprises two parts, i.e. microstructural characterization of ASR products (3 phases), and modeling of concrete damage due to ASR. The experimental results will provide new findings on the microstructure properties of ASR-damaged concrete.

The work in the first phase of the research aims at characterizing the micromechanical properties of ASR products by new techniques of nanoindentation and micro-indentation, with emphasis on their viscous behavior. The concrete samples were extracted from a heavily ASR-affected concrete pavement in Bécancour (Québec). The concrete is characterized by numerous fine-grained limestone aggregate particles with microcracks filled with secondary reaction products that extend into the cement into a network from one aggregate particle to another. After careful sample preparation (polishing), the surface of the aggregate particle and of the veinlets (i.e. cracks filled with crystalline ASR product within the aggregate particles) was examined by Atomic Force Microscopy (AFM) before nanoindentation testing. Both nanoscale and microscale indentation modulus and hardness of ASR products were measured. The test results show that ASR crystalline products exhibit important relaxation behavior of about 40%. Then, a simplified rheological model was proposed to fit the load relaxation curves and their asymptotic values. These results suggest that ASR product relaxation is significant and mostly irreversible.

The second research phase explored the use of the novel micro-scratch technique to characterize the fracture energy (i.e., toughness) of the ASR-affected limestone aggregate particles within a core specimen extracted from a heavily ASR-affected concrete bridge from the Québec City area. The ASR-affected aggregate particles were typically showing “zoning” (i.e. light grey and dark grey) surrounding white veinlets within reacted limestone aggregate particles. As a reference, an undamaged/virgin quarried limestone specimen from a local quarry was selected and subjected to similar testing. Besides the elastic properties, the toughness of the reactive aggregate particles was statistically measured to be around 1.5 $MPam^{1/2}$. The fracture toughness of reactive aggregate particles was affected neither by the bedding line directions nor by the “zoning” that was first thought to correspond to “reacted” portions of the particles. Besides the major cracks filled by ASR products, the results indicated that the surrounding reactive aggregate was not characterized by any significant internal damage distribution.

In the later phase of the experimental program, our research focused on characterizing the creep and stress relaxation properties of the ASR crystalline products typically filling microcracks within reactive limestone particles (specimen from the heavily ASR-affected concrete pavements in Bécancour (Québec) used in phase 1). The testing carried out was micro-indentation under controlled relative humidity. It was found that an increase in relative humidity strongly reduces the irreversible creep deformation of ASR crystalline products, which act a greater characteristic time. That is, the water content seems to favor irreversible sliding mechanisms along/between the ASR crystals under constant load.

Finally, the implications the research findings are discussed with respect to the stress build-up process within reactive aggregate particles. The rheological property of ASR products may play a critical role to releasing the internal stress induced by the ASR product expansion. Finally, a “1D thought model” is proposed as a new research avenue to account for the major results of this work into ASR-damaged concrete modeling, i.e., the visco-elastic property of ASR products and the damage toughness of reactive aggregates.

Table of Contents

List of Tables

List of Figures

Nomenclature

AAR	Alkali-Aggregate Reaction
AAR-1	Petrographic Examination (AAR-1)
AAR-2	Ultra-accelerated Mortar-bar test (AAR-2)
AFM	Atomic Force Microscopy
ACR	Alkali-Carbonate Reaction
ASR	Alkali-Silica Reaction
CE	Chemo-Elastic
CEV	Chemo-Elastic-Viscous
CEVD	Chemo-Elastic-Viscous-Damage
CMC	Continuous Multi Cycle (test)
CSEM	Swiss Center for Electronics and Microtechnology
CSM	Swiss Center for Microtechnology
CRIB	Centre de Recherché sur les Infrastructures en Béton
C-H	Calcium hydroxide (also called portlandite)
C-S-H	Calcium-silicate-hydrates (cement hydration product)
COPL	Centre d'Optique Photonique et Laser
DRI	Damage Rating Index
EDX/EDS/EDXS	Energy Dispersive X-ray Spectroscopy
EDSA	Energy Dispersive X-ray Spectroscopy Analysis
FEM	Finite Element Method
ITZ	Interfacial Transition Zone
MON	Calcium-sulfoaluminates-hydrate
NT	Nanoindentation Technique
LCPC- IFFSTAR	Laboratorie centre des Ponts et Chaussées Institute français des science et techenologies des transport, de l'aménagement et des réseaux
RH	Relative Humidity
RMS	Roughness-Mean-Square
RVE	Representative Volume Element
SBT-920	The Lapping and Polishing Machine - Model 920 (SBT-920)
SDT	Stiffness Damage Test
SEM	Scanning Electron Microscope

TAL	Threshold Alkali Level
TCAR-LD	Transport en commun de l'agglomération rounennaise Enterprise
UNHT	Ultra Nanoindentation Tester
UV	Ultravoilet-visible
VEPD	The Damageable Viscous-Elastic-Plastic Device
WDS	Wavelength Dispersive Spectroscopy
XRD	X-Ray Diffraction (XRD) analysis
Ca	Calcium
Ca^{2+}	Calcium ion
$Ca(OH)_2$	Calcium hydroxide
HCl	Hydrogen chloride
HSC	Polyetherpolyol solution
K	Potassium
K^+	Potassium ion
Na	Sodium
Na(OH)	Sodium hydroxide
Na^+	Sodium ion
OH^-	hydroxyl ions
Si	Silicon
SiC	Silicon Carbide
SiO_2	Silica
Si-OH	silanol groups
Si-O-Si	siloxane bonds
Å	Ångström (length Unit: 10^{-10} m)

To all the directors in my academic road and be grateful all the time.

谨以此论文献给学术路上的导师们，并一直心存感激

Acknowledgement

Firstly, I would like to express my gratitude to my director Prof. Luca Sorelli. It has been four most fruitful and colorful years working with him since the fellowship between University Laval (UL) and China Scholarship Council (CSC) was validated. Prof. Luca has a rich experience in his studies and academic career; therefore, he gained a very good reputation in the field of civil engineering, especially in the aspect of microstructure characterization of concrete. His research and teaching career at MIT and other top research institutes make our work challenging and very original.

Our research activities and results about the concrete microstructure and characterization in the past 4 years gained the high recognition from CSC and Education Bureau in China Embassy of Canada. In addition to providing guidance and advice in the academic field, Prof. Sorelli is a kind, patient and humorous person. One of the most impressed things for me about Prof. Sorelli is his high efficiency during working time.

Also, I do really appreciate the work done by Prof. Benoit Fournier who is my co-supervisor in the Geology and Geological Department at Université Laval.. His knowledge and experience in geological engineering, mineral, and use of aggregates in concrete helped me better understand the alkali-silica reaction's principles and mechanisms. I have been shocked several times by his serious character and spirit in science and research. I has never seen somebody evaluating my articles and thesis so strictly, with every single word and grammatical expressions. He also displays quite logical thinking and rigorous research attitude. He is such an example in my life, a mirror, a light, which keeps me calm modest and humble.

I consider myself very lucky to have another co-director – Prof. Josée Duchesne, who is a famous expert in geological engineering, concrete technology and applied Geology. Besides, she has a wide range of knowledge in chemistry, civil engineering, and materials engineering. For example, she studied concrete not only regarding thecivil engineering aspect, but also from the standpoint of materials and chemistry. Her comments on my papers and thesis expanded my mind with new ideas. Through discussions with her, I learned how to view a thing in a comprehensive way, and to understand a structure or construction more frommaterials or chemistry point-of-view. Breaking the boundaries between disciplines and to view a thing in a comprehensive way will help me in my future endeavours.

Prof. Josée Bastien, my other co-director, who specialized in reliability and rehabilitation and service life of the concrete infrastructure, is an expert in structural engineering and has a rich experience in supervising postgraduates and Ph.D. candidates. She broadly joins in academic research groups and organizations; therefore, she has a very good reputation in the academic field and the esteem amongst students. She always encouraged me and provided me with a lot of sound advices. She filters the key and important matters in her

gracious and profound way when professors and scholars argue their points in some scientific workshops and presentations at meetings.

Needless to say, I am the most fortunate student to spend such four entire years to focus on the interdisciplinary subject - *Microstructural characterization and modeling of concrete structures damaged by Alkali-Silica Reaction (ASR) expansion*. By the way, it is really impressive to view my four directors all turn into a little bit aggressive mode from peace and kindness when they argue the research issues.

At the same time, I want to give special thanks to the academic committee members in my Ph.D. defense, Prof. Stéphane Multon, Prof. Ahmed El Refai, and Prof. David Conciator. Especially lucky of me, Prof. Multon is currently visiting Université Laval for his sabbatical and has given an amazing presentation on ASR research and many beneficial guidelines and teachings from ASR mechanism, ASR modeling, ASR mass transportation to ASR structural effects. Most interesting discussions on the ASR research occurred with Prof. Multon and will hopefully continue after the completion of my PhD.

Once more, all the best wishes and sincere appreciation to the seven members in my Ph.D. Defense jury including my four directors.

Moreover, I do appreciate the assistance from the technician Stéphane Gagnon in COPL of Université Laval, who helped me to develop new skills in sample fine polishing. Also great appreciation to technician Edmond Rousseau, from the Geology and Geological Engineering Department, who helped me to do the initial preparation of the ASR-damaged concrete specimens before the fine polishing.

I would like to thank Post-doctoral student Leandro .F.M. Sanchez now Professor at the Civil Enginnering Department of Ottawa University, as well as Anthony Allard, PhD candidate at Université Laval, who provided some of the ASR-damaged concrete samples for my testing program. Also, my sincere thanks – Mr. Jessy Frech-Baronet, who shared with me his knowledge in physics and civil engineering. He helped me in manipulating nanoindentation machine and fought against with me in International and Chinese Chess.

I am pleased to acknowledge the financial support from China Scholarship Council (CSC) and the warm assistance of Education Bereau of China Embassy in Montreal of Canada. Thanks to all my research directors in my academic career from Jiangsu University, Huazhong University of Science and Technology in China to Konstanz in Germany and then University Laval here in Canada.

My sincere thanks and deepest love go to my family for their constant support during all those years of my studies in China and abroad.

The deepest and forever missing is dedicated to my grandmother – Huiqiu Luan!

Foreword

This Ph.D. thesis is composed of an Introduction (Chapter 1) that presents the general context and the objectives of the research. It is followed by a literature review (Chapter 2) that gives general information on alkali-silica reaction (ASR) in concrete and that also focuses on the microstructure/micromechanical characteristics of concrete affected or not by ASR; a summary of the main models for ASR is also presented. Chapter 3 then gives a global description of the three-phase experimental program carried out in this research. The heart of the thesis is then based on the following 3 papers:

1. **Chapter 4: Chi Zhang**[(1)], Luca Sorelli[(1)], Benoît Fournier[(2)], Josée Bastien[(1)], Josée Duchesne[(2)], Chen Zhao[(1)], Creep and Relaxation Behaviour of Alkali-Silica Reaction Products with Rosette-like Structure by Micro-indentation: Characterization and Simplified Modeling. Construction and Building Materials, 2017 (under review).

2. **Chapter 5: Chi Zhang**[(1)], Luca Sorelli[(1)], Benoît Fournier[(2)], Josée Bastien[(1)], Josée Duchesne[(2)], Micro scratch tests of reactive aggregate in ASR-damaged concrete, Material Characterization, 2017 (submitted).

3. **Chapter 6: Chi Zhang**[(1)], Luca Sorelli[(1)], Benoît Fournier[(2)], Josée Bastien[(1)], Josée Duchesne[(2)], Effect of the Relative Humidity on the Dual Creep-Relaxation behavior and its Recovery of ASR Products by Micro-indentation. Cement and Concrete Research, 2017 (completed).

The institutions of the co-authors are given below:

1) Université Laval, Civil and Water Engineering Department, 1065 avenue de la Médecine, PLT2928-A, G1V0A6, Québec, Canada.

2) Université Laval, Geology and Geological Engineering Department, 1065 avenue de la Médecine, G1V0A6, Québec, Canada.

The author of this Ph.D. thesis (Chi Zhang) is the first author of all these papers. For paper 1, 2 and 3, the author of this thesis did most of the research and writing work under the supervision of Ph.D. supervisor Prof. Luca Sorelli, Benoît Fournier, Josée Bastien and Josée Duchesne in Unversity Laval. Paper 1 involved a part of modeling work with my colleague Chen Zhao. The material part is completed under the supervision of Prof. Benoît Fournier. The chemical analysis is mainly from Prof. Benoît Fournier and Prof. Josée Duchesne.

In paper 2, the author of this Ph.D. thesis did all the micro scratch tests, which is the major part of this paper, while the preparation of the samples, especially ASR-damaged aggregate samples is a really time-consuming and energy-consuming work from Prof. Benoît Fournier and the technician in Geology laboratory. In paper 3, the author of this Ph.D. thesis did most of the micro-indentation tests under the controlled humidity with the chamber built by my colleague Jessy Frech-Baronet.

Chapter 7 presents a discussion on a model developed on the basis of the experimental data obtained in this research. It is followed by general conclusions and recommendations (suggested future outlooks) (Chapter 8).

1. Introduction

1.1 Industry problems

Stanton (1940) first encountered the problem of Alkali-Aggregate Reaction (AAR) in a concrete pavement in Bradley, California (USA). Since then, numerous cases of AAR damaged structures were reported from all around the world and AAR is considered today as one of the most important durability issues for concrete structures worldwide. This research focuses on Alkali-Silica Reaction (ASR), which is the most common form of AAR. The cost of repairing or replacing ASR-damaged structure is considerable as a significant number of civil engineering structures (bridges, road pavements, dams, etc.) are concerned (Ulm et al., 2000).

Briefly, ASR corresponds to the chemical reaction between hydroxyl ions from the alkaline concrete pore solution and certain siliceous aggregates containing “unstable” siliceous phases; it causes excessive expansion and extensive cracking in the concrete material and unexpected deformations in/between structural elements. The chemo-mechanical impact of ASR expansion on the dimensional stability is often quantitatively assessed as a viable means (Ulm et al., 2000).

Among a large number of concrete constructions damaged by ASR worldwide, some examples are (i) Parker Dam, a concrete arch dam with a height of 98 meters, starting its service in 1938. In 1940, numerous cracks were found to be caused by a deleterious reaction between alkali reactive sands and the high alkali Portland cement (Stanton, 1940); (ii) Chambon Dam in France, an arch dam of 90 meters high and 294 meters long, which was built in 1935. The alkali content of the cement used in the Chambon Dam is 0.59%, and 3000 thousand cubic meters of concrete were used in its construction (Prin et al., 1992). The ASR expansion started to appear after 50 years in service. Over 10 centimeters displacement along the height of the dam was measured due to ASR expansion; (iii) Moxoto Dam is an example of Brazilian dam which suffers ASR damage. The cement used in concrete construction had an alkali content of 1.0%. Cracks due to ASR were found since 1980 (Silveira, 1989). In the decade 1980-1990, the yearly expansion rate of the concrete was 0.7mm per year. Almost all concrete samples taken from the damaged dam were found to show dark reaction rims and some also contained certain alkali-silica reaction products; (iv) Beauharnois Power Station on the St. Lawrence River is a known example in Québec

(Canada) for ASR damage deterioration. Not only the northern part of the dam moved upstream by 11.7mm every year, but ASR-induced extensive cracking was also found to be in its water intake system and office building (Gocevski et al., 2000). Besides, several miles ahead of the dam along the St. Lawrence River, two suspension bridges also incorporating siliceous Potsdam sandstones were also damaged by serious cracking and large deformations (Bérubé et al., 2000); (v) Numerous cases of ASR involving siliceous limestones were identified in highway bridges, pavements, water control structures (locks and dams) located in different regions of the St. Lawrence Lowlands of Québec and Ontario (e.g. Bérubé et al., 2000, Rogers et al., 2000, Bérubé et al., 1987, Bérard et al., 1986). Those structures show extensive cracking and also suffered from extensive expansion, as it is the case of the Saunders dam, near Cornwall in Ontario (Grattan-Bellew, 1995).

1.2 Research problems

Although the ASR chemical mechanism is generally accepted in the scientific community, the damage mechanisms involved at both macro- and especially micro scales during ASR expansion are still under discussion. Up to today, several researchers have salient aspects of this complex phenomenon, but a clearly comprehensive model does not exist. For instance, some authors believe that ASR expansion occurs at the two-time steps (Ulm et al., 2000): (i) a latency time associated with the dissolution of reactive silica; (ii) a main expansion phase associated with the ASR product formation (seen in Figure 1.1a). Other researchers believe that the ASR expansion starts within the aggregate particles and microcracks developed within the reactive particles further extend into the cement paste when expansion due to ASR increases; the cracking pattern will then develop into a network connecting reactive coarse or fine aggregate particles with one another (Reinhardt et al., 2011, Benhaha et al., 2007, Sanchez et al., 2015). Multon et al. (2009) proposed that only when the porosity within the cement paste surrounding the reactive aggregate particle is filled with ASR gel, cracks will start to develop and extend further into the concrete (seen in Figure 1.1b).

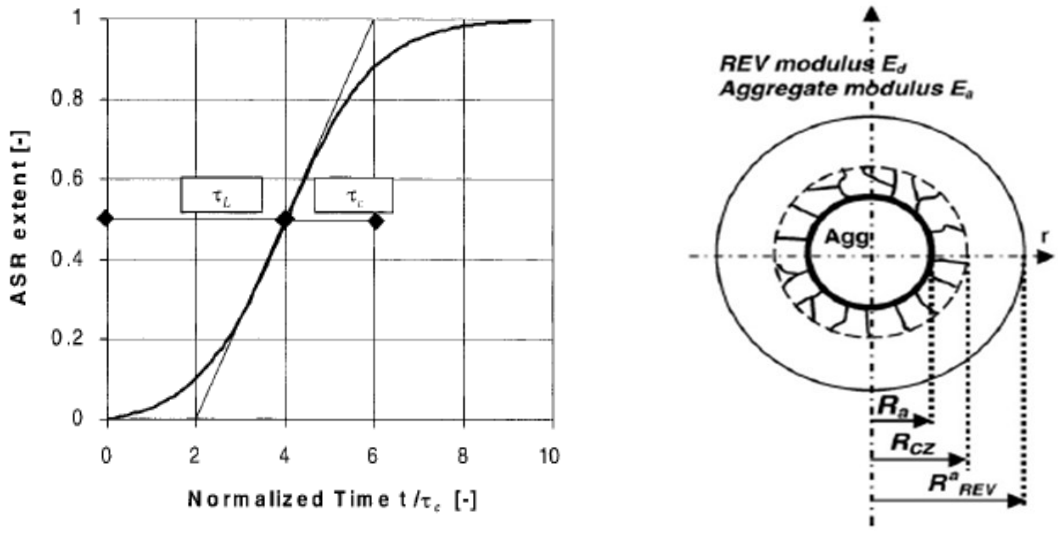

(a) (b)

Figure 1.1 (a) Reaction extent curve in Ulm's ASR damage model (Ulm et al., 2000); (b) Schematic of the crack formation surrounding a reactive aggregate particle in the Multon et al.'s (2009) damage model.

The limitations in existing characterization and knowledge of ASR are:

- Lack of information about the physical/mechanical properties of secondary reaction products from ASR;
- Lack of understanding about the parameters involved in the development of damage within the aggregate particles;
- Lack of data about the mechanical properties of ASR-damaged concrete at micro-scale level;

The main limitations in existing models for ASR are summarized below:

- The existing models consider the ASR product incompressible and undeformable;
- The existing ASR models are mainly phenomenological without considering the role of the aggregate particles in the damage evolution;

Based on the materials and samples used in this study, two key questions are proposed both in the characterization and modeling of ASR:

- Can we characterize the viscosity of reaction products and the aggregate's damage in the ASR-damaged concrete with latest technologies?
- Can we implement the new information into a simple two-scale mechanical model of ASR?

This approach combines new techniques of microstructural characterization and advanced modeling to highlight the key material-to-structure parameters for ASR damage.

1.3 Research objectives

The focus of this work is to investigate the mechanical behavior of ASR crystalline products which preferentially form within reactive aggregate particles in the ASR damage process. The objectives of this work are:

- **Objective 1:** Characterize the microstructure in ASR-damaged concrete with special emphasis on the evaluation of the viscoelasticity properties of ASR crystalline products (e.g., rosette-like structure) with emerging micro-indentation techniques;
- **Objective 2:** Characterize the effect of relative humidity on the visco-elastic response of ASR crystalline products by micro-indentation test within an environmental chamber;
- **Objective 3:** Characterize the fracture mechanics property of ASR “reacted and unreacted” aggregates by means of emerging micro-scratch techniques.

Finally, the implications of the results obtained in this work are discussed within a simplified 1D two-scale model. The present results bring a new perspective for the better understanding of the ASR mechanisms.

2. Literature survey

The following sections present a brief literature survey that focuses on the main topics covered by this research. Basics of ASR are first presented, followed by a description of the microtextural characteristics of concrete affected by ASR. The properties of ASR products are then discussed, while the final section briefly reviews the main types of models used for ASR.

2.1 ASR definition and mechanism

2.1.1 Essential conditions

ASR, namely alkali-silica reaction, is a chemical reaction between certain siliceous phases within different types of rocks and the hydroxyl ions (OH^-) associated with alkalis (Sodium and Potassium) in the concrete pore solution (seen in Figure 2.1). The three necessary conditions for ASR to occur are:

- A sufficient quantity of reactive silica within fine and/or coarse aggregates; these siliceous phases could be opal, metastable forms of quartz (e.g. cristobalite), micro- to cryptocrystalline or strained quartz and volcanic glass, that are present in a large variety of rock types (CSA Appendix B, 2014, CSA A23.2-14);

- A sufficient concentration of alkalis resulting in a high pH in the concrete pore solution. The alkalis can be provided by the hydraulic cement (mostly) or from other sources such as supplementary cementing materials, chemical admixtures, deicing chemicals, and the aggregates themselves (Thomas et al., 2013). The expansion caused by ASR relates to the smallest alkali content for ASR occurrence, which is called Threshold Alkali Level (TAL). Every aggregate has its own TAL above which deleterious reaction/expansion will develop;

- Sufficient moisture. The secondary reaction product from ASR called the alkali-silica gel, absorbs water from the environment, then swells thus creating internal pressure and cracking of the affected concrete. An 85% relative humidity content is generally seen as a threshold for deleterious expansion due to ASR to occur (Thomas et al., 2013).

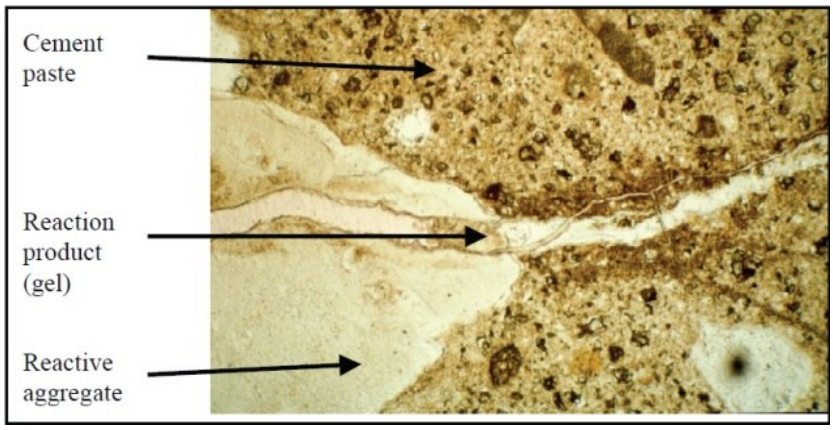

Figure 2.1 Micrograph of a thin section of concrete undergoing ASR (field of view~5mm) (Thomas et al., 2013).

2.1.2 Mechanisms of reaction and expansion

While the ASR chemical reaction process is generally accepted within the scientific community, the current understanding of the mechanisms of concrete swelling due to ASR is still opened to debate. The ASR process is schematically shown in Figure 2.2.

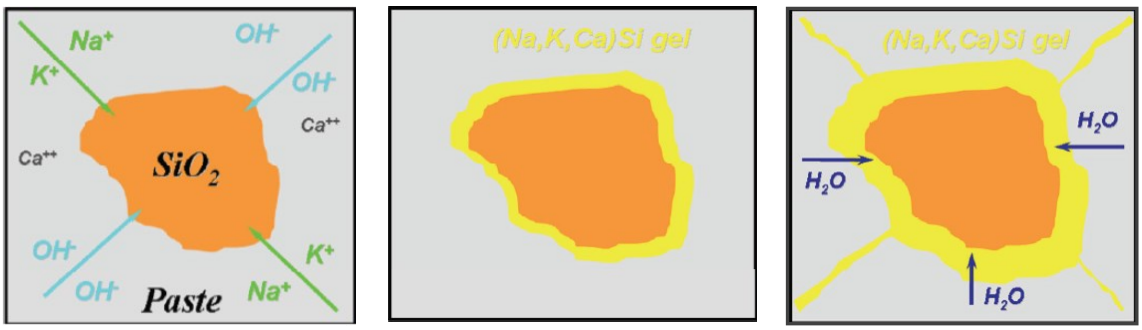

(a) (b) (c)

Figure 2.2 Simplified ASR progress: (a) Reactants; (b) Gel formation; (c) Water absorption, swelling and cracking (Thomas et al., 2013).

The pore solution in the cement paste is dominated by OH^-, Na^+, K^+ and minor Ca^{2+} ionic species. Therefore, the “unstable” silica around the edge, in “pockets” or along pre-existing cracks within the aggregate particles first react with the surrounding OH^-, Na^+ and K^+ ions. In this topochemical reaction, hydroxyl ions (OH^-) attack the silanol groups (Si-OH) and the siloxane bonds (Si-O-Si) of the “unstable” siliceous phase within the coarse or fine aggregate particles. The reactions have been represented by Dent Glasser and Kataoka (1981) as follows (Thomas et al., 2013):

$$Si\text{-}O\text{-}Si + OH^- \rightarrow Si\text{-}OH + OH\text{-}Si \quad (2.1)$$

$$Si\text{-}OH + OH^- \rightarrow Si^- + H_2O \quad (2.2)$$

As shown in Figure 2.2(b), the reaction product (gel) formed through this reaction is composed of sodium (Na), potassium (K), calcium (Ca), silicon (Si) and water molecules. Although the gel formation and ASR chemical principles are widely accepted, the expansion process and crack formation are somewhat still controversial. In the simplified model illustrated in Figure 2.2(c), the gel absorbs water from the cement paste thus exerting a swelling pressure. When the latter exceeds the tensile strength of the surrounding cement paste, cracking starts to occur.

Hansen (1944) suggested the cement paste around reactive aggregate particles acts as a semi-permeable membrane through which water (or pore solution) might pass, but the larger complex silicate ions cannot. Through this process, osmotic pressure cells are formed and increasing hydrostatic pressures are exerted on the surrounding cement paste, causing it to crack. The basis of the classical osmotic theory is that cracking of the surrounding cement paste “membrane” due to ASR would release the hydraulic pressure and prevent further expansion. An alternative mechanism is proposed by Powers and Steinour (1955a, 1955b), which suggests that the reaction product may act as a semi-permeable membrane itself, depending on its composition, and expansion/cracking results from the physical absorption of water by the alkali-silica gel and subsequent swelling of the gel.

Ulm et al. (2000) suggested that ASR expansion develops in two-time steps sequentially: (i) a latency time associated with the dissolution of reactive silica; (ii) the main expansion phase associated with the gel formation inside the aggregate of the selected ASR-affected concrete unit. Differently, Multon et al. (2009) believe that the ASR occurs when the gel fills the voids/porosity surrounding the reactive aggregate particles, thus generating cracks that extend into the surrounding cement paste. On the other hand, Reinhardt & Mielich (2011), Benhaha et al. (2007) and Sanchez et al. (Sanchez et al., 2015) rather believe that ASR starts within the aggregate particles and extends into the cement paste as expansion due to ASR develops. Multon & Sellier (2016) proposed a modified approach involving a distinction between gel pressure within the aggregate particles and average aggregate pressure on the surrounding concrete. The authors recognized that, in most cases of ASR, cracking starts in the aggregate particles and aggregate cracks filled by the gel induce the cracking of the

cement paste. Thus, the consequences of ASR-gel formations was first assessed at the aggregate scale then deduced at the concrete scale.

2.1.3 Reactive limestone aggregates

As mentioned earlier, limestone aggregates were found to induce deleterious expansion and cracking in numerous concrete structures in different regions of the St. Lawrence Lowlands in Québec and Ontario (Canada) (Bérubé et al., 2000, Rogers et al., 2000). The reactive rocks correspond to siliceous and more or less argillaceous limestones of the Trenton Group (Ordovician age). They are characterized by a fine-grained matrix mainly composed of carbonate material (calcite and some dolomite), fossil fragments, clay minerals (illite, interlayered illite-smectite, some chlorite) and disseminated micro-to cryptocrystalline quartz (Figure 2.3) (Fournier et al., 1991, Fournier, 1993).

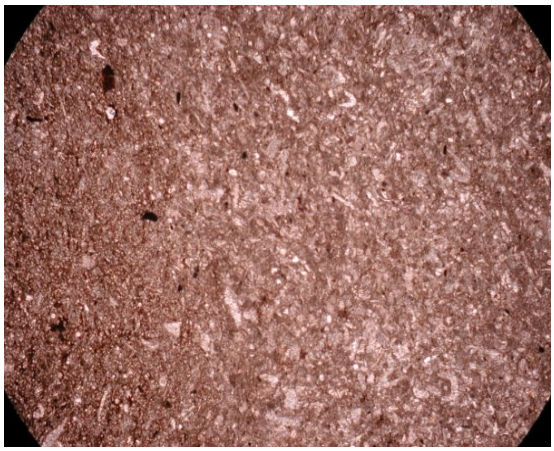

Figure 2.3 Thin section of upper Trenton limestone (Neuville Formation, Québec City area) showing fine fossil fragments disseminated in a fine-grained matrix composed of carbonate material, clay minerals and microcrystalline quartz (25x magnification) (Fournier, 1993).

The reactive material in the above limestone aggregates cannot be easily identified by conventional petrographic examination under thin sections. When polished sections of Trenton limestone are immersed in diluted hydrochloric acid, the carbonate materials are dissolved, leaving behind insoluble residues (Figure 2.4a). The examination of the insoluble residue under the Scanning Electron Microscope (SEM) reveals the presence of clay minerals and micro- to cryptocrystalline quartz forming a network surrounding the carbonate material dissolved by the acid attack (Figure 2.4b). The micro- to cryptocrystalline quartz forms the reactive material in that rock (Fournier, 1993).

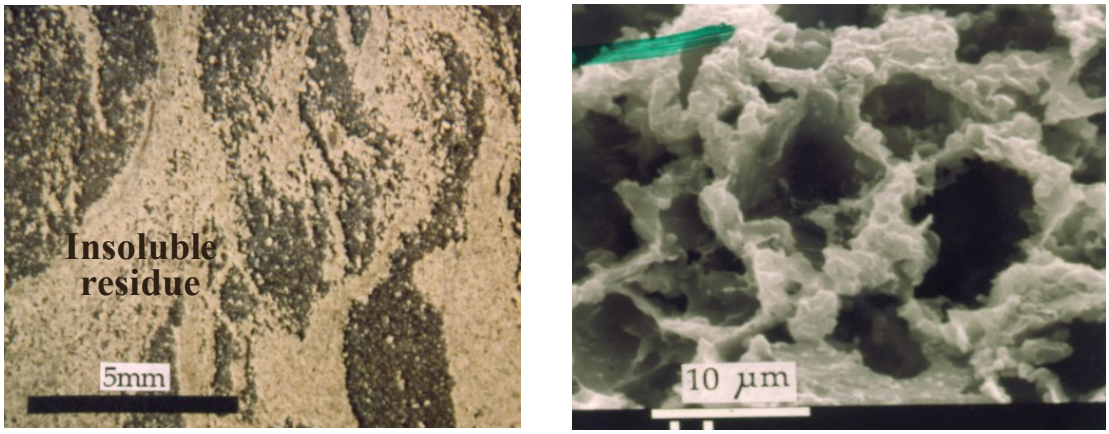

(a) (b)

Figure 2.4 (a) The polished limestone section after surficial HCl attacks, thus leaving behind an insoluble residue; (b) SEM micrograph showing the insoluble residue forming a network that was surrounding the calcite grains that were dissolved by the HCl attacks. The network is composed of very fine-grained (reactive) quartz and clay minerals (Fournier, 1993).

The different levels of the Trenton limestones across the St. Lawrence lowlands show different reactivity levels due to ASR as a function of the microcrystalline quartz content (Fournier, 1993). In Ontario, the Spratt limestone of the Bobcaygeon formation, exploited in the Ottawa area, is a well-known reactive aggregate that has been used as a control reactive aggregate in several research programs around the world. A siliceous limestone aggregate of similar geological age exploited in a quarry in Belgium was also found to induce deleterious cracking in concrete structures in the North-eastern part of France (Guedon-Dubied et al., 2000).

Concrete elements affected by ASR and incorporating siliceous limestone coarse aggregates show typical features of deterioration characterized by the presence of cracks filled with secondary reaction products forming white veinlets within the reactive aggregate particles (Bérard et al., 1986, Bérubé et al., 2000).

Sanchez et al. (2015) studied the development of damage in concrete specimens made with reactive limestone aggregates (Trenton Group) produced in the Québec City area. The test specimens were made from 25, 35 and 45MPa concrete mixtures and maintained in conditions conducive to the development of ASR (38℃, 100% relative humidity). At specific expansion levels (i.e. 0.05%, 0.12% and 0.20%), the specimens were cut and polished to perform petrographic examination following the Damage Rating Index Method (DRI). The authors found that the aggregate particles were already incorporating, at very low expansion levels, a fair amount of closed cracks that they associated, in good parts, to the processing

operations in the quarry. In many cases, those “pre-existing” cracks were found to be parallel to the bedding in the rock, most likely corresponding to “weakness planes” with the rock. They also reported that cracking in the aggregate particles was developing further with increasing expansion due to ASR and that those cracks were progressively extending into the cement paste and connecting reactive aggregate particles with one another, in a network, at high expansion levels.

Details on the typical petrographic features of ASR are described and illustrated in more details in the next section.

2.2 Microtextural and Compositional characteristics of ASR products

Several characterization techniques have been applied over the years to research on concrete damage by ASR. For example, the presence and distribution of cracking, as well as the microtextural characteristics of ASR products can be seen under the stereobinocular and petrographic microscope, i.e. at relatively low magnification, on broken surfaces, plane polished slabs and thin sections of ASR-affected concretes (e.g. BCA 1992, Walker et al., 2006, Fournier et al., 2010, Fernandes et al., 2016, Sims et al., 2016) (Figure 2.5a to d). The distribution and the extent of cracking due to ASR can be highlighted in plane polished and/or thin sections impregnated with epoxy incorporating a UV dye (e.g. Jensen et al., 1985, Lorenzi et al., 2006, Ingham, 2012).

Staining techniques have also been proposed to facilitate identification of the secondary reaction products in concrete affected by ASR (Natesaiyer et al., 1991, Stark, 1991, Guthrie et al., 1997). A technique developed at Cornell University (Natesaiyer et al., 1991) consists in applying an uranyl acetate solution on polished or fresh broken surfaces of concrete specimens to be examined followed by a visual observation of the section under a ultraviolet (UV) light; the technique has even been used on field structures (Stark 1991, AASHTO 1993, ASTM C856-02). Stark (1991) indicated that “by applying the uranyl acetate solution to a surface containing the gel, the uranyl ion substitutes for alkali in the gel, thereby imparting a characteristic yellowish-green glow when viewed in the dark using short wavelength ultraviolet light ASR gel fluoresces much brighter than cement paste due to the greater concentration of alkali and, subsequently, uranyl ion in the gel”.

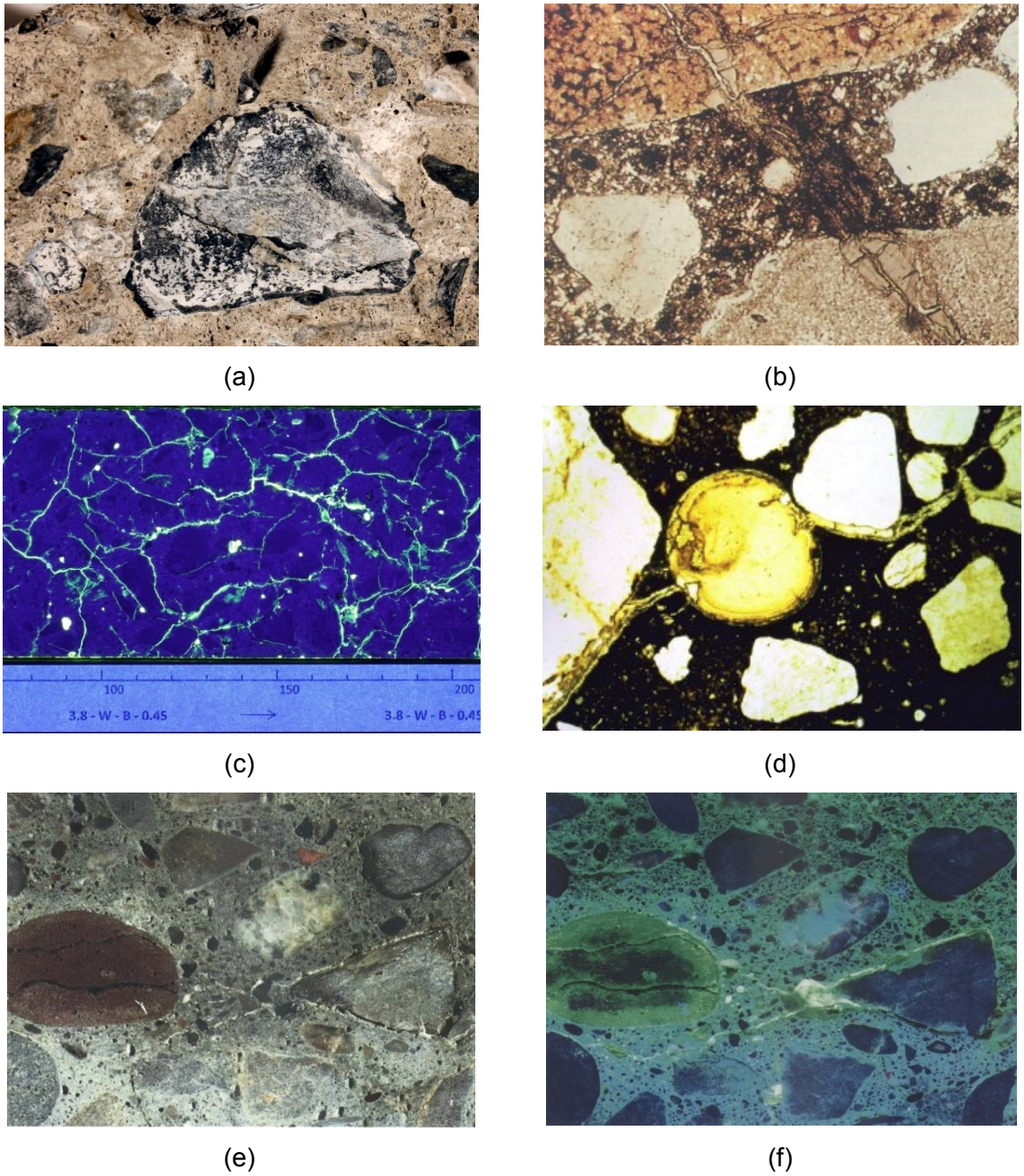

Figure 2.5 Microstructural characteristics of concrete affected by ASR. (a) Secondary products of ASR on the broken surface of reactive aggregate particles and of the adjacent cement paste; (b) Thin section micrograph showing cracks filled with gel in reactive aggregate particles at the cement paste; (c) Cracking in a plane polished section of concrete affected by ASR and impregnated with epoxy incorporating a UV dye (UV illumination); (d) Thin section showing cracking in concrete affected by ASR; specimen impregnated with epoxy incorporating a UV dye (UV illumination); (e) Plane polished section showing cracks in reactive aggregate particles and the adjacent cement paste (natural light); (f) Same section as in (e) Treated with uranyl acetate solution to enhance the presence of alkali-silica gel (UV illumination showing the gel in greenish-yellow staining color filling cracks in the cement paste in the vicinity of reactive aggregate particles); (b,e,f: Fournier et al., (2010); d: Poole et al., (2016); a,c: with compliments of Fournier (2017)).

Guthrie and Carey (1997) proposed a staining method which consists in treating fresh concrete surfaces to successive applications of Sodium Cobaltinitrite and Rhodamine B. Upon treatment, regions affected by ASR stain either yellow or pink. According to the authors, yellow staining would be associated with massive ASR-related precipitate with gel-like morphology as well as granular precipitate consisting of crystals that have grown from the gel. On the other hand, yellow stained regions would correspond to alkali-bearing siliceous reaction products resulting from ASR.

Examination of ASR-affected concrete specimens under the scanning electron microscope (SEM) equipped with energy-dispersive X-ray spectroscopy (EDS) allows a more thorough identification of secondary ASR products. Observations at low magnification (×25) under the SEM often reveal the presence of cracking within the aggregate particles and the cement paste, as well as deposits of secondary reaction products with a wide range of morphologies. For example, Figure 2.6 illustrates ASR products and ASR-induced cracking in concrete as observed in backscattered electron (BSE) mode in the SEM.

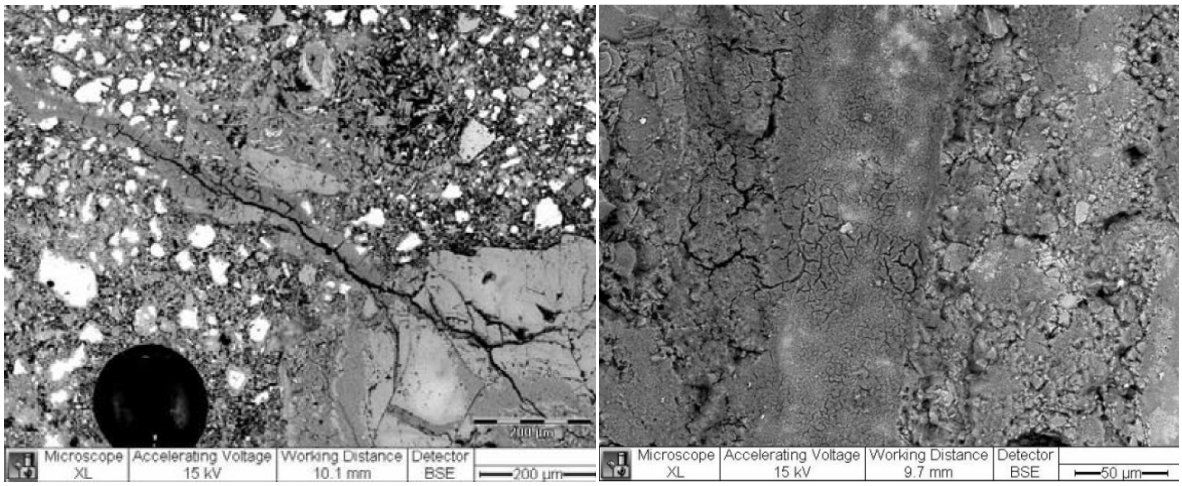

(a) (b)

Figure 2.6 BSE micrographs of ASR gel penetrates into the aggregate crack (a) and at the interface (b) between an aggregate particle (left) and the cement paste (right) (Schlangen et al., 2007).

In the secondary electron mode of the SEM, reaction products with different micro-textural and compositional characteristics can be observed (Figure 2.7). Massive gel deposits, generally rich in silicon (Si) and calcium (Ca) are found filling/lining cracks and voids of the cement paste, showing microcracking partly due to the high vacuum conditions used for SEM observations. The surface of the gel deposits can be relatively smooth (Figure 2.7a and b), while they can also show isolated protrusions (top of the picture) or contiguous

protrusions (lower part of Figure 2.7c and d); this is called *hummocky gel* Figure 2.7d) (Bérubé et al., 1986, Larive et al., 1992). In some cases, reaction products lose amorphous appearance and are roughly crystallized. The alveolar micro-texture illustrated in Figure 2.7e is actually not far from that of ordinary C-S-H.

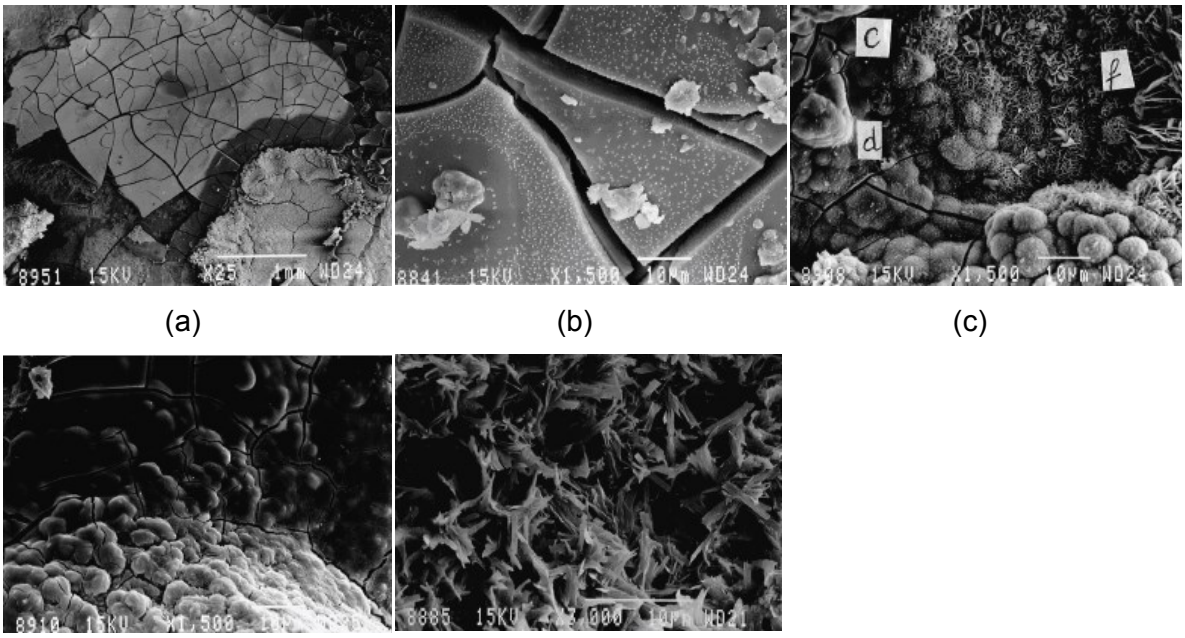

(a) (b) (c)

(d) (e)

Figure 2.7 Some characteristic features of reaction products in ASR-damaged concrete samples (observed by SEM) (Ollivier et al., 2008).

A typical feature of ASR affecting quartz-bearing rock types is the development of extensive cracking within the aggregate particles with increasing expansion due to ASR (Sanchez et al., 2015, 2017). This is very much the case of concrete incorporating siliceous limestone coarse aggregates where cracks within the reactive aggregate particles are filled with secondary reaction products and thus appear as white veinlets with a white powdery/chalky aspect on plane polished slabs of concrete affected by ASR (Figure 2.8a). On broken surfaces of those reactive aggregate particles, a particular arrangement of secondary reaction products can be observed (Figure 2.8b). Massive gel with Si, Ca and some alkalis can be found just at the border with the cement paste (Figure 2.8c), while it progressively changes, towards the inside part of the particle, to crystalline products showing a rosette-like microtexture composed of lamellar crystals (Figure 2.8d). Those products are rich in Si, K and have a smaller Calcium content than products found along cracks within the cement paste. This special arrangement of reaction products along cracked surfaces of reactive

particles is not limited only to reactive siliceous limestone aggregates and can be found with other types of alkali-silica reaction quartz-bearing rocks (Fournier et al., 2010).

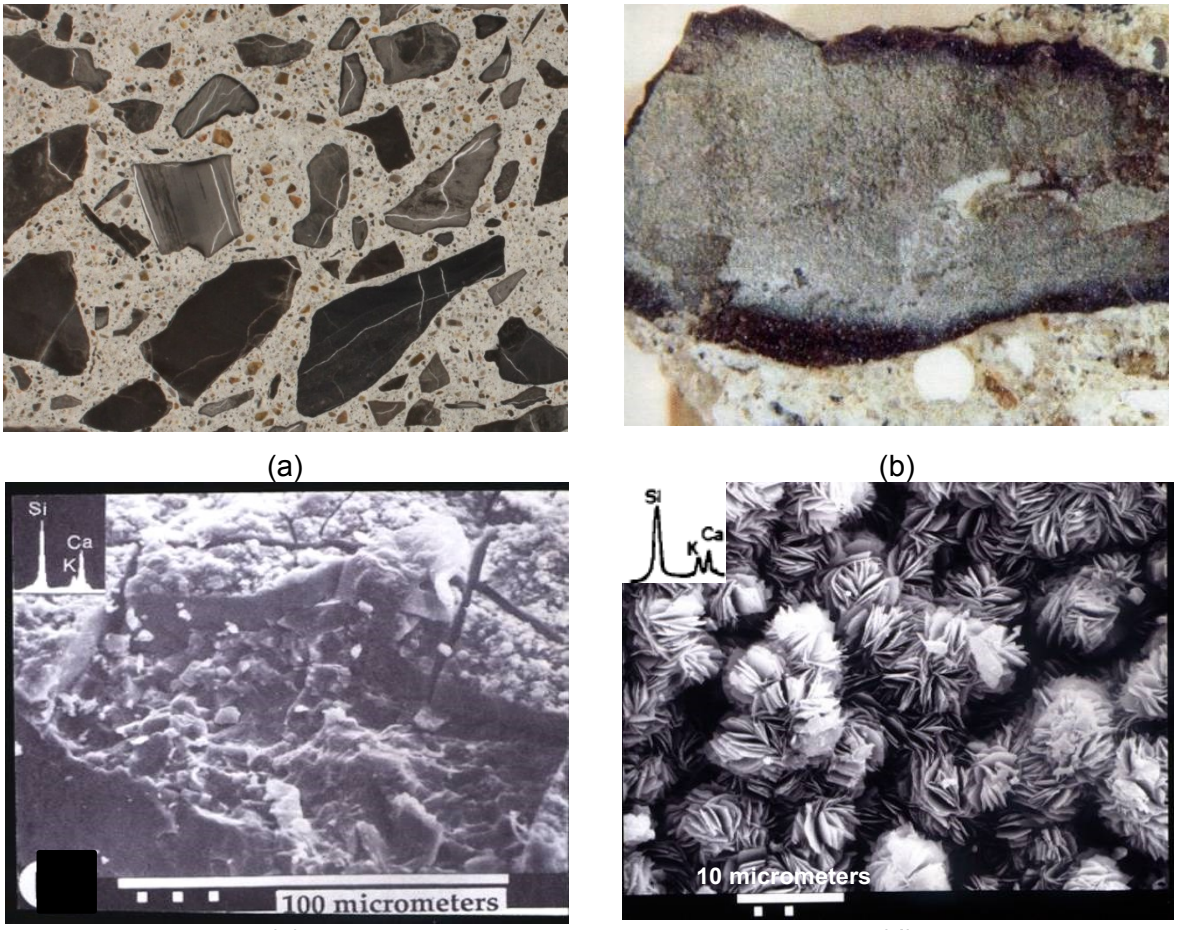

Figure 2.8 (a) Plane polished slabs showing white veinlets corresponding to ASR cracks filled with secondary reaction products; (b) Broken surface of a concrete core showing deposits of ASR products on the cracked surface of a reactive aggregate particle (corresponds to the white veinlets in (a). Secondary ASR products can also be seen filled an air-void below the aggregate particle; (c) SEM micrograph showing the layer of massive gel (containing Si, Ca, K) forming the dark rim on the broken aggregate surface illustrated in (b); (d) SEM micrograph of the crystalline products showing a rosette-like microtexture and corresponding to the white deposits inside the aggregate particle illustrated in (b). (a: with compliments of Fournier (2017); b,c,d: Fournier et al., (2010)).

The ASR product has a general composition of $(SiO_2)(Na_2O)_n\ (K_2O)_k(CaO)_C(H_2O)_x$, which can be written using cement chemistry notation as N-C-S-H, where N represents alkali oxide. In addition, a small concentration of Mg can be present in substitution for Ca (Vayghan et al., 2016). Thomas (2001) compared the composition (Ca/Si; (Na+K)/Si) of ASR products in 7-year-old laboratory concrete and a 55-year-old concrete dam; the results are illustrated in Figure 2.9. Despite the wide range of compositions obtained, a visible relationship shows a reduction in calcium content with decreasing potassium content in the products. The data

supports the concept that a cation exchange occurs as the gel migrates away from the aggregate particle into the calcium-rich cement paste, resulting in calcium replacing the alkali in the initially alkali-rich reaction product (Thomas et al., 2013). The data also suggests that the process continues slowly as the concrete ages, which tends to produce reaction products with low alkali content and a Ca/Si approaching that of C-S-H. Šachlová et al. (2010) conducted a comparative study on a large number of field and laboratory gels and concluded that the age of ASR gel and the chemical components of the surrounding cement paste considerably influence the morphology and the composition of ASR gels.

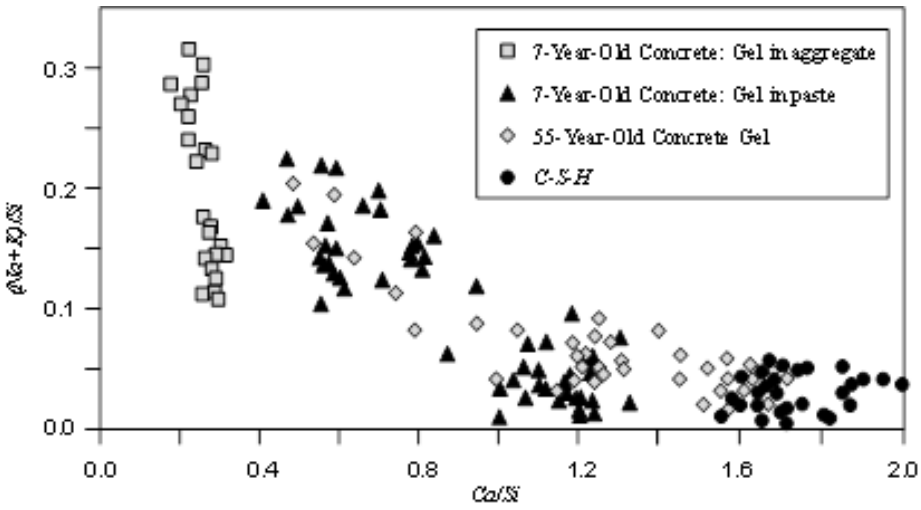

Figure 2.9 Composition of alkali-silica gels in laboratory and field concrete specimens (Thomas et al., 2013).

Dähn et al. (2016) reported the results of the analysis of the ASR products in cracks of aggregate particles of ASR-affected concrete specimens from Switzerland. The product corresponds to a crystalline phase with rosette-like texture, as illustrated in Figure 2.10; the chemical composition of the above product is given in Table 2.1. The crystalline ASR product filling the crack within the aggregate particle is characterized by a Ca-to-Si ratio of 0.23 and a significant alkali (Potassium) content of about 6%. Interestingly, the so-called “gel in aggregate” of the 7-year laboratory concrete illustrated in Figure 2.9 has a Ca-to-Si ratio ranging between 0.2 and 0.3 and may actually correspond to or include analyses of crystalline reaction products.

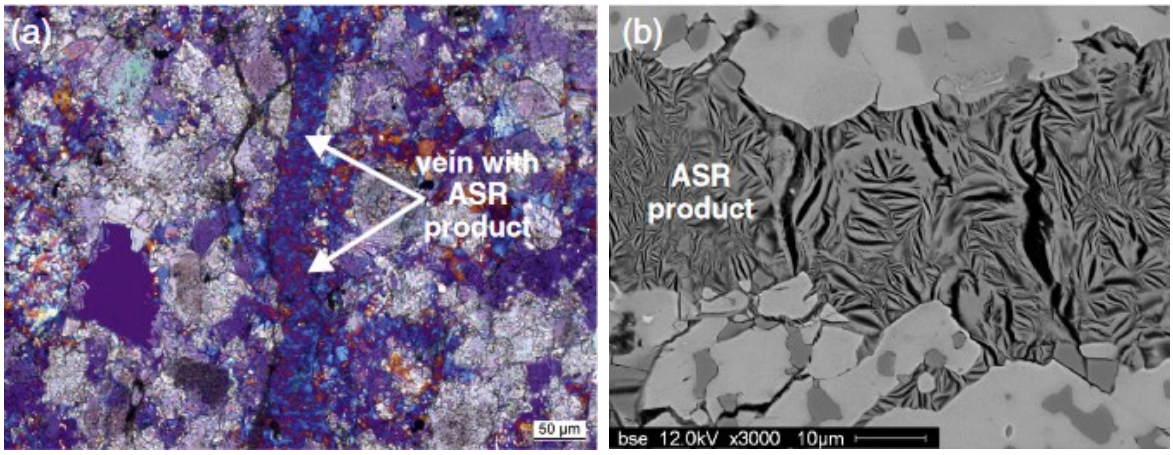

(a) (b)

Figure 2.10 (a) Optical image of the ASR product in the concrete aggregate obtained with a polarization microscope. Crossed polarizers with inserted gypsum plate; (b) SEM image of the vein with ASR product in the concrete aggregate. The light gray mineral of the aggregate is calcite, while the dark gray ones correspond to quartz and feldspar (Dahn et al., 2016).

Table 2.1 EDX analysis of the ASR product (140 analyzed points) within the vein (Dähn et al., 2016).

Elements	O	Na	Mg	Al	Si	S	K	Ca	Fe	Ca/Si	(Na+K)
	mol-%									[—]	/Si
Concentration[mol-%]	47.0	1.5	0.6	0.7	35.1	0.3	6.1	8.1	0.6	0.23	0.22
Standard deviation	±3.1	±0.5	±0.9	±0.3	±1.8	±0.2	±0.9	±1.1	±0.7	±0.03	±0.02

Katayama (2012) reported that ASR gel and crystalline rosettes are universal products of ASR formed from reactive silica phases. Rosette crystals constitute solid solutions with compositions of Na-K-Ca-silicate that are closed to hydrate minerals.

Vayghan et al. (2016) believe that the most deleterious factors in ASR damage mechanism are the gels with high pore solution pH, osmotic pressure, rheology (e.g., yield stress) and the swelling properties. The authors point out that the viscosity of gel determines the rate of flow, which is also dependent on the permeability of the surrounding paste and the residual internal pressure of gel. As the flow progresses, the gel's internal pressure continues to decrease to fractions of the initial yield strength. It should be noted that based on this argument although yield stress of ASR gels is likely to be more important than their viscosity, the two parameters are probably highly correlated; i.e., gels with high yield stress also have a high viscosity.

The effects of the composition (primarily Ca/Si and Na/Si) of synthetic ASR gels on these characteristics are also investigated, and regression analyses are done on the data. The

pessimum combination of osmotic and rheological properties was found in the case of gels having intermediate calcium and high sodium contents leading to the highest estimated swelling pressures. These gels also developed from the most alkaline pore solutions. While the highest yield stresses were observed in the gels with low Calcium and low Sodium contents, they showed negligible osmotic and swelling pressures.

Rajabipour et al. (2015) summarized the current state of understanding and the existing knowledge gaps with respect to reaction mechanisms and the roles of aggregate properties (e.g., composition, mineralogy, size, and surface characteristics), pore solution composition (e.g., pH, alkalis, calcium, aluminum), and exposure conditions (e.g., temperature, humidity) on the rate and magnitude of ASR. Despite decades of study, the underlying chemical and physical reaction mechanisms remain poorly understood, especially at molecular to micro-scale levels, and this has resulted in the inability to efficiently assess the risk, predict the service life, and mitigate deterioration in ASR-susceptible structures.

2.3 Mechanical properties of concrete microstructure

2.3.1 Characterization of the mechanical properties of concrete microstructure

Macroscopically, the concrete microstructure includes at least four phases: (i) hydrated products; (ii) aggregates; (iii) Interfacial Transition Zones (ITZ) around the aggregates; (iv) pores (Mehta et al., 2006).

(i) hydrated products

The microstructure of hydrated cement paste contains solids, voids, and water.

- Calcium-silicate-hydrates (C-S-H);
- Calcium hydroxide (CH);
- Calcium-sulfoaluminates-hydrates;
- Monosulfate hydrate (MON);
- Residual hydrated clinker phases;
- A wide range system of voids;
- Different forms of water.

With the appearance of advanced micro/nanoindentation technologies, a new approach for characterizing the microstructure and properties of the solid components of the hydrated cement paste was developed.

An example of the results of micro-indentation testing on the Calcium-Silicate-Hydrates (C-S-H) is given by Constantinides and Ulm (2004). By means of nanoindentation testing on nondegraded and calcium leached cement paste, the authors confirm the existence of two types of C-S-H, and they investigated the distinct role played by the two phases on the elastic properties of cement-based materials. They concluded that (1) high-density C-S-H are mechanically less affected by calcium leaching than low-density C-S-H, and (2) the volume fractions occupied by the two phases in the C-S-H matrix are not affected by calcium leaching. The nanoindentation results also provide quantitative evidence, suggesting that the elastic properties of the C-S-H phase are intrinsic material properties that do not depend on mix proportions of cement-based materials (Constantinides et al., 2004).

(ii) aggregates

The aggregate is principally responsible for the unit weight, elastic modulus, and dimensional stability of the concrete because its properties depend on the physical characteristics (strength, and bulk density) of the aggregate (Kurtis E.K.). In addition, porosity, shape, and texture of the aggregate are important for workability, durability, and strength. The chemical and mineralogical composition of the aggregate is often considered of less importance; however, some mineral phases within aggregates can generate deleterious reactions inducing major concrete durability issues (e.g. alkali-silica reaction, iron sulfide minerals).

While micro-scratch testing has already been performed on a large variety of materials, there are currently very little statistical micro-scratch test data on aggregates to acquire the micromechanical fracture information on such materials. Akono, A-T et al (2011) present results of a hybrid experimental and theoretical investigation of the fracture scaling in scratch tests and show that scratching is a fracture-dominated process. Validated for Jurassic limestone and other materials, they derive a model that provides a quantitative means to relate quantities measured in scratch tests to fracture properties of materials at multiple scales. The scalability of scratching for different probes and depths opens new venues towards miniaturization of our technique, to extract fracture properties of materials at even smaller length scales. Three test series for cement paste and four series for limestone were

conducted with scratch width, w=2.5mm, 5mm, 10mm and 15mm, and with scratch depth d=0.1–0.6mm, spanning almost 2 orders of magnitude of w/d, from 5 to 100.

(iii) Interfacial Transition Zones (ITZ)

It is experimentally difficult to characterize the interfacial transition zone in concrete with macro-scale tests. The ITZ shows characteristics that are quite different from the bulk cement paste. For instance, the sequence of its development can be summarized as follows. First, in freshly consolidated concrete, calcium, sulfate, hydroxyl, and aluminate ions, produced by dissolution of calcium sulfate and calcium aluminate compounds, combine to form ettringite and calcium hydroxide; then, with the progress of hydration, poorly crystalline C-S-H and a second generation of smaller crystals of ettringite and calcium hydroxide start filling the empty space that exists between the framework created by the large ettringite and calcium hydroxide crystals. This helps to improve the density and hence the strength of the interfacial transition zone (Mehta et al., 2006).

The evolution of the performance of concrete achieved during the past years is mainly due to the improvement of our understanding of the microstructure of the cement paste and especially of the ITZ. The ITZ of very high-performance concrete only extends to a few microns from the inclusions (anhydrous clinker phases, aggregates, fibers, supplementary cementing materials, etc.) and required the development of new techniques of investigations, such as nanoindentation. With this technique, it is possible to measure, in a composite material, the mechanical properties (elastic modulus, hardness) of particles having a size of a few cubic micrometers. This technique is based on the record of the load versus displacement curve at a very low load (less than 50mN). In a first step, the mechanical properties (elastic modulus) of the pure components of the clinker ($C_3S/C_2S/C_4AF/C_3A$) and of the cement paste (CH, C-S-H) have been studied. Then nanoindentation was applied to the high performance concretes.

The results show that the values of the elastic modulus obtained for the different constituents in the concrete are in agreement with those for the same constituents taken independently at constant porosity. In their study, the creep behavior of the C-S-H is also highlighted (Damidot et al., 2003).

2.3.2 Characterization of the mechanical properties of ASR products

Urhan (1987) summarized the results of several studies and proposed that the progressive passage from low viscosity alkali-silica gel to C-S-H is accompanied by a change in the physical and mechanical properties of the gel (Figure 2.11). While low-calcium gel may display high swelling capacity and very low viscosity, high-calcium gel is more rigid but does not swell (Thomas et al., 2013).

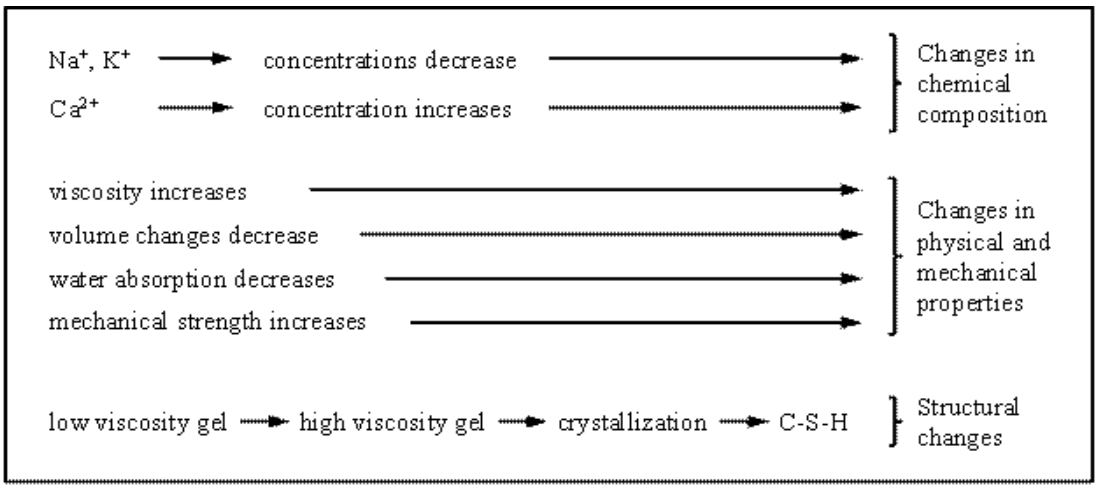

Figure 2.11 Changes in the nature and properties of the ASR product (Urhan, 1987).

Before 2013, there are limited to no data available in the literature regarding the properties of ASR gel, including the E-Modulus. The values used in ASR models actually had to be estimated from testing carried out on materials of similar composition. The E-Modulus of synthesized silica gels may reach values between 6.6 and 10.0 GPa (Murtagh et al., 1986). The bulk modulus of synthesized alkali-calcium-silica gels can range from 4-8 GPa at low $Ca(OH)_2$ content (0.08 M, average E-modulus ≈ 11.5 GPa) to 13-23 GPa at a high $Ca(OH)_2$ content (0.8 M, average E-modulus ≈ 34.5 GPa) (Phair et al., 2005).

Leemann and Lura (2013) characterized the hardness, E-modulus and composition of secondary reaction products in a polished concrete specimen affected by ASR using indentation testing and SEM + EDS analyses. As for the ASR products, they reported Vickers hardness and E-modulus values ranging between 10 and 19 GPa and from 7 to 9 GPa, respectively. Figure 2.12a shows a crack within a reactive limestone aggregate particle filled with secondary reaction products close to the interface with the cement paste. The

contact between the crystalline reaction products (left side) and the amorphous reaction product (right side) is visible. The white dashed line indicates the edge of cracking within the aggregate particle. The concrete fragment analyzed was epoxy impregnated and then polished for further testing. Some cracks are artifacts from drying the sample before impregnation with epoxy. To assess the influence of load level of the results of indentation testing, the tests were performed on the secondary products from different zones inside the crack in the aggregate particles, but with four loading levels ranging from 6mN to 50mN. A typical set of indentation measurements is shown in Figure 2.12b. Towards the edge of the aggregate particle and close to the cement paste, not only the microtexture of the reaction product changes from crystalline to amorphous, along with an increase in calcium content, but both the E-modulus and the Vickers hardness increase considerably, as can be seen in Figure 2.12c.

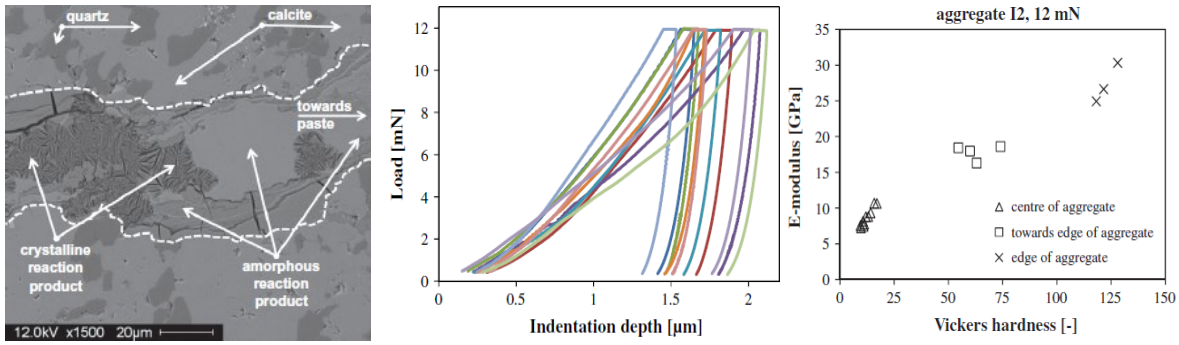

(a) (b) (c)

Figure 2.12 (a) A crack within a reactive limestone aggregate particles filled with reaction product; (b) Variation of indentation depth of the reaction product in the central area of aggregate particle at the load 12mN; (c) E-modulus versus Vickers hardness of the reaction product in the middle part of the crack at the center, towards the edge, and at the edge of the aggregate particle (Leemann et al., 2013).

2.4 Existing ASR models

Modelling ASR is a very complex challenge, influenced by many factors. It is indeed very difficult to make realistic predictions solely based on intuitive reasoning and on the present qualitative knowledge of the ASR chemistry. Therefore, several models have been developed to predict the ASR damage in concrete structures, but most of them only partially account for the key parameters that affect concrete structures, e.g., alkali content, humidity, aggregate's chemical component, structural sizes, etc. Lately, some models have been developed with the attempt of accounting for microstructural features (e.g., aggregate

diameter) so as to give a physical meaning to the model parameters. The ASR models are classified hereafter into three types: (i) macroscopic models, which are based on a phenomenological approach; (ii) mesoscale model, which are based on a *Representative Elemental Volume* (REV) over a reactive aggregate (as the first attempt to consider microstructure geometry); and (iii) microstructural models based on micromechanics. A brief description of those models will be presented in the following sections pointing out the major features and limitations.

2.4.1 Macroscopic models

Ulm et al. (2000) developed an ASR model in the classical thermodynamics framework, which allows for quantitatively assessing the ASR expansion in time and space. They developed a chemo-elastic model in which the ASR kinetics is reproduced by a swelling pressure exerted by ASR products on the cement paste in Figure 2.13a. The mechanical device of swelling gel is shown in Figure 2.13b. The model showed an accurate prediction of ASR timescale, i.e. the latency time associated with the dissolution of reactive silica and the characteristic time associated with the ASR product formation (see τ_l and τ_c in Figure 2.13c). However, the authors considered neither the moisture transport nor the viscosity of the cement paste in their model. The latter was implemented in a Finite Element Method (FEM) to study ASR damage in the concrete structure. They found that ASR deterioration of “massive” concrete structures is driven by the simultaneous activation of heat diffusion and reaction kinetics within a surface layer. In the case “slender” structure, the surface layer damage is rather driven by simultaneous activation of moisture diffusion and ASR kinetics.

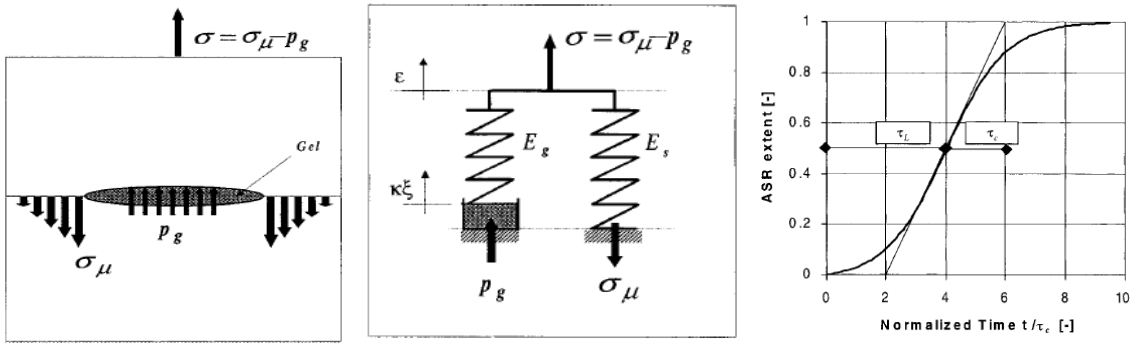

(a) (b) (c)

Figure 2.13 (a) Schematic of swelling gel; (b) Rheological model; (c) Reaction extent curve (Ulm et al., 2000).

In Bažant's model, the kinetics of ASR and the diffusion processes involved were modeled mathematically by considering a periodic cubic cell as *Representative Volume Element* (RVE), which comprises a spherical aggregate particle and the surrounding cement paste (Bažant et al., 2000). The model considers two basic problems: (i) the chemical and micro-diffusion processes kinetics, and (ii) the mechanical damage to concrete. The imbibition of water from the bulk of mortar towards the cell into the basic gel occurs with a delay. The gel swelling is directly estimated from the water imbibed by the basic gel.

Multon et al. (2009) developed a macroscopic model which considers the alkali diffusion in the reactive aggregate in a spherical REV. The ASR kinetic is described by the mass conservation of the alkali concentration. The formation of the ASR gel is calculated by considering the number of moles of ASR gel produced in the aggregate by the number of moles of Na_2O consumed by the reaction. The model considers a threshold alkali concentration as an original feature. One strong assumption of the model is that the ASR gel is incompressible compared to the cement paste. The expansion induced by ASR in each aggregate size fraction can thus be calculated. The stress in the cement paste is calculated by the imposed strain of the aggregate core. Three parts can be distinguished: (i) the central aggregate particle, (ii) the cracked cement paste filled by the gel, and (iii) the part of the REV not yet cracked. As for the cracked zone, the damaged concrete modulus is modeled with a damage variable. The effect of the imposed deformations in the aggregate particle and in the concrete filled by the gel can be compared to a pressure in both the aggregate particle and the cracked zone. The relationship between the damage and the expansion of one reactive aggregate particle was estimated but no data are available in the literature on the decrease of direct tensile strength with ASR expansion. The model was validated on several ASR damage test on mortars. With respect Bažant's model, Multon et al. (2009) model parameters are intrinsic and do not depend on the aggregate size.

Besides, Grimal et al. (2008a) extended the previous model to consider the interaction between viscosity, shrinkage, and damage. The model thus obtained is essentially a viscous-elastic-plastic orthotropic damage model with a chemical pressure induced by AAR. It was implemented in a finite element code to verify the capacity of the model to describe experimental observations. The model well reproduced the anisotropic swelling, the damage, and structural displacements observed during experiments, as well as the influence of oriented cracking induced by restrained AAR swelling on stress states (Grimal et al., 2008b).

In code Aster model of ASR, the reaction and its effects are modeled by using a phenomenological approach. This approach takes account of the various vital phenomena evolving within the concrete and influencing the chemical reaction. De-Bonniers. P. (2011) developed an ASR model to take the viscous-elastic-plastic property into account. As shown in Figure 2.14, the “VEP” represents the viscous-elastic-plastic device. The dependence between the evolution of swelling and the stress state is then a consequence of all these elemental phenomena; the mechanical effects of ASR are thus the consequences of an internal loading “long run” due to the evolution of the chemical pressure (P_g in Figure 2.14), combined with the offsite loading. The viscous-plastic behavior of the cement paste (in particular thanks to the HSC Grimal (2007) can limit the stress concentration and thus the propagation of microscopic cracks; the associated damage is also restricted.

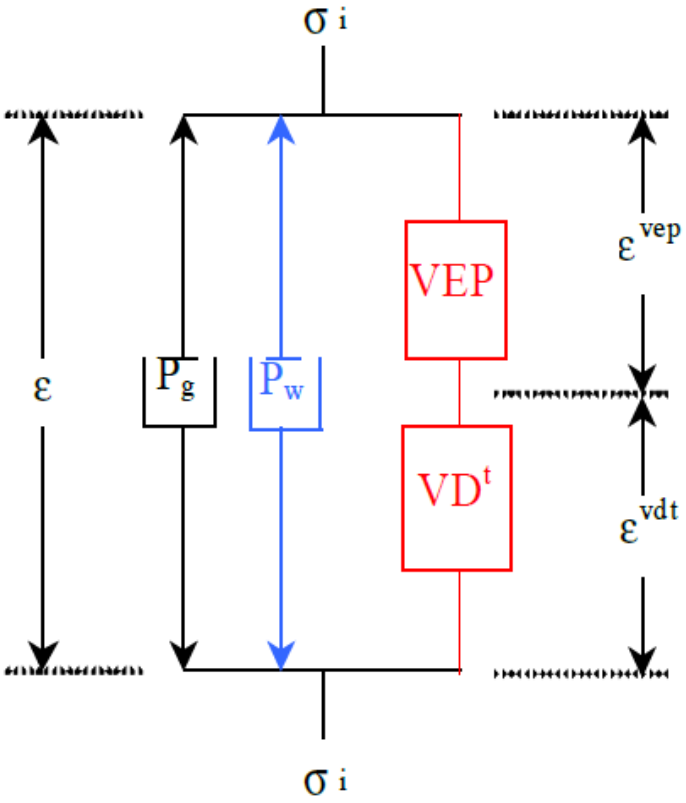

Figure 2.14 Principle of the model of the behavior of the concrete subjected to a pressure of swelling (De-Bonniers P., 2011).

Where:

P_g: gel swelling pressure,

P_w: water pressure,

σ_i: the external pressure,

ε: the total strain,

ε^{VEP}: Visco-elastoplastic strain,

ε^{Vdt}: modelization of the strain.

The Code-Aster of ASR model accounting for the swelling gel and visco-elastoplastic strain gives an open access to the FEM analysis of future models of the ASR-damaged concrete.

2.4.2 Mesoscopic models

The model developed by Dunant and Scrivener (2010) considers the interaction between the gel and the matrix. Its implementation in a Finite Element Method (FEM) was carried out in a mesoscale level where spherical aggregates are randomly distributed. Comby-Peyrot et al. (2009) developed a 3D mesoscopic model, which was used to describe homogeneous concrete damaged due to ASR. The two-phase mesoscopic model is composed of aggregate particles and cement paste, in which the aggregate is assumed purely linear elastic and the cement paste behaves as inelastic-damage material. The ASR expansion mechanism is simplified based on anisotropic dilatation phenomenon of reactive aggregate.

2.4.3 Micromechanical models

There are some other ASR models which focus on different aspects, especially the ion transportation and geometry. The micromechanical models are based on homogenization theory to better consider: (i) the anisotropic expansion of concrete through the computation of cracking direction; (ii) the effects of internal moisture and ion concentration on the transport properties of concrete; and (iii) the effect of pore size.

Wiwat et al. (2013) developed a coupled analytical chemo-mechanical model to include the effects of internal moisture and ion concentration on the transport properties of concrete. This chemo-mechanical model is implemented into a Finite Difference method considering aggregates of diverse shapes and sizes. The model well captures the anisotropic expansion of ASR-damaged concrete. Finally, the accuracy of the model is assessed through comparison with simulated laboratory tests.

Charpin et al. (2013) developed a micromechanics model on a multi-sphere microstructure which accounts for the damage developed in the ITZ zone around the aggregates. The

energy formulation is based on poromechanics approach. Once the porosity is filled, the gel builds up a pressure. The model is based on an energy minimization principle and the results capture the anisotropy induced by external loading. A finite element model is validated to simulate the coupled diffusion of alkali into concrete and subsequently to perform a nonlinear analysis. The model aims at predicting the anisotropy of the macroscopic expansion of concrete through the computation of the direction of annular cracks (in Figure 2.15) (Charpin et al., 2013).

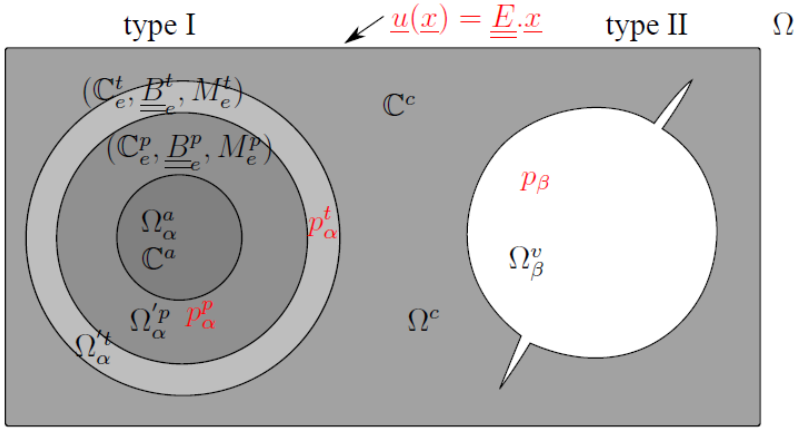

Figure 2.15 Micromechanical model with anisotropy computation of crack directions (Charpin et al., 2013).

Lemarchand et al. (2005) distinguished between the through-solution and topochemical reaction mechanism into the framework of micro-macro-homogenization theory. This model investigates expansive reactions from a micromechanical point of view, which allows bridging the scale from the local chemo-mechanical mechanisms to the macroscopically observable stress-free expansion. In their model, the effect of the microscopic geometry of pores and microcracks in the solid matrix on the macroscopic expansion has been considered. The second part deals with the transition from a topochemical to a through-solution-like mechanism that occurs in a solid matrix with inclusions (cracks, pores) of different morphology.

3. Research Program

As mentioned before, this research aims at contributing to a better understanding of the mechanisms of alkali-silica reaction (ASR) with new techniques, such as nano-, micro-indentation, and micro-scratch. The general description of the research program is illustrated in Figure 3.1. It is divided into three phases. These phases included experimental work

carried out on cores extracted from two ASR-affected concrete structures located in two regions of the St. Lawrence lowlands of the Province of Québec (Canada) and that were used for microstructural evaluations. The affected concretes typically include coarse dark grey, fine-grained siliceous/argillaceous limestone aggregates of the Trenton Group (Ordovician age). In such concretes, aggregate particles typically display ASR-induced cracks filled with secondary reaction products, thus forming white veinlets. In many cases, those veinlets seem to form preferentially along the bedding planes in the limestone particles. Also, several particles show light-grey zones where the white veinlets can be found. New techniques of microstructural characterization were thus used to investigate the development of damage within the above reactive aggregate particles, especially the mechanical properties of ASR products forming the white veinlets.

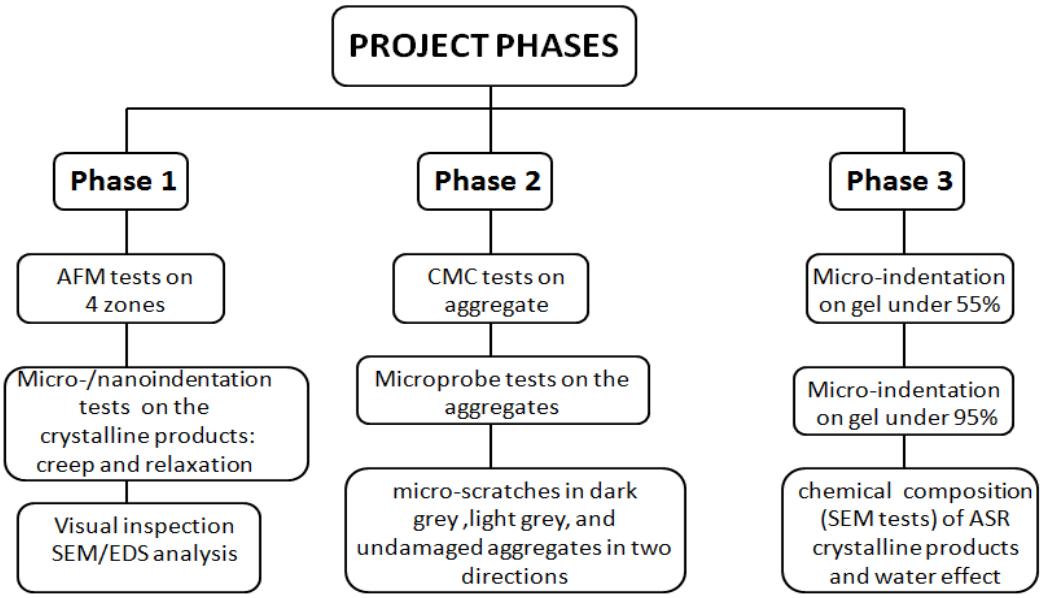

Figure 3.1 Experimental phases of the Ph.D. project.

3.1 Phase 1

The first phase aimed at evaluating the micromechanical properties of the secondary products forming white veinlets within the reactive limestone aggregate particles. Testing was carried out on a sample prepared from a core extracted from a concrete pavement located in the Becancour area (Québec) (Figure 3.2). The pavement was constructed in the 1960's using concrete incorporating a coarse limestone aggregate exploited in a quarry located on the North shore of the St. Lawrence River; this siliceous limestone is from the St. Casimir member (Neuville Formation) and is considered as highly reactive (Fournier B., 2013). The pavement in question shows signs of extensive expansion and cracking (Figure 3.2a to 3.2d). Cores were extracted from different sections of the pavement, including those showing well-developed map cracking (Figure 3.2e) (Allard et al. 2016). Immediately after coring, the surficial excess water was removed with a cloth and each core was wrapped with several layers of plastic film. The cores were then stored in a room maintained at 12℃ until due for testing; that temperature was selected in order to slow down/arrest the deleterious ASR process in the concrete. One of the core samples thus obtained (from a highly-damaged section of the pavement) was cut longitudinally with a diamond saw (with water) and the surface thus obtained examined under the stereomicroscope. The concrete was characterized by extensive microcracking in the cement paste and numerous aggregate particles with cracks filled with secondary reaction products (Figure 3.2f). For Phase 1, one aggregate particle incorporating several ASR-induced cracks filled with secondary reaction products was selected for micro- and nano-indentation testing under a fixed RH of 30% (Figure 3.2g).

Sample preparation in this whole research program followed a strict procedure that is described in Appendix 1. Following sample preparation, Atomic Force Microscopy (AFM) was applied for characterizing surface roughness prior to micro-/nano- indentation testing; the detailed results of AFM testing are presented in Appendix 2 and summarized in Chapter 4. E-modulus and Vickers hardness were then measured on the reaction products and compared to data available in the literature. The results of Phase 1 are presented in Chapter 4; the latter is built as a scientific paper and it was submitted for publication in Construction and Building Materials Journal.

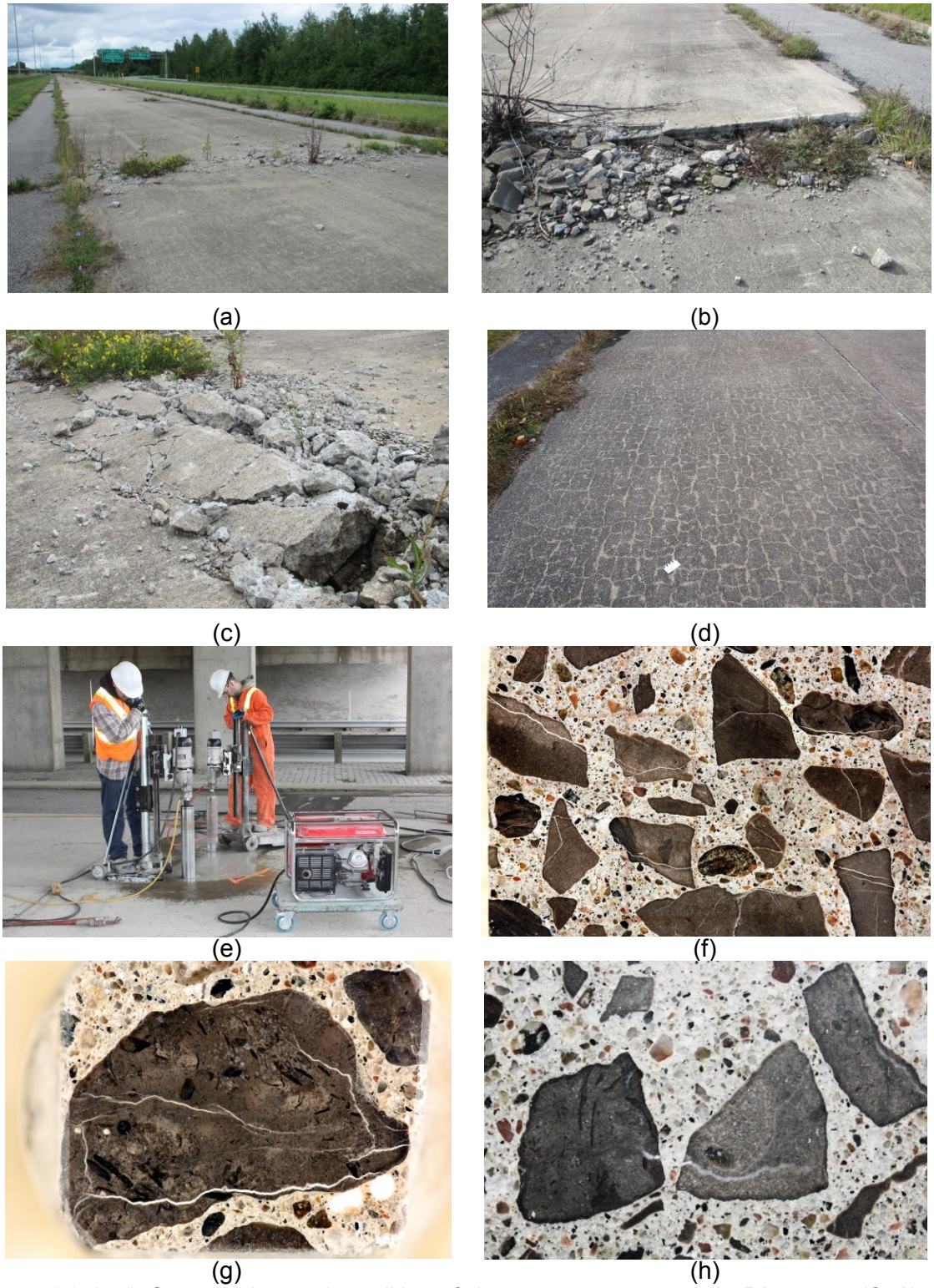

Figure 3.2 (a-d) General view and condition of the concrete pavement in Bécancour (Québec); blowing at joints and extensive cracking are observed in several sections of the pavement; (e) Coring of a concrete section of the pavement; (f) Plane polished slab prepared from a core extracted from an heavily-cracked section of the pavement; (g) Sample used for Phase 1 of the experimental program; (h) Sample used for Phase 3 of the experimental program.

3.2 Phase 2

The second phase aimed at determining whether the micromechanical properties of the coarse limestone aggregate are affected through the reaction developing within the particles due to ASR. In order to do so, a “fresh” rock sample was extracted from a quarry in Québec City. The whole stratigraphic sequence in the area is exploited in several quarries and relates to the Neuville Formation (Trenton Group); it is typically characterized by 10 to 20cm-thick beds of siliceous/argillaceous fine-grained and dark grey limestone with more or less important shale interbeds (Figure 3.3a) (Fournier B., 1993). One “typical” sample of such limestone was selected (Figure 3.3b), and a small rock block, approximately 30x30x15mm, cut perpendicular to the sedimentary bedding. After adequate sample preparation, micro-scratch testing was carried out in directions parallel and perpendicular to the bedding (Figure 3.3c).

In parallel, a number of aggregate particles in concrete cores extracted from a heavily ASR-affected concrete highway structure in the Québec City area were subjected to micro-scratch and micro-indentation testing, and this to determine their “residual” micro-mechanical properties. The concrete structure in question was built in the 1960’s and consists in a thick-deck superstructure supported by Y-shaped columns sitting on massive concrete foundation blocks (Figure 3.3d) (Fournier et al., 2015). The structure was demolished in 2010 and cores were extracted immediately before the demolition of the massive concrete foundation (Figure 3.3e and 3.3f). Immediately after coring, the surficial excess water was removed with a cloth and each sample wrapped with several layers of plastic film. The cores were then stored in a room maintained at 12^{o}C until due for testing.

Three cores were cut in half lengthwise. One face of each specimen was then polished with a portable hand wet polishing device, which uses diamond-impregnated rubber disks. The polished sections were typically showing extensive cracking both in the aggregate particles and in the cement paste (Figure 3.4a). One dark-grey (somewhat “less reacted”) and three particles showing light-grey zones “incorporating” white veinlets were subjected to micro-scratch testing (Figures 3.4b and 3.4c). A portion of the particle illustrated in Figure 3.4c was subjected to electron microprobe microanalysis. The results of Phase 2 are presented in Chapter 5; the latter is built as a scientific paper to be submitted for publication in a scientific journal.

Figure 3.3 (a) Typical sequence of Trenton limestones (Neuville formation) in a quarrying operation of the Québec City area; (b) Dark-grey and fine-grained limestone sample selected for micro-scratch testing; (c) Small rock slab 30x30mm in size, cut from the block sample in (b) and subjected to micro-scratch testing; (d) Highway bridge structure affected by ASR, Québec City area; (e&f) Core samples extracted from the massive foundation blocks supporting the Y-shaped columns.

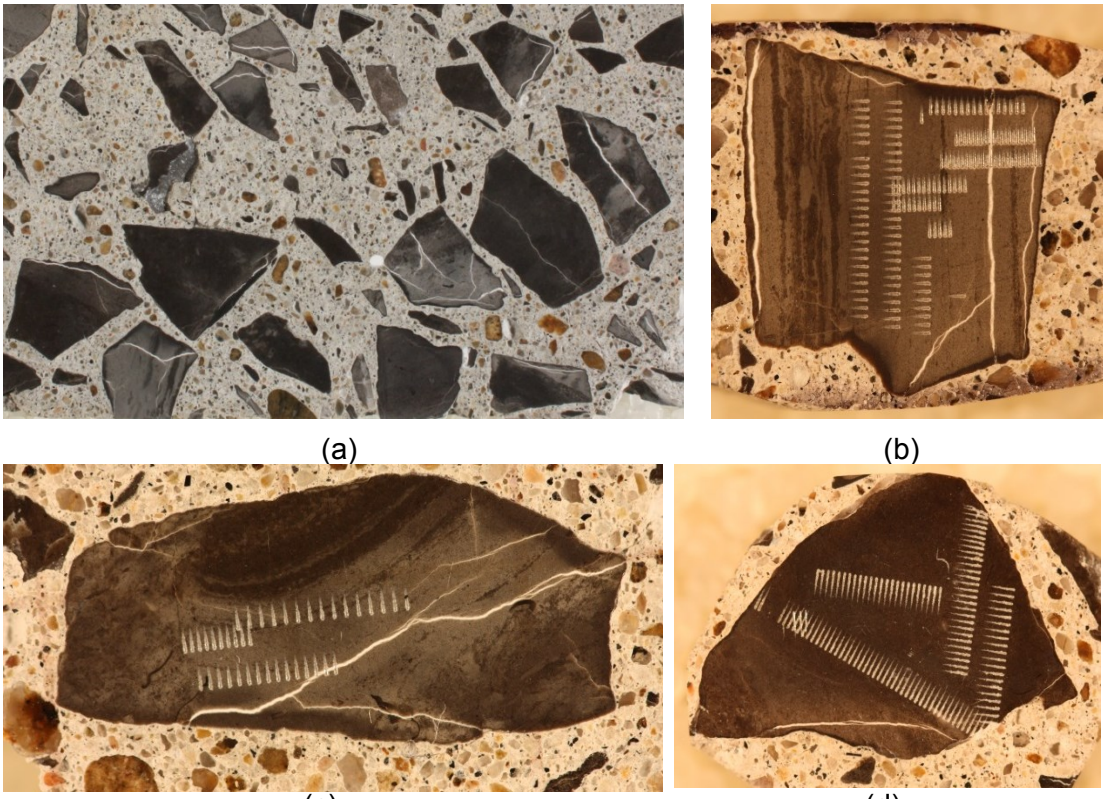

Figure 3.4 (a) Typical plane polished slab prepared from a core extracted from the foundation block illustrated in Figure 3.3d-f, and showing several aggregate particles with ASR-induced white veinlets; (b&c) Reactive limestone aggregate particles with light-grey zones and white veinlets; micro-scratch testing was carried out parallel and/or perpendicular to the bedding in the particle; (d) Dark-grey limestone aggregate particle selected from a polished slab (massive concrete foundation block) and subjected to micro-scratch testing.

3.3 Phase 3

The expansive character of ASR products is a function of its composition, including its moisture content. In the third phase, the micro-mechanical properties of the ASR products forming the white veinlets within coarse limestone aggregate particles are evaluated through micro-indentation testing. The sample used for testing was obtained from a core extracted from the concrete pavement described in section 3.1 (Figure 3.2h).

In order to do so, a special set-up was implemented to maintain the specimens under different relative humidities during testing, thus allowing measuring the viscoelastic properties of the crystalline ASR products forming the white veinlets within the reactive aggregate particles under ambient RH values of 65% and 95%. The nature of the above reaction products was also confirmed under the scanning electron microscope.

Finally, in the discussion chapter, a simplified predictive model is presented as first step stone towards an exploitation of the new knowledge generated by the original experimental work carried out as part of this research.

4. Article 1: Stress Relaxation of Crystalline Alkali-Silica Reaction Products: Characterization by Micro- and Nanoindentation and Simplified Modeling

Chi Zhang[(1)], Luca Sorelli[(1)] Benoît Fournier[(2)], Josée Duchesne[(2)], Josée Bastien[(1)] Chen Zhao[(1)]

1) Université Laval, Civil and Water Engineering Department, 1065 avenue de la Médecine, PLT2928-A, G1V0A6, Québec, Canada.

2) Université Laval, Geology and Geological Engineering Department, 1065 avenue de la Médecine, G1V0A6, Québec, Canada.

The paper under review for possible publication in "Construction and Building Materials" Journal.

Abstract

Alkali–silica reaction (ASR) is a major issue for the durability of concrete structures worldwide. Fostering recants work which revealed the elastic property of ASR products elastic property, this work aims at further characterizing the viscous property of ASR products. In particular, this study focuses on the relaxation behavior of ASR crystalline products rosette-like located in aggregate cracks. Moreover, two different length scales of characterization were considered by means of micro- and nanoindentation. First, the surface roughness and the chemical composition of ASR products in real field concrete were examined by Scanning Electron Scanning (SEM) and Energy Dispersive X-ray spectroscopy (EDS). Then, the viscous behavior of structured ASR products with rosette-like micro-texture was characterized by performing relaxation tests by micro-indentation, providing new knowledge on the relaxation behavior of the ASR crystalline products which was about 40%. Furthermore, nanoindentation tests at smaller scale were also carried to better understandings the possible length-scale effect. In spite of the large scatter due to the roughness noise, the characterization at lower scale by nanoindentation seems to show that the ASR rosette crystals have a greater modulus and lower relaxation rate. As a possible explanation, the difference is likely due to the visible microcracks between the ASR rosette crystals. Finally, a simplified rheological model was employed to estimate the viscosity and characteristic time of the ASR crystalline products.

Beyond providing a first estimation of the viscous behavior of ASR crystalline products, the present approach further advances a new research direction for characterizing the mechanical properties of ASR products, which not only can enhance current knowledge on the governing microstructure mechanisms but also supply input data for the multiscale models which are currently under development.

Keywords: alkali-silica reaction; concrete damage; microstructure; micro-indentation; nanoindentation; relaxation tests; viscous modeling.

4.1 Introduction

Expansion due to Alkali-Silica Reaction (ASR) is a long-term durability issue and a major cause of concrete deterioration for civil engineering structures, such as bridges, pavements, dams, etc. (Association, 1992; Fournier et al., 2000; Godart et al., 2013; Swamy, 2002). Although ASR was first reported in 1940 (Stanton 1940), its reaction-expansion mechanism is recognized to be rather complex and not yet fully understood (Helmuth, 1993; Rajabipour et al., 2015). Amorphous, metastable and poorly crystalline forms of silica, as well as microcrystalline and strained forms of quartz present in certain aggregates, are attacked by the hydroxyl ions present in the pore solution, causing their dissolution into silicate ions. The latter react with alkalis and calcium ions present in concrete pore solution, precipitating into a hydrous alkali-calcium-silica gel of variable stoichiometry, molar volume and mechanical properties (Fournier et al., 2000; Peterson et al., 2006; Rajabipour et al., 2015). The ASR gel has the capacity to imbibe water molecules causing extensive swelling, which, when constrained, can produce pressure and cracking in aggregate particles and surrounding cement paste (Ben Haha et al., 2007; Sanchez et al., 2016; Swamy, 2002; Swamy et al., 1988). The effect of concrete expansion on the performance of structural elements affected depends on the degree of ASR, but also on the local stress situation, the anisotropic growth of crack and gel migration (ISE, 1992; Multon et al., 2005; Multon et al., 2009). As for the damage process, the cracks develop in the reactive aggregate particles at lower expansion levels (i.e.: inferior to 0.05%), while cracking extends into the cement paste as the reaction/expansion progresses (Ben Haha et al., 2007; Reinhardt et al., 2011; Sanchez et al., 2015; Thomas et al., 2013).

ASR gels have a general composition of $(SiO_2)\cdot(Na_2O)_n\cdot(K_2O)_k\cdot(CaO)_c\cdot(H_2O)_x$ and can be rewritten using cement chemistry notation as N–C–S–H, where N represents alkali oxides. In addition, a small concentration of Mg may be present as a substitution for Ca (Vayghan et al., 2016b). ASR products often exhibit a layered structure hinting to a periodical sol/gel transformation induced by swelling and drying (Godart et al., 2013). Several authors observed that ASR products exhibited a rosette-like (or plate-like) microtexture within microcracks located in the center of reactive aggregate particles, while they become more amorphous in the proximity of the edge of the aggregate (Bérubé et al., 1986; Helmuth, 1993; Leemann et al., 2013). The amorphous (gel) ASR products in cracks near the edge of the aggregate particles and in cracks of the cement paste show a higher Calcium content as an uptake from the surrounding cement paste (Katayama, 2012; Leemann et al., 2013;

St John et al., 1998). Further kinds of ASR products have been reported in the literature, e.g. hummocky and/or stratified/recrystallized gel, alveolar micro-texture, etc. (Bérubé et al., 1986; Helmuth, 1993; Larive et al., 1992; Peterson et al., 2006), while they have been reported in coexistence with ettringite (i.e., a hydrous calcium aluminium sulfate mineral).

As for a modeling point of view (Ichikawa et al., 2007; Pan et al., 2012; Seignol et al., 2012), a large number of micro- to macroscale models have been developed to consider the effect of the ASR reaction kinetics on the damage and expansion of concrete (Bažant et al., 2000; Lemarchand et al., 2005; Multon et al., 2009; Pesavento et al., 2012; Ulm et al., 2000). In particular, discrete models have been recently developed to explicitly account for specific microstructure mechanisms due to expansive ASR gel, such as: anisotropic crack growth (Alnaggar et al., 2013) or the gel growth in aggregate pockets (Ben Haha et al., 2007; Dunant et al., 2010). Late versions of such models consider the elastic properties of the ASR products, but the visco-elastic nature of the gel is often ignored for lack of experimental data (Dunant et al., 2016). Interestingly, a chemo-physico-mechanical approach was developed to take into account the transport and mechanical properties of ASR products and explain the pessimism size effect (W. Jin, 1998).

In spite of the considerable research advancement in modeling ASR process in concrete, there are very few data available in the literature regarding the mechanical property ASR products. For instance, the E-modulus of the reaction product used in those models had to be estimated based on synthesized silica gels created in a laboratory for which the E-modulus varies from 11 GPa to 35 GPa, depending on the calcium content (Murthagh et al., 1986; Phair et al., 2005b). Recently, a micro-indentation technique has been successfully applied to characterize the elastic modulus and the indentation hardness of ASR products within the cracks of aggregate particles and cement paste (Leemann et al., 2013). Their results showed that, in the aggregate center, the E-modulus and Vickers hardness of the ASR products (crystalline rosette-like products) were 5-10 GPa and 10-20 GPa, respectively. However, the E-modulus and Vickers hardness of the ASR products in cracks and close to the edge of the aggregate particle (massive gel) reached maximum values of 45 GPa and 270 GPa, respectively. Moreover, their results showed a substantial creep of the ASR products, even for relatively small holding time of the force. However, they did not attempt to measure the indentation creep of ASR products.

During the ASR chemical reaction, the gel volume increases engendering high internal pressure, which, afterward, gradually relaxes (i.e., the stress is gradually released at constantly imposed deformation) due to the viscous behavior of the gel. Under confining stress, Jin et al. (2000) proposed that the viscous ASR gel is able to permeate into the surrounding porous ITZ and cement matrix, thereby relieving the pressure caused by the gel expansion. The observed expansion is, therefore, the result of the elastic and inelastic deformations caused by the net hydrostatic pressure, which depends on the elastic moduli of the matrix and aggregate, the viscosity of the ASR gel, the permeability of the matrix, and the aggregate size and content. As a consequence, the ASR gel internal pressure continues to decrease (Vayghan et al., 2016b).

This work aims at further applying indentation techniques for fully characterizing the viscous relaxation behavior of ASR products, especially for those with crystalline-like structures which are commonly found in the cracks inside the aggregate. The research significance of this work is the characterization of the relaxation behavior of in-situ ASR crystalline products and the quantification of their visco-elastic properties by a simplified analysis. The present study provides original results on the properties of ASR products which are critical for current research aiming to link the external expansion to the ASR reaction.

4.2 Materials and Methods

4.2.1 Material and sample preparation

Cores, 100 by 225mm in size, were extracted from an ASR-affected concrete pavement that was built in the 1970's in the Becancour area (Québec, Canada). The two-lane pavement, which has never been opened to traffic, is composed of 15 meter long sections that are linked by dowel bars. No records could be found of the specific mix design of the original concrete; however, the main Québec DOT specification at the time was requesting a compressive strength of about 31 MPa at 28 days for this type of application.

The concrete incorporated a highly-reactive siliceous limestone from the Neuville formation (St. Casimir member) exploited in the Trois-Rivières area across the St. Lawrence River (Fournier et al., 1991). The pavement section, from which full-depth coring (225mm) was carried out, displays extensive map cracking (Figure 4.1b). Despite the somewhat alarming

surficial condition of the concrete, Allard et al. (2016) reported compressive strength and E-modulus values averaging 47.5 MPa and 24.5 GPa (each measured on six 100mm cores), respectively. Interestingly, cores extracted from somewhat “protected” pavement sections under a bridge structure and showing only slight visual cracking, provided compressive strengths and E-Moduli ranging from 57.7-62.9 MPa and 33.6-35.8 GPa, respectively (Allard et al., 2016). Immediately after extraction, the cores were superficially dried and then wrapped in several layers of plastic sheets (cling film); the specimens were then brought to the laboratory where they were kept in a temperature-controlled room (12℃) until ready for further processing. The core selected for microanalysis was first to cut into 10mm-thick slabs with a concrete saw (with water). The slabs were examined with a stereomicroscope to identify aggregate particles with “large” cracks filled with ASR products (e.g. Figure 4.2a), and further cutting was carried out to produce a proper size specimen for indentation testing.

(a) (b)

Figure 4.1 (a) General view of the Becancour concrete pavement; (b) Surficial condition of the pavement section from which the cores used for the testing program were extracted.

The specimen was finely polished based on the protocol described by Leemann and Lura (2013), with an additional polishing step with diamond suspension with the size of 0.25μm to further reduce the roughness. As described in Table 4.1, the surface of the specimen was first subjected to three polishing steps using SiC sandpapers with a minimum amount of water. The fine finishing was then carried out using oil-based diamond suspensions and diamond paste (Table 4.1). The surface of the specimen was then protected in air-tight plastic bags and subjected to indentation testing within 24 hours after the completion of the polishing operations as done by Leemann et al. (2013). Figure *4.2* illustrates the specimen used for testing.

Table 4.1 Polishing protocol procedure adopted in this work.

Sandpaper	Microns [µm]	Methods	Duration [min]
SiC sandpaper 400-400	22	With water	10
SiC sandpaper 400-800	12	With water	10
SiC sandpaper 400-1200	6.5	With water	15
Oil based Diamond suspension	6	Acetone flush, air gun dry	40
Oil based Diamond suspension	1	Acetone flush, air gun dry	30
Diamond paste	0.25	Acetone flush, air gun dry	60

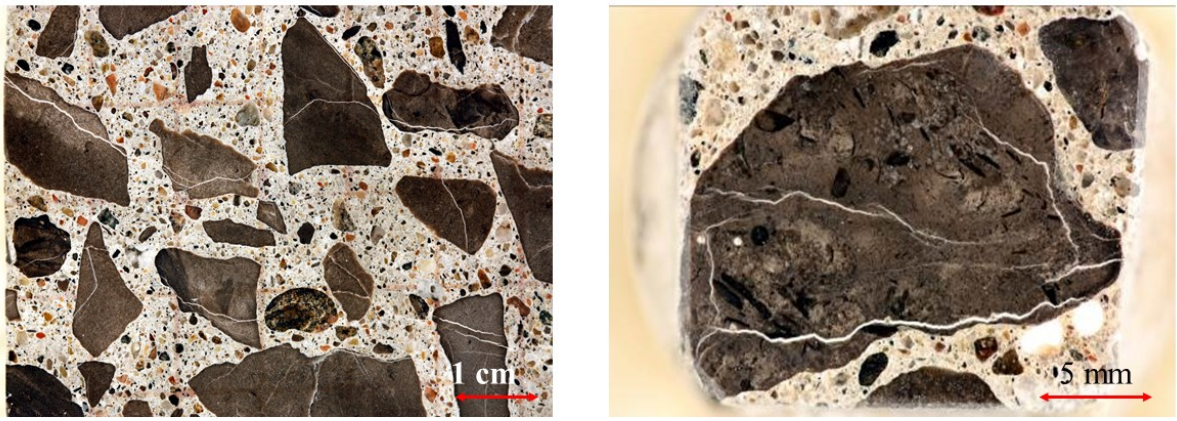

Figure 4.2 (a) Polished concrete section from the Becancour pavement showing numerous siliceous limestone aggregate particles with cracks filled with secondary alkali-silica reaction products; (b) Zoomed view of the specimen used for indentation testing.

4.2.2 AFM and SEM\EDS techniques

Atomic force microscopy (AFM) allows the topographical scanning the surface of a sample with a resolution of the order of fractions of a nanometer (Meyer, 1992). The AFM consists in a cantilever with a sharp tip (probe) that is used to scan the specimen surface. The AFM tests were carried out on a companion sample which was polished with the same exact protocol that was used for the sample (as explained in Table 4.1) tested by micro-/nanoindentation.

The sample subjected to indentation testing was further examined by scanning electron microscopy (SEM - JEOL JSM-840A) using secondary electron (SE) imaging and energy dispersive X-ray spectroscopy (EDS). Operating conditions were set at 15 kV. Prior to SEM observations, samples were gently dried for 24 hours at 50℃, and then coated with a thin layer of Au-Pd.

4.2.3 Basics of nanoindentation and micro-indentation

An indentation test consists of establishing contact between an indenter (typically diamond) and a sample, and subsequently measuring the load, P, and the penetration depth, h (Fischer-Cripps, 2004; Fischer-Cripps, 2000a, 2000b). Figure 4.3a shows a typical P-h curve for a test with an initial constantly increasing load, followed by a short hold and then a constant unloading. By analyzing the P-h curve with a continuum model (Galin et al., 1961; Harding et al., 1945; Oliver et al., 1992), the indentation hardness H and indentation modulus M can be derived as defined below:

$$H \overset{def}{=} \frac{P_{\max}}{A_C} \qquad (4.1)$$

$$M \overset{def}{=} \beta \frac{\sqrt{\pi}}{2} \frac{S}{\sqrt{A_c}} \qquad (4.2)$$

where the coefficient β accounts for slip contact for a Berkovich shape tip; A_c is the projected area of the indenter at a distance h_c; P_{max} is the maximum load and $S = \left(dP/dh\right)_{h=h_{\max}}$ is unloading indentation stiffness at the maximum penetration depth ($h=h_{max}$). The latter can be estimated by the well-established Oliver and Pharr method for which $A_c = 3\sqrt{3}h_c^2 \tan^2\theta$, where $h_c = h_{\max} - \varepsilon \frac{P_{\max}}{S}$ (Oliver et al., 1992). For the employed Berkovich indenter, $\beta = 1.034$ and $\varepsilon = 0.75$ (Fischer-Cripps et al., 2004; Sorelli et al., 2008). A typical P-h curve for an indentation test is shown in Figure 4.3c. The standard calibration procedure is carried out to define the contact area of the tip on a calibration sample of fused silica (Fischer-Cripps, 2002).

Contrarily to Leemann and Lura (2013), we preferred to carry out indentation test at imposed displacement rather than an imposed load for three reasons: (i) the Hardness value is not affected by the change of the contact area which is known during all the tests, and not estimated at the unloading phase (Fischer-Cripps, 2004); (ii) the viscous behaviour during a relaxation tests is not affected by possible delayed plasticity and it allows extracting the visco-elastic property (Vandamme et al., 2012); (iii) the volume of material probed is similar for all tests, as proportional to the penetration depth (Constantinides et al., 2006). In an indentation relaxation test, the penetration-time ramp P(t*)* is imposed and the maximum penetration depth (h_{max}) is achieved in a relatively short time (τ_L=*5s*), as shown in Figure 4.3a; then, the penetration depth is kept constant for the holding time (τ_H=*600s*), and finally

quickly unloaded (τ_U=*5s*), as shown in Figure 4.3b. For a viscous material, stress relaxation is the observed under sustained strain, that is, the load relaxes with time during the holding phase as shown in Figure 4.3a. As for an indentation test, the relaxation coefficient can be defined as the reduction of the load during the holding phase normalized to the maximum load as follows:

$$R \overset{def}{=} \left[P(\tau_L + \tau_H) - P(\tau_L)\right] / P(\tau_L) \tag{4.3}$$

For both micro- and nano-indentation testing carried out in this study, the indenter tip was a Berkovich shape. The Anton-Paar MCT micro indenter is endowed with a passive reference system which reduces the thermal drift, while the Anton-Paar UNHT nanoindenter is endowed with an active reference system which reduces the thermal drift (quite important at that scale) down to 1nm over 500 s (Nohava et al., 2009). All the tests were conducted in a laboratory room under controlled temperature (20℃ ± 0.5℃) and relative humidity (30% ± 1%).

The penetration depth of the indentation was suitably chosen to characterize the ASR structure at two different length scales. Leeman and Lura (2013) carried out the micro-indentation test by imposing a constant maximum load from 6 to 50mN, which corresponded to an average penetration depth varying from 0.8 and 4μm. Due to roughness issue, their results at the lowest load were very scattered, e.g., the Vicker Hardness varied from 10 to 25 GPa. In this study, we carried micro-indentation test by imposing a maximum penetration depth h_{max} of about 2μm and 0.5μm for the micro-indentation and nanoindentation tests, respectively. Notably, the volume probed by micro-indentation tests is approximately proportional to penetration depth h_{max}, such as $V_{probed} \sim \left(10\, h_{\max}\right)^3$ ~ 8000μm^3 (Panich et al., 2004; Vandamme et al., 2012). For nanoindentation testing, a maximum penetration depth (h_{max}) of about 0.5μm was chosen, which implies a probed volume of about 125μm^3, i.e. about 64 times smaller than that of the micro-indentation test.

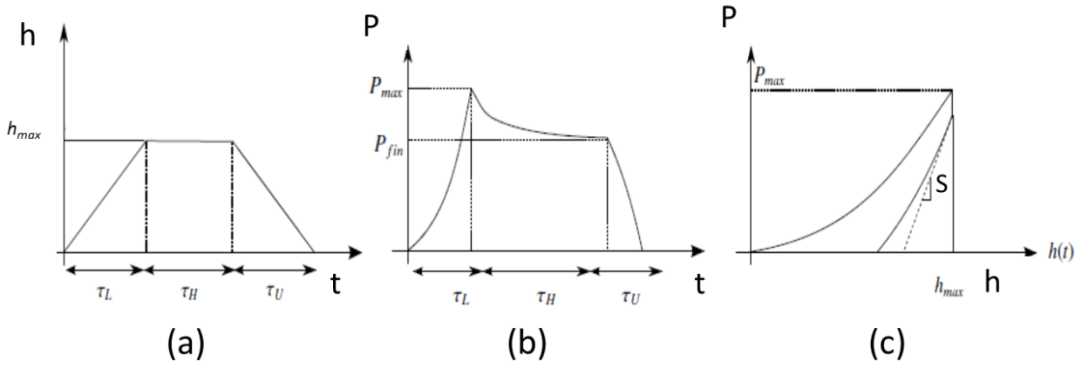

Figure 4.3 Example of a relaxation indentation test on a viscous material: (a) Imposed penetration depth-time (h-t) curve; (b) Measured load-time (P-t) curve; (c) Resulting load-penetration depth (P-h) curve.

4.3 Experimental results

4.3.1 AFM results

The scope of AFM tests is to verify the roughness of the sample surface as a critical factor for indentation testing, especially for nanoindentation. For instance, it was found that a surface roughness that is 10 times smaller than the penetration depth does not usually affect the indentation results (Miller et al., 2008). Figure 4.4 visually compares the surface roughness of the of a comparison sample with same features as those illustrated in Figure 4.4b and prepared following the exact same procedure for the following zones: (a) limestone aggregate surface; (b) ASR products filling the aggregate crack, and (c) cement paste surrounding the reactive aggregate.

Figure 4.5a compares the roughness of the different areas of the concrete sample after polishing in terms of Roughness Means Square (RMS) showing that the aggregate RMS is significantly higher than the other surfaces. The smoothest part of the employed polishing protocol (Table 4.1) was the cement paste, with the average value of about 20nm in accordance with previous studies with the similar polishing protocol (Miller et al., 2008; Sorelli et al., 2008). In order to consider a roughness value which is relevant for nanoindentation tests, as done in previous studies (Miller et al., 2008; Sorelli et al., 2008; Ulm et al., 2007; Vandamme, 2008), the waviness with a wavelength greater than 8μm, which is much greater than the penetration depth of a typical nanoindentation test (~100-500nm), is filtered out before calculating the Roughness Means Square (RMS). Thus, Figure

4.5b compares the RMS after filtering large waviness. The ASR products exhibited a RMS roughness of about 70-150nm which is about 13-28 times the penetration depth of nanoindentation tests, that is, the roughness is acceptable and not affecting the nanoindentation results (Miller et al., 2008).

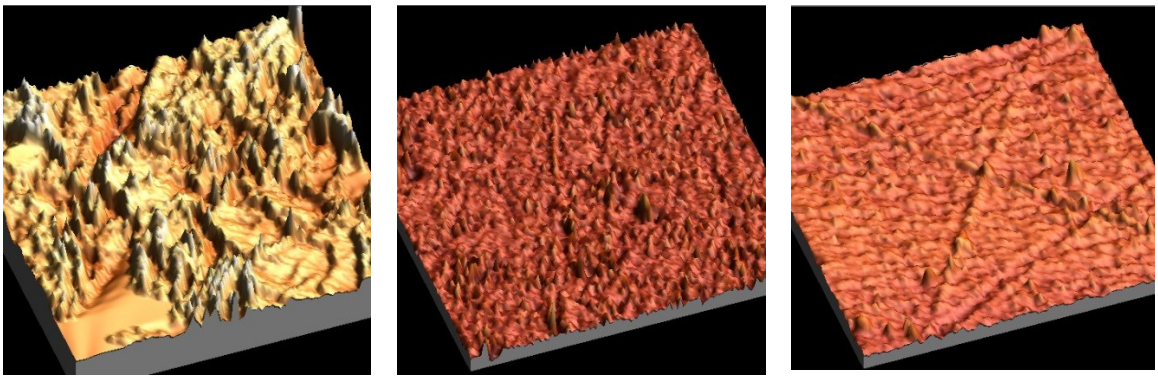

(a) (b) (c)

Figure 4.4 Comparison of surface roughness as observed at AFM micrographs for (a) Aggregate zone; (b) ASR products within a crack in the aggregate particle; (c) Cement paste zone.

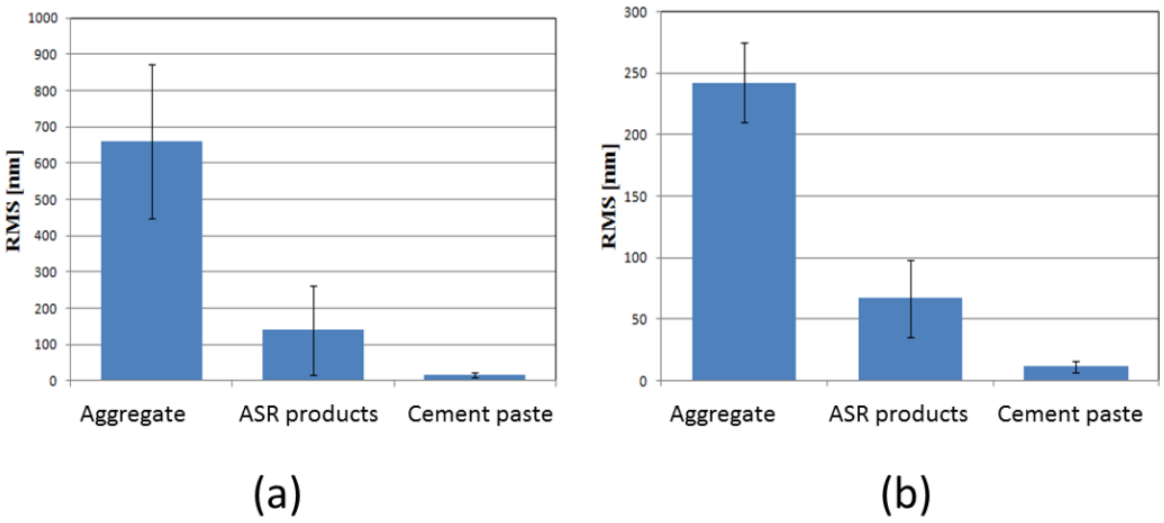

Figure 4.5 RMS roughness values of points in different zones of concrete paste (a) before and (b) after image filtering. The standard deviation is shown with the vertical thin bar.

4.3.2 SEM-EDX results

Figure 4.6a and 4.6b illustrate the typical micro-texture of the white veinlet within the reactive aggregate particle illustrated in Figure 4.2. Figure 4.6b shows the ASR rosette-like micro-texture with typical interlocked crystals and micro-cracking which are likely due to drying

shrinkage (De-Ceukelaire, 1991; Godart et al., 2013; Peterson et al., 2006; Leemann et al., 2013). Rosette crystals in ASR have natural counterparts of alkali-bearing calcium silicate hydrate minerals (Katayama, 2012). Furthermore, Figure 4.7 reports two typical Energy-dispersive X-ray spectrums of the studied ASR products as measured by SEM-EDX, confirming the typical signature of crystalline, rosette-like ASR products.

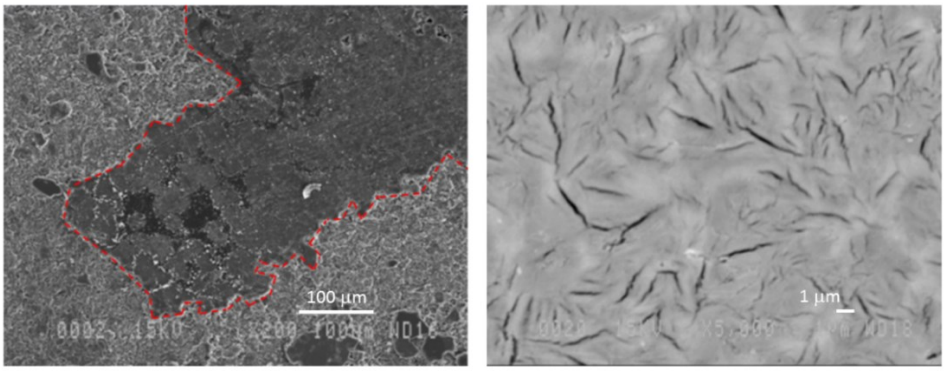

(a) (b)

Figure 4.6 SEM-image of the studied crystalline ASR products (rosettes): (a) Veinlet filled with ASR crystalline rosette-like product; (b) Zoomed view of the ASR crystalline rosette-like product (images in secondary electrons mode).

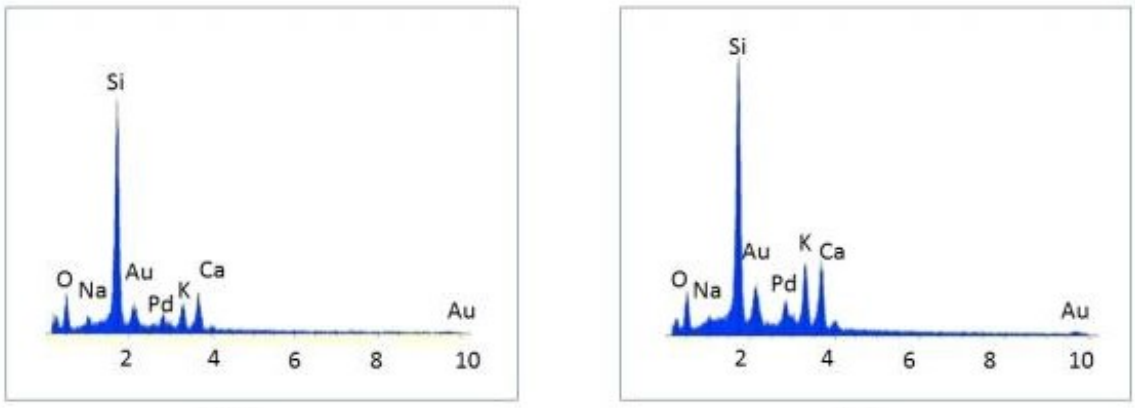

(a) (b)

Figure 4.7 Typical results of a SEM-EDX chemical analysis for ASR rosettes in 2 different zones.

4.3.3 Instrumented indentation results

The testing was carried out along the white veinlets illustrated in Figure 4.2b, more precisely in those sections of the veinlets located in the middle of the aggregate particle, i.e. where ASR crystalline products are predominant (Bérubé et al., 1986; Helmuth, 1993; Leemann et al., 2013). The observed crack width ranged between 50 and 200µm and the tests were

carried out in the largest width. As for the micro-indentation relaxation tests carried out at a penetration depth of 2µm (which corresponds to a probed volume of about 8000µm^3), Figure 4.8a and 4.8b show the load-penetration depth curve (P-h) and the relaxation curve load-time (P-t), respectively. As average, the maximum load was about 38.7mN at the penetration depth of 2µm (Figure 4.8a), and it relaxed down to 22.8mN (Figure 4.8b).

As for the nanoindentation relaxation tests performed at a smaller penetration depth of about 0.5µm (which corresponds to a probed volume of about 125µm^3), Figure 4.9a and 4.9b show the load-penetration depth curve (P-h) and the creep curve penetration depth-time (h-t), respectively. The average maximum load was about 13.6mN after loading (Figure 4.9a) which relaxed down to 9.7mN (Figure 4.9b). Visibly, the relaxation curve P(t) measured by nanoindentation differs from the one measured by micro-indentation as characterized by a greater characteristic time and a lower load relaxation after 600 seconds at constant penetration depth (Figure 4.9b).

As for the micro-indentation tests, Table 4.1 reports the measured properties of the ASR crystalline products, such as elastic modulus (E), the indentation Hardness (H), the equivalent Vickers Hardness (H_V), the indentation relaxation coefficient (R) in terms of mean value and standard deviation. ASR crystalline products were characterized by an E-modulus of about 14 GPa with a coefficient of variation of about 20% and a Hardness of about 230 MPa with a coefficient of variation of about 21% (which corresponds to an equivalent Vickers Hardness of about 21.5 with a coefficient of variation of about 21%). Those micro-indentation results are fairly well in agreement with the previous results obtained by Leemann and Lura (2013), which were carried out with a Vickers indenter shape with a similar penetration depth (2µm). Additionally, this work provides the relaxation coefficient of about 42%.

Table 4.1 reports also the properties of the ASR crystalline products measured at a smaller scale by nanoindentation. Interestingly, the E-modulus and Hardness (H and H_v) obtained from nanoindentation are about 65 GPa and 2494 MPa, respectively. The latter corresponds to an equivalent Vickers Hardness of 231 MPa. The mechanical stiffness and hardness values for ASR products measured by nanoindentation are about 5 and 10 times greater than the values measured at greater scale by micro-indentation.

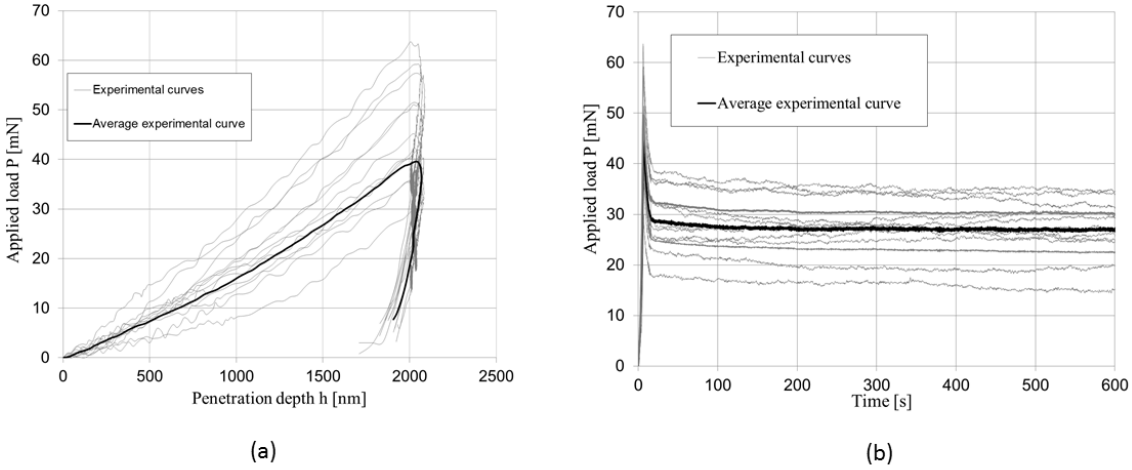

Figure 4.8 Micro-indentation test results in terms of load vs. penetration (a) and load vs. time (b).

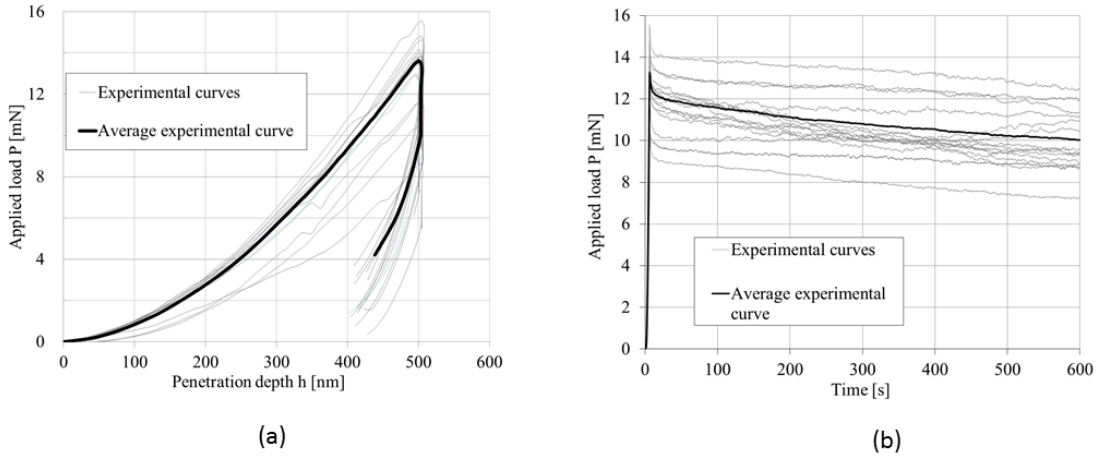

Figure 4.9 Nanoindentation test results in terms of load vs. penetration (a) and load vs. time (b).

Table 4.2 Summary of results for indentation parameters obtained from micro-indentation and nanoindentation tests: mean value ± standard deviation.

Indentation parameter	Micro-indentation h_{max}= 2 μm		Nano-indentation h_{max}= 0.5 μm	
h_{max} [μm]	2.02	± 0.01	0.502	± 0.003
P_{max} [mN]	38.8	± 9.1	13.6	± 1.3
Ac [μm^2]	115.4	± 3.2	3.92	± 0.28
H [MPa]	233	± 50	2494	± 453
H_V [MPa]	21.5	± 4.5	231	± 41
E [GPa]	14.0	± 2.8	65	± 12.3
R [%]	41.8	± 8.2	29.6	± 6.2

4.4 Analysis and Discussion

4.4.1 Indentation modulus and hardness of ASR products

Figure 4.10 compares the micro-indentation test results obtained in this study, in terms of E-modulus and Vickers hardness of the ASR products, with those published by Leemann and Lura (2013). The micro-indentation results of the present work (E~14 GPa, H_v~21) are slightly higher (about 20-35%), but close to those obtained by Leemann and Lura (2013) for crystalline reaction products located in the center of different reactive aggregates (E~9-11 GPa, Hv~13-18) for penetration depth between 2 and 4μm. Just as technical difference, note that Leemann and Lura employed a Vicker tip (a four-sided pyramid with a semi-vertical angle of 68°), while we employed a Berkovich tip (a three-sided pyramid with a semi-vertical angle of 65.3°).

The nanoindentation results also illustrated in Figure 4.10 shows that the measured E-modulus and Vickers hardness of the crystalline ASR products are much greater than those measured by micro-indentation testing. However, more scattering is found in the results, as likely due to the size of the probed volume (125μm^3) which is closer to the size of the micro-cracks and of the crystals (rosette) in Figure 4.6b. Moreover, the surface roughness of the ASR products (50-100nm from Figure 4.5) may be also partially responsible for that scattering. Nevertheless, nanoindentation testing suggests an average E-modulus and Vickers hardness H_v for the crystals themselves of 65 and 231 GPa, respectively.

Based on the average measured contact area (A_c) in Table 4.2, Figure 4.11 compares the size of the indentation imprint for nano and micro-indentation tests, respectively, with the observed micro-texture of the ASR crystalline products by SEM. This observation suggests that, while the micro-indentation test probes and ensembles of ASR crystals with a representative number of microcracks, the results of nanoindentation tests may be more related to the behavior of a single ASR crystal under highly confining stress condition due to the test configuration of an indentation test, which may cause a greater E-value. Also, the larger scattering in the nanoindentation data is likely related to the local impact of small shrinkage cracks disseminated within the reaction product. Katayama (2012) suggested that ASR rosette crystals constitute solid solutions between a wide range of hydrous (Na-K)-Ca silicate minerals, e.g. between mountainite ($Ca_2Na_2KSi_8O_{19.5}6.5H_2O$) and shlykovite ($(K,Na)_2Ca_2Si_8O_{19}7H_2O$), possibly extending to cryptophyllite ($(K,Na)_4Ca_2Si_8O_{20}.10H_2O$) and rhodesite ($KCa_2Si_8O_{18.5}6.5H_2O$), or a mixed layer of wider range which needs further study. Therefore, data on ASR products, however, need to be examined cautiously due to differences in composition and structures (Leemann et al., 2016). Katayama (2012) suggested that the continuous range of composition of rosette crystals is probably inherited from original ASR gel, formed by the diffusion of alkali and calcium ions between ASR gel and cement paste. Moreover, as crystalline phases are usually anisotropic, differences in the mechanical properties can depend on the crystal orientation in regard to the loading direction. Test results reported by Leemann and Lura (2013) indeed showed that ASR products within the same crack/veinlet but located close to the edge of the reactive aggregate particle exhibited greater values of E-modulus and Hardness, as shown by empty square and triangle symbols in Figure 4.10. The authors indicated that "*at the edge of the aggregates, the reaction product takes up calcium from the cement paste and changes its structure from crystalline to amorphous*". Leemann and Lura's data in Figure 4.10 indeed show that the E-modulus and the Vickers hardness increase, respectively, to values of about 30GPa and 125 GPa (*ASR gel at the aggregate edge*) for a load of 12mN. Further values of 45GPa and 270 were however obtained for ASR products also located in a crack close to the edge but of a different reactive aggregate and at a load of 25mN. Phair et al. (2005) reported, based on X-ray absorption and Brillouin spectroscopy measurements, that the E-modulus of ASR gel can range from 11 to 35 depending on their calcium content. Moreover, Moon et al. (2013) showed that the density of ASR products increases under pressure and that the bulk modulus can reach 33 GPa, which corresponds to an E-modulus of 63GPa

when a Poisson ratio of 0.18 is assumed (Leemann et al., 2013). Finally, Adachi and Sakka (1990) showed that highly densified ASR gel can reach E-modulus of 74 GPa.

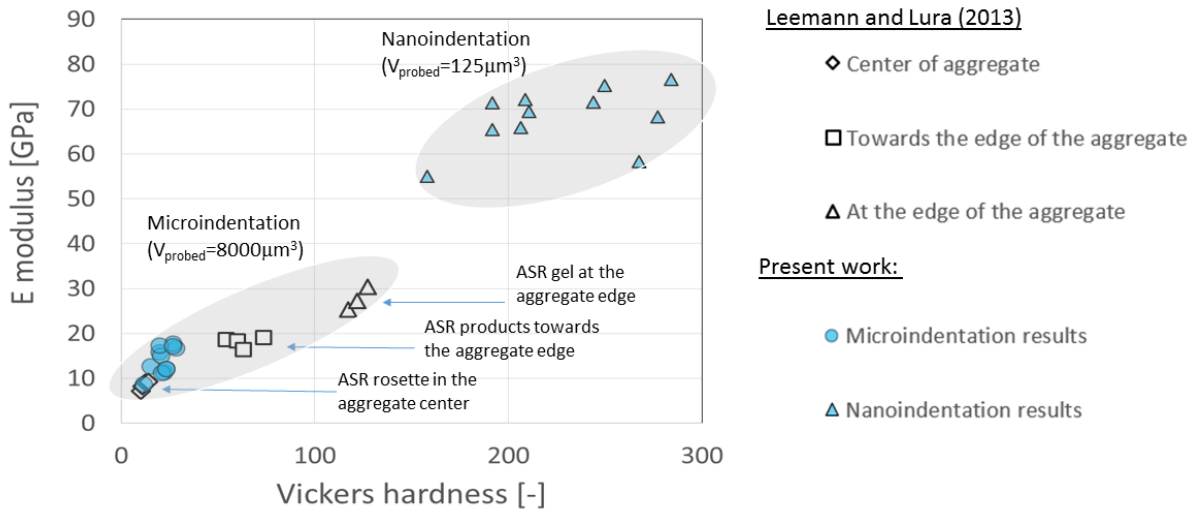

Figure 4.10 Comparison between the results obtained by Leemann et al. (2013) and the results of this work for E-modulus and Vickers hardness.

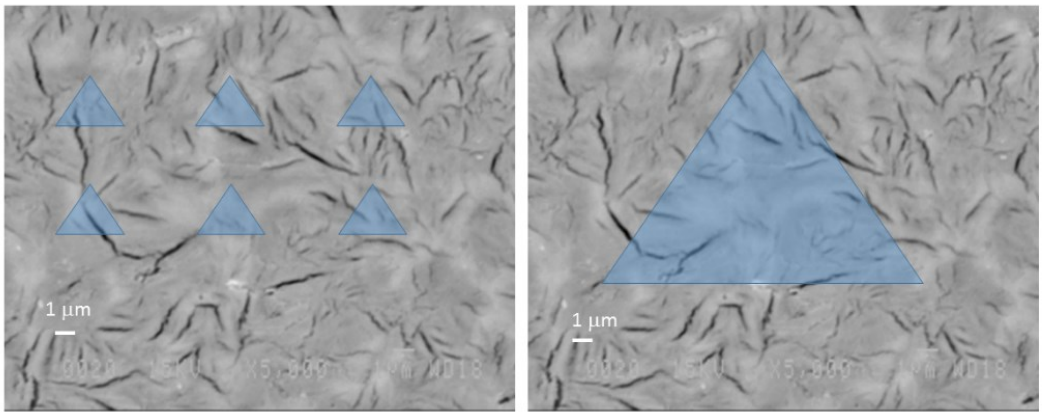

Figure 4.11 Visual representation of an indentation size for nanoindentation (a) and micro-indentation (b) from the measured contact area (Table 4.9) with respect to the ASR crystalline products morphology observed under the SEM.

4.4.2 Viscosity properties of ASR products by a simplified model

In this study, we considered a simplified approach to model the viscoelastic response of the crystalline ASR product by assuming a classical Burgers model (shown in Figure 4.12). Such a model is composed of two combined viscous units, such as a Kelvin-Voigt unit (E_2, η_2),

which describes the irreversible deformation (ε_1), and a Maxwell unit (E_1, η_1), which describes the reversible deformation (ε_2). The simplified underlying idea is that the Kelvin-Voigt creep parameters (E_2, η_2) can be associated with the reversible water movement (e.g., diffusion or absorption), while the Maxwell creep parameters (E_1, η_1) device can be associated to irreversible sliding of ASR rosette crystals along defect planes (e.g. microcracks, defect plan, etc.).

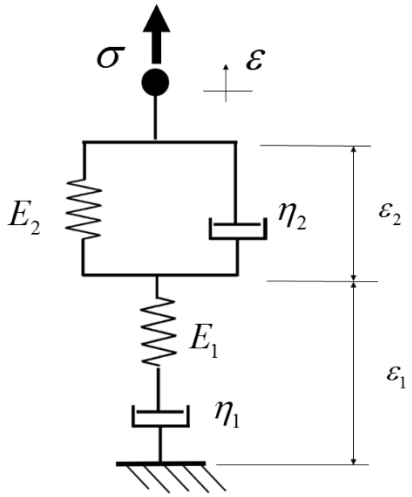

Figure 4.12 Rheological viscous-elastic indentation model employed in this study: a Maxwell unit (E_1, η_1) in series with a Kelvin-Voigt unit (E_2, η_2).

The viscous model is integrated for the axial-symmetric configuration of a conical indenter following the work of Vandamme (2008) and Vandamme et al. (2006). The creep compliance function of a Burgers model reads as follows:

$$J(t) = \frac{1}{E_1} + \frac{t}{\eta_1} + \frac{1}{E_2}(1 - e^{-\frac{E_2}{\eta_2}t}) \tag{4.4}$$

In the modeling, the Poisson's ratio was assumed to be constant and equal to 0.18, as proposed in a previous study (Leemann et al., 2013). For the imposed penetration depth shown in Figure 4.3a, the load relaxation P(t) during the holding phase shown in Figure 4.3b can be obtained analytically by integrating the Laplace transform of the Galin-Sneddon solution in the Laplace for the elastic solution of the axial symmetric indentation with the chosen Burgers' creep compliance (Galin et al., 1961; Harding et al., 1945; Vandamme, 2008; Vandamme et al., 2006). Then, in Laplace domain, the creep compliance reads as follows:

$$E(s) = \frac{1}{s^2 J(s)} = \frac{1}{s(\frac{1}{E_1} + \frac{1}{\eta_1 s} + \frac{1}{E_2 + \eta_2 s})} \tag{4.5}$$

Of which inversion reads,

$$E(t) = \frac{P(t)}{P_{\max}} E_0 = E_1 e^{-At}(\cosh(Bt) + C\sinh(Bt)) \tag{4.6}$$

Where,

$$A = \frac{1}{2}\left(\frac{E_1}{\eta_1} + \frac{E_1}{\eta_2} + \frac{E_2}{\eta_2}\right)$$
$$B = \sqrt{E_1^2\eta_1^2 + 2E_1^2\eta_1\eta_2 + E_1^2\eta_2^2 + 2E_1E_2\eta_1^2 - 2E_1E_2\eta_1\eta_2 + E_2^2\eta_1^2} \,/\, (2\eta_1\eta_2)$$
$$C = (E_2\eta_1 - E_1\eta_1 - E_1\eta_2) / \sqrt{E_1^2\eta_1^2 + 2E_1^2\eta_1\eta_2 + E_1^2\eta_2^2 + 2E_1E_2\eta_1^2 - 2E_1E_2\eta_1\eta_2 + E_2^2\eta_1^2} \tag{4.7}$$

Finally, we defined a parameter χ to assess the contribution on the relaxation load $P(t)/P_{max}$ of the irreversible component by the Maxwell unit (k_1, η_1) as follows:

$$\chi = \frac{E_{Maxwell}(t \to \infty)}{E(t \to \infty)} \tag{4.8}$$

where $E_{Maxwell}$ is the equivalent of the Eq.(4.6) for the visco-elastic model, but considering only the Maxwell model.

The elastic parameter E_1 is directly obtained from the elastic modulus E measured by indentation. The remaining parameters (E_2, η_1, η_2) of the simplified viscoelastic model were best-fitted to simulate the average mean relaxation curves of micro and nano-indentation. As for the relaxation behavior, Figures 4.13a and 4.13b compare the mean experimental curves and those obtained by simulation using the simplified Burger model for the relaxation tests at the micro-indentation and nanoindentation levels, respectively.

Table 4.3 reports the model parameters for the best fitting curves for both relaxation tests. Interestingly, the simplified model gives an interpretation of the importance of the two units in the relaxation behavior. One can note that for the micro-indentation tests, the irreversible

Maxwell unit is responsible for 65% of the load relaxation, while the Kelvin-Voigt unit, which is associated with reversible water movement, is responsible for 35% of the load relaxation. The characteristic time of the Kelvin-Voigt unit (τ_2 =7.5 s) is also much lower than that of the Maxwell unit (τ_1=10'769 s), suggesting that the viscous deformation under a load of reaction products composed of rosette crystals may take a longer time with respect to the water movement. The characteristic time of the reversible mechanism associated with water movement seems faster than that of sliding mechanisms possibly acting along interlock planes/ interfaces of the ASR crystalline products. On the other hand, for the nanoindentation test, the irreversible Maxwell unit is mainly responsible for the load relaxation (χ =95%), suggesting that the main mechanism is due to the sliding along interlocked plane/interfaces of ASR crystals. Finally, the viscosity of the Maxwell unit η_1 increases from 154'000GPa·s to 280'000GPa·s for micro-indentation and nanoindentation test, respectively. Yet, the presence of a large number of micro-cracks in the volume probed by micro-indentation has likely reduced the viscosity as expected in visco-damage micromechanics (Sanahuja et al., 2010).

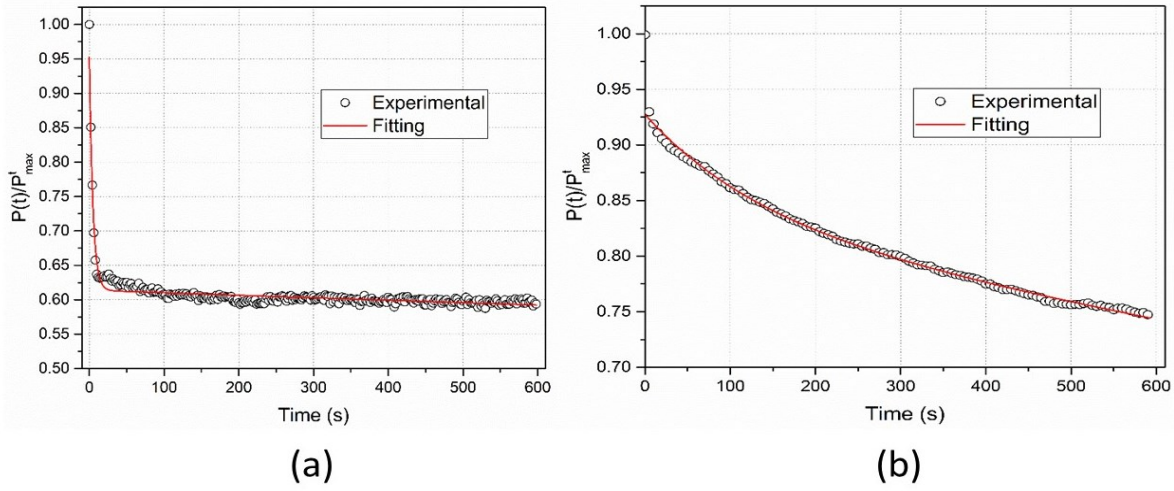

Figure 4.13 Comparison between the simulated and experimental relaxation curves for the relaxation indentation test at (a) micro-indentation: h_{max}= 2 μm and (b) nanoindentation: h_{max} =0.5 μm.

Table 4.3 Model fitting parameters.

	Micro-indentation	Nanoindnetation
E_1 [GPa]	14.3	61.0
η_1 [GPa s]	154'000	280'313
$\tau_1 = \frac{\eta_1}{E_1}$ [s]	10'769	4595
E_2 [GPa]	26	585
η_2 [GPa s]	193	86'482
$\tau_2 = \frac{\eta_2}{E_2}$ [s]	7.5	147
χ	65%	95%

4.5 Concluding Remarks

Fostering a recent work on the characterization of ASR products by micro-indentation testing, this work further characterized the *in-situ* relaxation behavior of ASR crystalline products with rosette-like microstructure by both micro and nanoindentation tests. Based on the present results, the following conclusions can be drawn:

1. As for micro-indentation tests, the average E-modulus and Hardness measured by micro-indentation of ASR crystalline products with rosette-like microstructure located in the aggregate center was about 14 GPa and 233 MPa, which is in satisfactory agreement with the results of Leemann and Lura (2013). For the first time, the relaxation coefficient of the ASR crystals was quantified to be about 40%, confirming the important delayed deformation of such ASR-products;

2. As for nanoindentation tests with a probed volume much smaller than that of the micro-indentation (i.e. 125 vs 8000μm^3), the test results were highly scattered, which was likely due to the presence of microcracks, a high surface roughness, and that the probed volume is closer to the ASR crystal size (i.e. individual rosettes). Nevertheless, the ASR crystals probed at smaller scale exhibited greater mean values of the E-modulus (~65 GPa) and hardness (H~2500 MPa, Hv~230), hinting for stiffer crystal between the visible microcracks of ASR products and the possible effect of the confining pressure. Due to the mentioned high scatter, further nanoindentation study at small penetration depth is needed for confirming this conclusion;

3. Finally, a simplified Burger model was applied to estimate the viscous properties of ASR products composed of crystalline products with rosette-like microstructure. This simplified model allows ideally describing the viscous behavior of the above ASR products with a double mechanism, one reversible due to water movement with lower characteristic time, the other one irreversible related to slippage along microcracks and/or interfaces along interlocked ASR crystals. The micro-indentation tests showed a rapid load relaxation after few seconds which is due to the low viscosity η_2~ 200GPa·s associated to reversible water movement in our simplified model, followed by a much slower viscous deformation with η_1~ 150'000 GPa·s due to the ASR crystal sliding. At the nanoindentation scale, the viscous behavior was mainly due to the irreversible sliding along interlocked ASR crystals with great viscosity η_1 ~ 280'000GPa·s, while the reversible viscosity η_2 has a limited contribution. This difference may be likely due to the sliding of ASR crystals at the microcracks' interfaces.

Further research is needed to analyze the properties of ASR products with different composition and morphologies. Moreover, in spite the tests were carried out in 24 hours after polishing as done in previous work, the effect of the RH conditions should be investigated in more details.

Acknowledgements

The authors would like to thank Mr. Jessy Frech-Baronet for the technical support on the nanoindentation tests and Dr. A. Leemann for the precious advice on the sample preparation. We also acknowledge the CSC-UL research program for the financial support of the first author.

References

Adachi, T., & Sakka, S. (1990). Dependence of the elastic moduli of porous silica gel prepared by the sol-gel method on heat-treatment. Journal of Materials Science, 25(11): 4732–4737.

Alnaggar, M., Cusatis, G., & Di Luzio, G. (2013). Lattice discrete particle modeling (LDPM) of alkali-silica reaction (ASR) deterioration of concrete structures. Cement and Concrete Composites, 41:45–59.

Association, B.C. (1992). The Diagnosis of alkali-silica reaction. British Cement Association, Crowthorne, Berks, RG1 6YS, United Kingdom.

Bažant, Z.P., & Steffens, A. (2000). Mathematical model for kinetics of alkali–silica reaction in concrete. Cement and Concrete Research, 30(3):419–428.

Ben Haha, M., Gallucci, E., Guidoum, A., & Scrivener, K.L. (2007). Relation of expansion due to alkali-silica reaction to the degree of reaction measured by SEM image analysis. Cement and Concrete Research, 37(8):1206–1214.

Bérubé, M.-A., & Fournier, B. (1986). Les produits de la reaction alcalis-silice dans le beton; etude de cas de la region de Québec. The Canadian Mineralogist, 24(2):271–288.

Constantinides, G., (2006). Invariant mechanical properties of calcium-silicate-hydrates (CHS) in cement-based materials: instrumented nanoindentation and microporomechanical modeling (Doctoral dissertation, Massachusetts Institute of Technology).

Dähn, R., Arakcheeva, A., Schaub, P., Pattison, P., Chapuis, G., Grolimund, D., & Leemann, A. (2016). 79:49–56.

De-Bonniers, Philippe. (2013). Code Aster handbook: Behavior model BETON_RAG. Feburary, 3rd, 3.

De-Ceukelaire, L. (1991). The determination of the most common crystalline alkali-silica reaction product. Materials and Structures, 24(3):169–171.

Dunant, C.F., & Scrivener, K.L. (2010). Micromechanical modeling of alkali–silica-reaction-induced degradation using the AMIE framework. Cement and Concrete Research, 40(4):517–525.

Dunant, C.F., & Scrivener, K.L. (2016). Physically based models to study the alkali–silica reaction. In *Proceedings of the Institution of Civil Engineers–Construction Materials*, 169(3):136–144.

Fischer-Cripps, A.C., 2000. Factors Affecting Nanoindentation Test Data. Springer New York, 61-82.

Fischer-Cripps, A.C. (2000). Introduction to contact mechanics. New York: Springer, 87.

Fischer-Cripps, A. C. (2004). Nanoindentation Springer-Verlag. New York, 164.

Fournier, B., & Bérubé, M.-A. (1991). Évaluation du potentiel de réactivité alcaline des granulats à béton produits dans les Basses-Terres du Saint-Laurent du Québec (Canada). Canadian Journal of Civil Engineering, 18(2):282–296.

Fournier, B., & Bérubé, M.-A. (2000). Alkali-aggregate reaction in concrete: a review of basic concepts and engineering implications. Canadian Journal of Civil Engineering, 27(2):167–191.

Galin, L.A., Moss, H., & Sneddon, I.N. (1961). Contact problems in the theory of elasticity. North Carolina State Univ. Releigh School of Physical Sciences and Applied Mathematics.

Godart, B., De-Rooij, M., & Wood, J.G. (2013). Reporting. In Guide to Diagnosis and Appraisal of AAR Damage to Concrete in Structures. Springer. 79–81.

Harding, J.W., & Sneddon, I.N. (1945). The elastic stresses produced by the indentation of the plane surface of a semi-infinite elastic solid by a rigid punch. In Mathematical Proceedings of the Cambridge Philosophical Society. Cambridge University Press. 41:16–26.

Helmuth, R. (1993). Alkali-silica reactivity: an overview of research (No. SHRP Report C-342).

Ichikawa, T., & Miura, M. (2007). Modified model of alkali-silica reaction. Cement and Concrete Research, 37(9):1291–1297.

ISE. (1992). Structural Effects of Alkali-Silica Reaction – Technical guidance appraisal of existing structures. The institution of Structural Engineers. 45.

Jin, W. (1998). Alkali-Silica Reaction in Concrete with Glass Aggregate - a Chemo-Physical-Mechanical Approach (Ph.D. Dissertation). Columbia University, New York, NY, 154.

Jin, W., Meyer, C., & Baxter, S. (2000). “Glascrete”-Concrete with Glass Aggregate. ACI Materials Journal, 97(2):208–213.

Katayama, T. (2012). Petrographic study of the alkali-aggregate reactions in concrete. Graduate School of Science, University of Tokyo, Department of Earth and Planetary Science.

Larive, C., & Louarn, N. (1992). Diagnosis of alkali-aggregate reaction and sulphate reaction in French structures. In *Proceedings 9th International Conference on Alkali-Aggregate Reactions*. Concrete Society. 587–598.

Leemann, A., & Lura, P. (2013). E-modulus of the alkali–silica reaction product determined by micro-indentation. Construction and Building Materials, 44:221–227.

Leemann, A., Katayama, T., Fernandes, I., & Broekmans, M.A. (2016). Types of alkali–aggregate reactions and the products formed. Proceedings of the Institution of Civil Engineers-Construction Materials, 169(3):128–135.

Lemarchand, E., Dormieux, L., & Ulm, F.-J. (2005). Micromechanics investigation of expansive reactions in chemoelastic concrete. Philosophical Transactions of the Royal Society of London A: Mathematical, Physical and Engineering Sciences, 363(1836): 2581–2602.

Meyer, E. (1992). Atomic force microscopy. Progress in Surface Science, 41(1):3–49.

Miller, M., Bobko, C., Vandamme, M., & Ulm, F.-J. (2008). Surface roughness criteria for cement paste nanoindentation. Cement and Concrete Research, 38(4):467–476.

Moon, J., Speziale, S., Meral, C., Kalkan, B., Clark, S.M., & Monteiro, P.J. (2013). Determination of the elastic properties of amorphous materials: case study of alkali–silica reaction gel. Cement and Concrete Research, 54:55–60.

Multon, S., Seignol, J.F., & Toutlemonde, F. (2005). Structural behavior of concrete beams affected by alkali-silica reaction. ACI Materials Journal-American Concrete Institute, 102(2):67–76.

Multon, S., Sellier, A., & Cyr, M. (2009). Chemo–mechanical modeling for prediction of alkali silica reaction (ASR) expansion. Cement and Concrete Research, 39(6):490–500.

Murtagh, M.J., Graham, E.K., & Pantano, C.G. (1986). Elastic Moduli of Silica Gels Prepared with Tetraethoxysilane. Journal of the American Ceramic Society, 69(11):

Nohava, J., Randall, N.X., & Conté, N. (2009). Novel ultra nanoindentation method with extremely low thermal drift: Principle and experimental results. Journal of Materials Research, 24(03):873–882.

Oliver, W.C., & Pharr, G.M. (1992). An improved technique for determining hardness and elastic modulus using load and displacement sensing indentation experiments. Journal of Materials Research, 7(06):1564–1583.

Pacheco-Torgal, F., Castro-Gomes, J., & Jalali, S. (2008). Alkali-activated binders: A review: Part 1. Historical background, terminology, reaction mechanisms and hydration products. Construction and Building Materials, 22(7):1305–1314.

Pan, J.W., Feng, Y.T., Wang, J.T., Sun, Q.C., Zhang, C.H., & Owen, D.R.J. (2012). Modeling of alkali-silica reaction in concrete: a review. Frontiers of Structural and Civil Engineering, 6(1):1–18.

Panich, N., & Sun, Y. (2004). Effect of penetration depth on indentation response of soft coatings on hard substrates: a finite element analysis. Surface and Coatings Technology, 182(2):342–350.

Pesavento, F., Gawin, D., Wyrzykowski, M., Schrefler, B.A., & Simoni, L. (2012). Modeling alkali–silica reaction in non-isothermal partially saturated cement based materials. Computer Methods in Applied Mechanics and Engineering, 225:95–115.

Peterson, K., Gress, D., Van Dam, T., & Sutter, L. (2006). Crystallized alkali-silica gel in concrete from the late 1890s. Cement and Concrete Research, 36(8):1523–1532.

Phair, J.W., Tkachev, S.N., Manghnani, M.H., & Livingston, R.A. (2005). Elastic and structural properties of alkaline-calcium silica hydrogels. Journal of Materials Research, 20(02):344–349.

Rajabipour, F., Giannini, E., Dunant, C., Ideker, J.H., & Thomas, M.D. (2015). Alkali–silica reaction: current understanding of the reaction mechanisms and the knowledge gaps. Cement and Concrete Research, 76:130–146.

Reinhardt, H.W., & Mielich, O. (2011). A fracture mechanics approach to the crack formation in alkali-sensitive grains. Cement and Concrete Research, 41(3):255–262.

Šachlová, Š., Přikryl, R., & Pertold, Z. (2010). Alkali-silica reaction products: Comparison between samples from concrete structures and laboratory test specimens. Materials Characterization, 61(12):1379–1393.

Sanahuja, J., & Dormieux, L. (2010). Creep of a CSH gel: a micromechanical approach. Anais Da Academia Brasileira de Ciências, 82(1):25–41.

Sanchez, L.F.M., Fournier, B., Jolin, M., & Duchesne, J. (2015). Reliable quantification of AAR damage through assessment of the Damage Rating Index (DRI). Cement and Concrete Research, 67:74–92.

Sanchez, L.F.M., Fournier, B., Jolin, M., Bedoya, M.A.B., Bastien, J., & Duchesne, J. (2016). Use of Damage Rating Index to Quantify Alkali-Silica Reaction Damage in Concrete: Fine versus Coarse Aggregate. ACI Materials Journal, 113:4.

Schlangen, E., & Çopuroglu, O. (2007). Concrete damage due to the alkali-silica reaction: a new method to determine the properties of expansive gel. Fracture Mechanics of

Concrete and Concrete Structures–high-Performance Concrete, Brick-Masonry and Environmental Aspects. Taylor & Francis Group, London, 1835–1841.

Seignol, J. F., & Godart, B. (2012). A collective effort to propose practical guidance on the use of numerical models to re-assess AAR-affected structures. In *14th International Conference on AAR in concrete*. Texas (USA): Austin.

Sorelli, L., Constantinides, G., Ulm, F.-J., & Toutlemonde, F. (2008). The nanomechanical signature of ultra high-performance concrete by statistical nanoindentation techniques. Cement and Concrete Research, 38(12):1447–1456.

St John, D.A., Poole, A.B., & Sims, I. (1998). Concrete petrography: a handbook of investigative techniques. Arnold; Copublished in North, Central and South America by J. Wiley.

Stanton, T.E. (1940). Influence of cement and aggregate on concrete expansion. Engineering News-Record.

Swamy, R.N. (2002). The alkali-silica reaction in concrete. CRC Press.

Swamy, R.N., & Al-Asali, M.M. (1988). Expansion of concrete due to alkali-silica reaction. Materials Journal, 85(1):33–40.

Thomas, M.D., Fournier, B., & Folliard, K.J. (2013). Alkali-aggregate reactivity (AAR) facts book (No. FHWA-HIF-13-019).

Ulm, F.-J., Coussy, O., Li, K.F & Larive, C. (2000). Thermo-chemo-mechanics of ASR expansion in concrete structures. Journal of Engineering Mechanics, 126(3):233–242.

Ulm, F.-J., Vandamme, M., Bobko, C., Alberto Ortega, J., Tai, K., & Ortiz, C. (2007). Statistical indentation techniques for hydrated nanocomposites: concrete, bone, and shale. Journal of the American Ceramic Society, 90(9): 2677–2692.

Vandamme, M. (2008). The nanogranular origin of concrete creep: a nanoindentation investigation of microstructure and fundamental properties of calcium-silicate-hydrates (Doctoral dissertation, Massachusetts Institute of Technology).

Vandamme, M., & Ulm, F.-J. (2006). Viscoelastic solutions for conical indentation. International Journal of Solids and Structures, 43(10): 3142–3165.

Vandamme, M., Tweedie, C.A., Constantinides, G., Ulm, F.-J., & Van Vliet, K.J. (2012). Quantifying plasticity-independent creep compliance and relaxation of Visco elastoplastic materials under contact loading. Journal of Materials Research, 27(01): 302–312.

Vayghan, A.G., Rajabipour, F., & Rosenberger, J.L. (2016). Composition–rheology relationships in alkali–silica reaction gels and the impact on the Gel's deleterious behavior. Cement and Concrete Research, 83:45–56.

Wang, S.-D., Pu, X.-C., Scrivener, K.L., & Pratt, P.L. (1995). Alkali-activated slag cement and concrete: a review of properties and problems. Advances in Cement Research, 7(27):93–102.

5. Article 2: Fracture Toughness of Reactive Aggregates in ASR damaged concrete by Statistical Micro-Scratch Techniques

Chi Zhang[(1)], Luca Sorelli[(1)] Benoît Fournier[(2)], Josée Duchesne[(2)], Josée Bastien[(1)] Chen Zhao[(1)]

1) Université Laval, Civil and Water Engineering Department, 1065 avenue de la Médecine, PLT2928-A, G1V0A6, Québec, Canada.

2) Université Laval, Geology and Geological Engineering Department, 1065 avenue de la Médecine, G1V0A6, Québec, Canada.

Paper to be submitted for possible publication in "Material Characterization" Journal.

Abstract

The fracture resistance of aggregates plays a key role in the initiation of the damage process of concrete due to the Alkali-Silica Reaction (ASR). This work aims at statistically characterizing the toughness (or fracture energy) of reactive aggregates at the microstructure level by applying a novel analysis technique based on micro-scratch testing.

The fracture toughness of Trenton limestone aggregates was statistically characterized by series of line scratch on the microstructure of both unreacted and reacted limestone aggregates. Firstly, micro-indentation tests were carried out to identify a suitable penetration depth for characterizing a representative volume. After calibrating the contact area on silica fuse, six series of micro-scratch tests were carried in two different directions, e.g., parallel and perpendicular to the bedding planes of the aggregate particles, on both reacted (light grey and dark grey) and unreacted aggregates. The results provide new insights on the fracture toughness at the aggregate microstructure scale on the mechanical effect of ASR gel on the properties of sedimentary reactive limestone aggregates.

Keywords: Micro-scratch, limestone aggregate, alkali-silica reaction, toughness, fracture energy.

5.1 Introduction

Alkali-Silica Reaction (ASR) is a major durability concern of concrete, which involves deleterious expansion, cracking, and loss of serviceability in pavements, dams, bridges piers and other critical infrastructures (Fournier et al., 2000a). Briefly, reactive forms of silica (e.g. amorphous, microcrystalline/cryptocrystalline/strained quartz) present in certain aggregates dissolve into silicate ions and react with alkalis and calcium ions to precipitate into hydrous alkali-calcium-silica gel of variable stoichiometry, molar volume and mechanical properties (Peterson et al., 2006; Rajabipour et al., 2015). ASR products present in reactive aggregate particles are highly confined and induce internal pressures through water absorption, thus causing the onset of cracking within the particle, followed by crack growth in the surrounding cement paste matrix (Ben Haha et al., 2007; Sanchez et al., 2016; Swamy, 2002; Swamy et al., 1988; BCA 1992; Poole et al., 2016). Depending on the local confining pressure, the gel viscosity and permeability within capillary pores or microcracks of the surrounding cement paste, ASR gel can migrate from the aggregate particles into the cement paste enforcing the continuous expansion (Giorla et al., 2015). At the structural level, anisotropic damage and expansion within an individual structural member or from one member to another are often observed due to several factors, such as the anisotropic crack growth, varying exposure conditions, external loadings, the steel reinforcement detailing, etc. (Multon et al., 2009, ISE 1992).

Some varieties of siliceous limestone aggregates have been found to deleteriously react and promote premature deterioration in concrete structures in several parts of the world (Fournier et al., 1987, Bérard et al., 1986, Fournier et al., 1991, Guédon-Dubied et al., 2000). As a good example of such a material, the Spratt aggregate from Ottawa (Canada) is commonly employed as control aggregate for ASR studies worldwide. The reactive rock type generally consists of a dark-grey and fine-grained siliceous limestone (SiO_2 content up to about 10-12%, typically), with micro-to-cryptocrystalline quartz disseminated in the rock matrix. Interestingly, plane polished concrete sections prepared from cores extracted from ASR-affected structures incorporating such reactive aggregates typically reveal the presence of extensive cracking in the aggregate particles extending into the cement paste from one aggregate particle to another; the cracks within the aggregate particles are typically filled with secondary reaction products thus forming white veinlets; the latter are typical signs of ASR (Bérard et al., 1986; Fournier et al., 2010).

In spite of the recognized importance of the aggregate resistance to cracking in concrete structures affected by ASR (Dunant et al., 2016; Reinhardt et al., 2011), there is limited information on the cracking resistance of reactive aggregates due to the difficulty to characterize rock types with complex textural and compositional characteristics in a statistically meaningful manner. By definition, the aggregate toughness would provide the sought value of fracture energy that is needed to create a crack surface. Besides nano- and micro-indentation techniques, which have been widely used in the last decade to characterize heterogeneous microstructure, micro-scratch techniques have been recently emerging for determining the fracture toughness at the microstructure level (Akono et al., 2011; Fischer-Cripps, 2011). Interestingly, in the past, scratch tests were empirically employed to quantify the scratch resistance of minerals (Tabor, 1954). More recently, by combining high-tech instrumented experiments, scaling analysis and theory, a novel scratch technique has been successfully applied to estimate the local fracture toughness (K_C) of ceramics, concrete and other quasi-brittle materials (Akono et al., 2011; Akono et al., 2011; Akono et al., 2012). Based on fracture mechanics, the crack onset occurs when the energy release rate (G) reaches the fracture energy (G_f) of a brittle material (Griffith, 1921). Alternatively, the crack onset occurs when the critical stress intensity factor (K_C), which is also called material toughness (Tada et al., 2000), reaches the critical value. The fracture energy (G_f) and the critical stress intensity factor (K_C) are linked by Irwin's relationship (Irwin, 1997), such as $G_f=K_C^2/E$. Notably, there exists a link between the statistical and spatial distributions of the local toughness at the microstructure level and the damage law at the macroscopic scale, also explained in random lattice/discrete models (Bažant et al., 1990; Grassl et al., 2009; Rossi et al., 1987) and micromechanics models (Pichler et al., 2007).

This work pioneers the application of novel techniques of micro-scratch for measuring (1) the fracture toughness of "unreacted" fine-grained limestone at the microstructure level, and (2) the effect on the fracture toughness of reactive limestone aggregate particles within concrete cores extracted from a heavily ASR-affected field structure.

5.2 Materials and Methods

5.2.1 Materials

Concrete cores, 100 in diameter by 200 to 300 mm in length were extracted from the massive foundations of Y-shaped columns of an ASR-affected concrete highway viaduct in the Québec City area and used for this study (Figure 5.1a). Plane polished sections prepared from the above cores revealed the presence of numerous aggregate particles incorporating cracks filled with ASR products. Typically, the original fine-grained reactive limestone display a dark-grey color; however, many particles actually display more or less widespread light-grey zones surrounding the white veinlets, suggesting “reacted” zones within those particles (Figure 5.1b and 1c). Also, in some cases, it was quite clear that the white veinlets were parallel to the bedding planes within the particles (Figure 5.1d), thus raising questions about the influence of the sedimentary orientation on the fracture toughness of the particles. It is worth noticing that such “de-coloration” of reactive aggregate particles is not commonly observed in accelerated ASR tests, but more for concrete sample damaged by ASR in field conditions.

Different aggregate particles were selected from the cores mentioned above to be subjected to micromechanical testing and chemical analysis. These consisted in: (i) two particles with clear light-grey zones surrounding the white veinlets (BE2A in Figure 1d and BE2B in Figure 5.1e). In Figure 5.1d, one can observe that the bedding plane is parallel to the larger white veinlets; (ii) one dark-grey particle (BE8A in Figure 5.1f); (iii) a reactive limestone aggregate particle with both dark grey and light grey zones surrounding white veinlets (BE11B1 in Figure 5.1c).

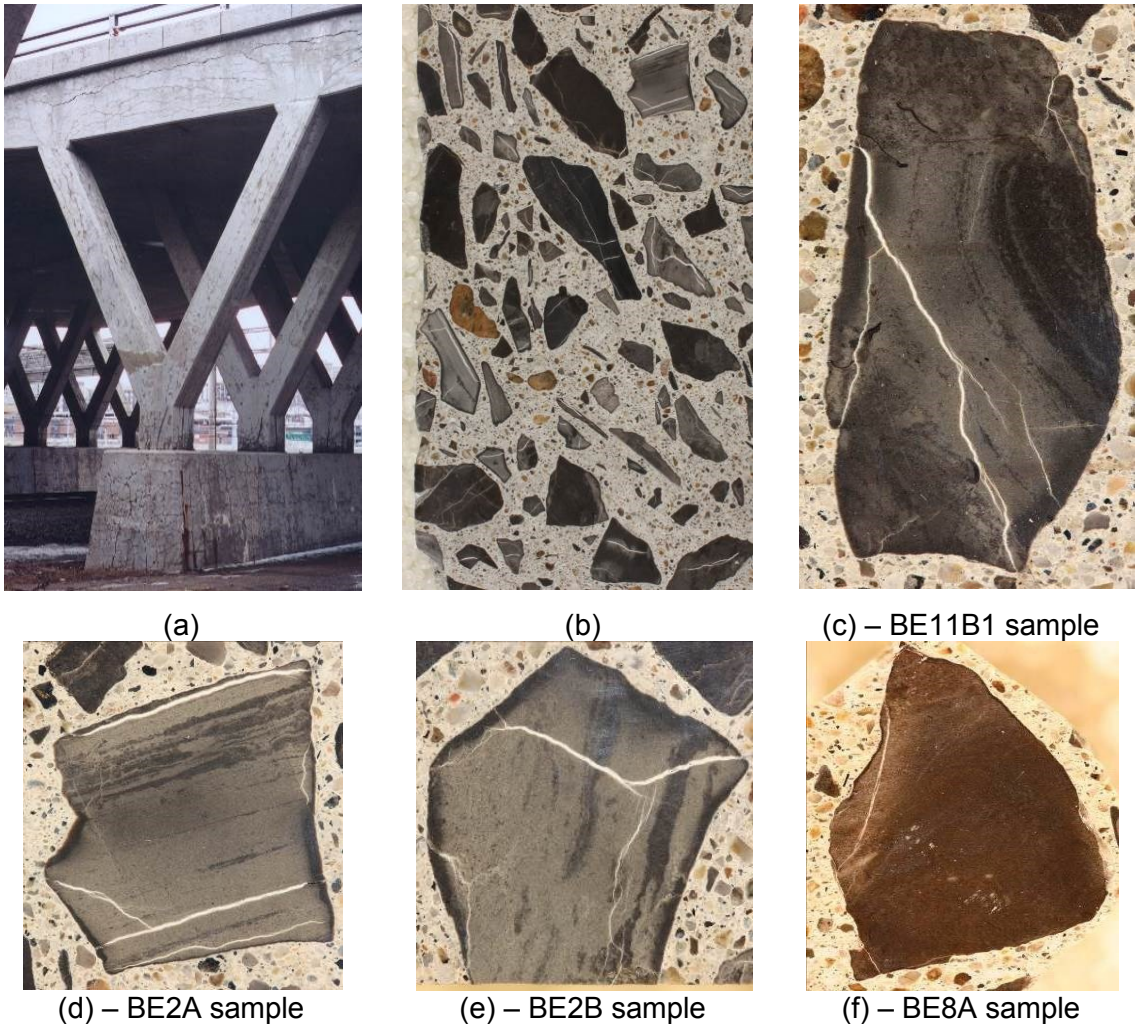

Figure 5.1 (a) ASR-affected concrete structure in the Québec City area; it is composed of Y-shaped columns sitting on massive foundation blocks and supporting a bridge deck with no shear reinforcement. Cores were extracted from the massive foundation blocks; (b) Plane polished section of a concrete core extracted from the foundation blocks; (c) Selected BE11B1 particle with both light-grey and dark-grey zones for microprobe analysis; (d) Selected BE2A particle for microscratch testing; (e) Selected BE2B particle for microscratch testing; (f) Selected BE8A particle for microscratch testing.

Furthermore, a sample of virgin limestone was obtained from a local quarry in the Québec City area (Neuville Formation, Trenton Group, Figure 5.2a). The stratigraphic sequence is rather homogeneous at the macroscale from one quarry to another in the area; it is typically characterized by 10 to 20 cm thick beds of siliceous/argillaceous fine-grained and dark grey limestone with more or less important shale interbeds, as shown in Figure 5.2a (Fournier et al., 1991). Being of sedimentary origin, variations in composition can be observed at the microscale within each bed of limestone, e.g. proportion of calcite, clay minerals (mainly illite, interlayered illite-smectite, some chlorite), dolomite, detrital minerals (quartz,

feldspars). A small rock section, approximately 30 x 30 x 15 mm, was wet cut perpendicular to the sedimentary bedding of a representative limestone bed with a diamond saw, to be tested by micro-scratch testing (N18 in Figure 5.2b). The bedding plane in this sample appears horizontally in the picture (Figure 5.2b). The chemical composition of the precise limestone sample used for testing is given in Table 5.1.

(a) (b)

Figure 5.2 (a) Typical sequence of Trenton limestones (Neuville formation) in a quarrying operation of the Québec City area; (b) Selected N18 block (Fournier, 1993) from which a polished section was prepared micro-scratch testing.

Table 5.1 Chemical composition of the quarried limestone samples used for micro-scratch testing.

	SiO_2	Al_2O_3	Fe_2O_3	MgO	CaO	Na_2O	K_2O	TiO_2	MnO	LOI
Sample	12.3	1.25	0.77	1.14	46.7	<0.10	0.20	0.05	0.02	37.5

LOI: Loss on ignition.

5.2.2 Material preparation

The face of the sawn core samples was then polished with a portable hand polishing device, which uses diamond-impregnated rubber disks (from coarse to very fine: no. 50, 100, 400, 800 to 1500 grit) (Figure 5.3a). The operation was done in wet condition. The four individual aggregate particles selected from the plane polished sections (i.e. Figures 5.1d to 5.1g) were extracted with a precision diamond saw in wet conditions.

Regarding the polishing of the quarried rock sample, the small block, 30 x 30 x 15 mm in size and described in the previous section, was carefully polished according to a protocol developed from the work of Akono et al. (2012), Leemann et al. (2013) and Miller et al.

(2008), which is summarized in Table 5.2. Figure 5.3 shows the grinding and polishing devices used in this study.

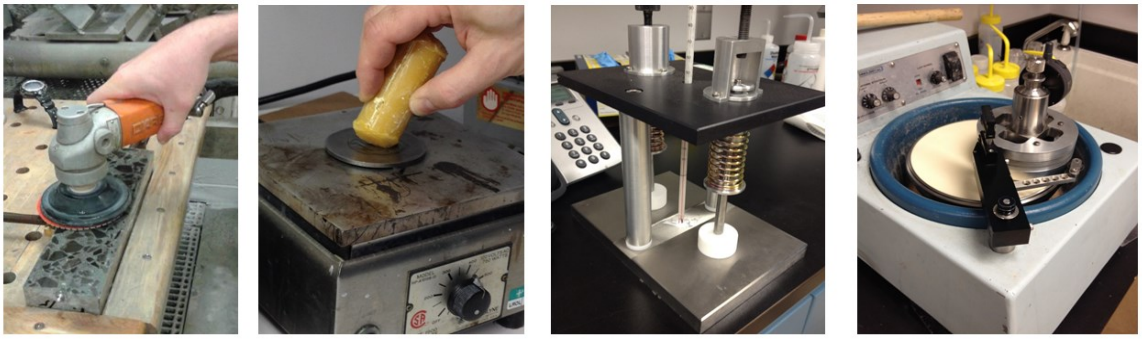

(a) (b) (c) (d)

Figure 5.3 (a) Hand polishing device used for polishing the plane polished concrete sections. (a to c): a device used for the polishing of the virgin limestone: (b) Wax melting for fixing the sample on a steel plate; (c) Pistol to ensure the sample's surface parallel to the supporting steel plate; (d) Rotating jig containing the sample on the polishing machine.

Table 5.2 Protocol procedure using the device illustrated in Figure 5.1d.

Sandpaper	Microns (μm)	Methods	Duration [min]
SiC sandpaper 400-180	76	flush with water	180
SiC sandpaper 400-240	50	flush with water	120
SiC sandpaper 400-400	22	flush with water	60
SiC sandpaper 400-800	12	flush with water	30
SiC sandpaper 400-1200	6.5	flush with water	30
Oil based Diamond suspension	1	Acetone flush, air gun dry	30

5.2.3 Scope of testing

With relationship to the samples illustrated in Figure 5.1 and Figure 5.2, the choice of samples and related testing was done as follows:

1. Micro-indentation testing to check the chosen penetration depth for micro-scratch tests due to possible roughness effect and probed volume representability;

2. Characterization of the fracture toughness of virgin quarried limestone (Figure 5.2b) to determine whether there is difference according to the micro-scratch direction, i.e. with respect to the bedding planes;

3. Characterization of the fracture toughness of light-grey zones in "reacted" limestone particles (i.e. BE2A and BE2B in Figures 5.1d and 5.1e) through micro-scratch testing

parallel and perpendicular to the bedding. The choice of two samples also allows verification of test results repeatability;

4. Characterization of the fracture toughness of dark grey (or “unreacted”) zone in an aggregate particle (i.e. BE8A in Figure 5.1f) to verify whether there is a difference with the material in the light-grey zones, through micro-scratch testing parallel and perpendicular to the bedding.

5. Chemical analysis by microprobe of the sample BE11B1 (Figure 5.1c), which exhibits both dark grey and light grey zones.

5.2.4 Basics of instrumented indentation tests

Micro-indentation techniques have been emerging to quantitatively characterize the mechanical properties of composite microstructures (Fischer-Cripps, 2011; Griepentrog, et al., 2013). During an indentation test, both the vertical force (P) applied and the penetration depth (h) are measured simultaneously (Figure 5.4a). Figure 5.4b shows a typical parabolic $P-h$ curve obtained with a conical indenter; it shows a first loading segment up to the maximum load $P_{\max}$ followed by an elastic unloading curve. As for the indentation properties, the indentation modulus (M) and the indentation hardness (H) are defined as follows (Galin et al., 1961; Oliver et al., 1992):

$$H \overset{def}{=} \frac{P_{\max}}{A_c} \tag{5.1}$$

$$M \overset{def}{=} \beta \frac{\sqrt{\pi}}{2} \frac{S}{\sqrt{A_c}} \tag{5.2}$$

Where the coefficient β accounts for slip contact for a tip indenter of Berkovich shape; A_c is the projected area of the indenter at a distance h_c back from its tip, as shown in Figure 5.4a; $P_{\max}$ is the maximum load and $S = (dP/dh)_{h=h_{\max}}$ is the unloading indentation stiffness at the maximum penetration depth ($P = P_{\max}$). The latter can be estimated by the well established Oliver and Pharr method for which $A_c = 3\sqrt{3}h_c^2 \tan^2\theta$, where $h_c = h_{\max} - \varepsilon(P_{\max}/S)$ (Oliver et al., 1992). Finally, a standard procedure is applied to account

for the diamond tip defect by calibrating the function $A_c=24.5h^2+C_1h^{1/2}+C_2h^{1/4}+..$ by employing a reference sample according to fused silica with known indentation modulus (Fischer-Cripps, 2011). For an elastic isotropic material, the indentation modulus M allows determining Young's modulus of the tested material E, provided that its Poisson's ratio (υ) is known along with the elastic properties of the diamond tip (E_i =1141 GP_a, υ =0.7) (Fischer-Cripps, 2011). In this, study the three-sided pyramid Berkovich shape, which can be considered an equivalent conical indenter with semi-angle θ of 70.72º (Figure 5.4a), was used. The geometry correction factor β and the intercept factor ε are 1.034 and 0.75, respectively (Blocken et al., 2004; Oliver et al., 1992).

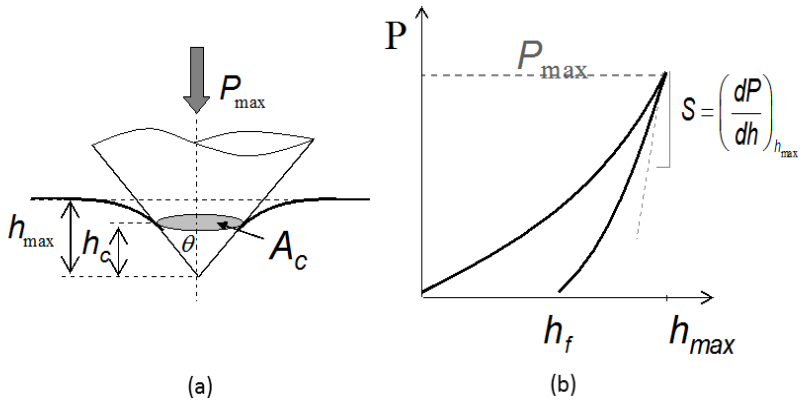

Figure 5.4 (a) Schematic view of an indentation test with a conical indenter; (b) Load vs. penetration depth response of a typical indentation test.

5.2.5 Basics of instrumented micro-scratch tests

The underlying concept of scratch testing consists of cutting, with a sharp device, the surface of a brittle material for quantifying the energy needed to fracture. In a micro-scratch test (Figure 5.5), the diamond tip is drawn across the material surface under a progressive load while the sample moves at a constant velocity. During such test, the tangential force (friction) and the penetration depth are simultaneously measured (Akono et al., 2012). As schematically shown in Figure 5.5b and 5.5c, the vertical force (F_N), the horizontal force (F_T), the penetration depth (d), the initial and residual depth (P_i and P_r), and the acoustic emissions (AE) are recorded as a function of the horizontal position. Note that, for sake of comparison with current works published in the open literature, micro-indentation and micro-

scratch tests use two different symbols for the penetration depth, namely h and d, respectively. After the scratch test, a panorama picture of the scratch groove is taken.

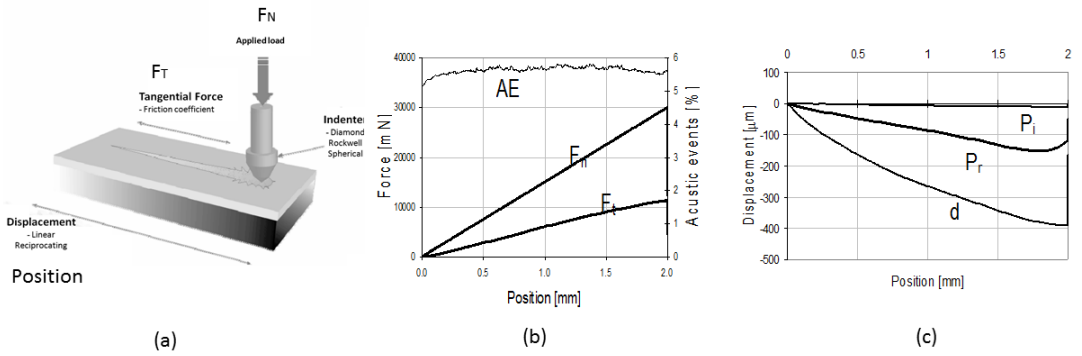

(a) (b) (c)

Figure 5.5 (a) Schematic of micro-scratch test set-up; (b,c) Typical variables applied (F_N) and measured (F_T, P_i, P_r, d) during a test.

Based on a simplified Linear Elastic Fracture Mechanics model, which estimates the energy release rate of a path independent contour around the moving crack, Akono et al. developed an analytical estimate of the fracture toughness K_C (Akono et al., 2011; Akono & Ulm, 2011). The method was applied to several materials, such as ceramics, polymers, and metals (Akono et al., 2012). In the case of isotropic, homogeneous and linear elastic materials, the fracture toughness can then be derived from the horizontal force measured (F_T) and the geometry of the probe as follows:

$$K_c = \frac{F_T}{\left[2p(d)A(d)\right]^{1/2}} \tag{5.3}$$

Based on the theory of Akono et al., the function $F_T/\left[2p(d)A(d)\right]^{1/2}$ converges to the fracture toughness K_C for increasing value of penetration depth d/R. The fracture toughness is determined through the indenter shape function $f(d)=2p(d)A(d)$, where perimeter p and the horizontally projected load bearing contact area (A) are both functions of penetration depth (d). Then, the fracture energy G_f can be evaluated from the well-known Irwin relationship: $G_f = K_c^2/E'$. In the present work, scratch tests were carried out with a Rockwell diamond tip with a conical probe of half-apex angle θ=60º which ends with a hemispherical tip with mean radius R. In this study, we employed a Rockwell tip with R=100 μm for which the

transition from the sphere to cone shape occurs at a rather deep penetration depth of about $d/R = 0.065$ (Akono et al., 2011).

The tests require calibrating the shape function $f(d/R)$, which takes into account the contributions from the conical α and spherical factor β as well as some blunting of the tip γ, as follows (Akono et al., 2012):

$$f\left(\frac{d}{R}\right) \overset{def}{=} \frac{2p(d)A(d)}{R^2} = R^3\left[\alpha\left(\frac{d}{R}\right)^3 + \beta\left(\frac{d}{R}\right)^2 + \gamma\frac{d}{R} + \delta\right] \tag{5.4}$$

where R is the indentation radius, and $(\alpha, \beta, \gamma, \delta)$ are calibration function parameters. In the ideal cases, for a conical tip: $f(d/R)$ is proportional to R^3, and for the spherical tip: $f(d/R)$ is proportional to R^2. As for hard materials, micro-scratch lines on the fused silica (made of 99.9% of SiO_2) are recommended (Akono et al., 2012).

5.2.6 Test setting

5.2.6.1 Cyclic micro-indentation tests

Preliminary tests of micro-indentation were carried on the virgin limestone (Figure 5.2b) to assess a suitable penetration depth, which is enough large to not affected by the surface roughness and to be representative of the particle microstructure (also called scale *separability* condition). This preliminary study was limited to the virgin limestone section, thus assuming that the effect of polishing and the grain size heterogeneity would be similar for all studied particles. The cyclic micro-indentation tests consist of carrying out several indentation tests on the same surface point by progressively increasing the maximum load. In more details, the cyclic tests consisted of 10 indentation tests with maximum load linearly increasing from 0.02 N to 8 N with 10 cycles. For each cycle, the load is unloaded down to 10% of the maximum load, loading/unloading time of about 10 seconds, and a pause between cycles of 5s. The indenter penetration depth (h) is measured during the cyclic loading. The tests were repeated 5 times on different points of the surface.

5.2.6.2 Micro-scratch tests

As for the calibration, the indenter shape function *f*(*d*) was estimated with micro-scratch tests on fused silica, which is a suitable reference material with known toughness value (e.g., fused silica with K_C = 0.58 $MP_a\sqrt{m}$) (Akono et al., 2012). The calibration tests were performed by imposing a progressive normal load F_N from 0.03N to 3 N over a scratch length of 2 mm with a scratch speed of 4 $mm/\min$. As shown in Figure 5.6, the best fitting indenter shape function *f*(*d*) was characterized by the following parameters: $\alpha = 0$, $\beta = 40.423$, $\gamma = 0.163$, $\delta = 0$ with a mean goodness R^2 of 0.95. The fact that $\alpha = 0$ indicates that the maximum penetration is in the range of the spherical part of the Rockwell tip contact with the material. Furthermore, δ = 0 means the interception of the fitting curve is 0.

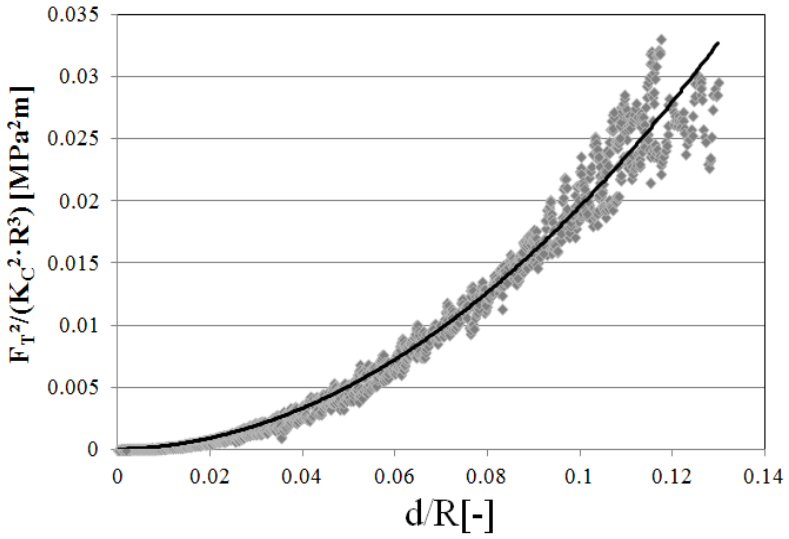

Figure 5.6 Indenter shape function calibration fitted curves for 3 calibration tests (the fitted curve is the black bold line).

As for the aggregate samples, the micro-scratch tests were carried out by selecting test locations far from cracks and visible voids as observed by a digital microscope. Both virgin and reacted aggregate particles (Figure 5.1d to 1f) were characterized by at least 50 tests imposing a progressive normal load F_N from 0.03 N to 7 N over a scratch length of 2 mm with a scratch speed of 2 mm/min. The indentation grid was carried out in direction parallel and perpendicular to the bedding direction of the particles.

Figure 5.7a and b give some examples of micro-scratch lines on the virgin limestone section and the light-grey zones of particle BE2B, respectively. The scratch lines close to the gel veinlet were not compiled and therefore were neglected.

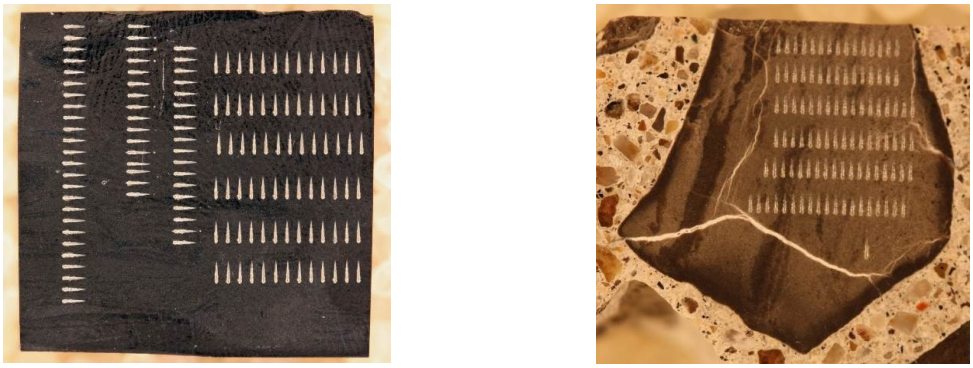

(a) (b)

Figure 5.7 (a) Micro-scratch testing in directions parallel and perpendicular to bedding in the virgin limestone; (b) Micro-scratch testing in a direction parallel to the bedding plane in the light grey zone of particle BE2B.

5.2.7 Electron probe microanalysis (EPMA)

One portion of the aggregate particle illustrated in figure 1d was subjected to the electron probe microanalysis (EPMA) in a CAMECA SX-100 microprobe equipped with five WDS detectors (LIF, TAP, PET) and one PGT prism EDS detector. The surface of the sample was first carbon coated and then probed by chemical mapping. The operating conditions were set at 15 kV and 40 nA at high vacuum (<10−5 Torr).

5.3 Results and Discussion

5.3.1 Cyclic indentation tests

Figure 5.8 shows the experimental load vs. penetration depth curves $P-h$ for the 3 test repetitions accompanied by the mean curve. By assuming Poisson's of 0.3, Young's modulus E of the aggregate can be estimated from the measured indentation Modulus M, as explained in section 3.4. Figure 5.9 shows the mean curves of Young's modulus and the Hardness as a function of the penetration depth. For the considered range of penetration depth (8-25 μm), the E-modulus and Hardness of the aggregates seem rather unaffected by any size effect. Therefore, micro-scratch test setting with a penetration depth of about 8μm

(which corresponds roughly to an applied load of 3mN based on Figure 5.8), should be acceptable for the representability and roughness considerations.

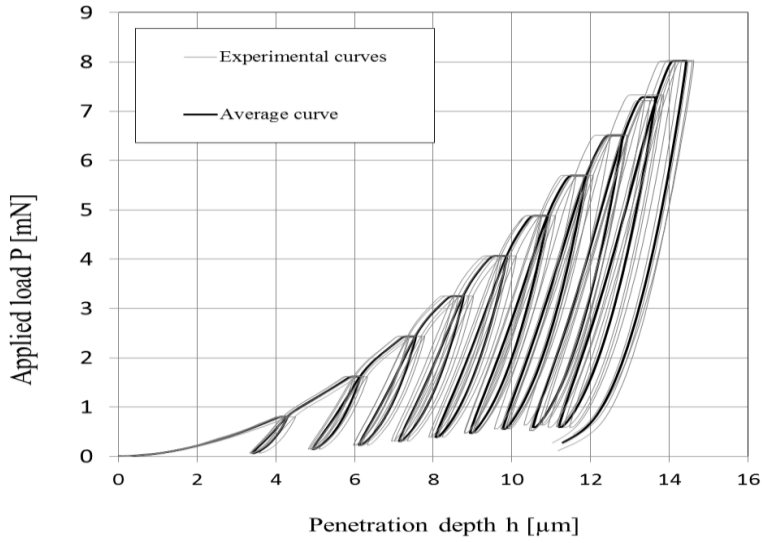

Figure 5.8 Load vs. penetration depth curve for cyclic preliminary indentation tests on the virgin limestone section (grey lines are the experimental curves, while black line is the mean curve).

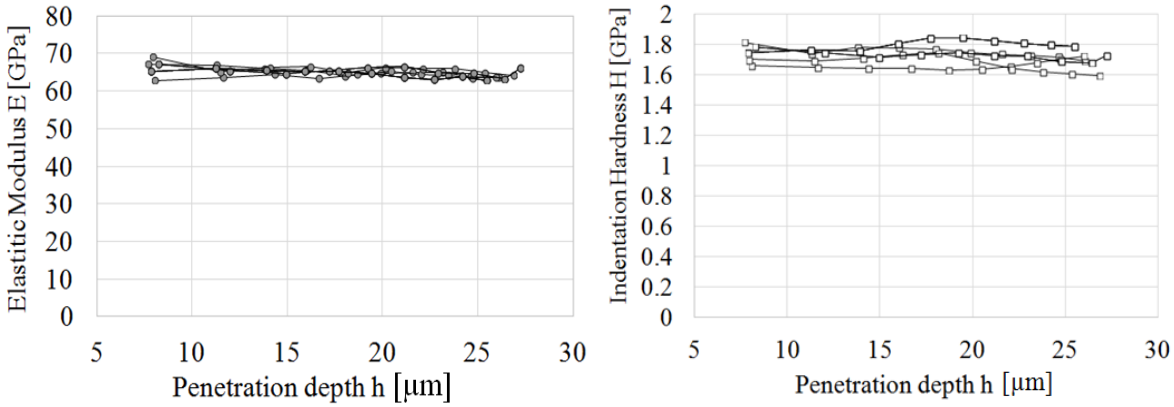

(a) *(b)*

Figure 5.9 (a) Young modulus E and (b) Hardness H vs. penetration depth for 5 CMC tests.

5.3.2 Micro-scratch tests

Based on the considered scratch analysis techniques (Akono et al., 2011), the curve $F_T / \sqrt{2pA}$ should converge to the toughness K_C at increasing value of penetration depths d / R. Figure 5.10a and 5.10b show typical results for a micro-scratch test on the virgin limestone section N18 with scratch lines parallel and perpendicular to the bedding plane,

respectively (Figure 5.10a). The curve $F_T / \sqrt{2pA}$ vs normalized penetration depth d/R converges nicely towards the toughness value K_C. Moreover, the corresponding pictures of the scratch groove are shown in Figure 5.10c and 10d.

Figure 5.11a and 5.11b show the same curves $F_T / \sqrt{2pA}$ vs. d/R for measurements carried out on the dark grey zone in particle BE8A (Figure 5.1f), with scratch lines parallel and perpendicular to the bedding plane (Figures 5.11c and 5.11d), respectively. It is interesting to note that the BE8A particle contained a crack filled with secondary reaction products (i.e. white veinlet on the left side of the particle in Figure 5.1f), thus confirming its reactive character.

Finally, Figure 5.12a and 5.12b show the curves $F_T / \sqrt{2pA}$ vs. d/R for the light grey zone in particle BE2A (Figure 5.1d) with scratch lines parallel and perpendicular to the bedding plane, respectively (Figures 5.12c and 5.12d).

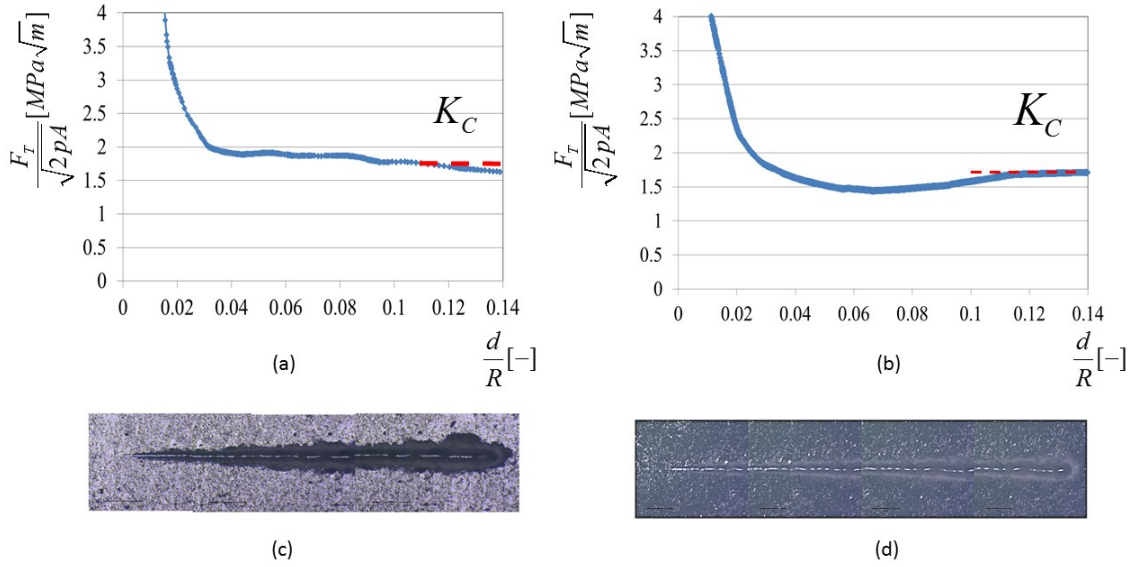

Figure 5.10 Example of K_C determination curve for virgin limestone section N18 for micro-scratch lines (a) parallel or (b) perpendicular to the bedding plane. Pictures of the scratch grooves for micro-scratch lines (c) parallel or (d) perpendicular to the bedding plane.

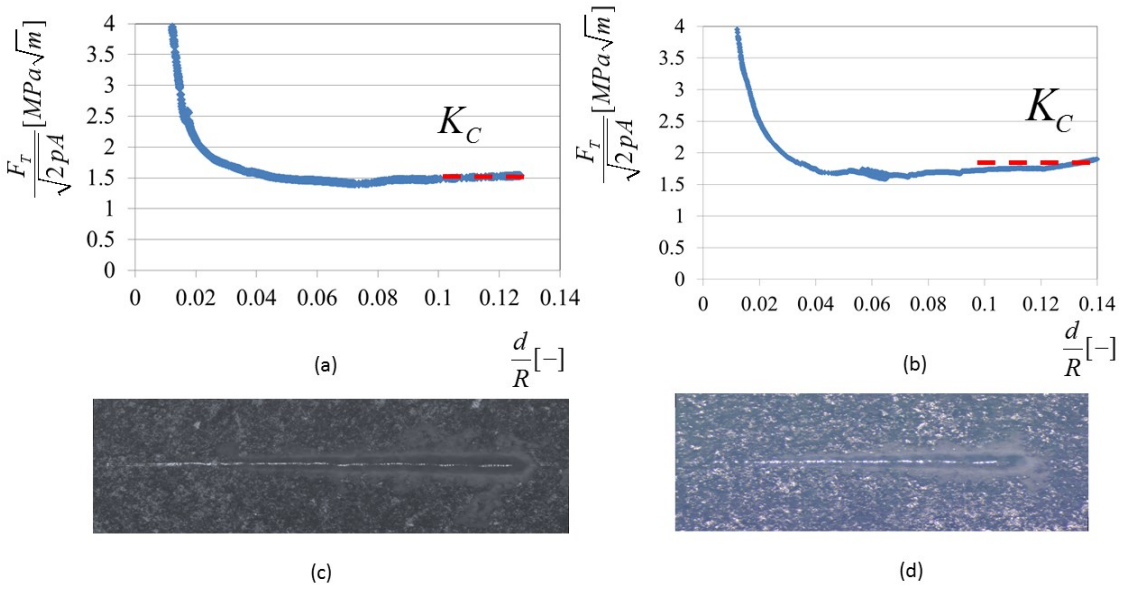

Figure 5.11 K_C determination for the dark grey zone in the aggregate particle BE8A for micro-scratch lines (a) parallel or (b) perpendicular to the bedding plane. Pictures of the scratch grooves for micro-scratch lines (c) parallel or (d) perpendicular to the bedding plane.

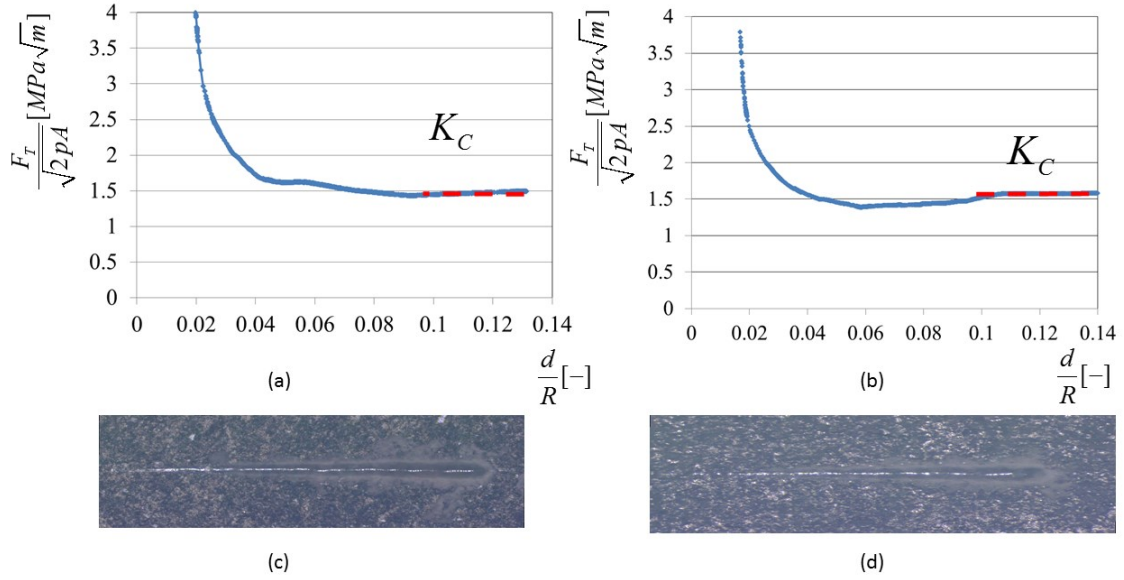

Figure 5.12 K_C determination for the light grey zone in particle BE2A for micro-scratch lines (a) parallel or (b) perpendicular to the bedding plane. Pictures of the scratch grooves for micro-scratch lines (c) parallel or (d) perpendicular to the bedding plane.

5.3.2.1 Effect of the orientation of testing (versus bedding plane)

Considering all the micro-scratch tests carried out (i.e. at least 50 on each particle), Figure 5.13 shows the frequency histogram of the toughness K_C values for all the studied particles.

Figure 5.13 reports the statistical information of the presented curves including the best fitting parameter for a Weibull distribution.

Comparison of Figure 5.13a and 5.13b indicates that the toughness K_C of the virgin limestone particle N18 is not significantly affected by the direction of the micro-scratch lines, i.e. parallel or perpendicular to the bedding plane A difference against the mean K_C values of only about 3% were obtained (average values of 1.66 and 1.60), with similar SD values of 0.10-0.11). The distribution is only slightly more asymmetric for the case of parallel scratch lines.

Figure 5.13c and 5.13d compare the toughness K_C values measured on the dark grey zone of particle BE8A with micro-scratch lines parallel and perpendicular to the bedding plane, respectively. In this case, a significant difference is observed with the average K_C value obtained from microscratch tests carried out parallel to the bedding plane (Figure 5.13c) being inferior to that of tests performed perpendicular to the bedding plane (Figure 5.13d).

Finally, Figure 5.13e and 5.13f compare the toughness K_C values for the light grey zone in particle BE2A with micro-scratch lines parallel and perpendicular to the bedding plane, respectively. Similar to the virgin aggregate N18, the effect of the scratch direction on the toughness values distribution appears negligible (K_C of 1.58 vs 1.61; SD of 0.08 and 0.12), although a much higher variability in the test results was obtained for tests carried out perpendicular to the bedding plane.

Table 5.3 reports the statistical information of the presented curves for a better comparison with also the best fitting parameter for a Weibull distribution. The statistical results quantitively confirm the previous observation. Comparison of statistical values of sample BE2A and BE2B with parallel micro-scratch direction confirms a different of 4% of the mean K_C value, which is a satisfactory test repeatability. Their standard deviation divided is also close. However, the shape of their Weibull distribution function is more asymmetric for the case BE2B hinting for the need of increasing the number of tests for better capturing the full distribution. For the unreacted particle N18, the effect of the micro-scratch direction with respect to the bedding plane direction involve a difference of mean K_C inferior of about 3%, which seems negligible.

Table 5.3 Statistical information and model parameter of the best fitting Weibull probability distribution functions for the toughness measurements of all studied particle (the unit of the measured toughness

is $MP_a m^{1/2}$).

	BE2A		BE2B	BE8A		N18	
Direction	//	∟	//	//	∟	∟	//
Mean	1.58	1.61	1.51	1.44	1.61	1.66	1.60
SD	0.08	0.12	0.11	0.07	0.10	0.10	0.11
Asymmetry	0.34	0.30	0.69	0.36	0.62	0.08	0.13
Flattening	2.84	2.80	3.4	2.86	3.25	2.711	2.718
alpha	0.205	0.323	0.244	0.196	0.220	0.324	0.365
beta	2.534	2.644	1.910	2.483	2.010	3.297	3.124
gamma	1.403	1.327	1.288	1.264	1.419	1.368	1.277
P-value	0.935	0.531	0.478	0.802	0.594	0.092	0.275
Acceptance test	Yes	Yes	Yes	Yes	Yes	Yes	Yes

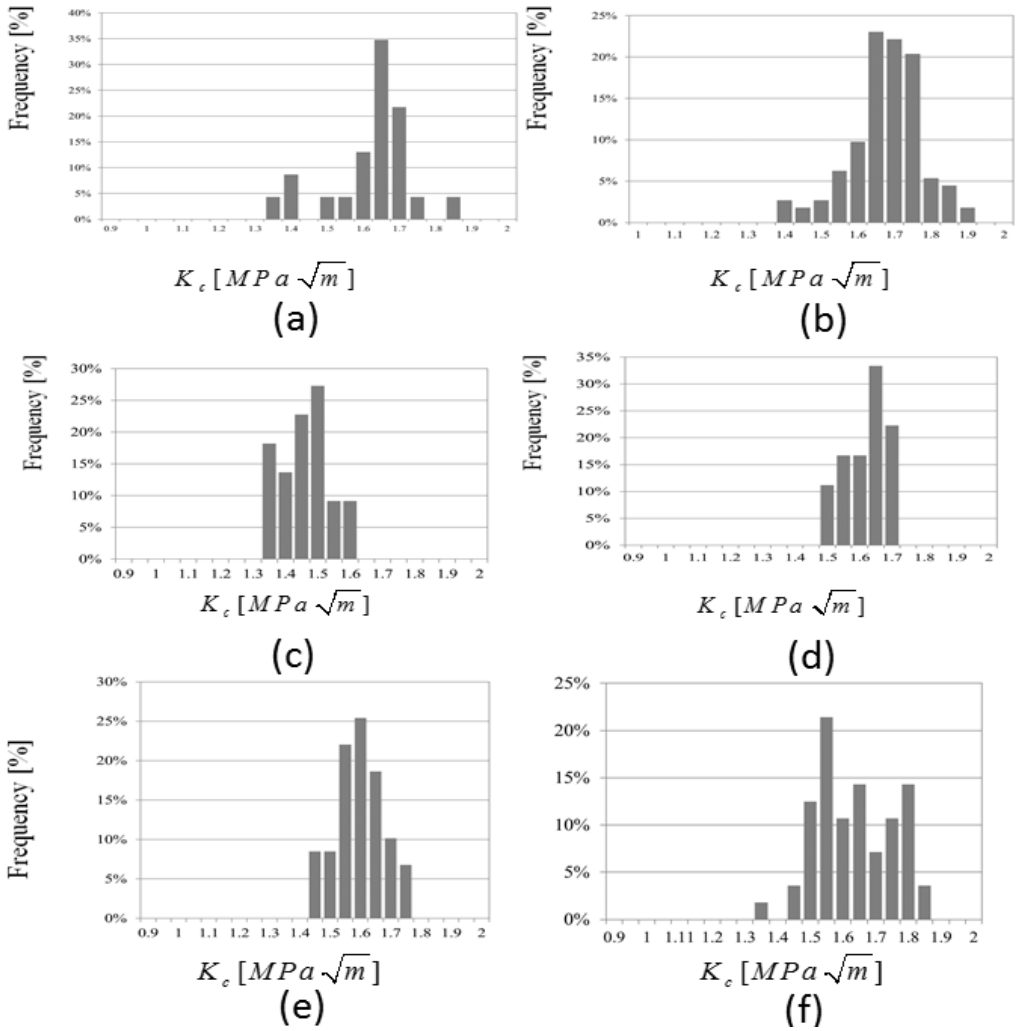

Figure 5.13 Experimental histogram of the toughness K_C values for: virgin limestone section N18 with micro-scratch lines (a) parallel and (b) perpendicular to the bedding plane; dark grey particle BE8A with micro-scratch lines (c) parallel and (d) perpendicular to the bedding plane; light grey zone in particle BE2A with micro-scratch lines (e) parallel and (f) perpendicular to the bedding plane.

5.3.2.2 Effect of particle characteristics

As for test repeatability, the scratch tests were carried on a light grey zone of a second aggregate particle, i.e BE2B, which was selected from another immediately adjacent core in the same massive concrete foundation. In this case, scratch lines were done only parallel to the bedding plane considering the surface available for testing. Figure 5.14a shows a typical toughness determination curve $F_T / \sqrt{2pA}$ vs d/R. Figure 5.14c shows the K_C histogram, while Table 5.3 gives the statistical information of the presented curves including the best fitting parameter for a Weibull distribution. Somewhat similar K_C values of 1.58 and 1.51 (considering the SD values of 0.08 and 0.11, respectively) were obtained for micro-scratch tests performed parallel to the bedding plane of both particles. The asymmetry in the data set is however slightly higher for the BE2B particle, stressing the need for increasing the number of tests for better capturing the full distribution.

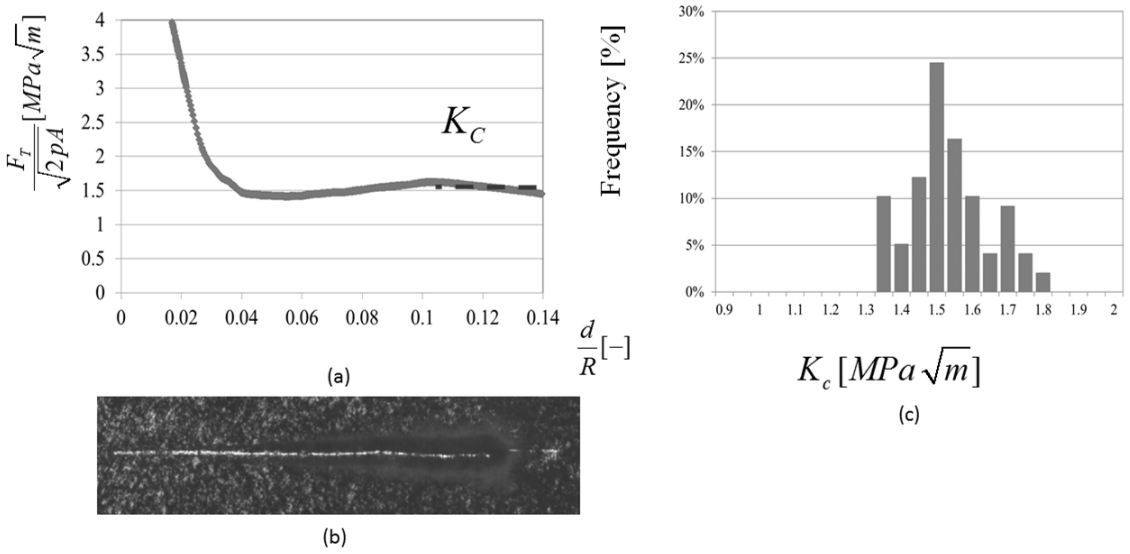

Figure 5.14 Test repetition on the light grey zone of a second aggregate particle (BE2B). (a) K_C determination curve for a micro-scratch line parallel to the bedding plane; (b) Picture of the scratch groove for a micro-scratch line parallel to the bedding plane; toughness histogram for the micro-scratch lines parallel to the bedding plane.

If we compare the data obtained between the light-grey zone of particle BE2A and the dark-grey zone of particle BE8A (suggesting a somewhat "unreacted" zone within that particle), identical average K_C values (1.61) (and SD: 0.12 – 0.10) were obtained perpendicular to the bedding; on the other hand, a reduction in the K_C values of about 9% (which is roughly double of their standard deviation and thus statistically significant) were found for the micro-scratch

lines parallel to the bedding planes in the case of the dark-grey particle (1.58 vs 1.44); this result suggests that the light-grey zone exhibits a slightly higher toughness value, in that direction than the dark colored zone.

The comparison of the statistical values obtained for N18 virgin limestone section and the light-grey zone in particle BE2A reveals a difference, in terms of the mean K_C values, of only about 3% for the parallel direction and 1.2% in the perpendicular direction. This suggests that there is no significant difference between the toughness values of the virgin limestone and of the light-grey zone, which was originally thought to represent a somewhat "reacted" zone surrounding microcracks filled with ASR products (white veinlets – Figure 5.1) in the aggregate particles. If we assume that the virgin limestone section is representative of the real field aggregate particles, the effect of ASR reaction on the local toughness K_C of the particles is rather limited. This suggests that the damage affecting the reactive particles is rather localized in the white microcrack veinlets visible in the aggrege, rather than a widely-distributed damage zone within the whole particle.

5.3.3 Electron probe microanalysis (EPMA)

Figure 5.15 illustrates the aggregate particle subjected to chemical mapping under the electron microprobe; Figure 5.15a highlights the zone on the aggregate particle that was subjected to the mapping (white box); it includes a dark zone in the upper left portion of the micrograph and a dark-grey zone in the bottom right portion. Figure 5.15b illustrates the area analyzed in back-scattered electron mode, with the two zones highlighted in Figure 5.15a. Figures 5.15c to 5.15f give the results of the X-ray microprobe mapping: Si Kα (c); Ca Kα (d); K Kα (e) and Al Kα (f). Basically, the light-grey area (bottom right portion) corresponds to a clay-rich area, which is characterized by a larger content in Potassium (K) and Aluminum (Al). That zone is also rich in Silicon since the clay minerals correspond to "flaky" silicate minerals. The darker zone (upper left portion of the micrographs), although it also contains disseminated (and very small) clay-rich beds (small light-grey subzones), is largely composed of calcite (carbonate mineral form with calcium). In general, we can probably say that the clay-rich zones are somewhat more porous and "softer" than the more "massive" calcite-rich zones. "Flaky" clay minerals also have the tendency to orient preferentially parallel to the bedding plane, which may impact on the results of micromechanical testing.

From the microprobe analyses, it appears that the upper left portion in Figure 15a, which corresponds to the dark-grey zone, is mainly composed of small calcite grains (micrite) with small clay-rich interbeds. Calcite is a low-hardness mineral form (3 on the Mohs scale) and that displays three-dimensional cleavages. On the other hand, the light-grey zone in the bottom-right portion of Figure 5.15a is composed of a mixture of clay minerals and possibly silica, which could reveal a somewhat higher hardness compared to the adjacent calcite-rich layers. Fournier (1993) had indeed shown that the insoluble residues of the limestones in the Québec City area are composed of a mixture of clay minerals (illite and interlayered illite/smectite, traces of chlorite) and micro- to cryptocrystalline quartz disseminated in the matrix of the rock, the fine-grained quartz corresponding to the reactive material in those rocks.

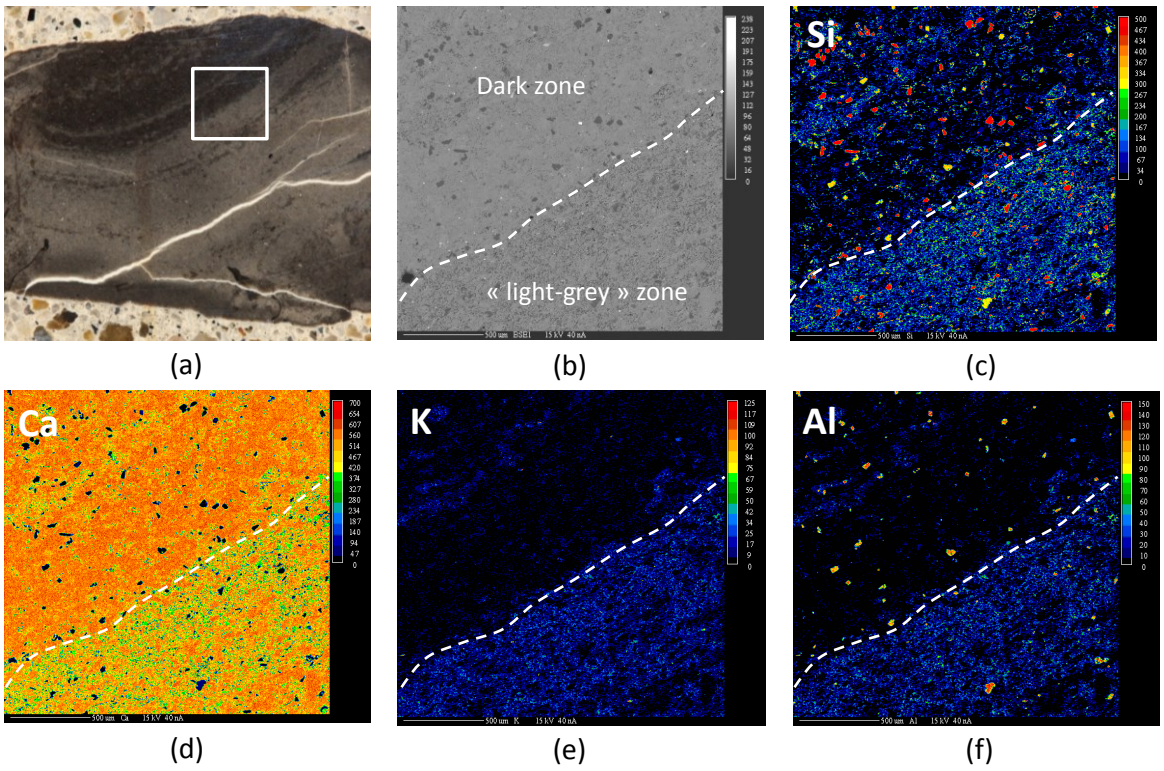

Figure 5.15 On the particle interface between the dark and bleached zone of the reacted aggregate: (a) Zoomed micrograph on the scratched lines; (b) Back-scattered electron image; (c) Mapping of Silicon; (d) Mapping of Calcium; (e) Mapping of Potassium; (f) Mapping of Aluminum.

5.4 Conclusions

A novel statistical micro-scratch techniques have been employed to characterize the toughness of limestone aggregates and reactive ASR limestone particles, which were extracted in real field concrete structures highly damaged by ASR expansion. The aggregate toughness is a critical parameter for describing the damage process of reactive aggregate in ASR-damaged concretes. Based on the present results, the following conclusions can be drawn,

1. As for the application to limestone aggregate, the micro-scratch techniques was successfully employed to assess the toughness distribution of aggregate at the microstructure level. The toughness was about 1.6 $MP_a\sqrt{m}$ with a coefficienf of variation of about 5%. The microsctarh depth (which was about 8 μm) was likely too deep to feel the effect of the direction of the bedding plane;

2. As for the application to reacted limestone agrgeate, the light-grey zone surrounding microcracks filled with ASR products in “reacted” limestone particles showed similar toughness values as the unreacted ones, with difference inferior of 4% in terms of the K_C mean values. From a micromechanical point-of-view, this suggests that the damage in the reacted particles remains localized in the white veinlet cracks (i.e., filled with ASR product) rather than a damage diffused within the particle;

3. Chemical analysis by microprobe revealed that there is a difference in chemical and mineralogical composition between the light and dark grey zones within the reactive aggregate particles. The difference in toughenss for such measurement was about 9%. The exact reason for the development of such light-grey zones within the “reacted” limestone aggregate particles remains uncertain.

Further studies are needed to be more conclusive, e.g., by considering different kinds of aggregates, by considering the toughness at smaller penetration depth, by further applying micro analytical analysis (mineralogical and chemical analyses) to better understanding the zoning observed in reacted aggregate particles and its potential effect on the damage development in the above particles. The present data can be useful for predicting and modeling the damage process in ASR reacted aggregates in current upscaling models. Further works are necessary.

Acknowledgements

We thank the CSC-UL fellowship program for providing the financial support for the first author of this work.

References

Akono, A.-T., Randall, N.X. & Ulm, F.-J. (2012). Experimental determination of the fracture toughness via micro-scratch tests. Journal of Materials Research, 27: 485-493.

Akono, A. T., Reis, P.M., & Ulm, F.-J. (2011). Scratching as a fracture process: From butter to steel. Physical Review Letters, 106(20): 204302.

Akono, A.-T., & Ulm, F.-J. (2011). Scratch test model for the determination of fracture toughness. Engineering Fracture Mechanics, 78(2), 334–342.

Bažant, Z.P., Tabbara, M.R., Kazemi, M.T., & Pijaudier-Cabot, G. (1990). Random particle model for fracture of aggregate or fiber composites. Journal of Engineering Mechanics, 116(8): 1686–1705.

Ben Haha, M., Gallucci, E., Guidoum, A., & Scrivener, K.L. (2007). Relation of expansion due to alkali-silica reaction to the degree of reaction measured by SEM image analysis. Cement and Concrete Research, 37(8): 1206–1214.

Berard, J. & Roux, R. (1986). La viabilité des bétons du Québec : le rôle des granulats. Canadian Journal of Civil Engineering 13: 12–24.

Blocken, B., & Carmeliet, J. (2004). A review of wind-driven rain research in building science. Journal of Wind Engineering and Industrial Aerodynamics, 92(13): 1079–1130.

British Cement Association, (1992). "The Diagnosis of Alkali-Silica Reaction—Report of a Working Party," UK, 44.

Dunant, C.F., & Scrivener, K.L. (2016). Physically based models to study the alkali–silica reaction. *Proceedings of the Institution of Civil Engineers–Construction Materials*, 169(3): 136–144.

Fischer-Cripps, A.C. (2011). Nanoindentation testing. In Nanoindentation. Springer New York, 21–37.

Fournier, B. (1993). Contribution à l'étude de la durabilité des structures de béton construites avec des granulats carbonatés produits dans les Basses-Terres du Saint-Laurent du Québec : les réactions alcalis-granulats.

Fournier, B., & Bérubé, M.-A. (2000). Alkali-aggregate reaction in concrete: a review of basic concepts and engineering implications. Canadian Journal of Civil Engineering, 27(2): 167–191.

Fournier, B., & Bérubé, M.-A. (1991). Évaluation du potentiel de réactivité alcaline des granulats à béton produits dans les Basses-Terres du Saint-Laurent du Québec (Canada). Revue canadienne de génie civil, 18(2): 282-296.

Fournier, B., Bérubé, M.-A., & Vézina, D. (1987). Conditions survey of concrete structures built with potentially reactive aggregates from the Québec City Area. Katherine and Bryant Mather international conference on concrete durability, April 1987, Atlanta (U.S.A.), ACI Special Publication SP-100, J.M. Scanlon Editor, 1343-1355.

Fournier, B., & Bérubé, M.-A. (1991). Évaluation du potentiel de réactivité alcaline des granulats à béton produits dans les Basses-Terres du Saint-Laurent du Québec (Canada). Revue Canadienne de Génie Civil, 18(2): 282–296.

Fournier, B., Bérubé, M.A., Folliard, K.J., & Thomas, M.D.A. (2010). Report on the diagnosis, prognosis and mitigation of alkali-silica reaction (ASR) in transportation structures.

Federal Highway Administration (FHWA), U.S. Dept of Transportation, FHWA-HIF-09-004, 154.

Galin, L.A., Moss, H., & Sneddon, I.N. (1961). Contact problems in the theory of elasticity. DTIC Document.

Giorla, A.B., Scrivener, K.L., & Dunant, C.F. (2015). Influence of viscoelasticity on the stress development induced by alkali–silica reaction. Cement and Concrete Research, 70:1–8.

Grassl, P., & Bažant, Z.P. (2009). Random lattice-particle simulation of statistical size effect in quasi-brittle structures failing at crack initiation. Journal of Engineering Mechanics, 135(2): 85–92.

Griepentrog, M., Krämer, G., & Cappella, B. (2013). Comparison of nanoindentation and AFM methods for the determination of mechanical properties of polymers. Polymer Testing, 32(3): 455–460.

Griffith, A.A. (1921). The Phenomena of Rupture and Flow in Solids. Philosophical Transactions of the Royal Society of London. Series A, Containing Papers of a Mathematical or Physical Character, 221:163–198.

Irwin, G.R. (1997). Analysis of stresses and strains near the end of a crack traversing a plate. SPIE MILESTONE SERIES MS, 137:167–170.

Guédon-Dubied, J.S., Cadoret, G., Durieux, V., Martineau, F., Fasseu, P., Van Overbecke, V. (2000): Study on Tournai limestone in Antoing Cimescaut Quarry. Petrological, chemical and alkali reactivity approach. In: Bérubé MA, Fournier B, Durand B (eds): *Proceedings of the 11th ICAAR*, Québec/CA: 335-344.

Irwin, G.R. (1997). Analysis of stresses and strains near the end of a crack traversing a plate. SPIE MILESTONE SERIES MS, 137:167–170.

Institution of Structural Engineers (ISE). (1992). Structural effects of alkali-aggregate reaction: technical guidance on the appraisal of existing structures. London, UK: The Institution of Structural Engineers (ISE); 44.

Leemann, A., & Lura, P. (2013). E-modulus of the alkali–silica reaction product determined by micro-indentation. Construction and Building Materials, 44: 221–227.

Miller, M., Bobko, C., Vandamme, M., & Ulm, F.-J. (2008). Surface roughness criteria for cement paste nanoindentation. Cement and Concrete Research, 38(4): 467–476.

Multon, S., Seignol, J.F., & Toutlemonde, F. (2005). Structural behavior of concrete beams affected by alkali-silica reaction. ACI Materials Journal-American Concrete Institute, 102(2):67–76.

Multon, S., Sellier, A., & Cyr, M. (2009). Chemo–mechanical modeling for prediction of alkali silica reaction (ASR) expansion. Cement and Concrete Research, 39(6):490–500.

Oliver, W.C., & Pharr, G.M. (1992). An improved technique for determining hardness and elastic modulus using load and displacement sensing indentation experiments. Journal of Materials Research, 7(06):1564–1583.

Peterson, K., Gress, D., Van Dam, T., & Sutter, L. (2006). Crystallized alkali-silica gel in concrete from the late 1890s. Cement and Concrete Research, 36(8):1523–1532.

Pichler, B., & Dormieux, L. (2007). Cohesive zone size of microcracks in brittle materials. European Journal of Mechanics-A/Solids, 26(6): 956–968.

Poole, A.B., & Sims, I. (2016). Concrete Petrography – A handbook of investigative techniques. CRC Press, Taylor and Francis Group, 780.

Rossi, P., & Richer, S. (1987). Numerical modeling of concrete cracking based on a stochastic approach. Materials and Structures, 20(5):334–337.

Rajabipour, F., Giannini, E., Dunant, C., Ideker, J.H., & Thomas, M.D. (2015). Alkali–silica reaction: current understanding of the reaction mechanisms and the knowledge gaps. Cement and Concrete Research, 76:130-146.

Reinhardt, H.W., & Mielich, O. (2011). A fracture mechanics approach to the crack formation in alkali-sensitive grains. Cement and Concrete Research, 41(3):255–262.

Rossi, P., & Richer, S. (1987). Numerical modeling of concrete cracking based on a stochastic approach. Materials and Structures, 20(5):334–337.

Sanchez, L.F.M., Fournier, B., Jolin, M., Bedoya, M.A.B., Bastien, J., & Duchesne, J. (2016). Use of Damage Rating Index to Quantify Alkali-Silica Reaction Damage in Concrete: Fine versus Coarse Aggregate. ACI Materials Journal, 113(4).

Swamy, R.N.(Ed.). (2002). The alkali-silica reaction in concrete. CRC Press, 28.

Swamy, R.N., & Al-Asali, M.M. (1988). Expansion of concrete due to alkali-silica reaction. Materials Journal, 85(1): 33–40.

Tabor, D. (1954). Mohs's hardness scale-a physical interpretation. *Proceedings of the Physical Society*. Section B, 67(3): 249.

Tada, H., Paris, P. C., & Irwin, G.R. (2000). The analysis of cracks handbook. New York: ASME Press, 2:1.

6. Article 3: Effect of the Relative Humidity on the Creep Rate and Recovery of ASR Products by Microindentation

Chi Zhang[1], Luca Sorelli[1] Benoît Fournier[2], Josée Duchesne[2], Josée Bastien[1] Chen Zhao[1]

3) Université Laval, Civil and Water Engineering Department, 1065 avenue de la Médecine, PLT2928-A, G1V0A6, Québec, Canada.

4) Université Laval, Geology and Geological Engineering Department, 1065 avenue de la Médecine, G1V0A6, Québec, Canada.

Paper to be submitted for possible publication in "Concrete and Cement Research" Journal.

Abstract

In the ASR damage, water plays multiple roles: the reactants (alkali hydroxides ions) transportation media, the simultaneous activation factor, the effect on the viscous elasticity of ASR expansive gel, etc. This work aims at characterizing the effect of water (Relative Humidity) on the micromechanical properties of ASR crystalline products in the aspects of creep, stress relaxation and recover by micro-indentation technique under controlled Relative Humidity (RH) conditions. Concrete cores used in this study were extracted from a heavily ASR-affected concrete pavement. The microindentation testing was carried out on ASR crystalline products filling cracks within reactive siliceous limestone coarse aggregate particles.

The results provide new insights on the water effect on the micromechanical properties of the ASR product, especially the micro-scale viscous elasticity. The creep coefficients and stress relaxation coefficients of the ASR products forming the secondary veinlets within the reactice aggregate particles were measured at the RH 55% and 95%. Meanwhile, the hardness and E-Modulus values are compared under these two relative humidities.

Keywords: Micro-indentation, ASR products, Creep, Stress Relaxation, Relative Humidity control, Recover Factor.

6.1 Introduction

Since its identification in the late 1930's, Alkali-silica reaction (ASR) has been identified affecting numerous concrete structures, such as hydraulic dams, highway bridges, pavements, locks, buildings, etc. all around the world (Charlwood et al., 2016; Folliard et al., 2016; Fournier et al., 2000; Godart et al., 2013; Swamy, 2002; Wang et al., 1995). The ASR damage mechanisms are still a matter of controversy in the scientific community and numerous models have been developed to try capturing the various and complex chemo-mechanical processes involved (Alnaggar et al., 2013; Dunant et al., 2010; Multon et al., 2009; Pan et al., 2012; Saouma, 2014; Seignol et al., 2012).

Through the process of ASR, secondary reaction products are formed when alkali hydroxides and calcium ions present in the pore solution migrate and react with reactive (i.e. amorphous, metastable, strained, micro-to-cryptocrystalline) siliceous phase(s) present within the coarse and/or fine aggregates. The reaction can proceed from the outer part of the reactive particles as well as through pre-existing microcracks originating from aggregate processing operations and various other processes (e.g. weathering, geologically-induced stresses, etc.). Secondary ASR products thus form along those "discontinuities", grain boundaries, etc. within reactive aggregate particles, and can then permeate into the adjacent cement paste and/or along microcracks extending from the aggregate particles into the cement paste. Reaction products showing microtextural characteristics ranging from amorphous (glassy aspect) to crystalline (porcelaneous/powdery aspect; rosette-like under the SEM) have indeed been identified along cracks within reactive aggregate particles and cracks/voids in the cement paste of laboratory concrete/mortar specimens and cores extracted from ASR-affected concrete structures (e.g. Bérubé et al., 1986, Larive et al., 1992, Bérubé et al., 1986; Leemann et al., 2016). While amorphous and crystalline products are found to co-exist in ASR-affected concretes, the exact formation process of crystalline products, e.g. whether or not they possess an amorphous precursor, and their exact contribution to expansive stresses generated within aggregate particles, are still uncertain.

It is generally accepted that ASR expansion is due to the pressure generated, within the reactive aggregate particles and the cement paste, by water absorption/flow by/through the secondary reaction products (imbibition, osmotic pressure, etc.). This process causes extensive damage (cracking) within the affected concrete, thus affecting the durability of

structures (Bérubé et al., 2000; Fournier et al., 1991; Katayama, 2012b; Leemann et al., 2016). The water content affects the swelling capacity of ASR products and their apparent viscosity. Larive et al. (2000) suggested that water only increases concrete expansion when it is available during formation of the ASR gel and that any subsequent water supplies will not result in extra swelling. Struble and Diamond (1981) reported a wide range of free swelling capacities of 0.5% to 81.6% as measured by a number of ASR gels, even for gels with fairly similar compositions; pre-drying was also found to disturb the structure and the swelling properties of gels. On the other hand, Multon and Toutlemonde (2010) mentioned that if water is supplied anytime over the life of an ASR-damaged structure, ASR gel already produced can rapidly swell, while new ASR gels can also form.

Leemann et al. (2016) recently presented a review of the types and compositional characteristics of ASR products. They reported that ASR products within reactive aggregate particles mainly consist of (hydrated) silicon, alkalis, and calcium with characteristic atomic ratios of (Na + K)/Si ~0·25 and Ca/Si ~0·25. Calcium is actually an essential constituent in the formation and expansion mechanism of ASR reaction products. The calcium content of reaction products within cracks of the reactive aggregate particles increases towards the edge of the particle while their alkali content often decreases. This “pattern” is even more pronounced when the reaction products are extruded along cracks within the cement paste. The incorporation of calcium by ASR products reduces their swelling potential compared with alkali-rich varieties which are rather found with reactive aggregate particles (Prezzi et al., 1997; Rodrigues et al., 2001; Wieker et al., 1998; Leemann et al., 2016).

The ASR damage to the concrete thus depends on the free swelling capacity of ASR products, but also on the confining pressure acting on the ASR products before being permeating into adjacent capillary pores and microcracks of the surrounding paste (Vayghan et al., 2016). For ASR reaction product to induce pressure on its environment, it needs to display a certain minimum viscosity or elastic modulus (Katayama, 2012b; Krogh, 1975; Leemann et al., 2016). Low calcium ASR product, which forms in the presence of high alkali (Na, K) contents, is characterized by a low viscosity so that it can permeate through the pore structure of the surrounding cement without generating significant stresses/damage/cracking (Kawamura et al., 2004). Ca-rich product (i.e., Ca/Si > 0.5 molar ratio) would start to approach the composition and properties of C–S–H, with high stiffness and low viscosity properties, thus reducing expansion (Powers et al., 1955). ASR product with intermediate Ca content are likely to be both expansive and capable of generating and

sustaining high-stress levels that cause damage to concrete. ASR permeation within adjacent microcracks allows releasing the internal pressure. Thus, the risk of cracking is greater for ASR products which are highly hydrophilic and expansive, but also with a high yield stress and viscosity to resist its migration. As schematically shown in Figure 6.1, ASR products under high pressure can move into the surrounding channels, e.g., microcracks within the aggregate particles or the cement paste, whereas releasing the hydraulic pressure. Understanding the pressure build-up process within reactive ASR aggregates requires a better knowledge of the ASR visco-elastic property (Dunant et al., 2010; Giorla et al., 2015). This latter point underlines the significance of rheological properties of ASR gels in the cracking process of concrete (Vayghan et al., 2016).

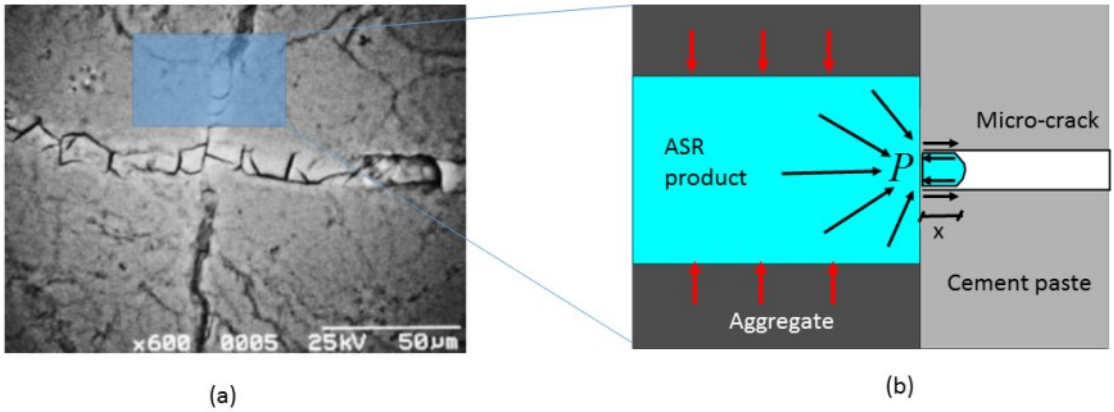

Figure 6.1 (a) Image of cracked aggregate with ASR products inside the large veinlet, adapted by (Kawamura et al., 2004); (b) Schematic view of the hydraulic pressure P generated in the ASR product relaxed by the possible transport towards surrounding voids and smaller cracks.

In their review of the current understanding of the reaction mechanisms and the knowledge gaps, Rajabipour et al. (2015) suggest that research is still needed to determine how much moisture is absorbed by ASR gel as a function of temperature and relative humidity, and to quantify the amount of swelling this causes. Also, in order to efficiently performing prognostic modeling of ASR-affected structures, better knowledge/understanding is required of the effect of confining pressure (e.g. reinforcement detailing) on the development of the reaction per se, as well as of the interaction between the aggregate physical/compositional/textural characteristics, the gel properties (e.g. composition, moisture content, yield strength and viscosity) and the permeability of the cement paste's pore network on the pressure generated by ASR.

6.2 Scope and Objectives of Work

Lately, micro-indentation techniques have allowed disclosing the mechanical properties of ASR products (Leemann et al, 2013). As also reported by Bérubé and Fournier (1986), the authors found a distribution pattern of ASR products along microcracks within reactive aggregate particles characterized by crystalline (rosette-like) products in the central portion of the particle and more massive gel towards the edge of the particle. The Elastic modulus of the ASR crystalline products and of the ASR gel varied from 10 to 50 GPa, respectively. They also found that the ASR products exhibited significant time-dependent (creep) deformation, which was unfortunately not quantified. Recently, relaxation micro-indentation tests showed that ASR products could exhibit relaxation coefficient of about 40% (Zhang et al., 2017). However, this study was limited to the low relative humidity of about 30%, which may not be representative of real field condition of ASR products, and only relaxation tests at constant displacement were carried out. Interestingly, recent models of ASR concrete damage takes into consideration the ASR products' property (Dunant et al., 2010; Multon et al., 2016).

Considering the critical importance of moisture on the swelling properties of ASR products, as stated in the previous section, this work aims at better understanding the viscous property of ASR crystalline products at the different level of Relative Humidity (RH), with emphasis on their irreversibility, as obtained through micro-indentation testing. In more details, the objective of this work is threefold: (i) to characterize their dual viscosity behavior by performing both creep and relaxation tests; (ii) to characterize the effect of relative humidity on their viscous properties; (iii) to characterize the recovery properties of the creep.

6.3 Materials and Methods

6.3.1 Material and sample preparation

Concrete specimens for the laboratory investigations were obtained from cores extracted from an ASR-affected concrete pavement located in the Bécancour area, Québec (Canada) (Figure 6.2). The pavement, which was built in the 1960's, has never been opened to traffic and shows extensive signs of deterioration, such as severe cracking and spalling/bursting at joints. The concrete incorporates a highly alkali-silica reactive siliceous limestone of the

Trenton Group exploited in Trois-Rivières, just across the St-Lawrence River from Bécancour, Siliceous limestones are commonly exploited as concrete aggregates and have caused serious distress in numerous concrete structures in the St-Lawrence Lowlands of Québec, from Québec City to Montréal and Ottawa, Canada (Fournier et al., 1991; Bérubé et al., 2000). Similar aggregate types have also induced premature concrete deterioration in the Northeastern part of France (Guedon-Dubied et al., 2000).

The cores were extracted from a zone of the pavement subjected to direct moisture (rain) and showing extensive cracking.

(a) (b)

Figure 6.2 (a) The pavement in Trois-Rivières made with reactive Trenton limestone and showing extensive map cracking; (b) Bursting at a joint of the pavement.

Immediately after extraction, the full depth cores, 100 mm in diameter x 225 mm in length, were superficially dried with a cloth to remove excess moisture and then wrapped in several layers of plastic film to avoid carbonation and water lost. The cores were then stored in a room at 12℃ to reduce/avoid any further expansion due to ASR in the specimens.

When ready to perform micro-indentation testing (i.e. about 8 weeks after extraction), the selected core was cut lengthways with a diamond saw and one of the surfaces thus obtained examined under the stereomicroscope to select an appropriate section for testing. A small concrete block, about 30 mm x 45 mm x 20 mm in thickness, incorporating a number of aggregate particles with microcracks filled with secondary reaction products, was then cut with a precision diamond saw and minimum water supply. The block was superficially dried and then glued with epoxy on a glass slide. The surface of the mount was then ground/polished with diamond-coated paper, with a small amount of water, down to grit 800 (different papers). Between each paper, the surface was cleaned to avoid scratching the surface. Upon completion of the “coarse” polishing, the surface was gently cleaned with

pressurized air and a piece of scotch tape placed on the surface to avoid carbonation (suggested by A. Leemann, EMPA). The fine polishing protocol was then performed following a method adapted from previous works (Leemann et al., 2013; Zhang et al., 2017); the various steps are described in Table 6.1. The specimens were then placed in a plastic bag, and the bag stored in a hermetic plastic bottle with a small amount of water in the bottom to avoid significant drying and carbonation of the specimens (suggested by A. Leemann, EMPA). The sample was tested for micro-indentation within 24 h after polishing. Figure 6.3 shows the polished concrete surfaces (prior to the fine polishing operations) with visible whitish ASR products in the micro-cracks passing trough the two neighboring aggregates and the cement paste. The rectangular windows located in the aggregate's center are the zones where the micro-indentation tests were performed.

Table 6.1 Protocol procedure.

Sandpaper	Microns (μm)	Methods	Duration [min]
SiC sandpaper 400-400	22	With water	10
SiC sandpaper 400-800	12	With water	10
SiC sandpaper 400-1200	6.5	With water	10

Figure 6.3 Picture of the concrete surface with an indication of the zones for micro-indentation testing (rectangular windows).

6.3.2 Basic of Micro-indentation

After having established a contact between an indenter (typically diamond) and the sample surface, a micro-indentation test consists in applying a load P, while measuring the

penetration depth h (Fischer-Cripps, 2011). Figure 6.4b shows a typical P-h curve for a test with an initial constantly increasing load, followed by a short hold and then a constant unloading. The indentation modulus M and indentation hardness H and indentation are then defined as follows:

$$M \overset{def}{=} \beta \frac{\sqrt{\pi}}{2} \frac{S}{\sqrt{A_c}} \tag{6.1}$$

$$H \overset{def}{=} \frac{P_{\max}}{A_C} \tag{6.2}$$

where the coefficient β accounts for slip contact for a Berkovich shape tip; A_c is the projected area of the indenter at a distance h_c back from its tip as shown in Figure 6.4(a); P_{max} is the maximum load and $S = \left(dP/dh\right)_{h=h_{\max}}$ is unloading indentation stiffness at the maximum penetration depth ($h=h_{max}$). The latter can be estimated by the Oliver and Pharr method for which $A_c = 3\sqrt{3}h_c^2 \tan^2\theta$, where $h_c = h_{\max} - \varepsilon(P_{\max}/S)$ (Oliver et al., 1992). For an indenter with Berkovich shape (i.e. a 3 face pyramidal with a contact angle of 65.3±0.3º), β=1.034 and ε=0.75.

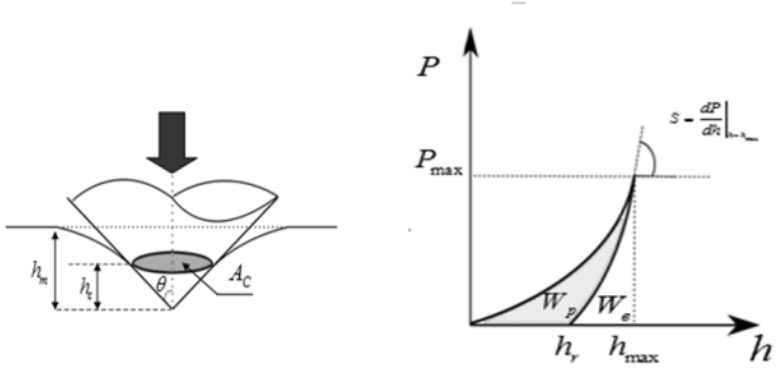

(a) (b)

Figure 6.4 (a) Schematic view of an indentation test with a conical indenter; (b) Load vs. penetration depth response of an indentation test.

In order to account for possible imperfections of the diamond tip, the contact area A_c is calibrated by measuring the indentation modulus of a calibrated fused silica sample (Fischer-Cripps, 2011) as follows:

$A_c\left(h_c\right)=24.5h_c^{\,2}+C_1h_c+C_2 3h_c^{\,1/2}+C_3 3h_c^{\,1/4}+\ldots$ .The P-h curve are then analyzed by continuum models (Galin et al., 1961; Oliver et al, 1992) in order to extract the desired material properties, such as the elastic modulus E of the probed material, such as: $E=\left(M^{-1}-\left(1-\nu_i^{\,2}\right)/E_i\right)^{-1}\left(1-\nu^{\,2}\right)$, where E_i=1141 GPa and ν_i=0.07 are the E-modulus and the Poisson's ratio of the diamond tip, respectively, and ν is the Poisson ratio of the tested material.

As for a viscous material, the penetration depth will creep if the load is kept constant for a certain time. A typically applied load history and measured penetration depth for a creep test are shown in Figure 6.4a. The indentation creep coefficient C is normally defined as:

$$C\overset{def}{=}\frac{h(\tau_L+\tau_H)}{h(\tau_L)} \tag{6.3}$$

where the $h(\tau_L+\tau_H)$ is the penetration depth at the end of the holding phase with the constant load and $h(\tau_L)$ is the penetration depth at the end of the loading phase. In addition, in order to study the creep recovery, a second holding phase can be added (τ_{H2}). For simplicity, the percentage of creep recovery can be then defined as follows:

$$\chi\overset{def}{=}\frac{h(\tau_L+\tau_H+\tau_U+\tau_{H2})-h(\tau_L+\tau_H)}{h(\tau_L+\tau_H)-h_p(\tau_L)} \tag{6.4}$$

where $h_p(\tau_L)$ is the plastic penetration depth developed at the end of loading. Analogously, a relaxation test consists of applying a constant penetration depth, while measuring the relaxation of the load, as illustrated in Figure 6.5b. The relaxation coefficient can be then defined as follows:

$$R\overset{def}{=}\frac{P(\tau_L+\tau_H)-P(\tau_L)}{P(\tau_L)} \tag{6.5}$$

where $h(\tau_L+\tau_H)$ is the penetration depth at the end of the holding phase with the constant load and $h(\tau_L)$ is the penetration depth at the end of the loading phase.

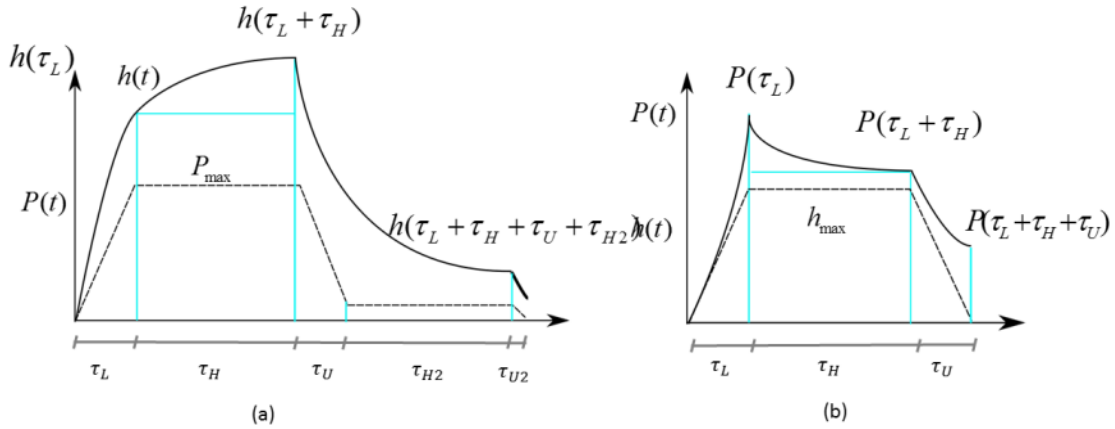

Figure 6.5 (a) Load and displacement vs. time of a creep indentation test with a holding phase at constant load; (b) Load and displacement vs. time of a relaxation indentation test with a holding phase at constant displacement.

6.3.3 Microindentation tests set up

As for the relaxation tests, the ASR products, the penetration depth was linearly increased up to the maximum penetration depth h_{max} of 2 μm in a period τ_L=5 seconds; then, the penetration depth was kept constant for τ_H=300 seconds, and then finally unloaded in τ_u =5 seconds. Similarly, the creep test was performed by applying a maximum load P_{max}=30mN in τ_L=5 seconds; then, the load was kept constant for τ_H=300 seconds, and then finally unloaded in τ_u =4.67 seconds. In order to assess the creep recovery, a second holding phase at P=2mN has been added with τ_H =150 seconds (see Figure 6.5a). The indentation test was performed using a 5 x 6 grid with an inter-distance of about 5 μm. When there was not enough room in the ASR veinlet, the indentation grid was adopted.

The microindenter was enclosed in a hermetic chamber to control the relative humidity (RH) and the carbon dioxide concentration (CO_2). The hermetic enclosure was connected in series with an Erlenmeyer flask containing a saturated salt solution and a pump in a closed loop system (Figure 6.6). A carbon dioxide absorber was also placed within the chamber to reduce the CO_2 content. The air was pumped continuously through the saturated salt solution within the hermetic system. The RH and CO_2 concentration were continuously monitored by two sensors within the chamber. By means of a saturated salt solution of

magnesium nitrate at 125.0g/100mL, a stable relative humidity of 55 ± 0.5% was achieved in the chamber. Additionally, a basin of liquid water allows reaching a stable relative humidity in the chamber of 95 ± 0.5%. The laboratory temperature was constant at 22℃ ± 0.5℃. Prior to microindentation testing, the specimen was left to equilibrate with the selected RH environment, i.e. 55% RH and 95% RH for a period of 24 hours, i.e. period over which the R.H. sensor indicated equilibrium in the chamber.

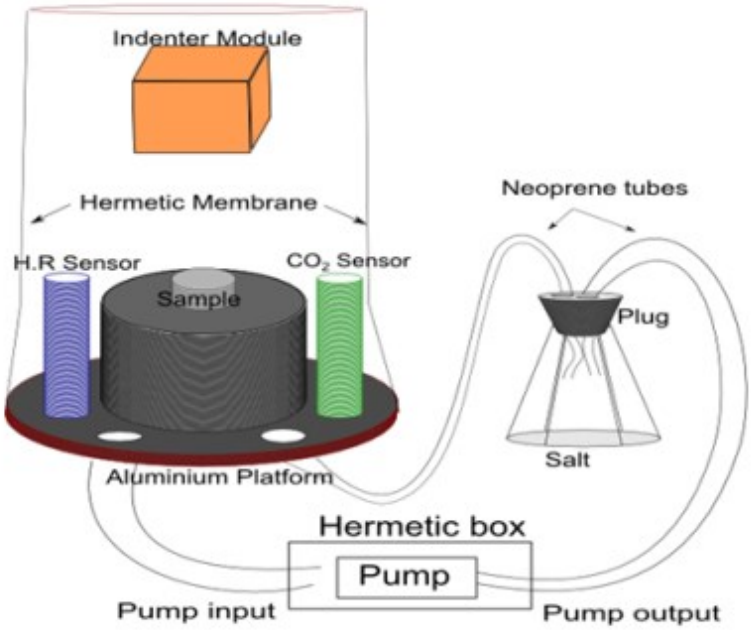

Figure 6.6 (a) The hermetic micro-indentation chamber for controlling the RH level (Frech-Baronet et al., 2016).

6.3.4 SEM-EDS tests

The sample subjected to indentation testing and illustrated in Figure 6.3, was further examined by scanning electron microscopy (SEM - JEOL JSM-840A) using secondary electron (SE) imaging and energy dispersive X-ray spectroscopy (EDS). Operating conditions were set at 15 kV. Prior to SEM observations, samples were gently dried for 24 hours at 50℃, and then coated with a thin layer of Au-Pd.

6.4 Experimental results and Discussion

6.4.1 SEM-EDS results

Typical images of the veinlet within the aggregate particle (left square on Figure 6.3a) and of the ASR products tested in this works, as observed by SEM-EDS, are illustrated in Figure 6.7a and 6.7b at two different magnifications. Indentation marks are visible in Figure 6.7b; also, since the sample was dried after the indentation measurements, for SEM analyses, shrinkage microcracks are visible in the reaction product. The SEM-EDS analysis of the product illustrated in Figure 6.7b is given in Figure 6.7c; it basically corresponds to that commonly reported for ASR rosette-like crystalline products.

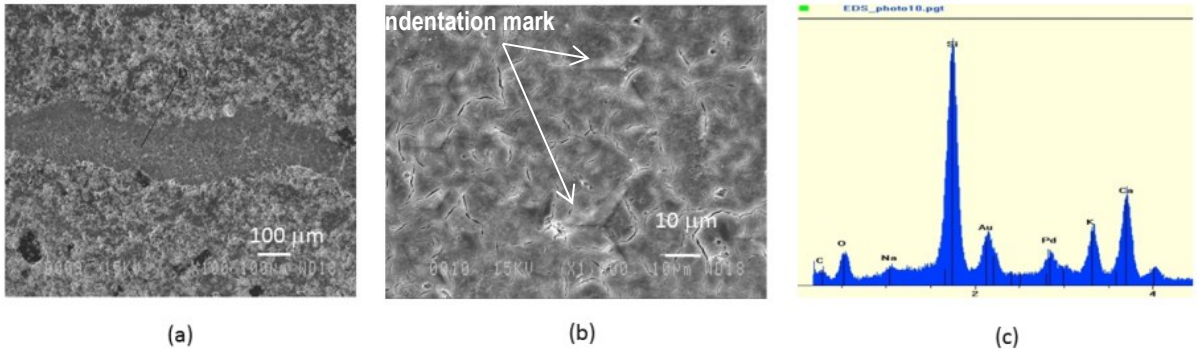

Figure 6.7 (a-b) SEM secondary electron images of the investigated zone (microcrack filled with secondary reaction product within a reactive siliceous limestone aggregate particle) at different magnification; (c) Typical SEM-EDS spectrum of the investigated product.

6.4.2 Micro-indentation on the reaction products within the crack of the aggregate particle

6.4.2.1 Relative humidity 55%

Figure 6.8 shows typical indentation grids performed in this study. The residual 5 x 6 indenter imprints are clearly visible on the micrograph. Note that the width of the veinlet within the aggregate particle is rather small, ranging between 50 and 100 µm in width. consequently, the indenter imprints are sometimes close to the aggregate interface. Considering that the volume probed by an indentation is about 5-10 times the indentation depth (Vandamme et al., 2012), it is expected that the indentation response may sometimes be affected by the

stiffer aggregate. Nevertheless, the measured time-dependent response can be attributed to the ASR product viscous behavior only.

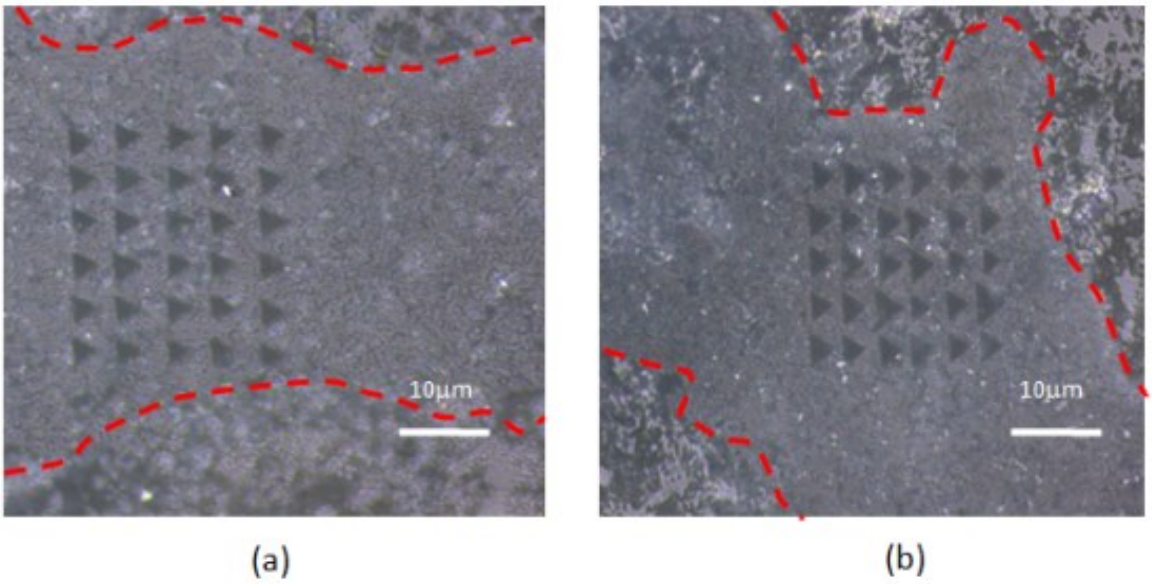

Figure 6.8 (a) Micrograph of indentation marks in creep test of ASR crystalline products in microcrack (veinlet) of the reactive aggregate particle under 55% RH; (b) Another location of indentation testing within the veinlet.

Figure 6.9a and 6.9b show the load-penetration curves (P-h) and the penetration depth-time curves (h-t), respectively, obtained for the creep tests. On the other hand, Figure 6.9c and 9d show the load-penetration curves (P-h) and the load-time curves (P-t), respectively, obtained for the relaxation tests. The mean curves appear as bold lines in the graphs. One can note that after unloading the residual deformation is rather significant, that is, most of the time-dependent deformation is not recoverable after unloading. The indentation properties of ASR crystalline reaction products at a relative humidity of 55% are summarized in Table 6.2. In the relaxation and creep tests, the penetration depth (h_{max}) and contact area (A_c) were similar as we choose a suitable load. The mean indentation modulus M is about 31-34 GPa for both tests, which is quite higher than previously measured values for ASR products (Leemann et al., 2013; Zhang et al., 2017). The indentation Vicker Hardness (Hv) was about 31 MPa and 25 MPa for creep and relaxation tests, respectively. Finally, the creep coefficient (C) was about 17% and the relaxation coefficient (R) about 40%.

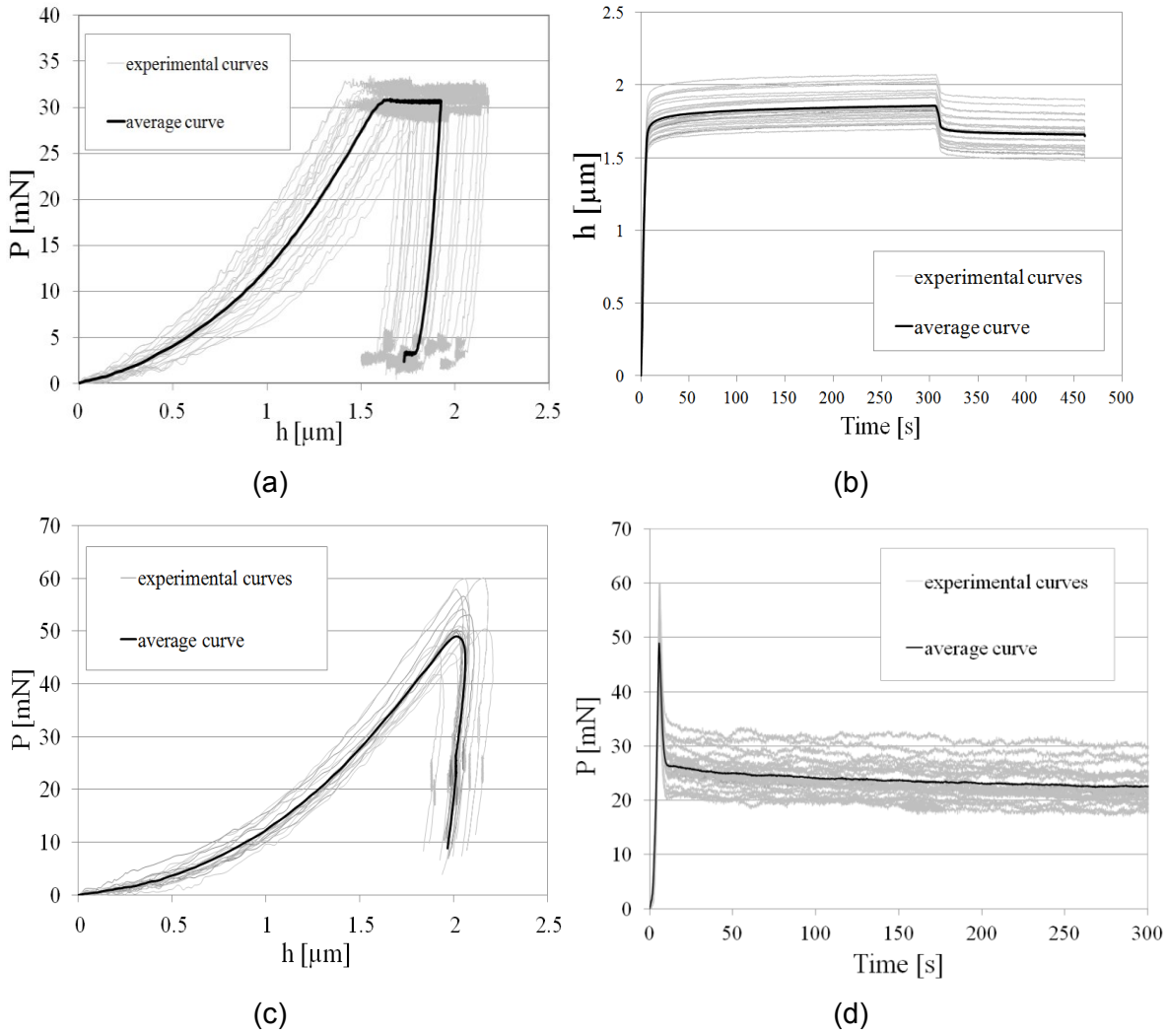

Figure 6.9 Results at RH=55% for creep tests: (a) P-h curves; (b) h-t curves. Results at RH=55% for relaxation tests: (c) P-h curves; (d) P-t curves.

Table 6.2 Indentation results for the creep tests at RH=55%.

	RH=55%	
Indentation parameter	Creep	Relaxation
h_{max} [μm]	1.85±0.10	2.01±0.06
P_{max} [mN]	30.30±1.3	28.07±4.0
A_c [μm^2]	90.1±10.3	104.8±4.0
H [MPa]	340.1±37.8	267.7±32.8
H_V [MPa]	31.4±3.5	24.8±3.0
M [GPa]	34.4±3.1	31.5±6.2
C [%]	17.2±2.6	n.a.
R [%]	n.a.	39.8±7.5

6.4.2.2 Relative humidity 95%

Figure 6.10 shows typical indentation grids performed on ASR products cured and tested at 95%. The width of the veinlets within the aggregate particle was sometimes so narrow that the indentation grid was carried out with an irregular shape.

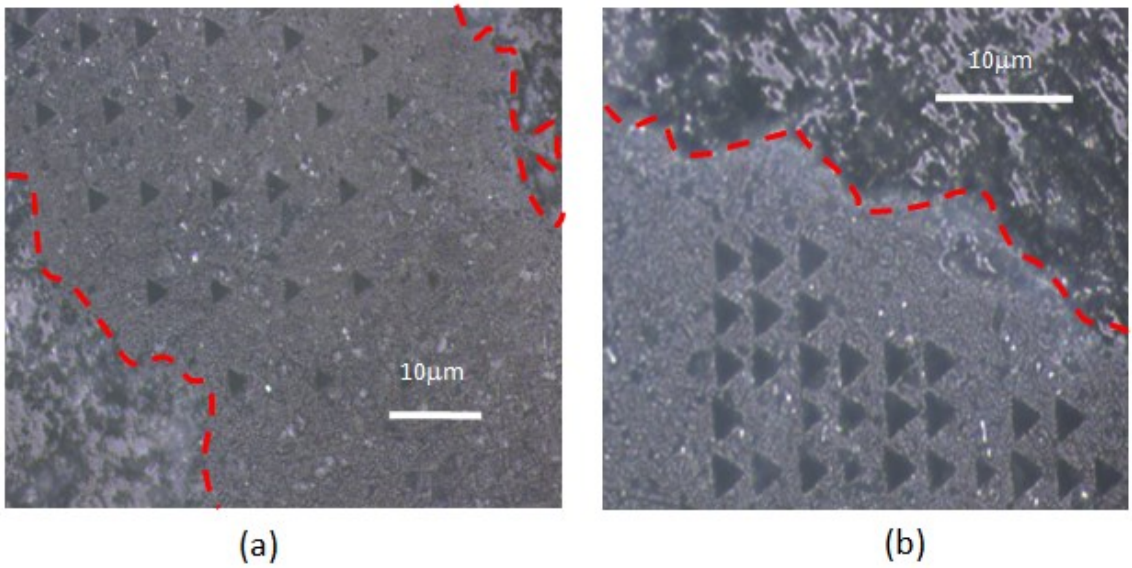

Figure 6.10 (a) Micrograph of indentation marks in creep test of ASR crystalline products in microcrack (veinlet) of the reactive aggregate particle under 95% RH; (b) Micrograph showing another test site.

As for the creep tests, Figures 6.11a and 6.11b show the load-penetration curves (P-h) and the penetration depth-time curves (h-t), respectively. As for the relaxation tests, Figure 6.11c and 6.11d show the load-penetration curves (P-h) and the load-time curves (P-t), respectively. The indentation properties of crystalline reaction products at a relative humidity of 95% are summarized in Table 6.3. In the relaxation and creep tests under the relative

humidity of 95%, the penetration depth (h_{max}) and contact area (A_c) were still similar. The mean indentation modulus M is about 31 GPa for both tests. The indentation Vicker Hardness (H_v) was about 29 MPa and 31 MPa for creep and relaxation tests, respectively. Finally, the creep coefficient (C) was about 24% and the relaxation coefficient (R) about 51%, which is higher than it in the relaxation tests under 55% relative humidity.

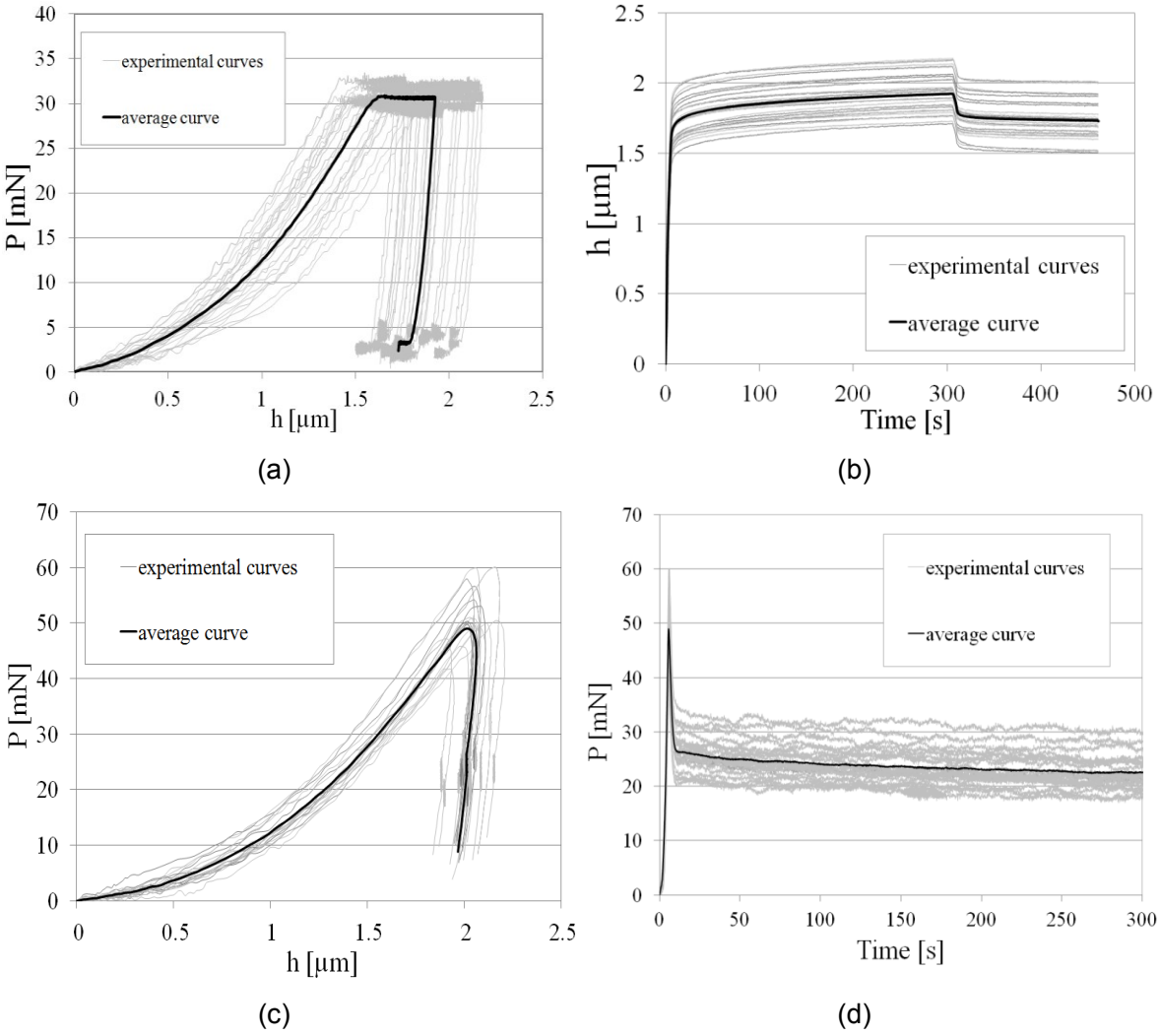

Figure 6.11 Results at RH=95% for creep tests: (a) P-h curves; (b) h-t curves. Results at RH=95% for relaxation tests: (a) P-h curves; (b) P-t curves.

Table 6.3 Indentation results for the creep tests at RH=95%.

	95%	
Indentation parameter	Creep	Relaxation
h_{max} [μm]	1.92±0.14	2.01±0.07
P_{max} [mN]	30.60±1.02	22.92±3.68
Ac [μm^2]	97.0±13.7	106.8±7.9
H [MPa]	321.2±43.8	267.7±32.9
H_V [MPa]	29.7±4.1	24.8±3.0
M [GPa]	31.2±3.1	31.5±6.2
C [%]	23.8±3.5	n.a
R [%]	n.a	50.7±4.7

6.4.3 Analysis and Discussion

As for simplified modeling of the behavior of ASR crystalline products during indentation testing, we analyzed the visco-elastic response of the above products by assuming a classical Burgers model (shown in Table 6.4), as done in a previous work (Zhang et al., 2017). The system is composed of a Kelvin-Voigt unit (E_2, η_2), which describes the reversible deformation (η_1), and a Maxwell unit (E_1, η_1), which describes the irreversible deformation (η_2). Ideally, reversible creep parameters (E_2, η_2) can be associated with the water movement (e.g., diffusion or absorption), while the irreversible creep parameters (E_1, η_1) can be associated to irreversible sliding between the "platelets" within ASR crystalline products. Usually, the variables $\tau_1=\eta_1/E_1$ and $\tau_2=\eta_2/E_2$ are defined as the characteristic time describing the irreversible and reversible part of the creep, respectively. That is, the material model can be alternatively described by the following 4 parameters: (η_1,$\tau_1=\eta_1/E_1$,η_2,$\tau_2=\eta_2/E_2$).

The macroscopic response of an indention test is calculated by integrating viscous model for the axial-symmetric configuration of a conical indenter following the work of (Vandamme et al., 2006). All the mathematical steps to estimate the h-t creep curves or the relaxation P-t by the material parameters (η_1,τ_1,η_2,τ_2) are presented in details in (Zhang et al., 2017). Furthermore, the creep test modeling requires estimating an additional model parameter, which is the plastic depth due to the plastic deformation at the end of the loading time $h_p(\tau_L)$. That is, the plastic deformation occurring during the fast loading period is disregarded in the viscous model.

As for RH=55%, Figure 6.12a and 6.12b show the comparison between the simulated and experimental curves for the relaxation and creep tests, respectively. Similarly, for RH=95%,

Figure 6.12c and 12d show the comparison between the simulated and experimental curves for the relaxation and creep tests, respectively. In spite of the simplified approach, the model well captures the relaxation and creep behavior measured by microindentation testing. Note that both creep and relaxation tests are modeled by the same parameters for each relative humidity (RH=55% and 95%). There is a slight overestimation of the creep curves at short time, but the rest of the curve slope, i.e., the creep rate, are well captured.

Table 6.4 shows the best fitting parameters for RH=55% and 95%. For sake of comparison, the model parameters of a previous work, which was limited to relaxation micro-indentation testing on a similar ASR crystalline products but at RH=30% (Zhang et al., 2017), are also reported. Note that the reversible creep parameters (η_2,τ_2) govern the initial part of the creep and relaxation as the characteristic time τ_2 is few seconds, while the irreversible creep parameters (η_1,τ_1) govern the initial part of the creep and relaxation as the characteristic time τ_1 is much greater.

Table 6.4 Left side: Simplified rheological viscous-elastic model employed in this study. Right side: Model parameters for best-fitting both creep and relaxation curves for the cases RH=55% and RH=95%.(RH=30% are obtained after Zhang et al., 2017).*

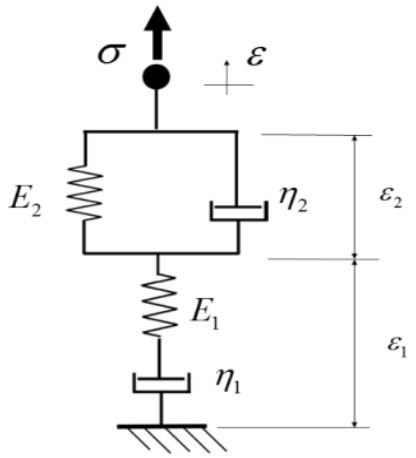

	Relative humidity		
Model parameter	30%(*)	55%	95%
η_1 [MPa/s]	154000(*)	105000	35000
τ_1 [sec]	10769(*)	3354	1118
η_2 [MPa/s]	193(*)	135	179
τ_2 [sec]	7.5(*)	3.3	5.2
$h_p(\tau_L)$	n.a.	0.85	0.84

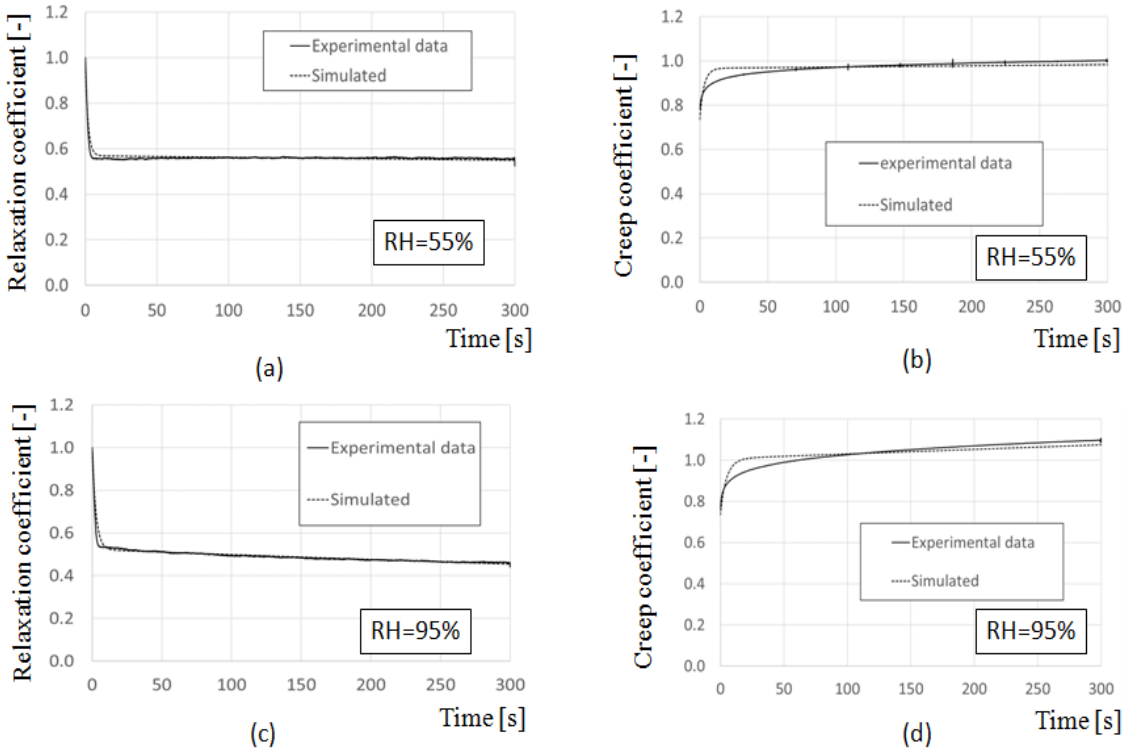

Figure 6.12 Comparison between experimental and simulated curves for (a) relaxation test at RH=55%; (b) creep test at RH=55%; (c) relaxation test at RH=95%; (d) creep test at RH=95%.

The present results suggest that the relative humidity has an evident impact on the apparent viscosity of ASR crystalline products as measured by microindentation. The major effect of the relative humidity on the creep and relaxation curves (Figure 6.12) is visible at the end of the test (~300 seconds), which is governed by the viscosity η_1 and τ_1 of the irreversible creep and creep curves. Figure 6.13a shows the estimated η_1 (eta_1) and τ_1 as a function of the relative humidity for RH=55% and 95%; the values obtained by Zhang et al. (2017) in a previous work for RH=30% are included in the graph. Evidently, the effect of changes in RH during testing is to reduce the viscosity rate (i.e., the slope of the creep and relaxation curves in function of time of Figure 6.12) by a factor of about 5 by passing from RH=30% to RH=95%. The effect on the characteristic time (τ_1) is also similar, i.e., high RH reduces the characteristic time of a factor of about 5. Again, the effect of high relative humidity is to increase irreversible creep. That suggests that water content favors sliding mechanisms at the interfaces between the "platelets" within the ASR crystalline product. Katayama (2012a) recently presented the results of the analyses of ASR gel and crystalline rosettes. The author mentioned that they correspond to universal products of ASR, Alkali-Carbonate Reaction

(ACR) and the alkali-silicate reaction of silica minerals. Based on his chemical analyses, Katayama indicated that the rosette crystals constitute solid solutions between mountainite [$Ca_2Na_2KSi_8O_{19.5}6.5H_2O$] and shlykovite [$(K,Na)_2Ca_2Si_8O_{19}7H_2O$], possibly extending to cryptophyllite [$(K,Na)_4Ca_2Si_8O_{20}10H_2O$] and rhodesite [$KCa_2Si_8O_{18.5}6.5H_2O$], or a mixed layer of a wider range of products. Despite the fact that the author mentioned that the understanding of the compositional characteristics of those products will need further study, the above results confirm the critical importance of the H_2O in the composition of those products, thus their dependency to RH/moisture conditions during microanalytical investigations. As pointed out by Leemann et al. (2016), the origin and exact contribution of the above crystalline product to expansive forces/stress generation during the development of ASR still remain largely unknown.

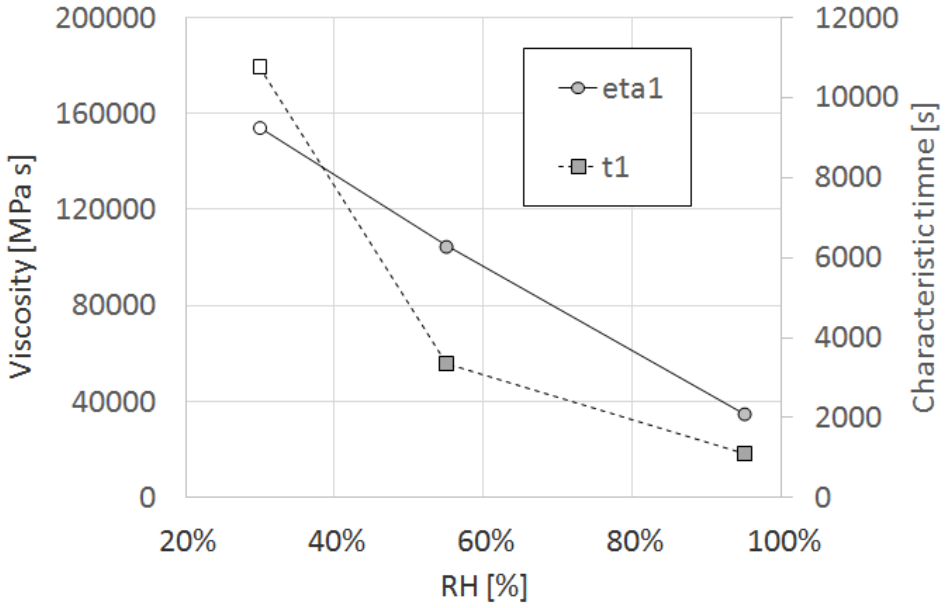

Figure 6.13 Comparison between the viscosity (η_1) and characteristic time (τ_1) of the irreversible Maxwell device for different RH levels (the data for RH=30% come from Zhang et al., 2017)

Finally, one can estimate the creep recovery by comparing the deformation at the end of the holding phase at the maximum load (P_{max}) with the residual deformation after unloading. Interestingly, the creep recovery varies from 20%±2% to 18%±3% by increasing the RH from 55% to 95%. That is, the creep recovery of ASR crystalline products time-dependent deformation is very limited and it is also slightly reduced by a change of RH. The sliding between ASR crystal interfaces during the indentation testing may be a possible mechanism of such irreversible creep deformation.

6.5 Conclusions

The present results provide new insights on the rheological property of ASR crystalline products within cracks formed in alkali-silica reactive aggregates from field damaged concrete. Based on the present results, the following conclusions can be drawn:

1) Microindentation technique appears a promising tool to characterize the apparent viscosity of in-situ ASR products.

2) The apparent viscosity of ASR crystalline products seems composed by a short term reversible part and a long-term irreversible one, which was well described by a classical viscous Burger model;

3) Increasing the RH level from 30% to 95% reduce the apparent viscosity of ASR crystalline products (η_1) of a factor of about 5. That is, the higher RH conditions or water content could favor the sliding of ASR crystal products along lubrificated micro-cracks under high pressure. Contrarely η_2 viscosity is less affected by RH;

4) The creep deformation of ASR crystalline products under pressure is mostly irreversible. A higher RH level seems to increase the irreversibility of the creep deformation. The irreversible sliding between the platelets of ASR crystalline products seems a possible mechanism for the observed time-dependent deformations.

Further studies are needed to investigate the different composition of ASR products, especially the ASR massive gel, which can be found towards the edge of microcracks within reactive aggregate particles, as well as within the cracks extending into the cement paste from the aggregate cracking. Moreover, the advanced analysis is required to relate the apparent viscosity to the rheological property of the ASR products.

Acknowledgements

Authors would like to thank Mr. Andre Ferland in the assistance of the SEM/EDS equipment. The financial support to the first Author from China Scholarship Council (CSC) is greatly appreciated.

References

Alnaggar, M., Cusatis, G., & Di Luzio, G. (2013). Lattice discrete particle modeling (LDPM) of alkali-silica reaction (ASR) deterioration of concrete structures. Cement and Concrete Composites 41:45–59.

Bérubé, M.-A., & Fournier, B. (1986). Les produits de la reaction alcalis-silice dans le beton; etude de cas de la region de Québec. The Canadian Mineralogist 24:271–288.

Bérubé, M.-A., Durand, B., Vézina, D., & Fournier, B. (2000). Alkali-aggregate reactivity in Québec (Canada). Canadian Journal of Civil Engineering 27:226–245.

Bokern, J., & Eberhard, S. (2004). "Alkali-silica reaction in Germany–Transfer of laboratory results to practice." In *12th International Conference on AAR in Concrete*, Beijing, China, 490-498.

Charlwood, R.G., & Sims, I. (2016). Expansive chemical reactions in dams and hydroelectric projects. *Proceedings of the Institution of Civil Engineers-Construction Materials*, 169(4):197-205.

Dunant, C.F., & Scrivener, K.L. (2010). Micromechanical modeling of alkali–silica-reaction-induced degradation using the AMIE framework. Cement and Concrete research 40:517–525.

Dunant, C.F., & Scrivener, K.L. (2016). Physically based models to study the alkali–silica reaction. Proceedings of the Institution of Civil Engineers: Construction Materials (Part 1 of a themed issue on AAR), 169 (CM4): 136-144.

Fischer-Cripps, A.C. (2011). Nanoindentation testing, in: Nanoindentation. Springer New York, 21–37.

Folliard, K.J., Thomas, M.D., Fournier, B., Drimalas, T., & Ahlstrom, G. (2016). Mitigation of alkali–silica reaction in US highway concrete. *Proceedings of the Institution of Civil Engineers-Construction Materials*. (Part 2 of a themed issue on AAR), 169 (CM4): 215–222.

Fournier, B., & Bérubé, M.-A. (1991). Évaluation du potentiel de réactivité alcaline des granulats à béton produits dans les Basses-Terres du Saint-Laurent du Québec (Canada). Canadian Journal of Civil Engineering 18:282–296.

Fournier, B., & Bérubé, M.-A. (2000). Alkali-aggregate reaction in concrete: a review of basic concepts and engineering implications. Canadian Journal of Civil Engineering 27:167–191.

Frech-Baronet, J., Sorelli, L., & Charron, J.-P. (2016). New evidences on the effect of the internal relative humidity on the creep and relaxation behaviour of a cement paste by micro-indentation techniques. Cement and Concrete Research.

Galin, L.A., Moss, H., & Sneddon, I.N. (1961). Contact problems in the theory of elasticity. DTIC Document.

Giorla, A.B., Scrivener, K.L., & Dunant, C.F. (2015). Influence of visco-elasticity on the stress development induced by alkali–silica reaction. Cement and Concrete Research 70:1–8.

Godart, B., de Rooij, M., & Wood, J.G. (2013). Reporting, in: Guide to Diagnosis and Appraisal of AAR Damage to Concrete in Structures. Springer, 79–81.

Guédon-Dubied J.S., Cadoret, G., Durieux, V., Martineau, F., Fasseu, P., & Van Overbecke, V. (2000): Study on Tournai limestone in Antoing Cimescaut Quarry. Petrological,

chemical and alkali reactivity approach. In: Bérubé MA, Fournier B, Durand B (eds): Proceedings of the 11th ICAAR, Québec/CA: 335-344.

Haha, M.B., Gallucci, E., Guidoum, A., & Scrivener, K.L. (2007). Relation of expansion due to alkali-silica reaction to the degree of reaction measured by SEM image analysis. Cement and Concrete Research 37:1206–1214.

Katayama, T. (2012a). ASR gels and their crystalline phases in concrete—universal products in alkali–silica, alkali–silicate and alkali–carbonate reactions, In *Proceedings of the 14th International Conference on Alkali-Aggregate Reactions* (ICAAR), Austin, Texas. 20–25.

Katayama, T. (2012b) Petrographic Study of the Alkali–Aggregate Reactions in Concrete. Doctoral thesis (Science), Department of Earth and Planetary Science, Graduate School of Science, University of Tokyo, Japan.

Kawamura, M. (1998). The composition of ASR gels and expansion of mortars. In Materials Science of Concrete-Special Volume: The Sidney Diamond Symposium. American Ceramic Society. 261-276.

Kawamura, M., & Iwahori, K. (2004). ASR gel composition and expansive pressure in mortars under restraint. Cement and concrete composites 26:47–56.

Kawamura, M., Noriyuki, A., & Terashima, T. (1998). Mechanisms of suppression of ASR expansion by fly ash from the viewpoint of the gel composition. Materials Science of Concrete.

Krogh, H. (1975). Examination of synthetic alkali–silica gels. In Proceedings of Symposium on Alkali–Aggregate Reaction. Icelandic Building Research Institute, Reykjavik, Iceland, 133–163.

Larive, C., Laplaud, A., & Coussy, O. (2000). The role of water in alkali–silica reaction, *11th ICAAR, International Conference on Alkali Aggregate Reactions*, Québec.

Larive, C., & Louarn, N. (1992). Diagnosis of alkali-aggregate reaction and sulphate reaction in French structures, *Proceedings 9th International Conference on Alkali-Aggregate Reactions*. Concrete Society, 587–598.

Leemann, A., & Lura, P. (2013). E-modulus of the alkali–silica-reaction product determined by micro-indentation. Construction and Building Materials 44:221–227.

Leemann, A., Katayama, T., Fernandes, I., & Broekmans, M.A.T.M. (2016). Types of alkali aggregate reactions and the products formed. Proceedings of the Institution of Civil Engineers: Construction Materials (Part 1 of a themed issue on AAR), 169 (CM4): 128-135.

Multon, S., & Sellier, A. (2016). Multi-scale analysis of alkali–silica reaction (ASR): Impact of alkali leaching on scale effects affecting expansion tests. Cement and Concrete Research 81:122–133.

Multon, S., & Toutlemonde, F. (2010). Effect of moisture conditions and transfers on alkali-silica reaction damaged structures. Cement and Concrete Research 40:924–934.

Multon, S., Sellier, A., & Cyr, M. (2009). Chemo–mechanical modeling for prediction of alkali-silica reaction (ASR) expansion. Cement and Concrete Research 39: 490–500.

Oliver, W.C., & Pharr, G.M. (1992). An improved technique for determining hardness and elastic modulus using load and displacement sensing indentation experiments. Journal of materials research 7:1564–1583.

Pacheco-Torgal, F., Castro-Gomes, J., & Jalali, S. (2008). Alkali-activated binders: A review: Part 1. Historical background, terminology, reaction mechanisms and hydration products. Construction and Building Materials 22:1305–1314.

Pan, J.W., Feng, Y.T., Wang, J.T., Sun, Q.C., Zhang, C.H., & Owen, D.R.J. (2012). Modeling of alkali-silica reaction in concrete: a review. Frontiers of Structural and Civil Engineering 6:1–18.

Powers, T.C., & Steinour, H.H. (1955). An interpretation of some published researches on alkali-aggregate reaction. Part 2. A hypothesis concerning safe and unsafe reaction with reactive silica in concrete. Journal of American Concrete Institute 26:785–811.

Prezzi, M., Monteiro, P.J.M., & Sposito, G. (1997). The alkali–silica reaction, part I: use of the double-layer theory to explain the behavior of reaction-product gels. ACI Materials Journal 94(1):10–16.

Rajabipour, F., Giannini, E., Dunant, C., Ideker, J.H., & Thomas, M.D.A. (2015). Alkali–silica reaction: Current understanding of the reaction mechanisms and the knowledge gaps. Cement and Concrete Research 76:130-146.

Rodrigues, F.A., Monteiro, P.J.M., & Sposito, G. (2001). The alkali–silica reaction. The effect of monovalent and bivalent cations on the surface charge of opal. Cement and Concrete Research 31(11):1549–1552.

Sanchez, L.F.M., Fournier, B., Jolin, M., & Duchesne, J. (2015). Reliable quantification of AAR damage through assessment of the Damage Rating Index (DRI). Cement and Concrete Research 67:74–92.

Saouma, V.E. (2014). Numerical modeling of AAR. CRC press, February, 5.

Schlangen, H., & Copuroglu, O. (2010). Modeling of expansion and cracking due to ASR with a 3D lattice model, in FraMCos-7: *Proceedings of the 7th International Conference on Fracture Mechanics of Concrete and Concrete Structures*, Jeju Island, Korea, May, 23-28.

Seignol, J.F., & Godart, B. (2012). A collective effort to propose practical guidance on the use of numerical models to re-assess AAR-affected structures, *14th International Conference on AAR in Concrete*. Texas (USA): Austin.

Struble, L.J., & Diamond, S. (1981). Swelling properties of synthetic alkali silica gels, J. Am. Ceram. Soc. 64 (11), 652–655.

Swamy, R.N. (2002). The alkali-silica reaction in concrete. CRC Press, 28.

Ulm, F.-J., Coussy, O., Kefei, L., & Larive, C. (2000). Thermo-chemo-mechanics of ASR expansion in concrete structures. Journal of engineering mechanics 126:233–242.

Vandamme, M., & Ulm, F.-J. (2006). Viscoelastic solutions for conical indentation. International Journal of solids and structures 43:3142–3165.

Vandamme, M., Tweedie, C.A., Constantinides, G., Ulm, F.-J., & Van Vliet, K.J. (2012). Quantifying plasticity-independent creep compliance and relaxation of viscoelastoplastic materials under contact loading. Journal of Materials Research 27: 302–312.

Vayghan, A.G., Rajabipour, F., & Rosenberger, J.L. (2016). Composition–rheology relationships in alkali–silica reaction gels and the impact on the Gel's deleterious behavior. Cement and Concrete Research 83: 45–56.

Wang, S.-D., Pu, X.-C., Scrivener, K.L., & Pratt, P.L. (1995). Alkali-activated slag cement and concrete: a review of properties and problems. Advances in cement research 7: 93–102.

Wieker, W., Hubert, C., Heidemann, D., & Ebert, R. (1998) Alkali–aggregate reaction – a problem of the insufficient fundamental knowledge of its chemical base. In *Proceedings of Sidney Diamond Symposium on Materials Science and Engineering of Concrete and Cement-Based Composites* (Cohen M, Mindess S and Skalny J (eds)). Materials Science of Concrete, American Ceramic Society, Westerville, OH, USA. 395–408.

Zhang, C., Sorelli, L., Fournier, B., Bastien, J., Duchesne, J., & Chen, Z. (2017). Creep and Relaxation Behaviour of Alkali-Silica Reaction Products with Rosette-like Structure by Micro-indentation: Characterization and Simplified Modeling. Construction and Building Materials (accepted with minor corrections).

7. Discussion

7.1 Summary of test results and main findings

The presented research findings have brought new insights on the viscous-elastic properties of ASR products and the fracture toughness of alkali-silica reactive limestone aggregates. For the first time, the apparent viscosity of ASR crystalline products has been characterized by micro-indentation techniques.

In spite of the previous work which has attempted to measure the viscosity rheological properties of ASR gels (Figure 7.5d), very limited results are available today on the rheological properties of ASR products in the open literature (Vayghan et al., 2016). The rheological properties of ASR products may play a critical role in the build-up of internal stress needed to damage the reactive aggregate particles (Vayghan et al., 2016).

After having statistically characterized the viscous behavior of ASR crystalline products in microcracks of reactive limestone aggregate particles (specimens from a heavily ASR-affected concrete pavement) by micro-indentation (Figure 7.1), a simplified model has allowed distinguishing the reversible and irreversible parts of the viscous-elastic behavior of ASR crystalline products. Figure 7.2a and 7.2b show the estimated reversible and irreversible viscosity and characteristic time, respectively, which best fit the experimental results presented in Chapters 4 and 6. The major effect of the relative humidity is to reduce the irreversible viscosity (η_2), which governs the deformation rate at the longer characteristic time.

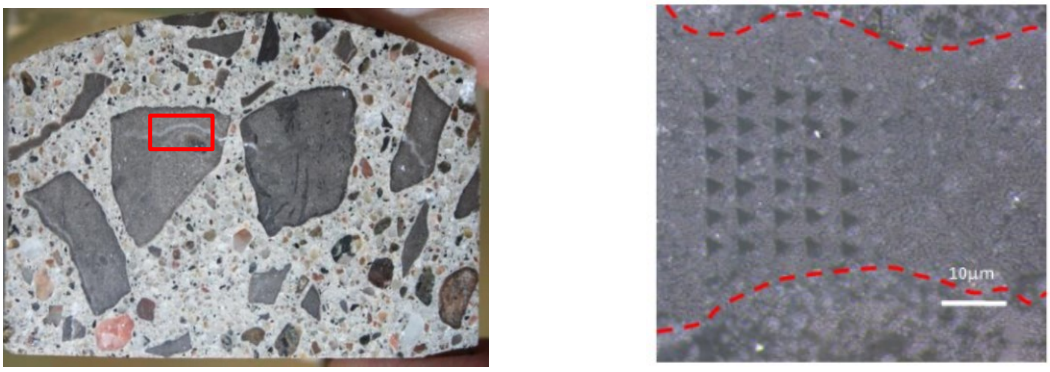

(a) (b)

Figure7.1 Picture of the polished concrete specimen. (a) Used for micro-indentation testing; (b) An illustration of the zone used for micro-indentation testing (rectangular window in (a)).

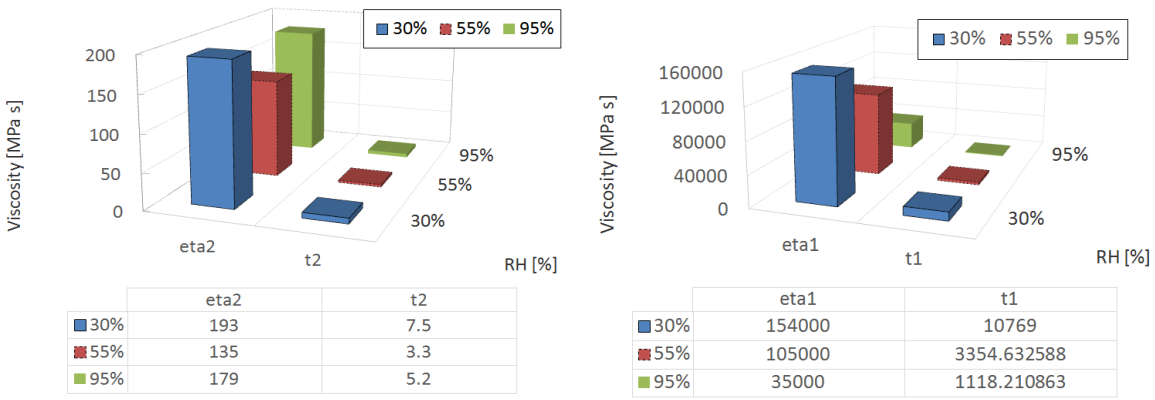

	eta2	t2
30%	193	7.5
55%	135	3.3
95%	179	5.2

(a)

	eta1	t1
30%	154000	10769
55%	105000	3354.632588
95%	35000	1118.210863

(b)

Figure 7.2 (a) Histograms for the viscous parameter of the (a) reversible part and irreversible part (b) as best fit by the proposed simplified model.

Moreover, this research has applied a novel micro-scratch technique to measure the toughness (i.e., the cracking resistance) of reactive aggregate particles in ASR-affected concrete specimens. Micro-scratch testing was carried out parallel and perpendicular to the bedding direction/plane in virgin (unreacted from a local quarry) and “reacted” limestone aggregate particles; also, some particles were showing zoning/discoloration to light-grey color surrounding the microcracks filled with ASR products, which suggested “reacted” zones within the particles (Figure 7.3). Electron probe microanalyses revealed that the dark-grey areas are mainly composed of calcium carbonate micrograins (calcite; a mineral of low-hardness - 3 on the Mohs scale). On the other hand, the light-grey zone is composed of a mixture of calcite, clay minerals and possibly silica, which could reveal a somewhat higher hardness compared to the adjacent calcite-rich layers. Figure 7.4 shows the mean toughness values of different reactive aggregates by considering scratch lines parallel and perpendicular to the bedding plane. The results obtained on the virgin limestone (N18) are also given. The presented results showed that the observed decolored light grey zones close to the major cracks filled by ASR products have somewhat similar toughness values compared to the dark-grey zones of the particles. Also, those values are similar to that obtained for the virgin (“unreacted”) limestone. This suggests that (1), testing performed parallel or perpendicular to the bedding plane did not result in significant differences in fracture toughness, which might be explained by the very fine-grained nature of that reactive limestone, and (2) the damage occurring in the reactive aggregate particles is mainly localized in the crack filled by ASR products, rather than affecting the overall aggregate particles, which was “suggested” by the light-grey color/zoning within the particles.

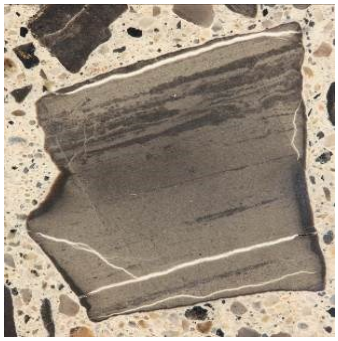

Figure 7.3 Plane polished section prepared from a concrete core extracted from the foundation block of a heavily ASR-affected highway bridge, and showing an aggregate particle with white veinlets (i.e. crack filled with secondary ASR products). The original color of the fine-grained limestone is dark-grey but discoloration to light-grey is largely observed within the particle. Also, the bedding plane in the particle appears parallel to the main orientation of the white veinlets.

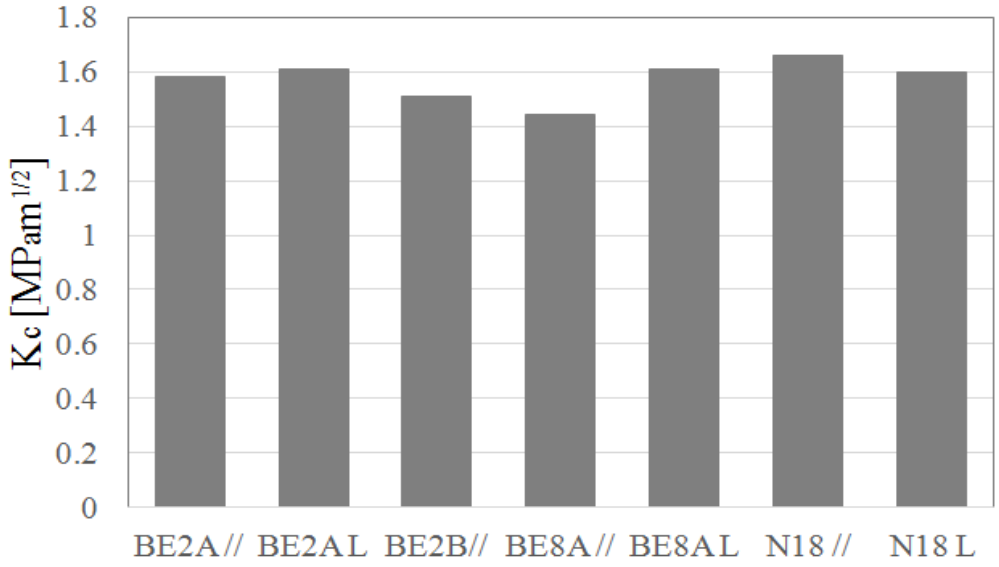

Figure 7.4 Micro-scratch testing results in limestone aggregate parallel and in directions parallel and perpendicular to bedding. For samples BE2A and BE2B, the testing was performed in light-grey zones. For sample BE8A, the testing was performed in dark-grey zones. The N18 sample corresponds to a polished virgin limestone sample collected from a local quarry.

Therefore, how can the new knowledge on the gel viscosity and the damage properties of the reactive aggregates be employed in engineering macroscopic models?

Based on the present results, the following section aims at (i) proposing a simplified interpretation of the effect of the viscous-elastic property of the ASR products on the damage of the reactive aggregate particles, and (ii) to suggest a preliminary/new micro-to-micro model for future developments.

7.2 Simplified model for build-up pressure

Figure 7.5 shows typical ASR products which have induced damage within reactive aggregate particles. One can note that ASR products have filled the larger cracks of the particles, but the surrounding sub-micrometer cracks seem still empty. Also, cracks filled with ASR products are generally much larger in the aggregate particles than their extension into the cement paste. Thus, it is suggested that the concrete damage induced by ASR is not only controlled by the free swelling capacity of the ASR products, but also by the capacity of those products to flow into adjacent capillary pores and microcracks within the surrounding cement paste. Such flow would likely relieve the internal pressure build-up, which is responsible for damaging the reactive aggregate particles. High viscosity ASR products are likely inducing large stresses and are probably the most deleterious; on the other hand, reaction products that are less viscuous and thus can flow readily may not result in high stress build-up / expansive character. This point underlines the significance of rheological properties of ASR products in the stress build-up, which is damaging reactive aggregates and subsequently the extension of cracking into the surrounding cement paste.

As first approach, one could consider a classical Darcy's permeation law to describe the pressure build-up, which is schematically shown in Figure 7.6. Based on a simple Darcy's law the permeation flow (w) reads:

$$w = \frac{K}{v^{fl}} \frac{dP}{dx} \tag{7.1}$$

where the $v^{fl} = \eta^{fl} / \rho^{fl}$ is the kinetic viscosity which depends on the dynamic viscosity and the density, and K is the permeability which depends on the tortuosity and porosity distribution (Coussy, 2011). That is, the build-up of the hydraulic pressure P generated by the restrained expansion of the ASR products will relax depending on the viscosity of the fluid, i.e., $dP/dx = w\, v^{fl} / K$. The stress build-up is a result of competing mechanisms between the confining stress of the ASR expansion $\Delta V(t)$, which depends on the compressibility modulus of the fluid, and the stress relaxation due to the capacity of ASR products to permeate surrounding micro-cracks and cavities. Interestingly, in this work, we have estimated the aggregate toughness, which somehow describes the resistance capacity of the aggregate to withstand such pressure without cracking. This simple explanation suggests future model developments which can account for the ASR products viscosity and

aggregate toughness which have been firstly characterized by novel techniques in this research. A viscous and expansive ASR product will favor aggregate cracking first, and micro-cracking in the surrounding cement paste later.

The ASR products' viscosity may play a role in the formation of the internal pressure, but also in the reaction kinetics under confinement condition, and the rate of migration of ASR products. Finally, the toughness of the reactive aggregate particle will decide the cracking onset of the aggregate under internal pressure.

More in general, water and absorbed metal ions (such as Calcium ions: Ca^{2+}, Potassium $K^{+,}$ and Sodium Na^{+}) may change the rheological property of ASR products and, then, affect the damage mechanisms aforementioned.

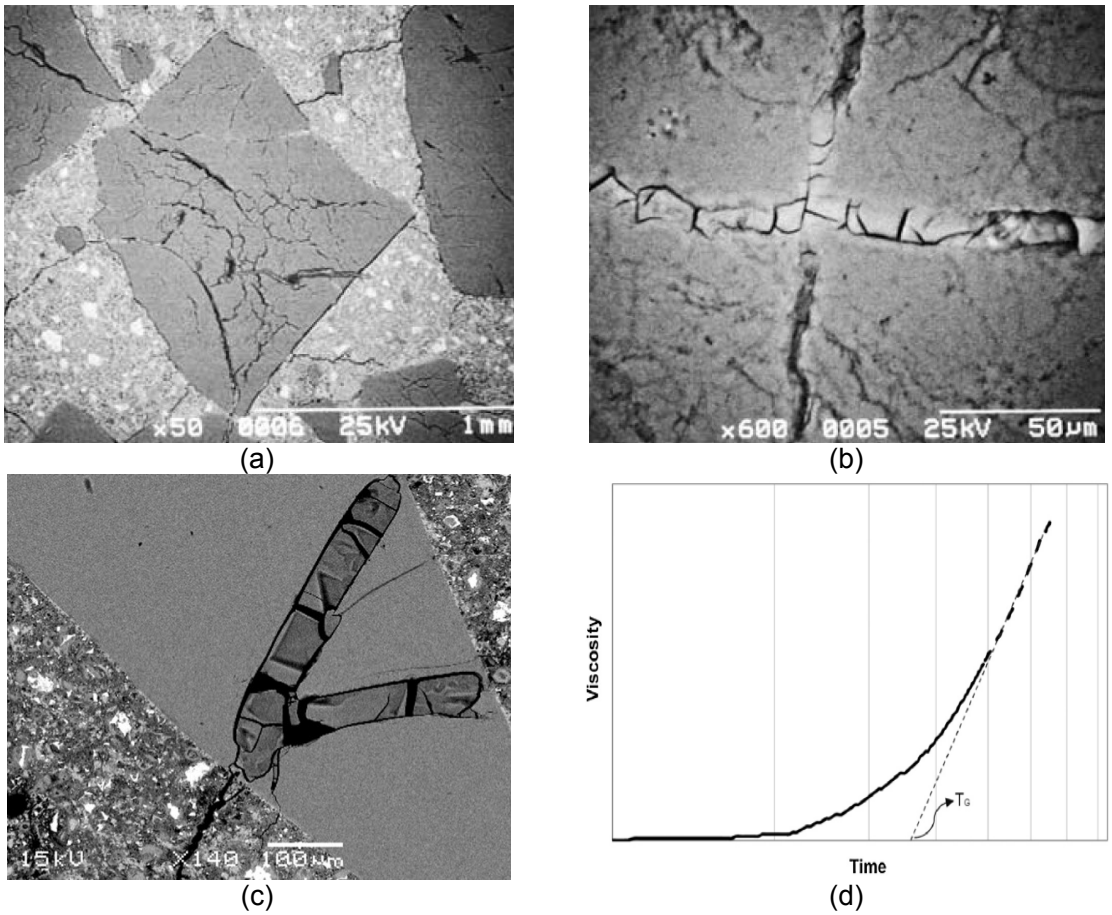

Figure 7.5 (a-b) Figures of ASR products within damage aggregate particles in concrete (Kawamura et al., 2004); (c) Another example of ASR products within an aggregate particle in concrete (Vayghan et al., 2016); (d) Typical viscosity development time series of the alkali silicate gels used for determining the gelation time (Vayghan et al., 2016).

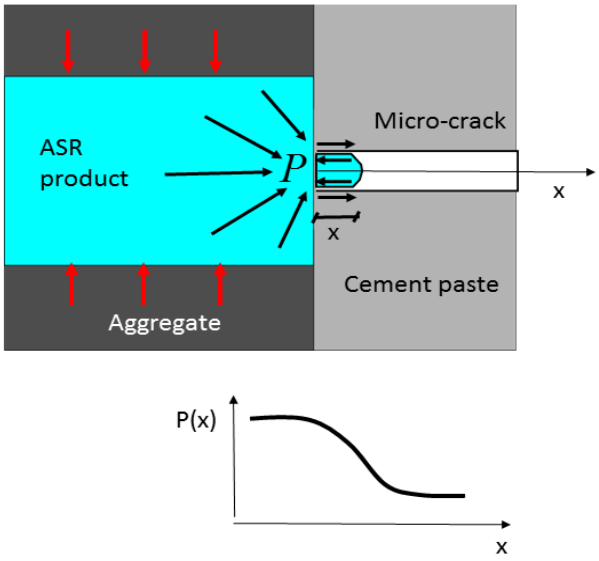

Figure 7.6 Schematic representation of the pressure head driving possible ASR permeation through a close microcrack channel.

7.3 Suggestions for a new micro-to-macro model

Although outside the scope of this thesis, this section suggests a simplified macroscopic model which can account for the new data obtained in this research for predicting the overall behavior of the ASR-damaged concrete observed at the macro-scale. The scope of this section is thus to suggest a simple "1D thought model" for future developments, which could consider the ASR product viscosity and the reactive aggregate toughness.

As presented in Chapter 2, the model proposed by Ulm et al. (2000) (shown in Figure 7.7), is here extended. Ulm's simplified model accounts for the ASR free expansion based on two characteristic times: (a) a latency time associated with the dissolution of reactive silica; (b) a characteristic time associated with the ASR product formation (Larive et al., 1992). When this ASR expansion is restrained, a local pressure builds-up within the reactive aggregate particle and the surrounding cement paste.

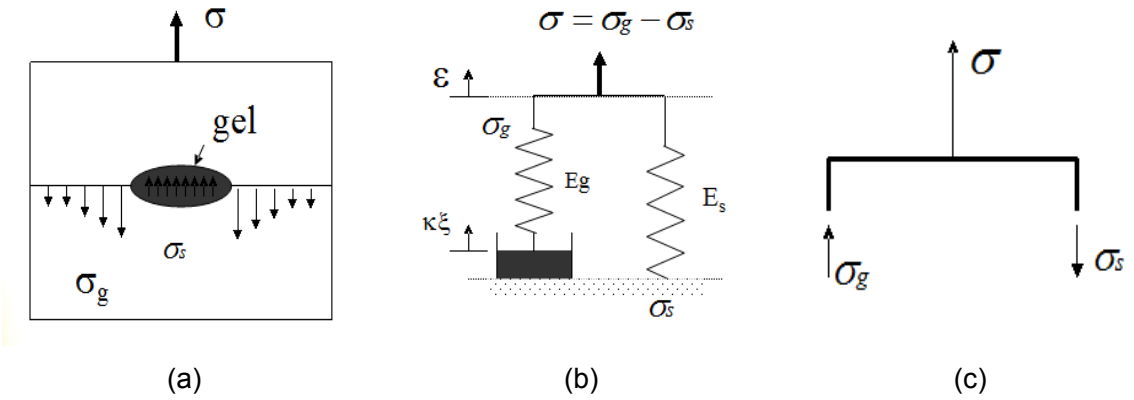

Figure 7.7 (a) The concrete unit containing the expansive gel; (b) 1D thought model; (c) Force equilibrium (Ulm et al., 2000).

Under stress-free conditions, the internal swelling pressure σ_g of the expansive products is equilibrated by the tension in the cement matrix. This simple model is able to capture the expansive material behavior at a macro level. Figure 7.7b shows the idealized 1D though model proposed by Ulm et al. (2000). In this figure, σ_s is the macroscopic stress due to external forces, and ε is the corresponding overall strain. The stress in the elastic spring of stiffness E_s is denoted by $\sigma_s = E_s\varepsilon$, and swelling pressure in the chemical pressure cell is denoted by $\sigma_g = E_g\varepsilon$. Let ξ be the extent of this chemical reaction and assume that the volume increase of the ASR products is proportional to the reaction extent. Neglecting free expansion space in which the products can freely expand, the force equivalence is:

$$\sigma = \sigma_g - \sigma_s = E_s\varepsilon + E_g(\varepsilon - \kappa\xi) \tag{7.2}$$

The overall stress is proportional to reaction extent with chemical coefficient:

$$\varepsilon = \frac{\kappa E_g}{E_g + E_s}\xi = \beta\xi \tag{7.3}$$

where E_g is the E-Modulus of ASR product, E_s is the E-Modulus of cement paste, κ: intrinsic dilation coefficient of the reaction, β is the chemical expanding coefficient. In a simplified ASR model, the reaction affinity, A_m, is a function of reaction extent and governs the reaction rate. The affinity $A_m(\xi)$ decreases progressively from an initial value $A_m(\xi = 0) = A_m$,0 which starts the reaction, to equilibrium $A_m(\xi = 1) = 0$, at which the reaction stops (i.e., = 0). For simplicity, a kinetics linear law is applied:

$$A_m(\xi) = k_d \dot{\xi} = k_d \frac{d\xi}{dt} \tag{7.4}$$

By considering a linear affinity law $A_m(\xi)$, the previous equation reads,

$$1 - \xi = t_c(\theta, \xi) \frac{d\xi}{dt} \tag{7.5}$$

The characteristic time t_c can be determined from a stress-free expansion tests carried out at a different constant temperature (Ulm et al., 2000), and it has also been found to depend on both temperature θ_0 and reaction extent ξ. As the first approach, one can utilize Larive's coefficient λ to describe the ASR free expansion (Larive et al., 1998) as follows:

$$t_c = \tau_c(\theta_0) \cdot \lambda(\xi, \theta_0) \tag{7.6}$$

$$\lambda(\xi, \theta_0) = \frac{1 + e^{-t_l(\theta_0)/t_c(\theta_0)}}{\xi + e^{-t_l(\theta_0)/t_c(\theta_0)}} \tag{7.7}$$

Substituting (7.7) and (7.6) into (7.5), the equation below is achieved:

$$\dot{\xi} = \frac{\xi}{\tau_c} \cdot \frac{-}{\lambda} \Rightarrow \dot{\xi} = \frac{\xi}{\tau_c} \cdot \frac{-e^{-\tau_l/\tau_c}}{\xi + e^{-\tau_l/\tau_c}} \tag{7.8}$$

By solving equation (7.8) with natural initial conditions, the reaction reads,

$$\xi(t) = \frac{1 - e^{-t/\tau_c}}{1 + e^{(-t/\tau_c + \tau_l/\tau_c)}} \tag{7.9}$$

In the expression above, τ_c is the characteristic time corresponding to the chemical reaction. The latency time τ_l is corresponding with the dissolution of silica. The data can be referenced in Ulm et al. (2000).

Based on the research findings, the Ulm's model can be improved to consider:

- the visco-elastic behavior of the ASR products;
- the damage of the reactive aggregate particles;
- the damage and creep of the cement matrix (Multon et al., 2009).

Therefore, Figure 7.8 shows a new "1D thought model" for ASR based on this research, which can account for gel viscous-elastic properties and cracking onset in the aggregate particle. This simplified model involves the reactive aggregate particle (the left side device) and the cement paste (the right side device), which both are at the millimeter scale. In addition, the central gray light device represents the ASR gel, which expands ($\kappa\xi_g$) and relaxes from its own viscosity (η_g).

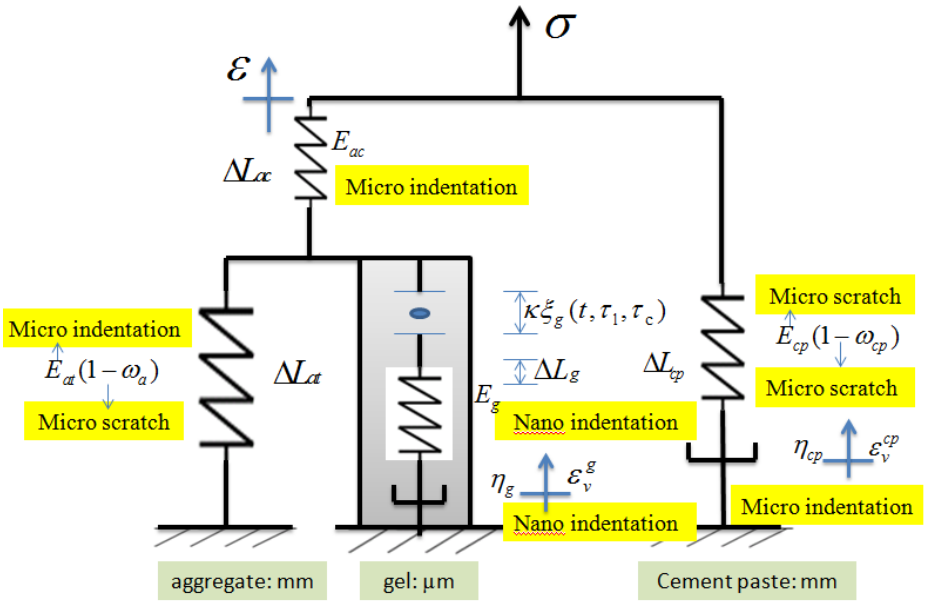

Figure 7.8 New two-scale ASR concrete damage model.

The variables in this model are listed below:

ξ_g: reaction extent which contains two time constants;

E_{at}: the Young modulus of the aggregate in traction;

E_{ac}: the Young modulus of the aggregate in compression (e.g., it can be related to the microindentation results presented in this work);

E_g: ASR product E-modulus (e.g., it can be related to the apparent viscosity measured by microindentation in this work);

E_{cp}: cement paste modulus;

κ: expansion coefficient (Ulm et al., 2000);

η_{cp}: cement paste viscosity or creep (e.g., it can be estimated by micro-indentation (Frech-Baronet et al., 2017; Zhang et al., 2014);

η_g: gel viscosity or creep (e.g., it can be related to the apparent viscosity measured by microindentation in this work);

ω_a: aggregate damage parameter (e.g., the fracture area of the damage stress-strain curve can be determined from micro-scratch tests on aggregate);

ω_{cp}: cement paste damage parameter;

ε_v^{cp}: creep strain of cement paste;

ε_g^v: creep strain of gel;

ε_g^t: total strain of gel;

ε: total strain.

One could use a simplified Mazars damage model (Jirásek, 2002) for the cement paste and aggregate with (scalar) damage variable ω_{cp} and ω_a, respectively. In that case, an exponential damage law is employed depending on two parameters, e.g., A_{cp}, B_{cp} (A_a, B_a) to define the damage parameter function expression. The aggregate toughness measured in this work, by micro-scratch testing, would allow making a link between those coefficients A_a, B_a as the area underneath the damage stress-strain law is the fracture energy.

This 1D though model suggests a way to consider the effect of gel viscous behavior in a two-scale model for aggregate and cement paste. This is a first proposal, which needs to consider more complex phenomena, such as:

- The diffusion model which starts ASR is macroscopically described by simplified reaction kinetics approach based on the Arrhenius concept. That is, the ion transport through the cement paste towards the reactive aggregate is over-simplified by a 1D reaction kinetics, as proposed by Ulm (Ulm et al., 2000);
- A 3D formulation is needed for considering realistic stress and strain fields;
- The proposed two-scale model does consider two different scales: the gel at the micrometer scale and the cement paste/aggregate at the millimeter scale. However, the model is still macroscopic in the sense that it does not consider the microstructure geometry, as the reactive aggregate size, the cement paste pore size, etc…(Multon et al., 2009);

- A damage anisotropic description of damage evolution under stress loading is needed (Alnaggar et al., 2013; Multon et al., 2009). This is a major limitation that needs to be extended to anisotropic fashion to describe preferential crack orientation (especially the ones induced by loadings) in future works.

As practical applications of the presented findings, we can foresee the following points:

• Disclosing of the viscosity property of the ASR products will enhance our understanding about the ASR damage mechanism and provide new support for developing multi-scale methods in the real field ASR-damaged concrete structures;

• The application of the present method to young ASR gel may help the research community to better understand the effect of gel migration on the cracking process;

• Disclosing the fracture toughness of reactive aggregates is a key factor for understanding and enhancing fracture mechanics models for ASR damaged concrete;

• The discussion of the ASR product's viscosity properties under two controlled relative humidity in the third part of the thesis can help to better understand the water role. It may be helpful to find advanced preventive methods by dealing with water content control;

• The proposed simplified the "1-D thought" model may inspire new works in multiscale models which want directly to accounts the ASR gel property and its different morphology and chemical variations.

8. Conclusions and Future Outlooks

Based on the present results, the main conclusions of this thesis are the following:

1. The Hardness (H) and Young Modulus (E) of ASR crystalline products were measured by microindentation confirming the results ontained in previous recent words. Smaller-scale tests by nanoindentation suggested that the mechanical properties of the ASR single rosette-like crystals may even be greater than those measured by microindentation, as reduced by ASR inter-crystal spacing and interfaces. It is the first time in the word to measue the creep values of the ASR crystalline products;

2. It was found that ASR crystalline rosette-like products exhibit important visco-elastic properties with relaxation coefficient of about 40%. Most of the time-dependent deformation seems irreversible. The sliding of ASR crystals may be the major mechanisms of the observed time-deformation under constant stress;

3. For the first time, the effect of relative humidity (RH) on the viscous property of ASR crystalline products, especially on the irreversible creep in the longer term is discussed in the work. Quantitatively, the irreversible creep rate (*eta1*) reduces by a factor of 5 passing from RH=30% to 95%;

4. The toughness of ASR-damaged aggregates was statistically characterized by novel micro-scratch techniques with emphasis on the bedding direction and the decolored zone observed around the larger cracks filled by ASR products within the aggregate particldes. Testing was also carried out on virgin fine-grained limestone from local quarry and served as control. Based on the penetration depth chosen in this work, no effect of the bedding direction were observed on the measured toughness, both in the virgin rock sample and the “reacted” aggregate particles. The color difference (light grey and dark grey) within the “reacted” limestone aggregate particles of anheavily ASR-damaged concrete specimen does not affect significantly the fracture critical stress intensity factor K_C, although some chemical differences were observed through electron probe microanalysis (EPMA). This suggests that the damage of the reactive aggregate is more localized in the major cracks rather than diffused in sub-micrometer cracks within the decolored zone of the reactive aggregate particles;

5. A new simplified 1D though model was proposed as a first approach to consider the new knowledge developed in this work, such as the visco-elastic property of the ASRcrystalline products and the toughness of the aggregates. A discussion on the pressure build-up within the aggregate highlighted the importance of measuring the viscoelastic property of ASR products. The more the ASR product is viscous and expansive, the more the risk of aggregate cracking is.

The following are the recommendations for future work based on the findings of this research:

1. The present promising approach needs to be further applied to different ASR products, in particular ASR gel which is generally found towards the edges along microcracks within reactive aggregate particles, i.e. close to the cement paste;

2. It is interesting to further study the water effect and function in the ASR product and damage formation progress. More research should be carried out about the mixture of ASR gel and crystalline products (rosette-like) to explain the transition/progress from the possible initial reaction product gel to the secondary form of rosette structure;

3. The correlation between the damage resistance or fracture thoughness of reactive aggregate particles and the properties of different ASR products (gel and rosette-like structure), ITZ, cement paste on the long-term prediction of concrete expansion may need further studies;

4. Further coupling between micromechanical and quantitative chemical analysis should be carried out to understand the effect of the particular zoning commonly observed within reactive limestone aggregate particles in heavily ASR-affected concrete elements in various portions of the St-Lawrence Lowlands of Québec, Canada;

5. In the future, the proposed 1D though model could provide inspiration for developing new models which consider directly the mechanical properties of the ASR products as well as the damage within reactive aggregate particles.

9. References

AASHTO (American Association of State Highway and Transportation Officials). (1993). Standard Method of Test for Rapid Identification of Alkali-Silica Reaction Products in Concrete (Uranyl Acetate Procedure). AASHTO T299-93.

Adachi, T., & Sakka, S. (1990). Dependence of the elastic moduli of porous silica gel prepared by the sol-gel method on heat-treatment. Journal of Materials Science, 25(11): 4732–4737.

Akono, A. T., Reis, P.M., & Ulm F.-J. (2011). "Scratching as a fracture process: From butter to steel." Physical review letters 106(20): 204302.

Alnaggar, M., Cusatis, G., & Di Luzio, G. (2013). Lattice discrete particle modeling (LDPM) of alkali-silica reaction (ASR) deterioration of concrete structures. Cement and Concrete Composites, 41: 45–59.

Association, B.C. (1992). The Diagnosis of alkali-silica reaction. British Cement Association, Crowthorne, Berks, RG1 6YS, United Kingdom.

ASTM C 856-02. (2003). “Standard Practice for Petrographic Examination of Hardened Concrete”. Annual book of ASTM Standards 2003, Section Four, Concrete and Aggregates, 04(02): 434-450.

Bažant, Z.P., & Alexander, S. (2000). Mathematical model for kinetics of alkali–silica reaction in concrete. Cement and Concrete Research, 30(3): 419–428.

Ben Haha, M., Gallucci, E., Guidoum, A., & Scrivener, K.L. (2007). Relation of expansion due to alkali-silica reaction to the degree of reaction measured by SEM image analysis. Cement and Concrete Research, 37(8): 1206–1214.

Bérard, J., & Roux, R. (1986). La viabilité des bétons du Québec: le rôle des granulats. Canadian Journal of Civil Engineering 13: 12–24.

Bérubé, M.-A., & Fournier, B. (1986). Les produits de la réaction alcalis-silice dans le béton: étude de cas de la région de Québec. Canadian Mineralogist, 24: 271-288.

Bérubé, M.-A., Durand, B., Vézina, D., & Fournier, B. (2000). Alkali-aggregate reactivity in Québec (Canada). Canadian Journal of Civil Engineering, 27(2): 226-245.

Beste, U., Lundvall, A., & Jacobson, S. (2004). Micro-scratch evaluation of rock types—a means to comprehend rock drill wear. Tribology International, 37(2): 203-210.

British Cement Association (BCA). (1992). “The Diagnosis of Alkali-Silica Reaction – Report of a Working Party,” Wexham Springs, Slough (UK), SL3 6PL, 44.

Characterization of the effects of the swelling caused by the reaction alkali-silica on the mechanical behavior of a concrete structure (The Thesis of doctorate of university Paul Sabatier).

Charpin, L., & Ehrlacher, A. (2013). Anisotropy of Alkali-Silica Reaction under loading. In Poromechanics V: *Proceedings of the 5th Biot Conference on Poromechanics*, 794-803.

Comby-Peyrot, I., Bernard, F., Bouchard, P. O., Bay, F., & Garcia-Diaz, E. (2009). Development and validation of a 3D computational tool to describe concrete behavior at mesoscale. Application to the alkali-silica reaction. Computational Materials Science, 46(4): 1163-1177.

Constantinides, G. (2006). Invariant mechanical properties of calcium-silicate-hydrates (CHS) in cement-based materials: instrumented nanoindentation and micro poromechanical modeling (Doctoral dissertation, Massachusetts Institute of Technology).

Constantinides, G., & Ulm, F.-J. (2007). The nanogranular nature of C–S–H. Journal of the Mechanics and Physics of Solids, 55(1): 64-90.

Coussy, O. (2011). Mechanics and physics of porous solids. John Wiley & Sons.

CSA (Canadian Standards Association) Appendix B – Alkali-Aggregate Reaction, 2014, CSA A23.2-14. CSA International, Mississauga, Ontario, Canada, 158–180.

Dähn, R., Arakcheeva, A., Schaub, P., Pattison, P., Chapuis, G., Grolimund, D., Wieland, E., & Leemann, A. (2016). Application of micro X-ray diffraction to investigate the reaction products formed by the alkali–silica reaction in concrete structures. Cement and Concrete Research, 79: 49-56.

Damidot, D., Velez, K., & Sorrentino, F. (2003). Characterization of the interstitial transition zone (ITZ) of high-performance cement by nanoindentation technique. In *Proceeding of the 11th ICCC, Durban*, South Africa, 314-323.

De-Bonniers, P. (2011). Code Aster handbook: Behavior model BETON_RAG.

De-Ceukelaire, L. (1991). The determination of the most common crystalline alkali-silica reaction product. Materials and Structures, 24(3):169–171.

Dunant, C.F., & Scrivener, K.L. (2010). Micromechanical modeling of alkali–silica-reaction-induced degradation using the AMIE framework. Cement and Concrete Research, 40(4): 517–525.

Dunant, C.F., & Scrivener, K.L. (2016). Physically based models to study the alkali–silica reaction. Proceedings of the Institution of Civil Engineers–Construction Materials, 169(3):136–144.

Dunbar, P.A., & Grattan-Bellew, P.E. (1995). “Results of Damage rating Evaluation of Condition of Concrete from a Number of Structures Affected by AAR”. *In Proceedings of CANMET/ACI International Workshop on AAR in Concrete*, Dartmouth, Nova Scotia, CANMET, Department of Natural Resources Canada, 257-265.

Fernandes, I., & Broekmans, M.A. (2013). Alkali–silica reactions: an overview. Part I. Metallography, Microstructure, and Analysis, 2(4): 257–267.

Fernandes, I., Bibeiro, M.D.A., Broekmans, M.A.T.M., & Sims, I. (2016). Petrographic atlas: characterization of aggregates regarding potential reactivity to alkalis. RILEM TC 219-ACS recommended guidance AAR-1.2, for use with the RILEM AAR-1.1 petrographic examination method. Springer, ISBN 978-94-017-7382-9, 193.

Fischer-Cripps, A. C. (2000). Factors Affecting Nanoindentation Test Data. Springer.

Fischer-Cripps, A. C. (2000). Introduction to contact mechanics. Springer.

Fischer-Cripps, A. C. (2004). Nanoindentation Springer. New York.

Fournier, B. (1994). Contribution à l'étude de la durabilité des structures de béton construites avec des granulats carbonates produits dans les basses-terres du Saint-Laurent du Québec: les réactions alcalis-granulats (Doctoral dissertation, Université Laval).

Fournier, B. (2013). Personal communication with Professor Benoît Fournier on August 16th, and on October 9th.

Fournier, B., & Bérubé, M.-A. (1991). Évaluation du potentiel de réactivité alcaline des granulats à béton produits dans les Basses-Terres du Saint-Laurent du Québec (Canada). Canadian Journal of Civil Engineering, 18(2): 282–296.

Fournier, B., & Bérubé, M.-A. (2000). Alkali-aggregate reaction in concrete: a review of basic concepts and engineering implications. Canadian Journal of Civil Engineering, 27(2): 167–191.

Fournier, B., Bérubé, M.A., & Vézina, D. (1987). Conditions survey of concrete structures built with potentially reactive aggregates from the Québec City Area. Katherine and Bryant Mather international conference on concrete durability, April 1987, Atlanta (U.S.A.), ACI Special Publication SP-100, J.M. Scanlon Editor, 1343-1355.

Fournier, B., Bérubé, M.A., Folliard, K.J., & Thomas, M.D.A. (2010). Report on the diagnosis, prognosis, and mitigation of alkali-silica reaction (ASR) in transportation structures. Federal Highway Administration (FHWA), U.S. Dept of Transportation, FHWA-HIF-09-004, 154.

Fournier, B., Sanchez, L.F.M, & Beauchemin, S. (2015). Outils d'investigation de la réactivité alcalis-granulats dans les infrastructures en béton. Rapport Final, Ministère des transports du Québec, Service des matériaux d'infrastructure, Secteur béton de ciment, 293.

Frech-Baronet, J., Sorelli, L., & Charron, J.-P. (2017). New evidences on the effect of the internal relative humidity on the creep and relaxation behaviour of a cement paste by micro-indentation techniques. Cement and Concrete Research, 91:39–51.

Galin, L.A., Moss, H., & Sneddon, I.N. (1961). Contact problems in the theory of elasticity. North Carolina State University Raleigh School of Physical sciences and Applied Mathematics.

Gao, X.X., Multon, S., Cyr, M., & Sellier, A. (2013). Alkali–silica reaction (ASR) expansion: pessimum effect versus scale effect. Cement and Concrete Research, 44: 25-33.

Gocevski, V., & Pietruszczak, S. (2000). "Assessment of the Effects of Slot-Cutting in Concrete Dams Affected by Alkali-Aggregate Reaction". In *Proceedings of the 11th International Conference on Alkali-Aggregate Reaction in Concrete*, Québec City, Canada, Editors: Bérubé, M.A., Fournier, B., & Durand, B. 1303-1312.

Godart, B., de Rooij, M.R., & Wood, J.G. (2013). Guide to Diagnosis and Appraisal of AAR Damage to Concrete in Structures. Springer-Verlag, 79–81.

Grattan-Bellew, P.E., & Danay, A. (1992). "Comparison of laboratory and field evaluation of AAR in large dams." In *Proceedings of the International Conference on Concrete Alkali–Aggregate Reactions in Hydroelectric Plants and Dams*, Fredericton, NB, vol. 28.

Grattan-Bellew, P.E. (1992). "Comparison of laboratory and field evaluation of alkali-silica reaction in large dams". In *Proceedings of the First International Conference on Concrete Alkali-Aggregate Reactions in Hydroelectric Plants and Dams*, September-October 1992, Fredericton, NB, Canada, 23.

Grattan-Bellew, P.E. (1995). Laboratory evaluation of ASR in concrete from Saunders Generating Station. ACI Materials Journal, 92(2): 9.

Grimal, E. (2007) Caractérisation des effets du gonflement provoqué par la réaction alcali-silice sur le comportement mécanique d'une structure en béton[D]. Toulouse. 3.

Grimal, E., Sellier, A., Page Y.-L., & Bourdarot, E. (2008a). Creep, Shrinkage, and Anisotropic Damage in Alkali-Aggregate Reaction Swelling Mechanism — Part I: A Constitutive Model. ACI Material Journal, 105: 227–235.

Grimal, E., Sellier, A., Page Y.-L., & Bourdarot, E. (2008b). Creep, Shrinkage, and Anisotropic Damage in Alkali-Aggregate Reaction Swelling Mechanism — Part II: Identification of model Parameters and Application, 105: 236–242.

Guédon-Dubied, J.S., Cadoret, G., Durieux, V., Martineau, F., Fasseu, P., & Van Overbecke, V. (2000). "Study on Tournai limestone in Antoine Cimescaut Quarry–petrological, chemical and alkali reactivity approach." In *Proceedings of the 11th international conference on AAR in concrete*, Québec City, Canada, 335-344.

Guthrie, G.G. Jr., & Carey, J.W. (1997). "A Simple Environmentally Friendly, and Chemically Specific Method for the Identification and Evaluation of the Alkali-Silica Reaction". Cement and Concrete Research, 27(9): 1407-1417.

Hansen, W.C. (1944). "Studies relating to the mechanism by which the alkali-aggregate reaction proceeds in concrete." Journal of the American Concrete Institute, 15(3): 213-227.

Harding, J.W., & Sneddon, I.N. (1945). The elastic stresses produced by the indentation of the plane surface of a semi-infinite elastic solid by a rigid punch. In *Mathematical Proceedings of the Cambridge Philosophical Society*. Cambridge University Press, 41:16–26.

Helmuth, R. (1993). Alkali-silica reactivity: an overview of research (No. SHRP Report C-342).

Hoover, C. (2013) Creep, shrinkage and durability and analytical models, 364-365.

Ichikawa, T., & Miura, M. (2007). Modified model of alkali-silica reaction. Cement and Concrete Research, 37(9): 1291–1297.

Ingham, J.P. (2012). A color guide – Geomaterials under the microscope. Academic Press – an imprint of Elsevier. ISBN 978-0-12-407230-5, 192. ISE. (1992). Structural Effects of Alkali-Silica Reaction – Technical guidance appraisal of existing structures. The institution of Structural Engineers. 45.

Jensen, A.D., Eriksen, K., Chatterji, S., Thaulow, N., & Brandt, I. (1985). Petrographic analysis of concrete. Danish Building Export Council, 12.

Jin, W. (1998). Alkali-Silica Reaction in Concrete with Glass Aggregate-a Chemo-Physical-Mechanical Approach (Ph.D. dissertation). Columbia University, New York, NY, 154.

Jin, W., Meyer, C., & Baxter, S. (2000). "Glascrete"-Concrete with Glass Aggregate. ACI Materials Journal, 97(2): 208–213.

Jirásek, M. Fragments of Lecture Notes by Milan Jirásek. (2002): Modeling of localized Inelastic Deformation, Technical University of Catalonia (UPC), Barcelona, November, 18-22.

Katayama, T. (2012). ASR gels and their crystalline phases in concrete – universal products in alkali-silica, alkali-silicate and alkali-carbonate reactions. In 14th International Conference on alkali-aggregate reaction (AAR) in concrete, Austin (Texas).

Katayama, T. (2012). Petrographic study of the alkali-aggregate reactions in concrete. Graduate School of Science, University of Tokyo, Department of Earth and Planetary Science.

Kawamura, M., & Iwahori, K. (2004). ASR gel composition and expansive pressure in mortars under restraint. Cement and Concrete Composites, 26(1): 47–56.

Kimberly, K. (2007). Presentation of “Structure of the Hydrated Cement Paste”.Dr. Kimberly Kurtis, School of Civil Engineering, Georgia Institute of Technology, Atlanta, Georgia.

Larive, C. (1998). ‘‘Apports combine´s de l’expe´rimentation et de la mode´lisation a` la comprehension de l’alcali-reaction et de ses effets me´- caniques.’’ Monograph LPC, OA 28, Laboratoires des Ponts et Chausse´es, Paris (partially translated into English).

Larive, C., & Louarn, N. (1992). Diagnosis of alkali-aggregate reaction and sulphate reaction in French structures. In *Proceedings 9th International Conference on Alkali-*Aggregate Reactions. Concrete Society, 587–598.

Larive, C.K., Guerra, L., & Rabenstein, D.L. (1992). Cis/trans conformational equilibrium across the cysteine6-proline bond of oxytocin, arginine vasopressin, and lysine vasopressin. Journal of the American Chemical Society, 114(19): 7331-7337.

Leemann, A., Katayama, T., Fernandes, I., & Broekmans, M.A. (2016). Types of alkali–aggregate reactions and the products formed. In *Proceedings of the Institution of Civil Engineers-Construction Materials*, 169(3): 128–135.

Leemann, A., & Lura, P. (2013). E-modulus of alkali-silica-reaction product determined by micro-indentation. Construction and Building Materials, 44: 221-227.

Lemarchand, E., Dormieux, L., & Ulm, F.-J. (2005). Micromechanics investigation of expansive reactions in chemoelastic concrete. Philosophical Transactions of the Royal Society of London A: Mathematical, Physical and Engineering Sciences, 363(1836): 2581–2602.

Lorenzi, G., Jensen, J., Wigum, B., Sibbick, R., Haugen, M., Guédon, S., & Akesson, U. (2006). Petrographic atlas of potentially alkali-reactive rocks in Europe. Royal Belgian Institute of Natural Sciences, Geological survey of Belgium professional paper 1– N.302: 63.

Meyer, E. (1992). Atomic force microscopy. Progress in Surface Science, 41(1): 3–49.

Miller, M., Bobko, C., Vandamme, M., & Ulm, F.-J. (2008). Surface roughness criteria for cement paste nanoindentation. Cement and Concrete Research, 38(4): 467–476.

Moon, J., Speziale, S., Meral, C., Kalkan, B., Clark, S. M., & Monteiro, P.J. (2013). Determination of the elastic properties of amorphous materials: case study of alkali–silica reaction gel. Cement and Concrete Research, 54: 55–60.

Multon, S., Sellier, A., & Cry, M. (2009). Chemo–mechanical modeling for prediction of alkali silica reaction (ASR) expansion. Cement and Concrete Research, 39(6): 490–500.

Multon, S., & Sellier, A. (2016). Multi-scale analysis of alkali–silica reaction (ASR): Impact of alkali leaching on scale effects affecting expansion tests. Cement and concrete research, 81: 122-133.

Multon, S., Seignol, J.-F., & Toutlemonde, F. (2005). Structural behavior of concrete beams affected by alkali-silica reaction. ACI Materials Journal-American Concrete Institute, 102(2): 67–76.

Multon, S., Sellier, A., & Cyr, M. (2009). Chemo–mechanical modeling for prediction of alkali silica reaction (ASR) expansion. Cement and Concrete Research, 39(6): 490–500.

Murtagh, M.J., Graham, E.K., & Pantano, C.G. (1986). Elastic moduli of silica gels prepared with tetraethoxysilane. Journal of the American Ceramic Society, 69(11):775-779.

Natesaiyer, K., Stark, D., & Hover, K.C. (1991). “Gel Fluorescence Reveals Reaction Product Traces”. Concrete International, January 1991, 25-28.

Nohava, J., Randall, N.X., & Conté, N. (2009). Novel ultra nanoindentation method with extremely low thermal drift: Principle and experimental results. Journal of Materials Research, 24(03): 873–882.

Oliver, W., & Pharr,. G. (1992). An improved technique for determining hardness and elastic modulus using load and displacement sensing indentation experiments, Journal of Materials Research 7: 1564 – 83.

Ollivier, J.-P., & Victor, A. (2008). La durabilité des bétons, Presses Ponts et chaussées.

Pacheco-Torgal, F., Castro-Gomes, J., & Jalali, S. (2008). Alkali-activated binders: A review: Part 1. Historical background, terminology, reaction mechanisms and hydration products. Construction and Building Materials, 22(7): 1305–1314.

Pan, J.W., Feng, Y.T., Wang, J.T., Sun, Q.C., Zhang, C.H., & Owen, D.R.J. (2012). Modeling of alkali-silica reaction in concrete: a review. Frontiers of Structural and Civil Engineering, 6(1): 1–18.

Panich, N., & Sun, Y. (2004). Effect of penetration depth on indentation response of soft coatings on hard substrates: a finite element analysis. Surface and Coatings Technology, 182(2): 342–350.

Pesavento, F., Gawin, D., Wyrzykowski, M., Schrefler, B.A., & Simoni, L. (2012). Modeling alkali–silica reaction in non-isothermal partially saturated cement based materials. Computer Methods in Applied Mechanics and Engineering, 225: 95–115.

Peterson, K., Gress, D., Vandam, T., & Sutter, L. (2006). Crystallized alkali-silica gel in concrete from the late 1890s. Cement and Concrete Research, 36(8): 1523–1532.

Phair, J.W., Tkachev, S.N., Manghnani, M.H., & Livingston, R.A. (2005). Elastic and structural properties of alkaline-calcium silica hydrogels. Journal of Materials Research, 20(02): 344–349.

Pietro, L., & Leemann, A. (2014). The email sent to Prof. Luca Sorelli on ASR paper and collaboration on February, 4th.

Poole, A. B., & Sims, I. (Eds.). (2015). Concrete Petrography: A Handbook of Investigative Techniques. CRC Press.

Powers, T.C, & Steinour, H.H. (1955a). An investigation of some published researches on alkali-aggregate reaction. Part I. The chemical reactions and mechanism of expansion. Journal of American Concrete Institute, 26(6): 497–516.

Powers, T.C, & Steinour, H.H. (1955b). An interpretation of some published researches on alkali-aggregate reaction. Part 2. A hypothesis concerning safe and unsafe reaction with reactive silica in concrete. Journal of American Concrete Institute, 26(8): 785–811.

Prin, D., & Brouxel, M. (1992). Alkali-aggregate reaction in northern France: A review in *the 9th International Conference on Alkali-aggregate reaction in Concrete*, July, London, Vol 2.

Puatatsananon, W., & Saouma, V. (2013). Chemo-mechanical Micromodel for Alkali-Silica Reaction. ACI Material Journal, 110 (2013): 67–77.

Rajabipour, F., Giannini, E., Dunant, C., Jason, H., Ideker, D.A., & Thomas, M. (2015). "Alkali–silica reaction: Current understanding of the reaction mechanisms and the knowledge gaps." Cement and Concrete Research 76: 130-146.

Ramyar, K., Çopuroğlu, O., Andiç, Ö., & Fraaij, A.L.A. (2004). Comparison of alkali‐silica reaction products of fly-ash-or lithium-salt-bearing mortar under long-term accelerated curing. Cement and Concrete Research, 34(7): 1179-1183.

Reinhardt, H. W., & Mielich, O. (2011). A fracture mechanics approach to the crack formation in alkali-sensitive grains. Cement and Concrete Research, 41(3): 255–262.

Rivard, P., Fournier, B., & Ballivy, G. (2000). "Quantitative Petrographic Technique for Concrete Damage Due to ASR: Experimental and Application". Cement, Concrete & Aggregates, 22(1): 63-72.

Rivard, P., Fournier, B., & Ballivy, G. (2002). "The Damage Rating Index Method for ASR-Affected Concrete – A Critical review of Petrographic Features of Deterioration and Evaluation Criteria". Cement, Concrete & Aggregates, 24(2):1-11.

Rogers, C.A., Grattan-Bellew P.E., Hooton, R.D., Ryell, J., & Thomas M.D.A. (2000). Alkali-aggregate research in Ontario. Canadian Journal of Civil Engineering, 27(2): 246-260.

Šachlová, Š., Přikryl, R., & Pertold, Z. (2010). Alkali-silica reaction products: Comparison between samples from concrete structures and laboratory test specimens. Materials Characterization, 61(12): 1379–1393.

Sanahuja, J., & Dormieux, L. (2010). Creep of a CSH gel: a micromechanical approach. Anais Da Academia Brasileira de Ciências, 82(1): 25–41.

Sanchez, L.F.M. (2013). Personal communication with Leandro F.M. Sanchez in October of 2013.

Sanchez, L.F.M. (2014). Personal communication with Leandro F.M. Sanchez in March of 2014.

Sanchez, L.F.M., Fournier, B., Jolin, M, & Duchesne, J. (2015). Reliable quantification of AAR damage through assessment of the Damage Rating Index (DRI). Cement and Concrete Research, 67: 74-92.

Sanchez, L.F.M., Fournier, B., Jolin, M., Bedoya, M.A.B., Bastien, J., & Duchesne, J. (2016). Use of Damage Rating Index to Quantify Alkali-Silica Reaction Damage in Concrete: Fine versus Coarse Aggregate. ACI Materials Journal, 113(4).

Sanchez, L.F.M., Fournier, B., Jolin, M., Mitchell, D., & Bastien, J. (2017). Overall assessment of Alkali-Aggregate Reaction (AAR) in concretes presenting different strengths and incorporating a wide range of reactive aggregate types and natures. Cement and Concrete Research, 93: 17-31.

Schlangen, E., & Çopuroglu, O. (2007). Concrete damage due to the alkali-silica reaction: a new method to determine the properties of the expansive gel. Fracture Mechanics of Concrete and Concrete Structures–high-Performance Concrete, Brick-Masonry, and Environmental Aspects. Taylor & Francis Group, London, 1835–1841.

Seignol, J.F., & Godart, B. (2012). A collective effort to propose practical guidance on the use of numerical models to re-assess AAR-affected structures. In *14th International Conference on AAR in concrete*. Texas (USA): Austin.

Silveira, J.F.A. (1989). The opening of expansion joints at the Moxoto powerhouse to counteract the alkali-silica reaction. In *Proceedings of 8th International Conference in Alkali- Aggregate Reaction*, Kyoto, Japan.

Sims, I., livre, P., & Stark, D. (1991). “Handbook for the Identification of Alkali-Silica Reactivity in Highway Structures”. No.: SHRP-C/FR-91-101, TRB National Research Council, 49.

Sorelli, L., Constantinides, G., Ulm, F.-J., & Toutlemonde, F. (2008). The nanomechanical signature of ultra high-performance concrete by statistical nanoindentation techniques. Cement and Concrete Research, 38(12): 1447–1456.

St John, D.A., Poole, A.B., & Sims, I. (1998). Concrete petrography: a handbook of investigative techniques. Arnold; Copublished in North, Central and South America by J. Wiley.

Stanton, T.E. (1940). Expansion of Concrete Through Reaction Between Cement and Aggregate, proceedings. American Society of Civil Engineers Transactions, 66: 1781.

Stanton, T.E. (1940). Influence of Cement and Aggregate on Concrete Expansion. Engineering News-Record, 124(5): 59.

Swamy, R. N. (2002). The alkali-silica reaction in concrete. CRC Press.

Swamy, R. N., & Al-Asali, M.M. (1988). Expansion of concrete due to alkali-silica reaction. Materials Journal, 85(1): 33–40.

Thomas, M.D.A. (2001). “The role of calcium hydroxide in alkali recycling in concrete.” Materials Science of Concrete Special Volume on Calcium Hydroxide in Concrete, (Ed. J. Skalny, J. Gebauer and I. Odler), American Ceramic Society, Westerville, OH, 269-280.

Thomas, M.D.A., Fournier, B., & Folliard, K.J. (2013). Alkali-aggregate reactivity (AAR) facts book. Federal Highway Administration (FHWA), U.S. Dept of Transportation, FHWA-HIF-13-019, 212.

Ulm, F.-J., Olliver, C., Li, K., & Larive, C. (2000). Thermo-chemo-mechanics of ASR expansion in concrete structures. Journal of Engineering Mechanics, 126(3): 233–242.

Ulm, F.-J., Vandamme, M., Bobko, C., Alberto Ortega, J., Tai, K., & Ortiz, C. (2007). Statistical indentation techniques for hydrated nanocomposites: concrete, bone, and shale. Journal of the American Ceramic Society, 90(9): 2677–2692.

Urhan, S. (1987). “Alkali-silica and pozzolanic reactions in concrete. Part 1: Interpretation of published results and a hypothesis concerning the mechanism.” Cement and Concrete Research, 17: 141-152.

US Department of Transportation, FHWA, (2012). Alkali-Aggregate Reactivity (AAR) Workshops For Engineering and Practitioners.

Vallée, D., Sorelli, L., & Chen, J. (2013). Chemo-mechanical Characterization of Cement Paste Microstructures: a One-to-One Coupling of SNT and SEM-EDS, Cement and Concrete Research, submitted in September.

Vandamme, M. (2008). M. I. of Technology. Dept. of Civil, E. Engineering, The Nanogranular Origin of Concrete Creep: A Nanoindentation Investigation of Microstructure and Fundamental Properties of Calcium silicate hydrates, Ph.D. Thesis. Massachusetts Institute of Technology, Department of Civil and Environmental Engineering.

Vandamme, M., & Ulm, F.-J. (2006). Viscoelastic solutions for conical indentation. International Journal of Solids and Structures, 43(10): 3142–3165.

Vandamme, M., Tweedie, C.A., Constantinides, G., Ulm, F.-J., & Van Vliet, K.J. (2012). Quantifying plasticity-independent creep compliance and relaxation of Visco elastoplastic materials under contact loading. Journal of Materials Research, 27(01): 302–312.

Vayghan, A.G., Rajabipour, F., & Rosenberger, J.L. (2016). Composition–rheology relationships in alkali–silica reaction gels and the impact on the Gel's deleterious behavior. Cement and Concrete Research, 83: 45–56.

Velez, K., Maximilien, S., Damidot, D., Fantozzi, G., & Sorrentino, F. (2001). Determination by nanoindentation of elastic modulus and hardness of pure constituents of Portland cement clinker. Cement and Concrete Research, 31(4): 555-561.

Walker, H.N., Lane, D.S., & Stutzman, P.E. (2006). Petrographic Methods of Examining Hardened Concrete: A Petrographic Manual (Revised 2004), Federal Highway Administration publication FHWA-HRT-04-150, July, 333.

Wang, S.-D., Pu, X.-C., Scrivener, K.L., & Pratt, P.L. (1995). Alkali-activated slag cement and concrete: A review of properties and problems. Advances in Cement Research, 7(27): 93–102.

Zhang, Q., Le Roy, R., Vandamme, M., & Zuber, B. (2014). Long-term creep properties of cementitious materials: Comparing microindentation testing with macroscopic uniaxial compressive testing. Cement and Concrete Research, 58: 89–98.

Appendix 1: Sample preparation

This appendix provides detailed information on the sample preparation techniques/approaches used in this research. The objective is to describe how to obtain a surface as smooth as possible thus minimizing the effect of the roughness on indentation results ($R < h_{max}/5$). Accordingly, the polishing demand of nanoindentation testing is higher than that necessary for micro-indentation and micro-scratch testing.

A1.1 Summary of sample preparation for the experimental program

A summary of the sample preparation process used for the different phases of the experimental program is given hereafter. References are then given to specific procedures that are also described in details.

Phase 1: micro- and nano-indentation testing carried out on the reaction products forming white veinlets in one aggregate particle. The general sample preparation process was as follows:

- A core from an ASR-affected concrete road pavement in Trois-Rivières was selected.
- The selected core was cut lengthways with a diamond saw (with water). The sawed-cut surface was then examined under the stereomicroscope.
- Two aggregate particles with white veinlets were located/selected and small concrete specimens incorporating the above individual particles were cut with a precision diamond saw (with water).
- The small concrete pieces the obtained were embedded in epoxy in a cylindrical mould with no epoxy touching the surface of the specimens. *Coarse polishing* of the specimens was carried out following the procedure described in section A1.2.
- *Fine polishing* was completed following the procedure described in section A1.3.
- AFM testing was carried out on the first sample to characterize surface roughness.
- Micro- and nanoindentation testing were carried out on the second specimen (white veinlets).
- The top surface of the sample was then coated with gold-palladium and examined under the SEM to characterize the reaction products.

Phase 2: micro-scratch testing carried out on fresh rock sample and on individual aggregate particles from concrete cores showing extensive signs of ASR. The general sample preparation process was as follows:

Rock samples from quarry:

- A fresh rock block was first selected from a typical quarrying operation in the Québec City area.
- A 20mm-thick slice was then cut perpendicular to the bedding in the above rock block with a diamond saw (with water); small blocks of 30 x 30 mm were further cut with a precision diamond saw (with water).
- The surface sample preparation for micro-scratch testing was performed in accordance with the procedure described in section A1.3.
- Micro-scratch testing was carried out in directions parallel and perpendicular to the bedding of the sedimentary rock.

Concrete samples incorporating dark-grey and light-grey aggregate particles:

- Cores from an ASR-affected concrete highway structure in Québec City were selected.
- The cores were cut lengthways with a diamond saw (with water).
- Polishing of one face of the above half-cores slab was carried out following the procedure described in section A1.4.
- The polished surfaces were then examined under the stereomicroscope and four individual aggregate particles were selected from three concrete cores.
- Small concrete specimens incorporating each the above particles were cut with a precision diamond saw (with water).
- Micro-scratch testing was carried out on the surface of the aggregate particles.
- The surface of one sample was then coated with carbon and examined under the electron microprobe (chemical mapping) (without any further polishing).

Phase 3: micro-indentation testing carried out on the reaction products forming white veinlets in two aggregate particles. The general sample preparation process was as follows:

- A core from an ASR-affected concrete road pavement in Trois-Rivières was first selected (same structure as Phase 1).
- The core was cut lengthways with a diamond saw (with water). The sawed-cut surface was examined under the stereomicroscope.
- Two aggregate particles showing white veinlets were selected and a small concrete specimen was cut with a precision diamond saw (with water) to isolate those particles in a small concrete cube.
- Coarse polishing of the specimens was carried out following the procedure described in section A1.2.
- Fine polishing was completed following the procedure described in section A1.3.
- The top surface of the sample was then coated with gold-palladium and then examined under the SEM to characterize the reaction products.

A1.2 Coarse polishing (Phases 1 and 3)

The following steps were carried out in the laboratories of the Geology and geological engineering department. The concrete specimens incorporating the individual particles were first dried at 50℃ for 3 days. The specimens were then placed in small cylindrical moulds containing fresh epoxy resin to manufacture a cylindrical mount, thus allowing proper operations with the polishing equipment and generate parallel top/bottom surfaces for indentation testing (Figures A1.1a and A1.1b).

The surface of the mount is ground/polished with diamond-coated paper, with a small amount of water, down to grit 800 (different papers). Between each paper, the surface is cleaned to avoid scratching the surface. Upon completion of polishing, the surface was cleaned with pressurized air and a piece of scotch tape placed on the surface to avoid carbonation (suggested by A. Leemann, EMPA). The specimens were then placed in a plastic bag, and then the bag stored in a hermetic plastic bottle with a small amount of water in the bottom to avoid significant drying and carbonation of the specimens (suggested by A. Leemann, EMPA) (Figure A1.1c).

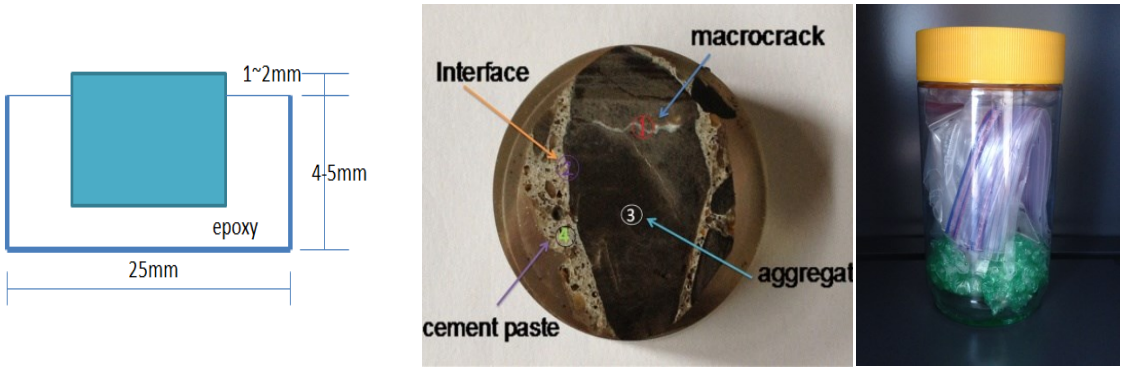

(a) (b) (c)

Figure A1.1 (a) Schematic diagram of the samples after embedding in the epoxy moulding and coarse polishing; (b) Sample mount ready for testing; (c) Hermetic bottle with samples inside plastic bags and water at the bottom.

A1.3 Fine polishing (Phases 1 and 3);

Following the coarse polishing operations described in section A1.2, samples for indentation testing (i.e. Phases 1 and 3) were further polished as described hereafter.

The Lapping and Polishing Machine - Model 920 (SBT-920) by South Bay Technology Inc. is used for fine polishing operations. The concrete specimen is first fixed on a steel disc using a mounting wax (TCAR-LD from Thermocarbon Inc) (Figure A1.2a). The disk is first heated on a hot plate (up to 300℃), thus allowing the wax to melt on its surface to properly fix the specimen prior to polishing. The steel disc is provided with the SBT-920 and therefore fits perfectly into the assembly. A "spring set-up" can be used to apply a constant pressure on the sample to allow a good adhesion of the sample until the wax hardens (Figure A1.2b). The sample is then mounted on a specially designed jig (Figure A1.2c) containing 8 supports and the surface of the sample underneath must equally touch a flat surface (Figure A1.2d).

The jig is mounted on the machine and grinding/polishing performed (8-inch silicon carbide discs 400, 800 and 1200 grit from Anamet) (Figure A1.2e). The gravity pushes the interior cylinder of the jig downward. No additional load is applied to the interior cylinder as if provides itself sufficient weight for grinding the ASR-affected concrete specimens. The specimens and the jig are held on the abrasive paper at about 3 to 4cm from the center of the lapping wheel, and the jig is allowed the rotate freely (Vandamme et al., 2008 (Figure A1.2f)). The wheel is then spun at 1 cps (centimeter per second), so the typical velocity underneath the sample is 18 to 25cm/s (Vandamme et al., 2008). It is important to clean the

disks very well between each operation (≠ disks) using ethanol and turning the disc at relatively high speed to “flush it”. When cement paste testing is carried out, AFM is used for determining how many hours of polishing are necessary to reach the quality of surface roughness required for testing. The fine polishing time also depends on the starting roughness (i.e. after coarse polishing) and the slower the rotating speed, the flatter the surface is. If after this step, the bottom and top surfaces of the specimen are not entirely parallel, the process is repeated until they become parallel.

For very fine polishing, the abrasive paper is then removed from the lapping wheel of the polishing machine and replaced by the polishing pad (Perforated Polishing Cloth from Anamet) (Figure A1.2g). The pad is charged with oil-based diamond suspensions (6µm, 1 µm, and 0.25µm) (Figure A1.2h). In addition to the oil-diamond suspension, additional oil on the desks (about 1 drop per 20 seconds) in order to dissipate any heat build-up. After each polishing step (6, 1 et 0.25µm), the specimens are quickly flushed with acetone and an air gun to remove loose particles. Once again, the specimens and the jig are held on the pad at about 3 to 4 cm from the center of the lapping wheel, and the jig is allowed the rotate freely (Miller et al., 2008). The wheel is then spun at 1 cps, so the typical velocity underneath the sample is 18 to 25 cm/s (Miller et al., 2008). The fine polishing progress lasts for 130 minutes. After the polishing, the surface of the sample may be cleaned with a very soft cloth and isopropanol by applying a very gentle pressure.

When polishing is completed, the specimens are quickly placed in a plastic bag. The bag is then stored in a hermetic plastic container with some water at the bottom of the container to avoid drying of the specimens. Indentation testing is then carried out within 24 hours following the completion of polishing operations (Figure A1.1c).

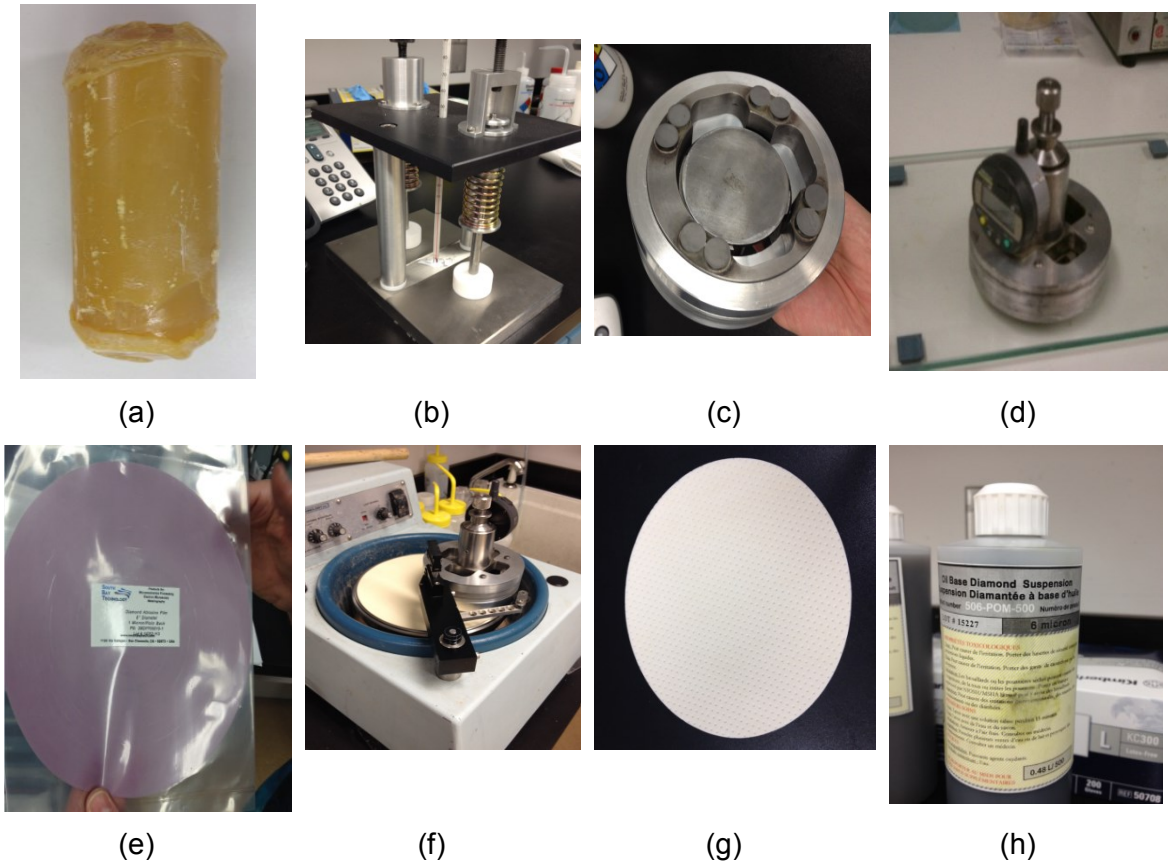

Figure A1.2 (a) wax for adhering samples; (b) "spring set-up" applying a constant pressure on the sample for keeping top and bottom surfaces parallel; (c) designed jig with its eight supports; (d); designed jig on a flat glass surface; (e) 8-inch silicon carbide discs from Anamet; (f) Lapping and Polishing Machine - Model 920 by South Bay Technology Inc with jig.; (g) perforated polishing cloth from Anamet; (h) oil-based diamond suspension. .

A1.4 Polishing (Phase 2 – micro-scratch testing);

As mentioned before, the aggregate samples for micro-scratch testing were selected from polished concrete slabs that were subjected to the polishing operations described hereafter.

One face of each concrete slab that was previously cut with a diamond saw was polished with a portable hand polishing device. This device uses a series of diamond-impregnated rubber disks, coarse to fine, i.e. No. 50 (coarse), 100, 400, 800 to 1500 (very fine) (Figure A1.3). The operation was done in wet condition (water).

(a) (b)

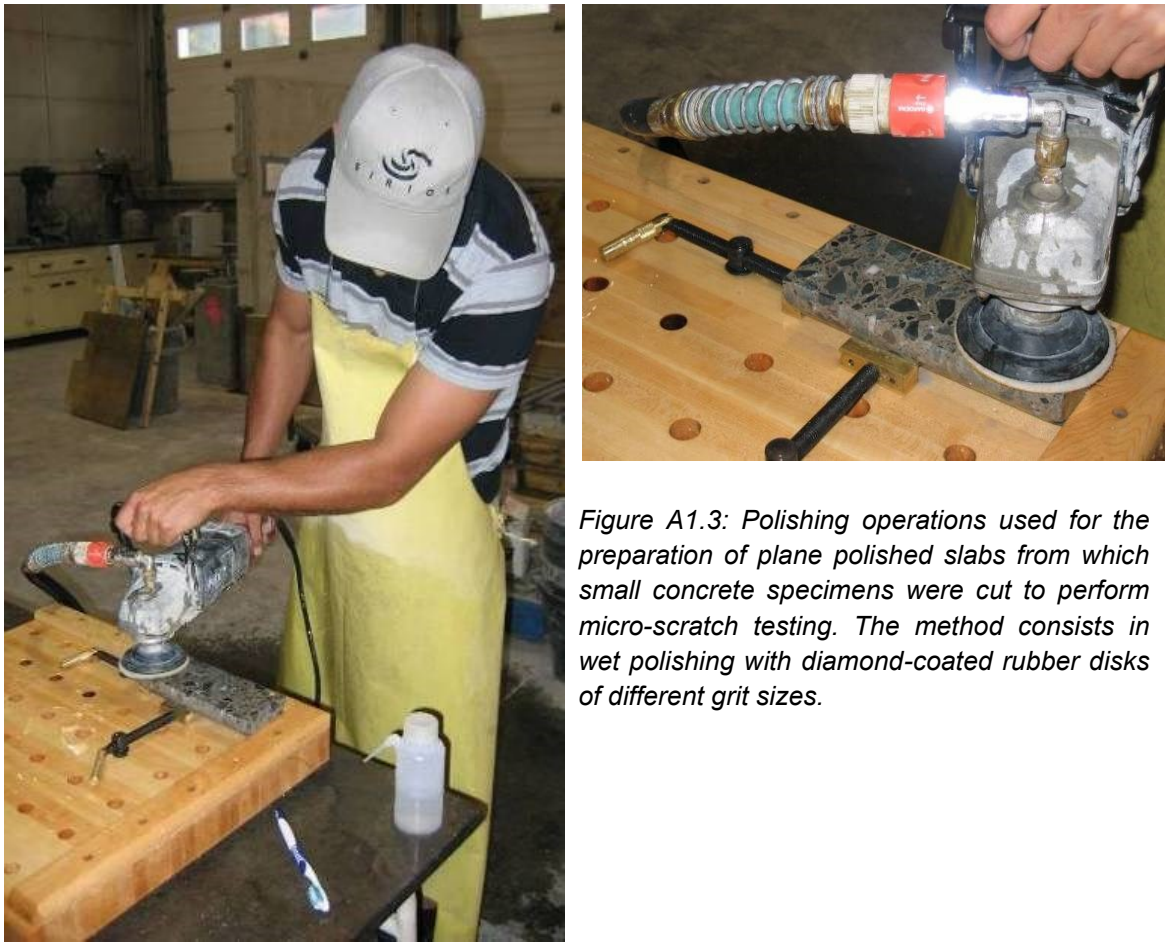

Figure A1.3: Polishing operations used for the preparation of plane polished slabs from which small concrete specimens were cut to perform micro-scratch testing. The method consists in wet polishing with diamond-coated rubber disks of different grit sizes.

Appendix 2: ASR concrete surface morphology

Atomic Force Microscope (AFM) tests are introduced to measure surface roughness and to acquire the morphological surface appearance of the ASR-damaged concrete samples used in this study. The AFM tests were performed on a companion specimen (Phase 1) subjected to the polishing operations described in Appendix 1, and prior to micro/nano- indentation testing. The roughness values of the components (aggregate, ASR products in cracks, ITZ and cement paste) in ASR-damaged concrete samples is one main reference index for applied forces or loading penetration depths in the subsequent indentation testing.

AFM is the technique to measure material roughness by the characterization of the atomic force variation as the distance changes. AFM tests provide a quantitative assessment of the surface roughness of the specimens examined. The specimen used for AFM testing (Figure A2.1) was polished in accordance with the procedure described in sections A1.2 and A1.3 (Appendix 1).

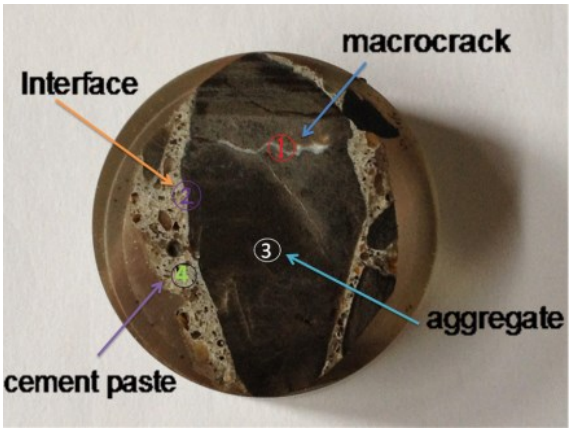

Figure A2.1 The ASR-affected concrete specimen used for AFM testing. Four zones were classified as follows: Zone 1: macrocrack; Zone 2: an interface; Zone 3: aggregate; Zone 4: cement paste.

Table A2.1 presents the roughness values of the macrocrack zone (white veinlet) in the ASR-damaged concrete specimen illustrated in Figure A2.1. In Table A2.1, P_a means average roughness, P_q means Roughness-Mean-Square (RMS) roughness and P_t means Peak to valley height. Six areas, 10μm ×10μm in size, were selected for measuring the roughness. In addition, the left overview, the side view, and the stereoscopic view are shown in Figure A2.2 for one area of the macrocrack zone.

Table A2.1 Roughness values of the macrocrack zone in the ASR-damaged concrete specimen illustrated in Figure A2.1.

No.	Name	Size	P_a	P_q	P_t
1	Crack_100µm.000	100µm	0.1 µm	0.12 µm	0.75 µm
2	Crack_100µm.001	100µm	0.14 µm	0.17 µm	0.91 µm
3	Crack_100µm.002	100µm	0.1 µm	0.13 µm	0.63 µm
4	Crack1.000	10µm	80 µm	96.64nm	424.64nm
5	Crack1.001	100µm	40.08nm	151.94nm	151.94nm
6	Crack1.002	200µm	6.95nm	40.90nm	40.90nm

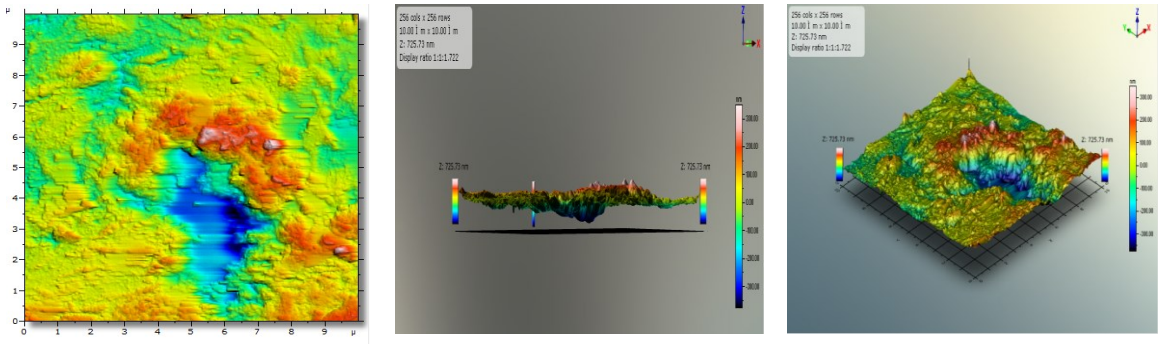

(a) (b) (c)

Figure A2.2 Surface appearance of 1 point from different views in the crack zone of the concrete specimen: (a) left overview; (b) side view; (c) stereoscopic view.

The roughness pictures of the four different zones (i.e. aggregate, ASR products in macrocrack, ITZ and cement paste) of the concrete specimen illustrated in Figure A2.1 are given in Figure A2.3. It is to be noted that the macrocrack zone correspond to a crack filled with secondary reaction products with rosette-like microtexture.

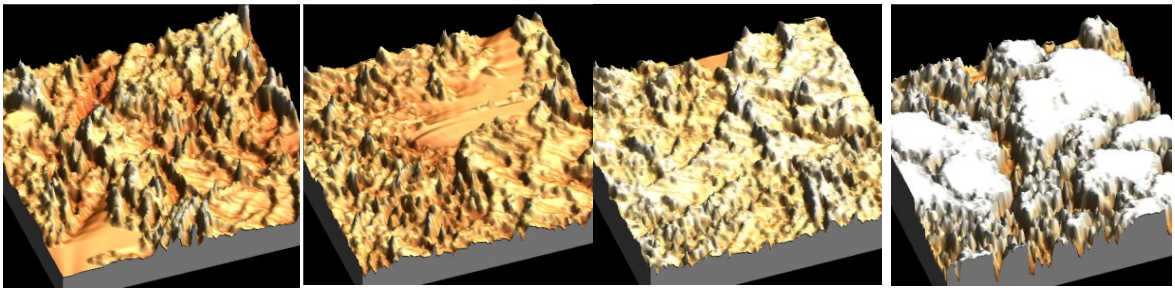

(a) (b) (c) (d)

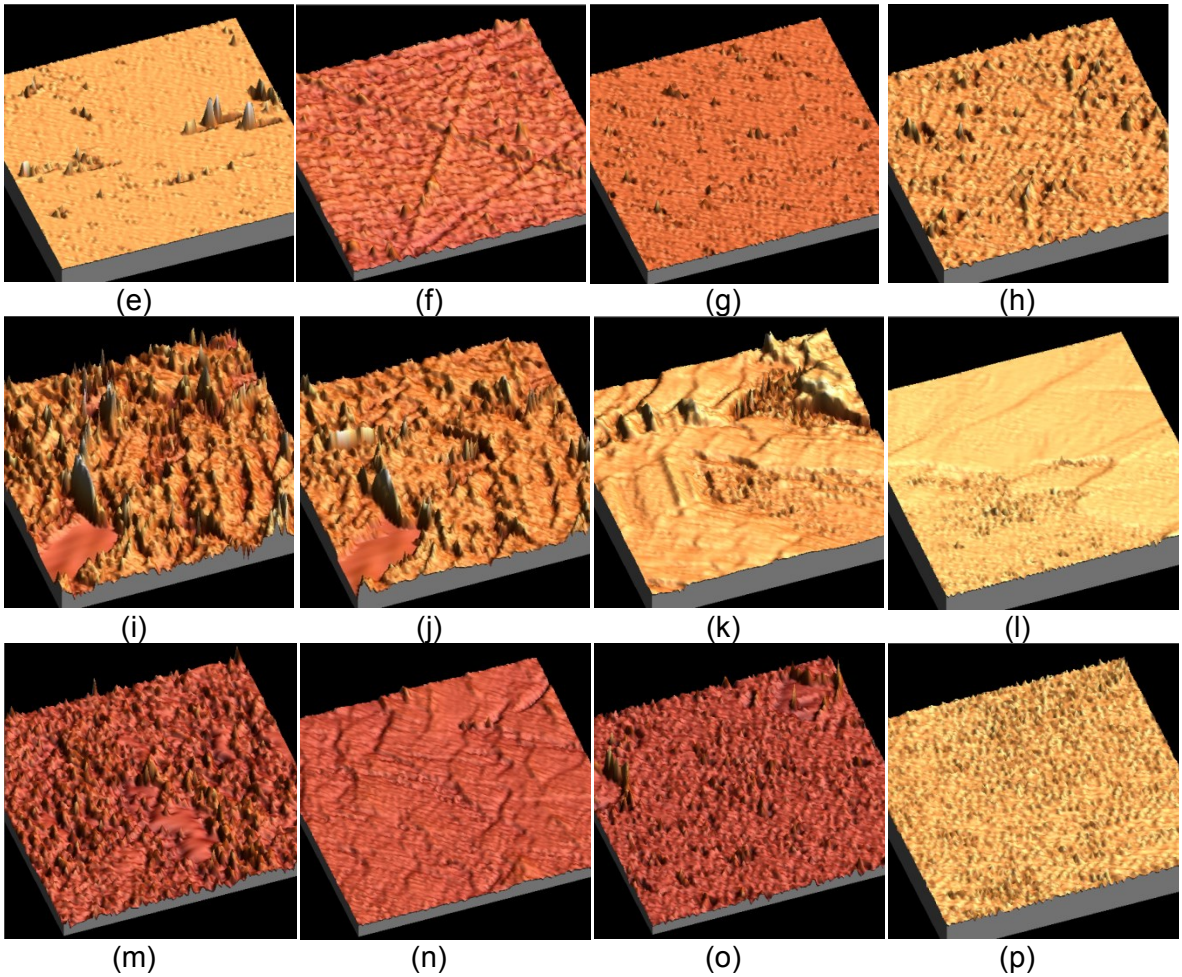

Figure A2.3 Surface pictures of four areas of the four zones illustrated in Figure A2.1 (i.e. aggregate, ASR products in macrocrack, ITZ and cement paste). : (a)(b)(c)(d) point 1,2,3,4 in the aggregate zone,_20 μm×20μm in size; (e)(f) points 1,2 in the cement paste zone_80 μm×80μm in size; (g)(h) points 3,4 in the cement paste zone,_20 μm×20μm in size; (i) (j) (k)points 1,2,3 in the interface zone, 10 μm×10μm in size; (l) point 4 in the interface zone, 100 μm×100μm in size; (m) point 1 in the macrocrack zone, 10μm×10μm in size; (n)(o) points 2,3 in the macrocrack zone, 100μm×100μm in size; (p) point 4 in the macrocrack zone, 200μm×200μm in size.

Table A2.2 reports the average measurements of the RMS values of the four zones.

Table A2.2 RMS values of the four zones in the specimen illustrated in Figure A2.1, i.e. macrocrack, aggregate, interface and cement paste (nm).

Zone \ Point	A	B	C	D	E	F
Macrocrack	60.9725	15.074	96.2279	368.252	152.459	147.888
Aggregate	1079.45	1213.86	282.939	36.4816		
Interface	756.13	677.491	644.123	897.663	321.455	
Cement paste	17.3206	20.2986	28.324	9.1188	23.035	

The before & after Gaussian filtered RMS values of different points in the 4 zones of the ASR-damaged concrete specimen are presented in Figure A2.4.

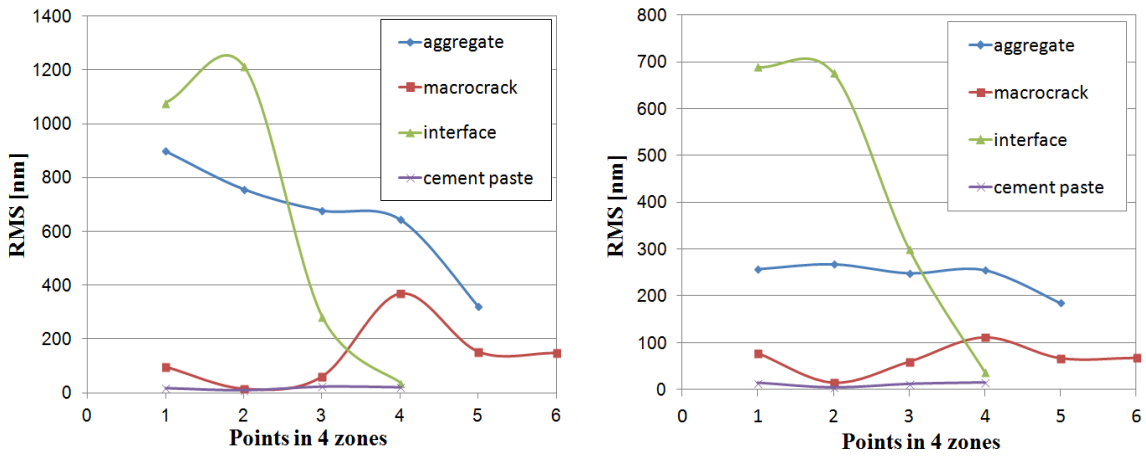

(a) (b)

Figure A2.4 RMS roughness values of points in the four different zones of the concrete specimen illustrated in Figure A2.1: (a) RMS values before filtering; (b) RMS values after filtering.

The *aggregate zone* roughness is significantly higher with an average value of 653nm. In the *interface* zone (ITZ), there is a large dispersion in the roughness values within the different areas of interface zone, as it ranges from a relatively flat area (RMS=36nm) to a very rough area (RMS=1079nm). The Figure shows P_q values which present Roughness-Mean-Square (RMS) roughness. The *macrocrack zone* shows a relatively low roughness with an average RMS value of 140nm. The smoothest part of this concrete sample is the *cement paste*, with the average value of 17nm. Three different pictures were taken in each one point of the four zones (macrocrack, interface, aggregate, cement paste) on the surface of the specimen. The RMS value of each point is the mean value of the 3 different pictures.

After Gaussian filter, the roughness values of these 4 zones in the ASR-damaged concrete sample are respectively: 242.394nm (aggregate), 66.88517nm (macrocrack), 425.298nm (ITZ), 11.4777nm (cement paste).

Appendix 3: Scanning Element Microscopy (SEM) tests in Article 1

SEM observations and analyses were carried out on the different zones illustrated in Figure A3.1, i.e. 6 zones on sample #1 (Figures A3.2 to A3.7) and 4 zones on sample #2 (Figures A3.8 to A3.10).

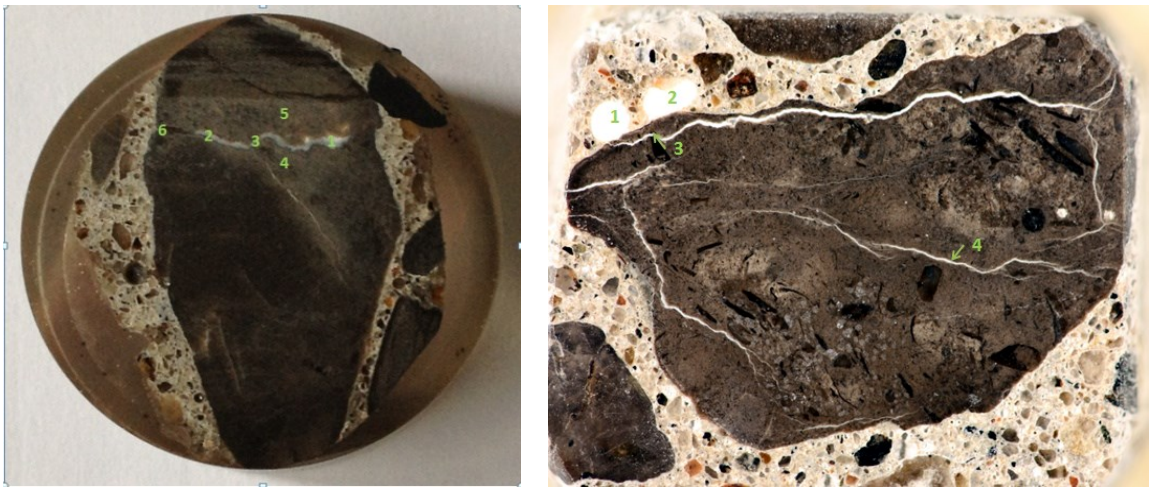

(a) (b)

Figure A3.1 (a) sample 1 with 6 analyzed zones in the white veinlet; (b) sample 2 with four analyzed zones.

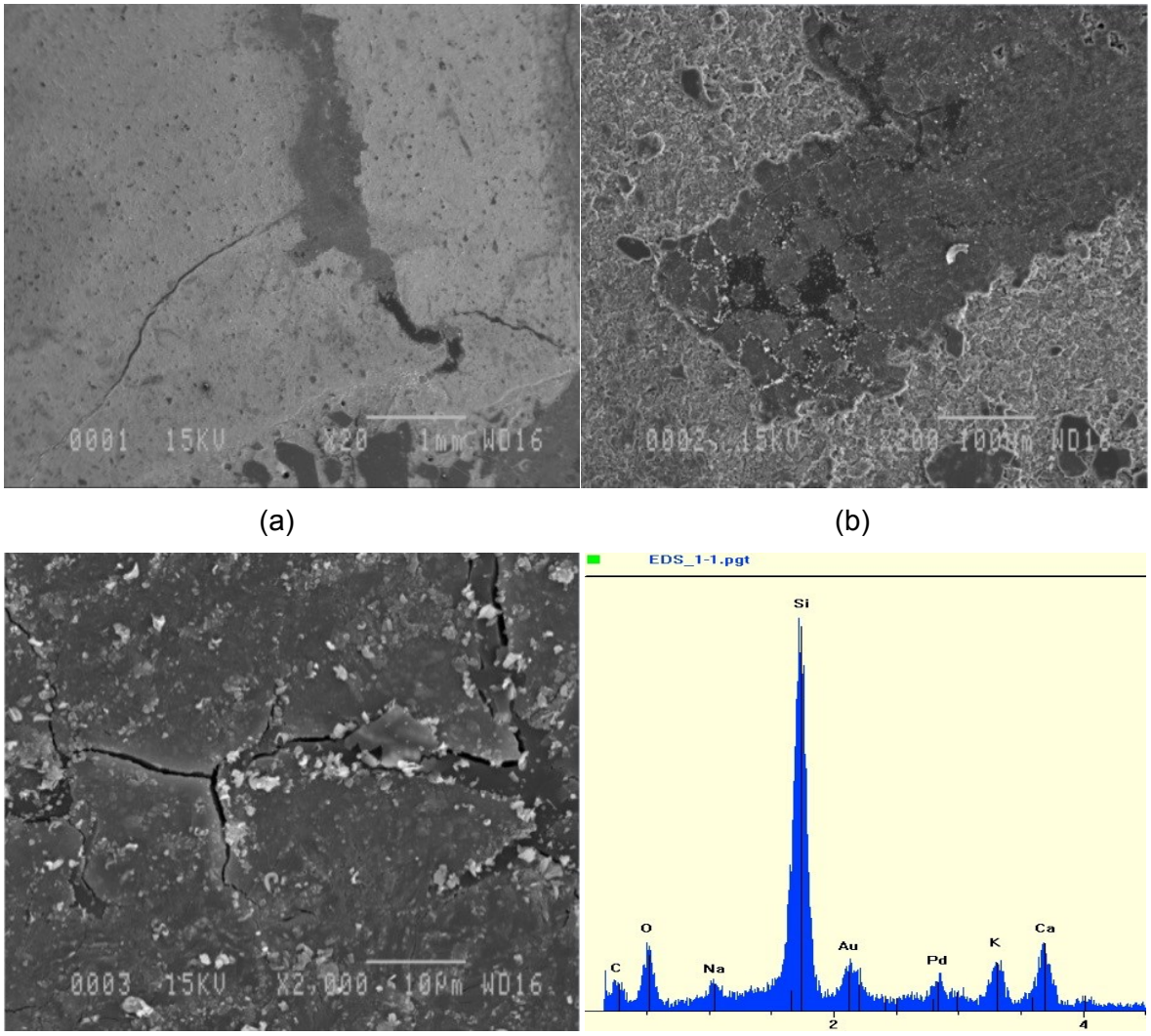

(a) (b)

(c) (d)

Figure A3.2 (a-c): SEM micrographs in secondary electron mode. *(a) General view of the veinlet (dark gray) within the aggregate particle (20x) (Sample 1 - zone 1 on Figure A3.1a); (b) enlargement of the central portion of the previous micrograph showing the veinlet (dark gray) (200x); (c) enlargement of the microtexture of the veinlet showing desiccation cracking (2000x); (d) EDS analysis of the material illustrated in (c). The main elements are Si, K, Ca and Na; despite the somewhat massive appearance of the product illustrated, this composition is quite typical of that of crystalline rosette-like alkali-silica reaction products.*

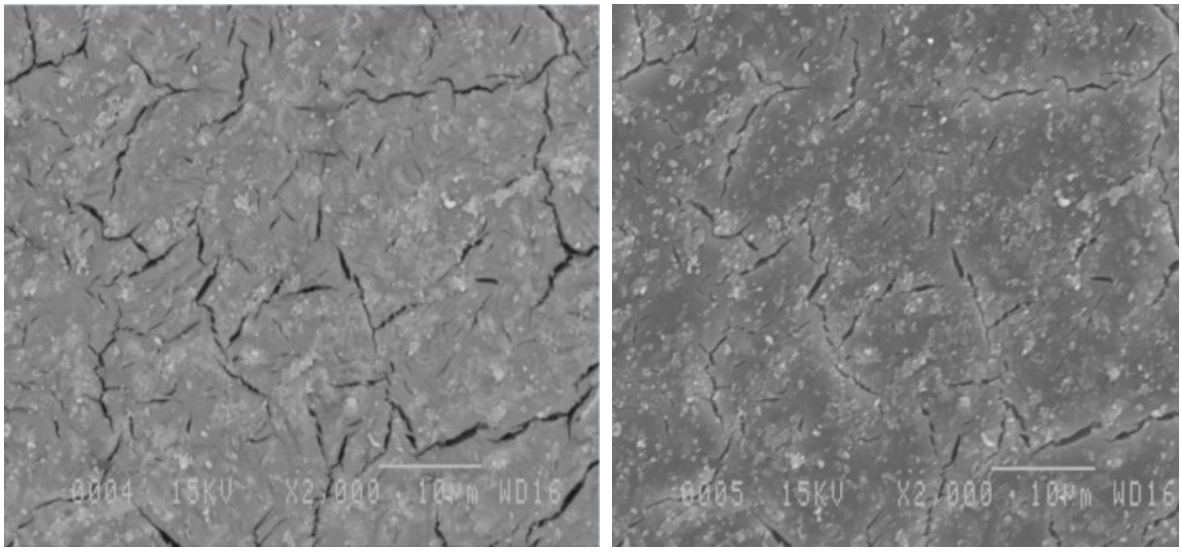

(a) (b)

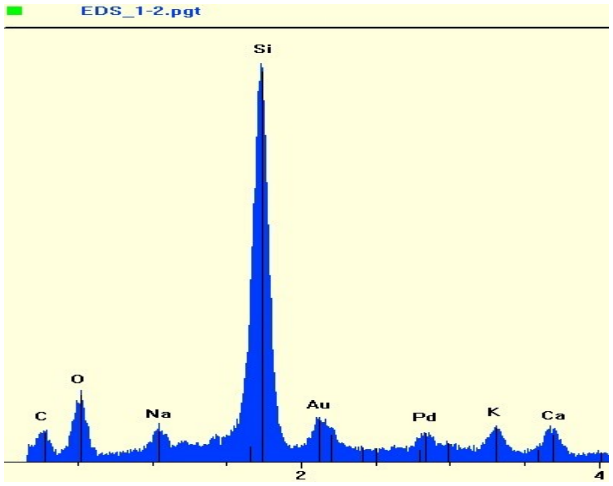

(c)

FigureA3.3 (a-b): SEM micrographs in secondary electron mode. Magnification (x2000) of the reaction products in the white veinlet (Sample 1 - zone 2 on Figure A3.1a); desiccation cracking is observed (2000x); (c) EDS analysis of the above products. The main elements are Si, K, Ca and Na; this composition is quite typical of that of crystalline rosette-like alkali-silica reaction products.

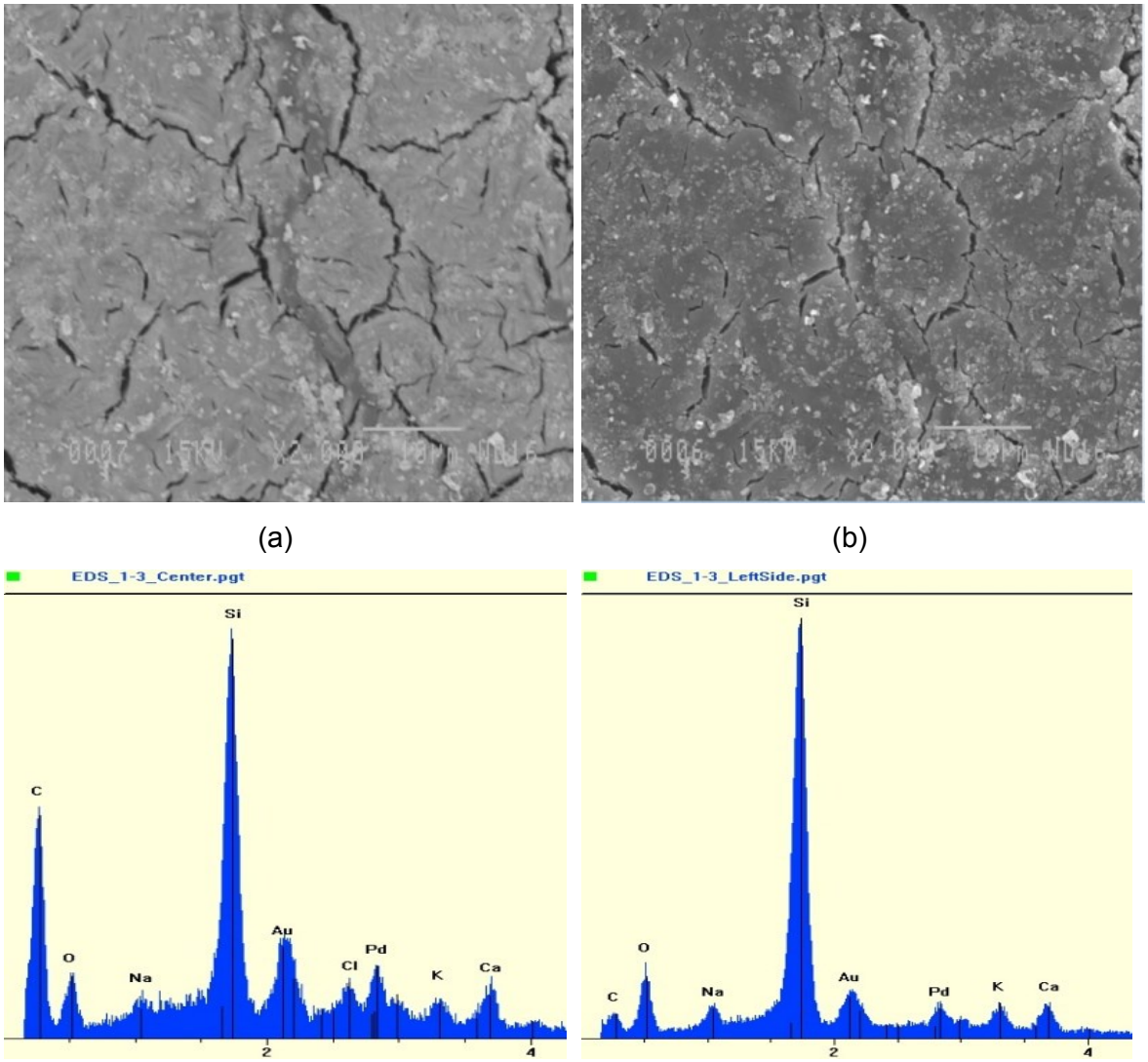

Figure A3.4 (a-b): SEM micrographs in secondary electron mode. (a & b) reaction products with desiccation cracking (2000x) (Sample 1 - zone 3 on Figure A3.1a); (c) EDS analysis of the above products, the center of the veinlet; (d) EDS analysis of the above products, the left side of the veinlet. (c-d) the main elements are Si, K, Ca and Na; this composition is quite typical of that of crystalline rosette-like alkali-silica reaction products.

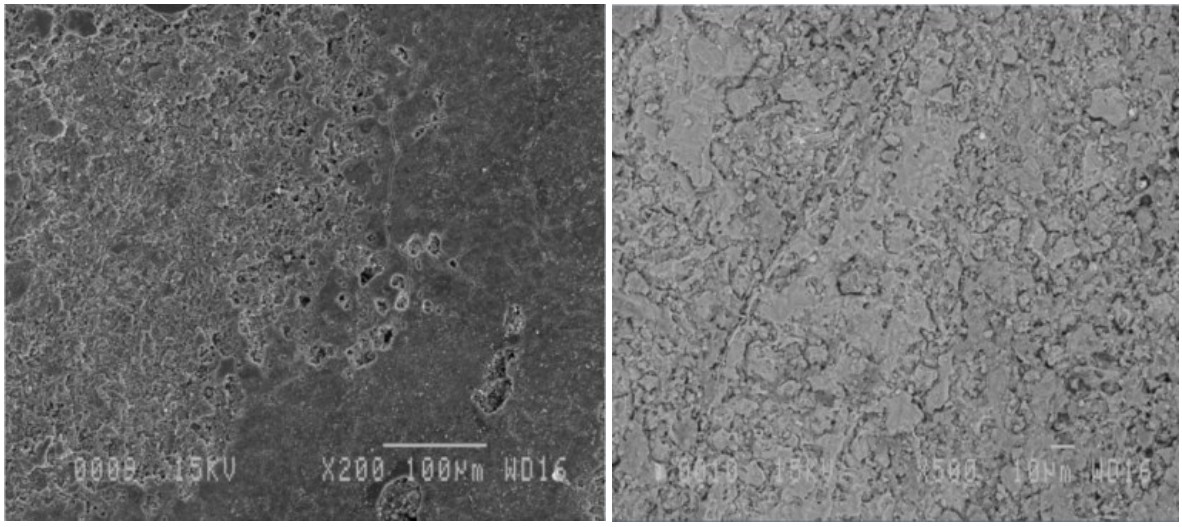

(a) (b)

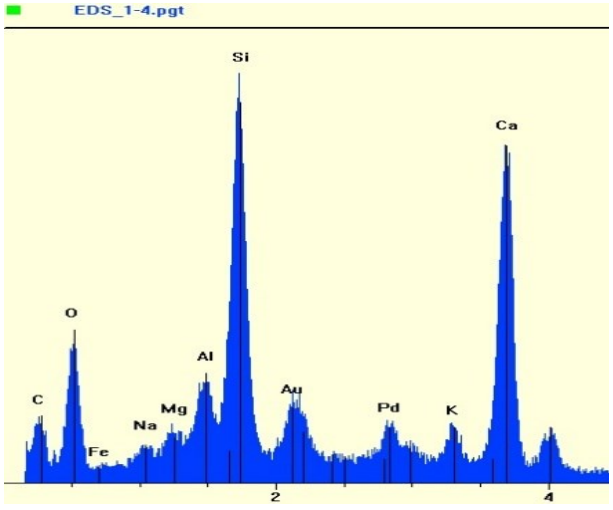

(c)

Figure A3.5: (a) SEM micrographs in secondary electron mode (200x) (Sample 1 - zone 4 on Figure A3.1a) the aggregate part near the macrocrack with veinlets: (b) SEM micrographs in secondary electron mode (500x) (Sample 1 - zone 4 on Figure A3.1a) the aggregate part near the macrocrack with veinlets; (c) EDS analysis of the zone from macrocrack with ASR products to the neighboring aggregate; the main elements are Si, K, Ca, Al and some Na.

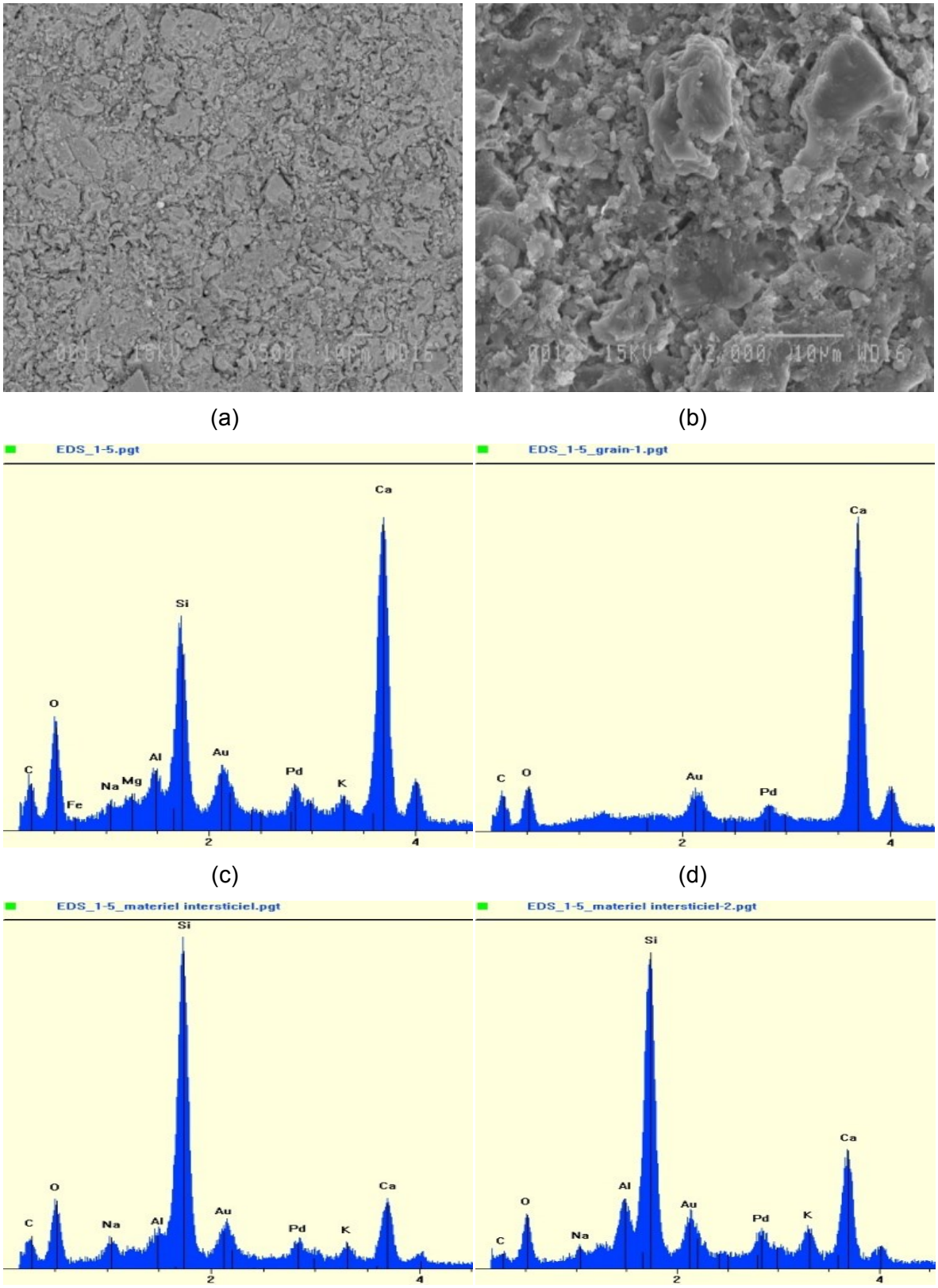

Figure A3.6: (a) SEM micrographs in secondary electron mode (500x) (Sample 1 - zone 5 on Figure

A3.1a) the transition zone from macrocrack with veinlet to the neighbouring aggregate; (b) SEM micrographs in secondary electron mode (2000x) (Sample 1 - zone 5 on Figure A3.1a) the transition zone from macrocrack with veinlet to the neighbouring aggregate; (c) EDS analysis of the transition zone from macrocrack with veinlet to the neighboring aggregate; the main elements are Si, K, Ca and, Al. (d) EDS analysis of a calcite grain; (e) EDS analysis of the material interstice 1 in the zone from macrocrack with veinlet to the neighbouring aggregate (near veinlet) ; the main elements are Si, K, Ca and Na; (f) EDS analysis of material interstice 1 in the zone from macrocrack with veinlet to the neighbouring aggregate (near veinlet); the main elements are Si, K, Ca and Na.

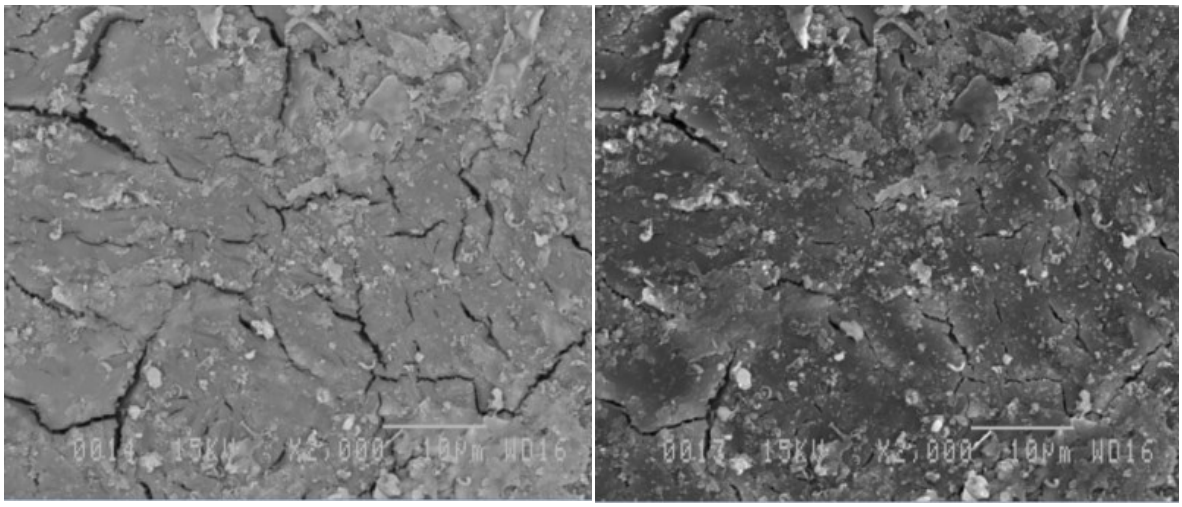

(a) (b)

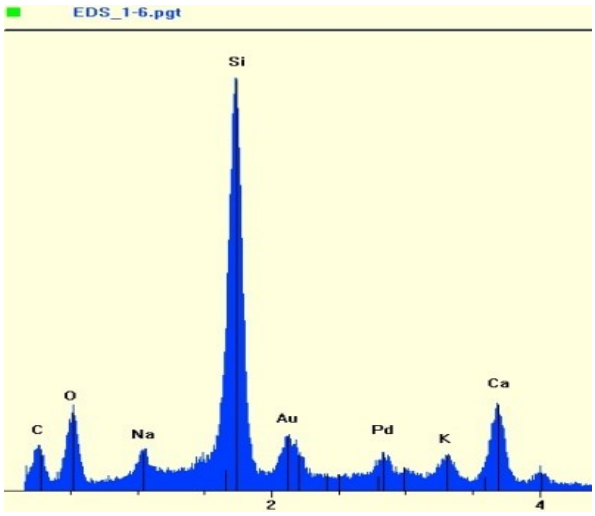

(c)

Figure A3.7 (a-b): SEM micrographs in secondary electron mode. Magnification of the reaction products in the white veinlet (Sample 1 - zone 6 on Figure A3.1a); desiccation cracking is observed (2000x); (c) EDS analysis of the above products. The main elements are Si, K, Ca and Na; this composition is slightly richer in calcium than that of typical crystalline rosette-like alkali-silica reaction products.

The sample 2's SEM tests analysis are presented below:

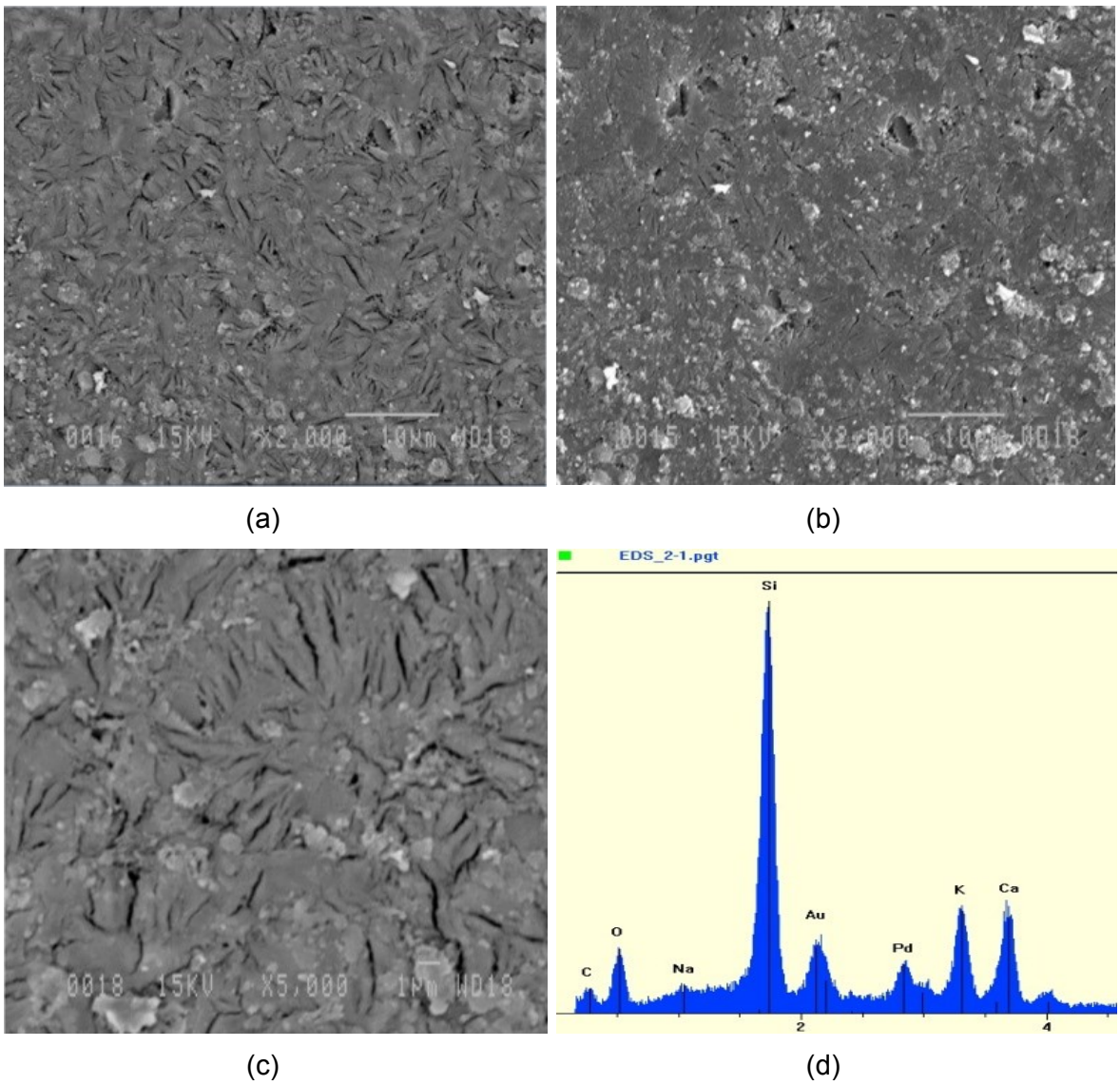

Figure A3.8 (a-c): SEM micrographs in secondary electron mode. Magnification of the reaction products in the white veinlet (Sample 2 - zone 3 on Figure A3.1b); desiccation cracking is observed (a-b: 2000x; c: x5000); (d) EDS analysis of the products illustrated in (a). The main elements are Si, K, Ca and some Na; this composition is typical of crystalline rosette-like alkali-silica reaction products.

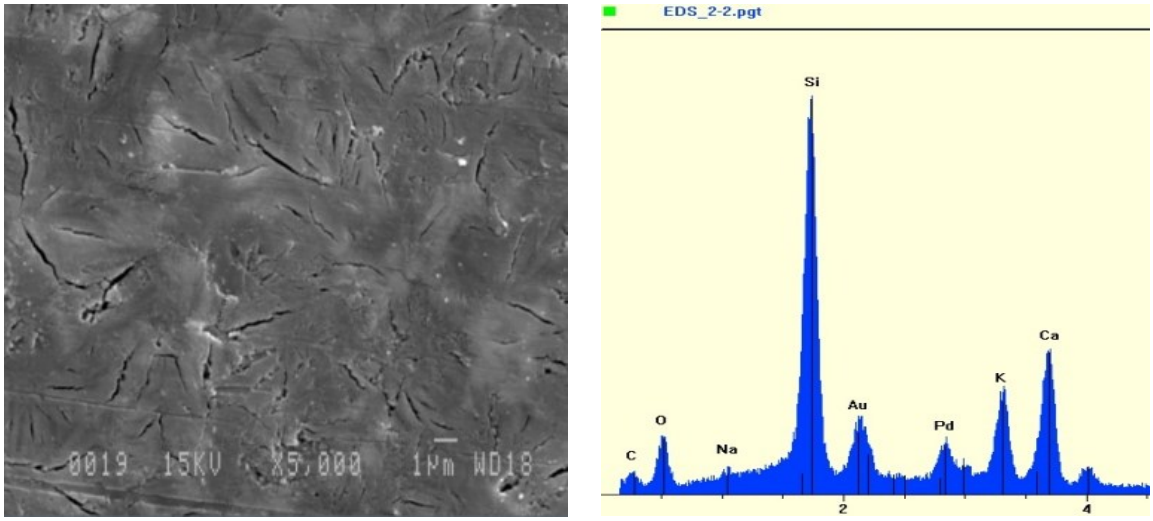

(a) (b)

Figure A3.9 (a): SEM micrographs in secondary electron mode. Magnification of the reaction products in the white veinlet (Sample 2 - zone 3 on Figure A3.1b); desiccation cracking is observed (5000x); (b) EDS analysis of the products illustrated in (a). The main elements are Si, K, Ca and some Na; this composition is typical of crystalline rosette-like alkali-silica reaction products.

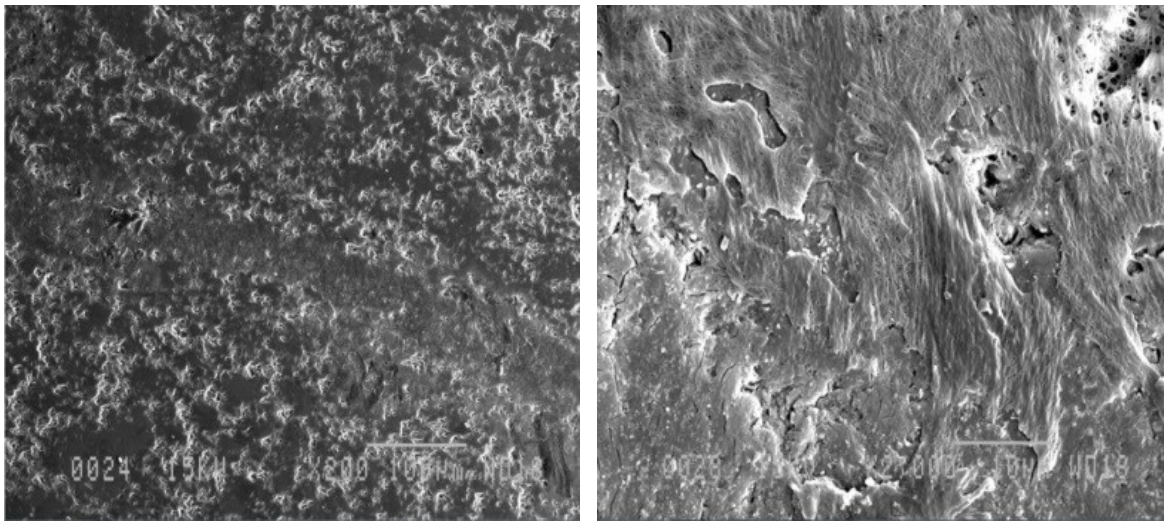

(a) (b)

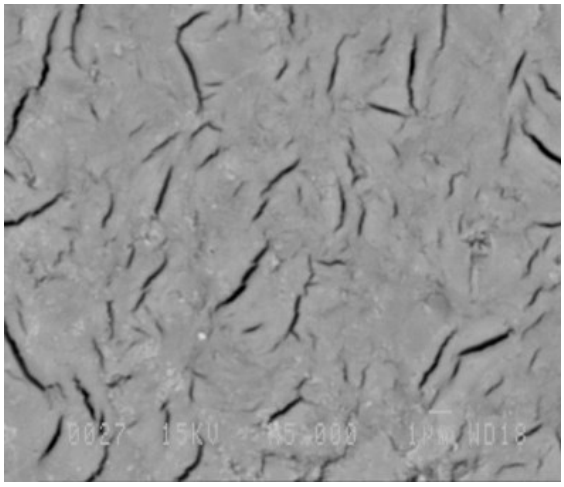

(c)

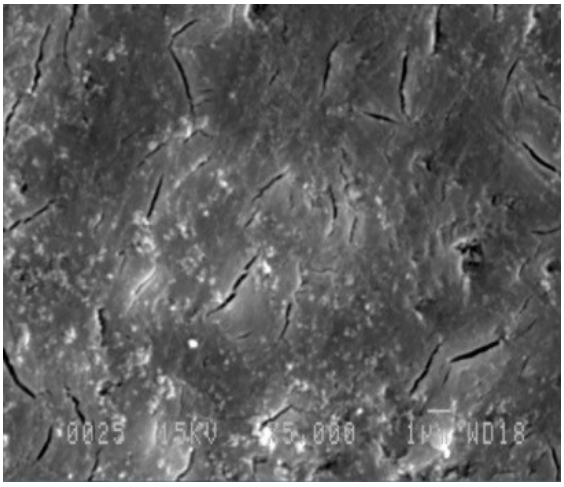

(d)

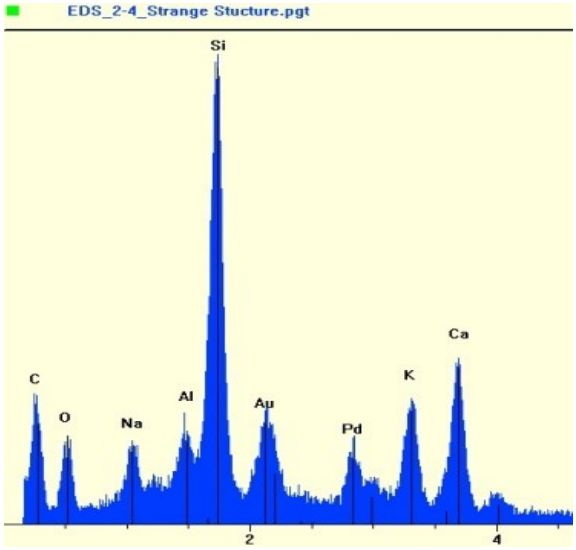

(e)

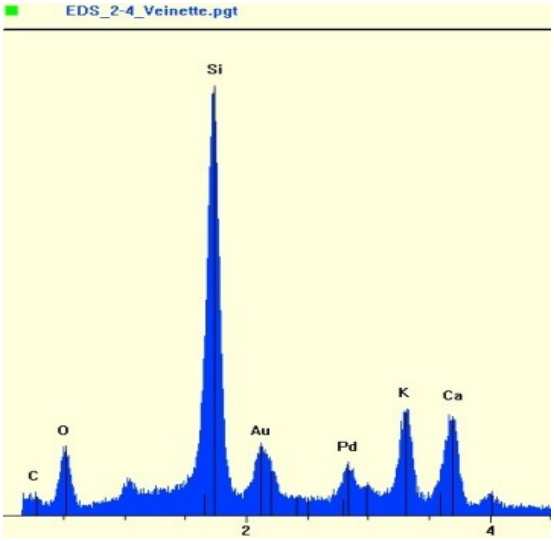

(f)

Figure A3.10 (a): SEM micrographs in secondary electron mode. Magnification of 200(Sample 2 – zone1 on Figure A3.1b); (b) SEM micrographs in secondary electron mode. Magnification of 2000 (Sample 2 – zone 1 on Figure A3.1b); (c-d) Magnification of the reaction products in the white veinlet (Sample 2 - zone 3 on Figure A3.1b); desiccation cracking is observed (5000x); (e) EDS analysis of the products illustrated in (c). The main elements are Si, K, Ca and some Na; this composition is typical of crystalline rosette-like alkali-silica reaction products; (f) EDS analysis of the products illustrated in (d). The main elements are Si, K, Ca and some Na; this composition is typical of crystalline rosette-like alkali-silica reaction products.

Appendix 4: Scanning Element Microscope (SEM) tests in Article 3

The results of the SEM examination of the test sample used in Phase 3 of this project are summarized in the micrographs A4.1 to A4.4:

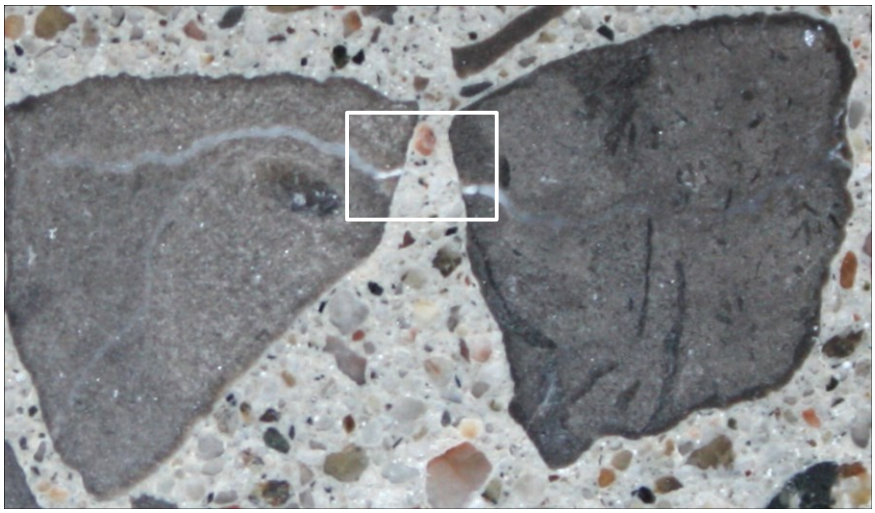

Figure A4.1: Micrograph of the sample analyzed under the SEM. Two aggregate particles can be seen with white veinlets connecting from one aggregate particle to the other through the cement paste.

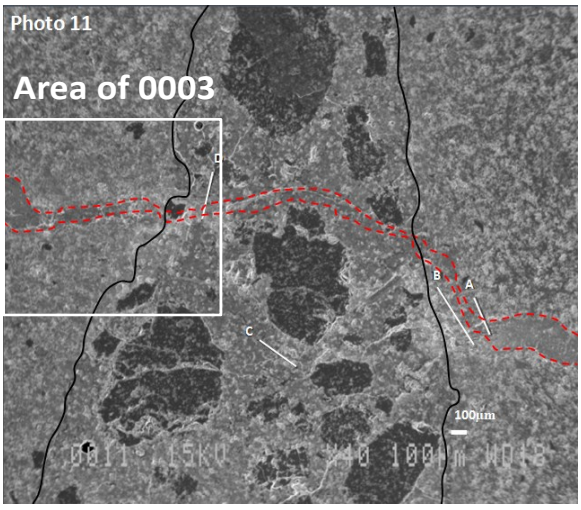

(a)

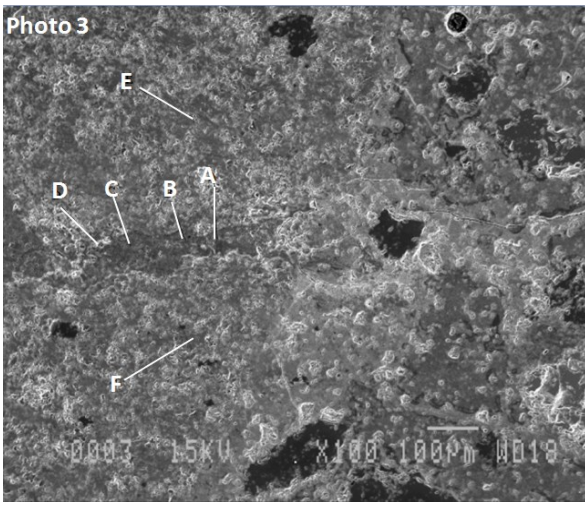

(b)

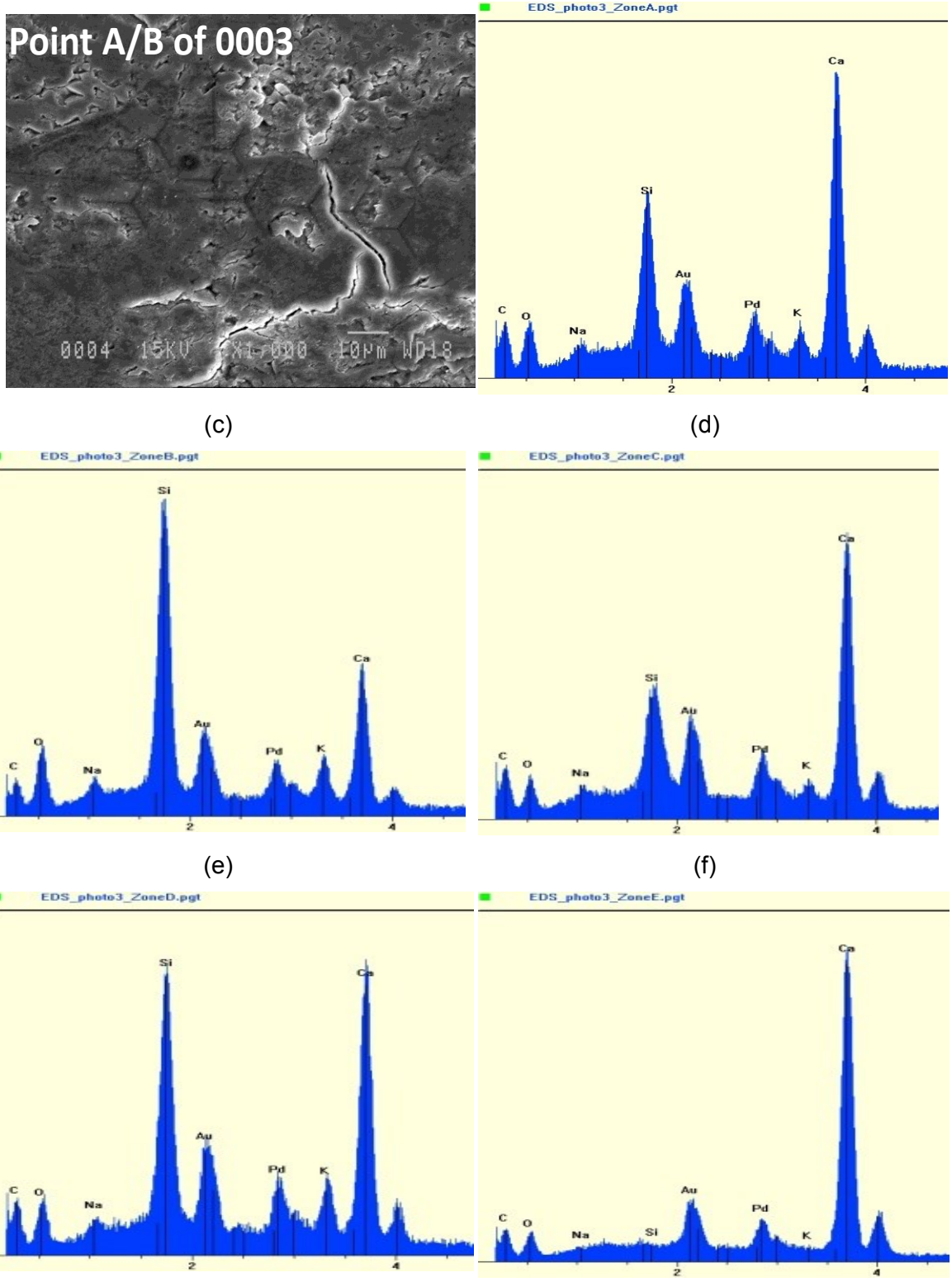

Figure A4.2 (a) micrograph 0011 (40x) (secondary electron mode): an overview of the area examined (compare with Figure A4.1); (b) micrograph 0003 (100x) with zones A to D marked inside the white veinlet within the aggregate particle on the left of (a). Zones E and F correspond to the limestone

aggregate; (c) micrograph 0004 (1000x) showing reaction products near Zones A and B (secondary electron mode); (d) EDS corresponding to Zone A in micrograph 0003 (high calcium gel); (e) EDS corresponding to Zone B in micrograph 0003 (transition between high calcium gel and crystalline rosette-like products); (f) EDS corresponding to Zone C in micrograph 0003 (high calcium gel); (g) EDS corresponding to Zone D in micrograph 0003 (alkali-rich high-calcium gel); (h) EDS corresponding to Zone E in photo 0003 - zones E and F correspond to the limestone aggregate – calcium in calcite.

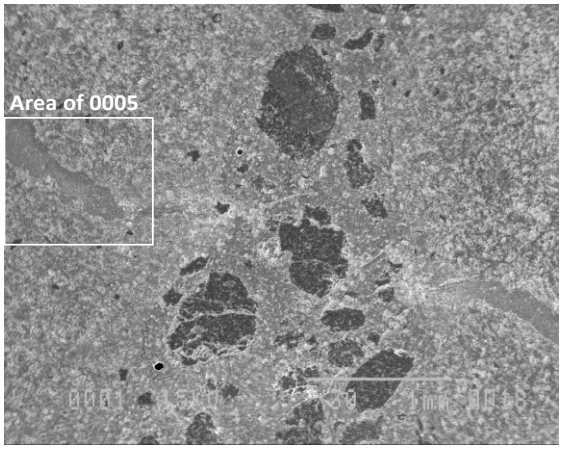

(a)

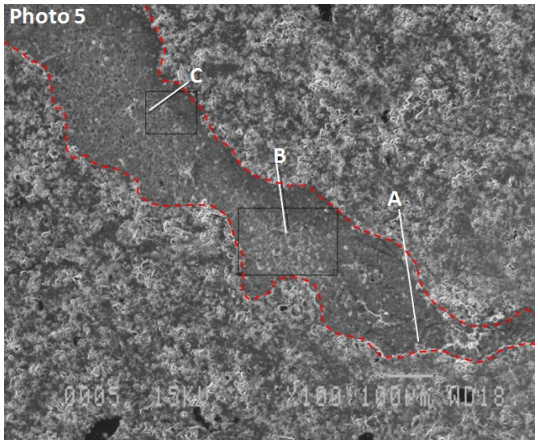

(b)

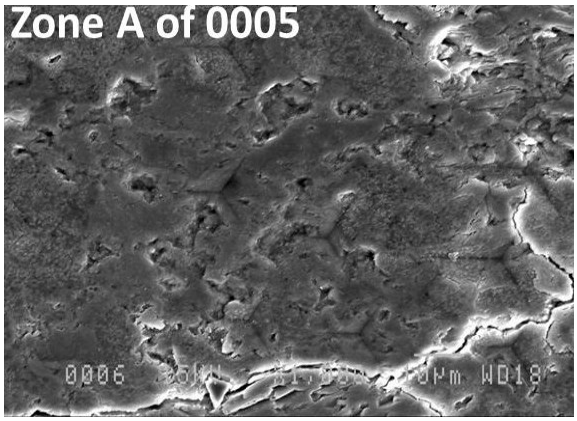

(c)

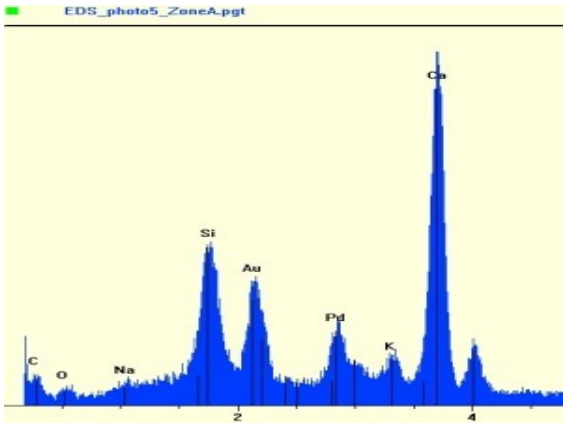

(d)

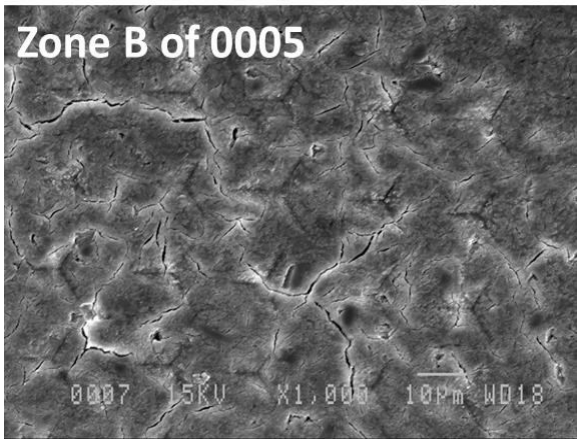

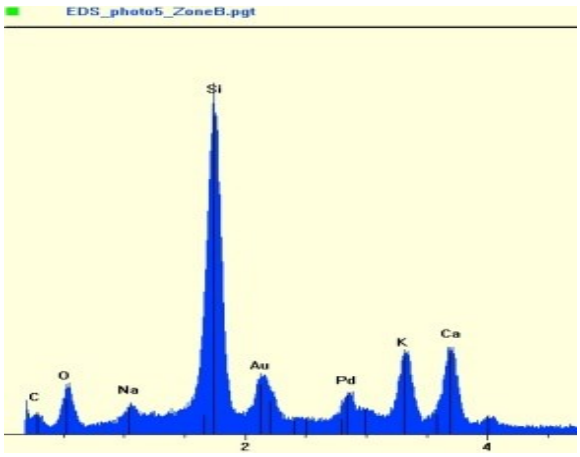

(e) (f)

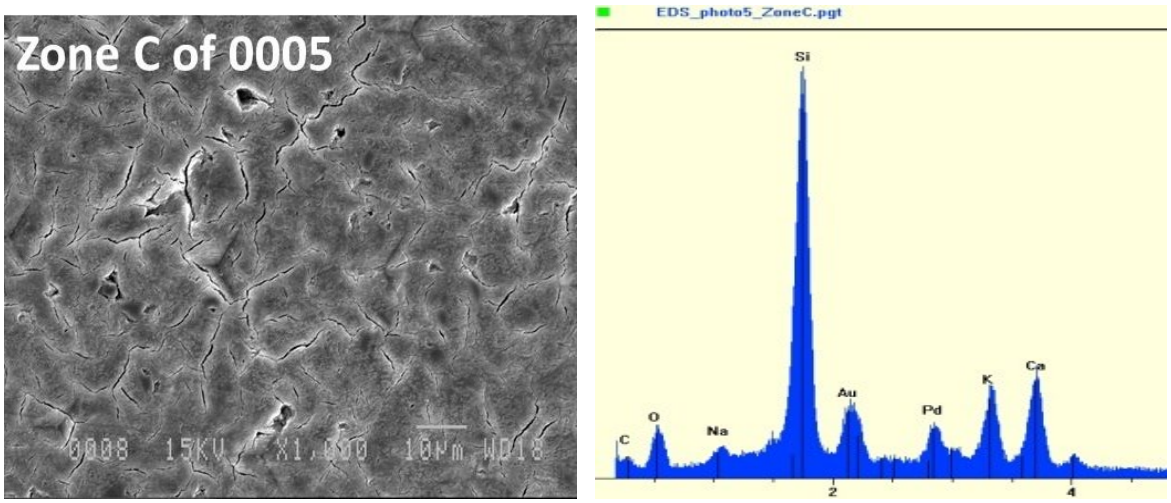

(g) (h)

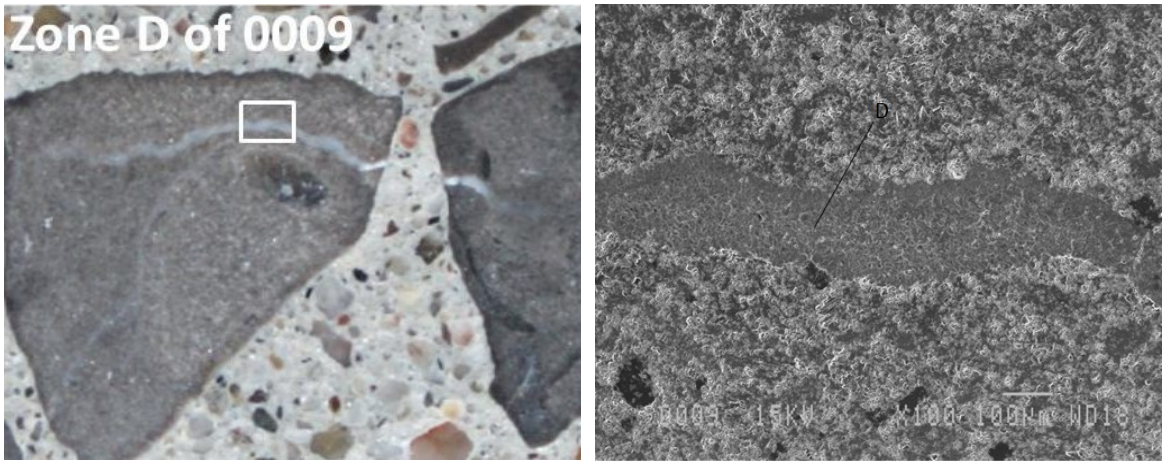

(i) (j)

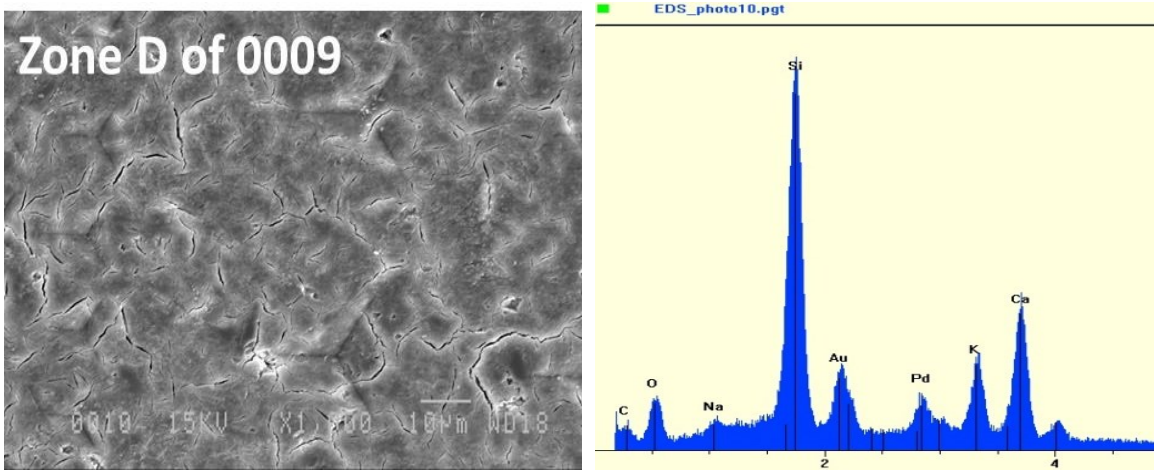

(k) (l)

Figure A4.3 (a) micrograph 0001 (30x) showing the two aggregate particles (both sides) with the cement paste in the middle, as well as the area of micrograph 0005 (secondary electron mode); (b)

micrograph 0005 (100x) illustrating the crack filled with secondary reaction product in the aggregate particle on the left side of micrograph (a), along with zones A,B,C used for further analyses (secondary electron mode); (c) micrograph 0006 (1000x) illustrating zone A of micrograph 0005 (secondary electron mode); (d) EDS corresponding to Zone A of micrograph 0005 (high-calcium gel with alkalis); (e) micrograph 0007 (1000x) corresponding to Zone B of micrograph 0005 (secondary electron mode); some desiccation cracking is visible; (f) EDS corresponding to Zone B of micrograph 0005 (the main elements are Si, K, Ca and some Na; this composition is typical of crystalline rosette-like alkali-silica reaction products); (g) micrograph 0008 (1000x) corresponding to Zone C of micrograph 0005 (secondary electron mode); some desiccation cracking is visible; (h) EDS corresponding to Zone C of micrograph 0005 (the main elements are Si, K, Ca and some Na; this composition is typical of crystalline rosette-like alkali-silica reaction products); (i) photograph of the polished concrete specimen showing Zone D of micrograph 0009 (illustrated in (j)); (j) micrograph 0009 (100x) corresponding to central part of white veinlet in micrograph (i) (secondary electron mode); (k) micrograph 0010 (1000x) corresponding to Zone D of micrograph 0009 (secondary electron mode); some desiccation cracking is visible; (h) EDS corresponding to micrograph 0010 (the main elements are Si, K, Ca and some Na; this composition is typical of crystalline rosette-like alkali-silica reaction products).

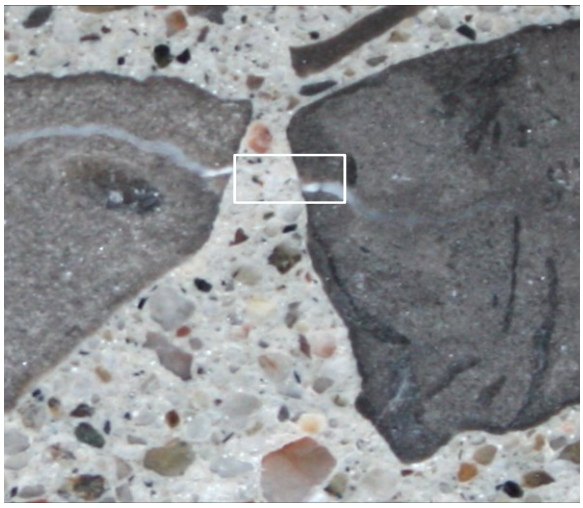

(a)

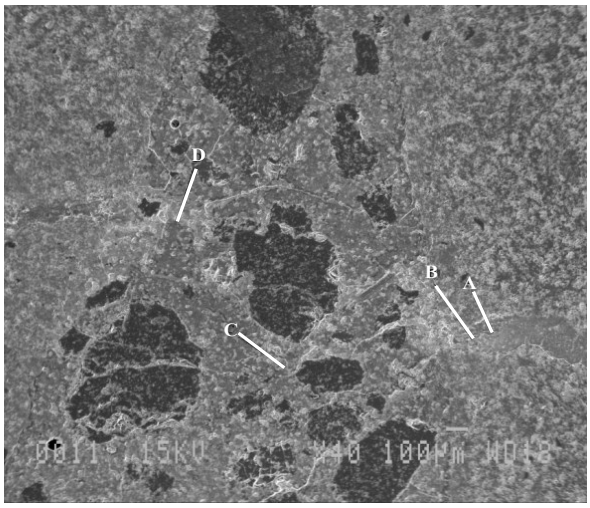

(b)

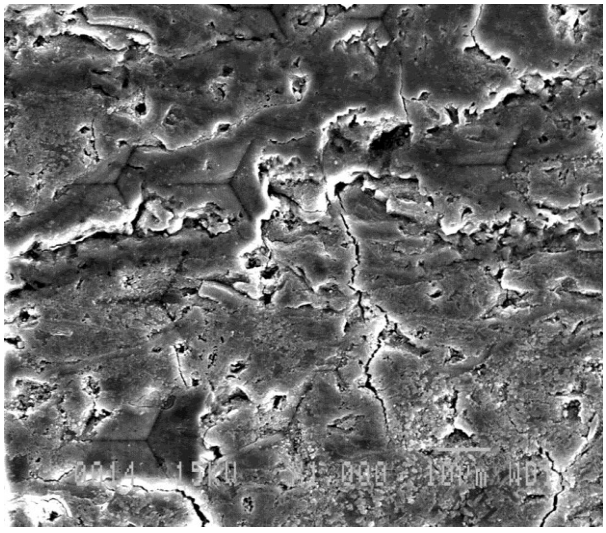

(c)

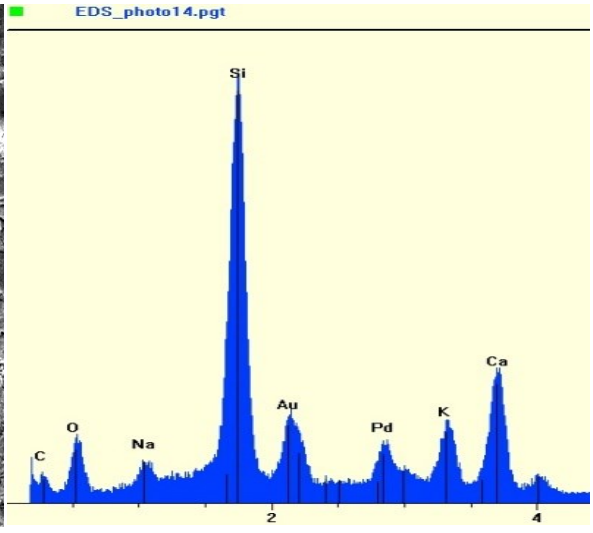

(d)

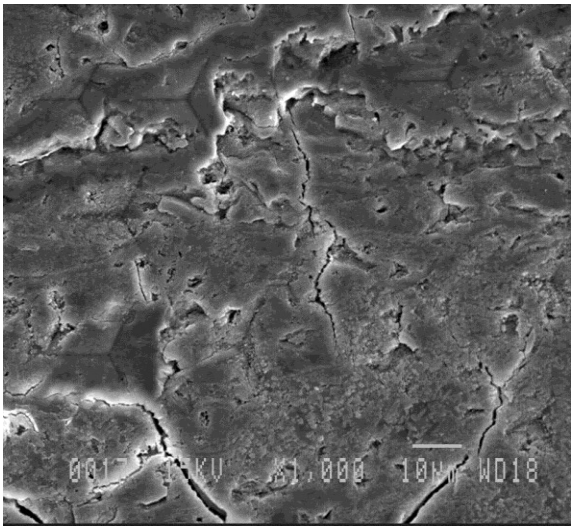

(e)

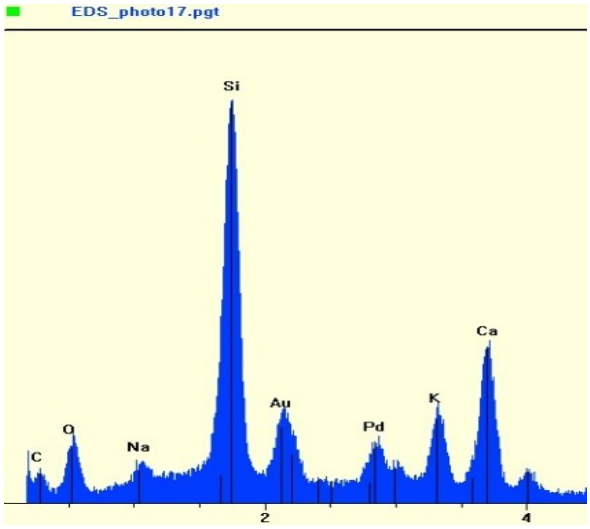
EDS_photo17.pgt
Si
Ca
Au
K
O
Pd
Na
C
2
4

(f)

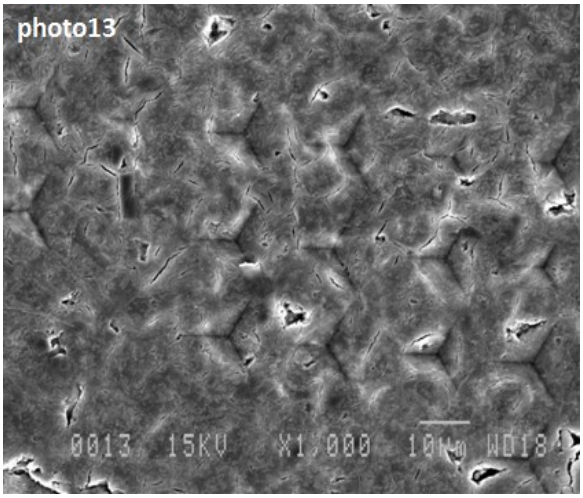
photo13

(g)

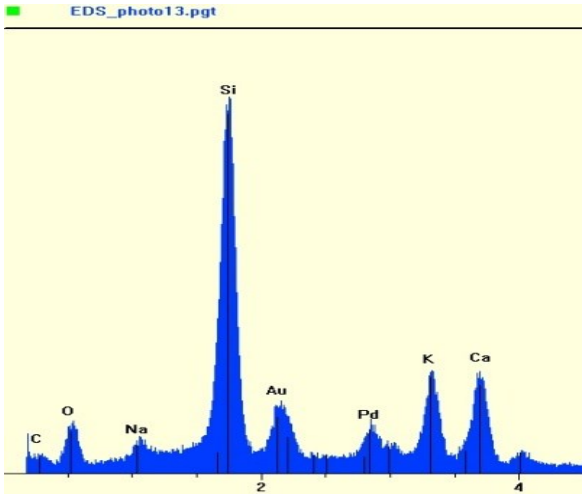
EDS_photo13.pgt
Si
K
Ca
Au
O
Pd
Na
C
2
4

(h)

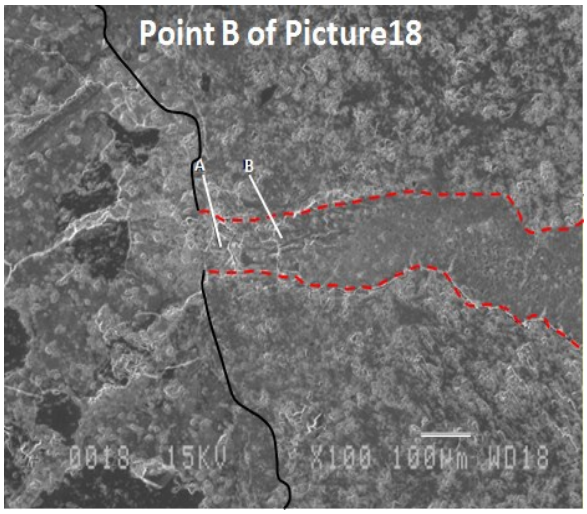
Point B of Picture18
A
B

(i)

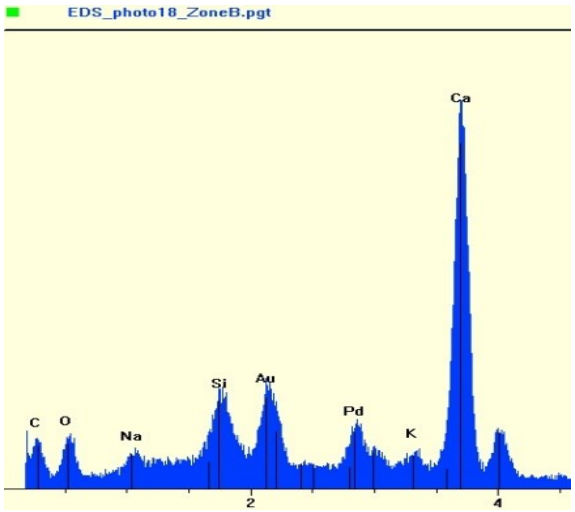
EDS_photo18_ZoneB.pgt
Ca
Si
Au
Pd
C
O
Na
K
2
4

(j)

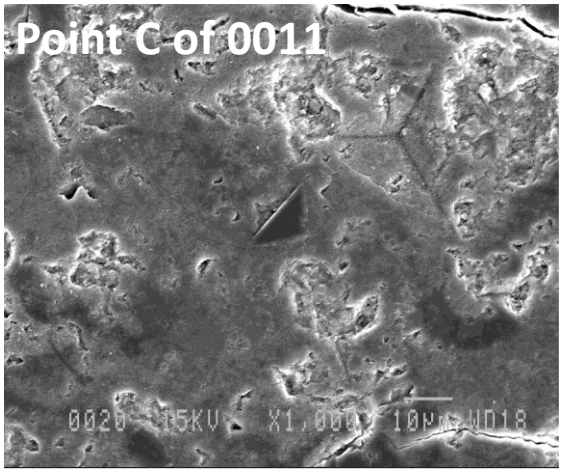

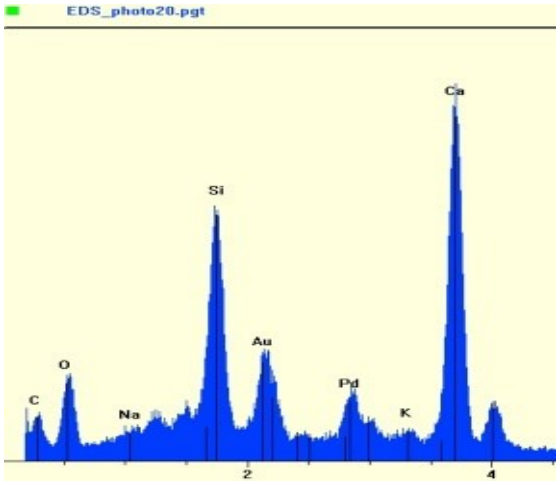

(k) (l)

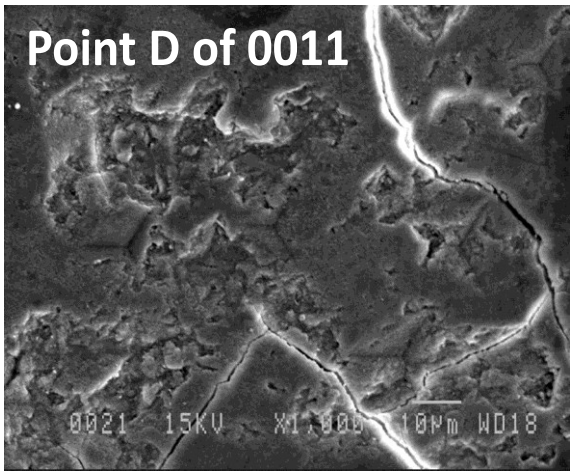

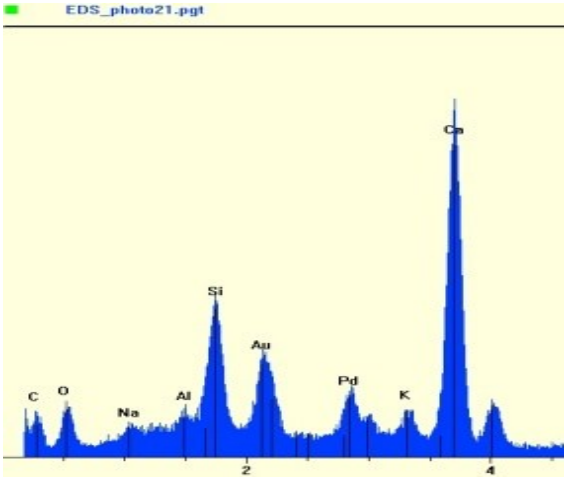

(m) (n)

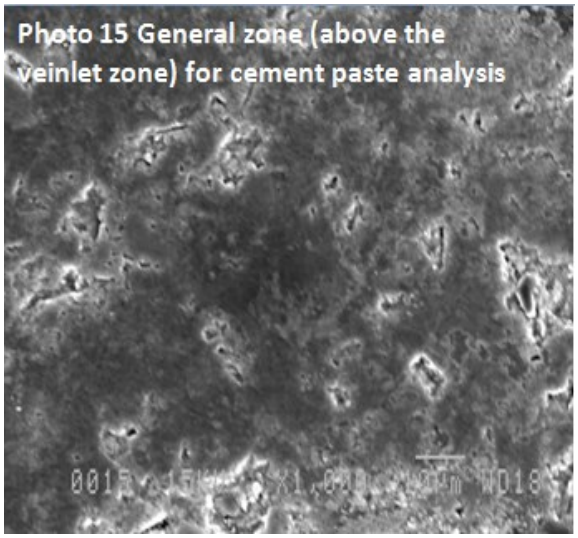

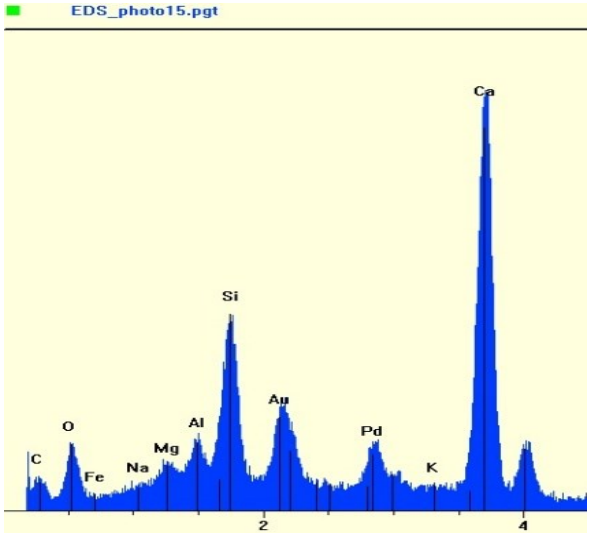

(o) (p)

Figure A4.4 (a) photograph of the polished concrete specimen showing the global zone (white box)

described hereafter; (b) micrograph 0011 (40x) showing the two aggregate particles (both sides) with the cement paste in the middle, as well as zones A to D used for further analyses (A&B: white veinlet within the aggregate particle on the right side; C&D: crack filled with gel in the cement paste) (secondary electron mode); (c) micrograph 0014 (1000x) showing zone A of micrograph 0011 (secondary electron mode); (d) EDS corresponding to Zone A of micrograph 0011 (the main elements are Si, K, Ca and some Na; this composition is typical of crystalline rosette-like alkali-silica reaction products with, perhaps, a slightly higher calcium content); (e) micrograph 0017 (1000x) showing zone B of micrograph 0011 (secondary electron mode); (f) EDS corresponding to Zone B of micrograph 0011 (the main elements are Si, K, Ca and some Na; this composition is typical of crystalline rosette-like alkali-silica reaction products with, perhaps, a slightly higher calcium content); (g) micrograph 0012 (1000x) showing the reaction products in the veinlet on the right of zone A of micrograph 0011 (secondary electron mode); (h) EDS corresponding to reaction products illustrated in (g) (the main elements are Si, K, Ca and some Na; this composition is typical of crystalline rosette-like alkali-silica reaction products); (i) micrograph 0018 - close-up view of the area where the microcrack filled with reaction products in the aggregate particle on the right side of micrograph 0011 (k) reaches the cement paste (100x) (secondary electron mode); (j) EDS corresponding to zone B of micrograph 0018 (the main elements are Ca, Si, and some K and Na; this composition is believed to correspond to that of a high calcium alkali-silica reaction gel); (k) micrograph 0020 (1000x) showing zone C of micrograph 0011 (secondary electron mode); (l) EDS corresponding to Zone C of micrograph 0011 (the main elements are Ca, Si with, perhaps some K and Na; this composition is thought to correspond to that of high-calcium gel / CSH; (m) micrograph 0021 (1000x) showing zone D of micrograph 0011 (secondary electron mode); (n) EDS corresponding to Zone D of micrograph 0011 (the main elements are Ca, Si with some K and Na; this composition is thought to correspond to that of high-calcium gel containing some alkalis in the cement paste; (o) micrograph 0015 (1000x) showing a zone of cement paste way above the area potentially affected by "alkali-silica gel impregnation" (secondary electron mode); (n) EDS corresponding to the zone illustrated in micrograph 0015 (o) (the main elements are Ca, Si with some Al but no K and Na; this composition is thought to correspond to that of cement paste hydrates, mainly CSH.